

# **THIN FILM ENGINEERING FOR TRANSPARENT THIN FILM TRANSISTORS**

**Khairi Muftah Abusabee**

A thesis submitted in partial fulfilment of the requirements of  
Nottingham Trent University for the degree of Doctor of Philosophy

School of Science and Technology  
Nottingham Trent University

**January 2014**

## **Copyright Statement**

---

This work is the intellectual property of the author, and may also be owned by the research sponsor and/or Nottingham Trent University. You may copy up to 5% of this work for private study, or personal, non-commercial research. Any re-use of the information contained within this document should be fully referenced, quoting the author, title, university, degree level and pagination. Queries or requests for any other use, or if a more substantial copy if required, should be directed in the first instance to the author.

## Abstract

---

Zinc oxide (ZnO) and Indium Gallium Zinc Oxide (IGZO) thin films are of interest as oxide semiconductors in thin film transistor (TFT) applications, due to visible light transparency, and low deposition temperature. There is particular interest in ZnO and IGZO based transparent TFT devices fabricated at low temperature on low cost flexible substrates. However, thermal annealing processes are typically required to ensure a good performance, suitable long term stability, and to control the point defects which affect the electrical characteristics. Hence there is interest in post deposition processing techniques, particularly where alternatives to high temperature thermal treatments can be utilised in combination with low temperature substrates. This thesis presents the results of a series of experimental studies as an investigation into photonic (excimer laser) processing of low temperature ZnO and IGZO thin films deposited by RF magnetron sputtering and/or by high target utilisation sputtering (HiTUS), to optimise the microstructure and electrical properties for potential use in thin film electronic applications.

ZnO thin films were grown at various deposition parameters by varying oxygen flow rates, RF power, oxygen concentration, and growth temperatures. Subsequently, the films were subjected to three different annealing processes: (i) Thermal Annealing (furnace): samples were thermally annealed in air at temperatures ranging from 300 °C to 880 °C for 1 hour. (ii) Rapid Thermal Annealing: samples were annealed in nitrogen and oxygen environment at temperatures of 600 °C, 740 °C, 880 °C, and 1000 °C, and dwell times of 1-16 s. (iii) Excimer laser annealing: samples were annealed at ambient conditions using a Lambda Physik 305i 284 nm, 20 ns pulse KrF excimer laser with a beam delivery system providing a homogenised 10 mm x 10 mm uniform irradiation at the sample plane. Processing was undertaken at fluences in the range of 0 to 350 mJ/cm<sup>2</sup> at single and multiple pulses.

IGZO thin films were also investigated following RF magnetron deposition without intentional substrate heating and at various other deposition conditions, followed by laser processing in air at laser energy densities in the range of 0 to 175 mJ/cm<sup>2</sup> with single pulse.

Processed ZnO films were characterised by room temperature photoluminescence excitation which exhibited that laser annealing at high fluences resulted in suppression of the observed visible deep level emission (DLE) with evolution of a strong UV near band emission (NBE) peak, indicating a reduction of intrinsic defects without film degradation or materials loss that occurred by thermal and rapid thermal annealing. Also the intensity of the NBE peak was strongly influenced by the films growth temperature, with the results showing that as the growth temperature increased beyond ambient; the intensity of the resultant NBE peak decreased as a function of laser energy. TEM studies demonstrate that laser processing provides a controlled in-depth crystallisation and modification of ZnO films. Therefore, laser processing is shown to be a suitable technique to control the crystal microstructure and defect properties as a function of two lasers processing parameters (fluence, number of pulses) – realising optimised film properties as a localised region isolated from the substrate or sensitive underlying layers. In terms of electrical properties, the results indicated a significant drop in sheet resistance as a function of laser anneal from highly resistive (>5 MΩ/sq.) to about 860 Ω/sq.

To produce IGZO thin films without intentional substrate heating with lowest sheet resistance as a function of laser processing, low deposition pressure, low oxygen concentration, and high RF power are required. Room temperature Hall effect mobility of 50 nm thick IGZO increased significantly as the laser energy density increased from 75 mJ/cm<sup>2</sup> to 100 mJ/cm<sup>2</sup> at single pulse reaching values of 11.1 cm<sup>2</sup>/Vs and 13.9 cm<sup>2</sup>/Vs respectively.

## Acknowledgements

---

All praise and thanks to Allah the Almighty, for giving me strength and ability to complete this study.

I would like to express my heartfelt appreciation and gratitude towards my Director of Studies Prof. Wayne Cranton, for providing me this great opportunity to undertake this project. None of this work would have been possible without his support and guidance. I am deeply grateful to him for taking so much care of his student's personal career and promoting their results. It was a great pleasure and a humbling experience to have Dr. Demosthenes Koutsogeorgis in the supervision team of my project. I am deeply grateful to him for his availability and help, not only in the research, but also in all other aspects of the PhD. Next, special thanks for Dr. Robert Ranson for his supervision, guidance and encouragement throughout my work.

I would like to thank Dr. Costas Tsakonas who helped me to carry out my work in the lab successfully, and trained me to use the lab equipment. I am also very grateful to him for his support and invaluable knowledge throughout my work.

Many thanks to the nice people I worked in collaboration with for this researcher project: Dr. Catherine Ramsdale, and Dr. Peter Downs (from PragmatIC Printing Ltd) for their support and for providing samples, TFT devices, and helping with the characterisation. Also would like to acknowledge Dr. Flora Li (from Cambridge University) for providing samples.

I sincerely thank my extended friends and research colleagues: Dr. Gabriel Boutaud, Dr. Nikolaos Kalfagiannis, Dr Neranga Abeywickrama, and Mr Salem EL Hamali, for their assistance and helpful discussions during the course of my work.

Finally, and most importantly I would like to express my deep gratitude to my family (brothers, and sisters), all my relatives and friends, for their endless encouragement, and for supporting me whenever fear or discouragement were looming over me.

## List of Publications

---

C. Tsakonas, W. Cranton, F. Li, K. Abusabee, A. Flewitt, D. Koutsogeorgis and R. Ranson, "Intrinsic photoluminescence from low temperature deposited zinc oxide thin films as a function of laser and thermal annealing," *J. Phys. D*, vol. 46, pp. 095305, 2013.

K. Abusabee, W. Cranton, C. Tsakonas, S. El-hamali, D. Koutsogeorgis, and R. Ranson, "The effect of laser annealing on photoluminescence of ZnO deposited by RF magnetron sputtering at various rf power and substrate temperatures". To be submitted to *Journal of physics D: Applied Physics*.

### Conferences:

Abusabee K., Cranton WM., Tsakonas C., Koutsogeorgis D.C., Ranson R., Down P.F., Ramsdale C.M., Price R.D, Photonic processing of RF magnetron sputtered indium gallium zinc oxide thin films, TCM 2012, 4th International Symposium on Transparent Conductive Materials, Crete, Oct. 2012.

K. Abusabee, WM. Cranton, C. Tsakonas, F. Li, A. Flewitt, D. Koutsogeorgis, R. Ranson, Thin Film Device Engineering for Transparent Thin Film Transistors, Electronic Display Conference, Nuremberg, Germany, March 2012 [ awarded 3<sup>rd</sup> place in Robert Bosch Student Paper Competition].

## List of Abbreviations

---

a-Si	Amorphous silicon
a-Si:H	Amorphous silicon hydrogenated
Al <sub>2</sub> O <sub>3</sub>	Aluminium oxide
Ar	Argon
AMLCD	Active matrix liquid crystal display
ALD	Atomic layer deposition
AOS	Amorphous oxide semiconductor
Au	Gold
au	Arbitrary unit
BCE	Back channel-etch
BE	Binding energy
CB	Conduction Band
CBM	Conduction band minimum
CdSe	Cadmium sulphide
CCS	Constant current stress
COMS	Complementary metal oxide semiconductor
Cr	Chromium
DLE	Deep level emission
DOS	Density of states
Dt	Dwell time
ELA	Excimer laser anneal
E <sub>g</sub>	Energy gap
ES	Etch stopper
FWHM	Full width at half maximum
FPD	Flat panel display
GCA	Gradual channel approximation
Ge	Germanium
Hz	Hertz

HiTUS	High target utilisation system
He:Cd	Helium cadmium
IGZO	Indium gallium zinc oxide
IGO	Indium gallium oxide
InO <sub>3</sub>	Indium oxide
KE	Kinetic energy
KrF	Krypton fluoride
LCD	Liquid crystal display
MOSFET	Metal oxide semiconductor field effect transistor
MFC	Mass flow controller
NBE	Near band edge emission
NTU	Nottingham Trent University
n-type	Negative type semiconductor
Nd:YAG	Neodymium : yttrium aluminium garnet Nd:Y <sub>3</sub> Al <sub>5</sub> O <sub>12</sub>
n	Refractive index
O <sub>2</sub>	Oxygen
OLED	Organic light emitting diode
O <sub>i</sub>	Oxygen interstitial
PL	photoluminescence
Poly-Si	Ploy silicon
PLS	Plasma launch system
PLD	Pulsed laser deposition
PECVD	Plasma enhanced chemical vapour deposition
RF	Radio frequency
RTA	Rapid thermal anneal
RT	Room temperature
Si	Silicon
SiO <sub>2</sub>	Silicon dioxide
SnO <sub>2</sub>	Tin oxide

SiN	Silicon nitride
sccm	Standard cubic per centimetre
s	Second
TA	Thermal anneal
TCOs	Transparent conducting oxide
TFT	Thin film transistor
TEM	Transmission electron microscopy
UV	Ultraviolet
V	Voltage
VB	Valance band
$V_{zn}$	Zinc Vacancy
$V_o$	Oxygen vacancy
W	Watt
XRD	X-ray diffraction
XPS	X-ray photoelectron spectrometry
XeCl	Xenon chloride
$Y_2O_3$	Yttrium oxide
ZnO	Zinc oxide
ZTO	Zinc tin oxide
ZIO	Zinc indium oxide
$Zn_i$	Zinc interstitial

## List of Symbols

---

$\text{\AA}$	Angstrom (1X10 <sup>-10</sup> metres)
$C_o$	Capacitance per unit area of dielectric layer
$^{\circ}\text{C}$	Degree Celsius
D	Drain
eV	Electron volt
J	Joule
mTorr	MilliTorr
nm	Nanometer
$Q_i$	Induced charge
S	Source
S	Sub-threshold swing
$V_D$	Drain voltage
$V_G$	Gate voltage
$V_{GS}$	Gate-source voltage
$V_{DS}$	Drain-source voltage
$V_D$	Drain voltage
$V_G$	Gate voltage
$I_{DS}$	Drain current
$V_{th}$	Threshold voltage
W	Width
L	Length
$\lambda$	Wavelength
$\mu$	Mobility
$\theta$	Angle
$\Omega/\text{sq}$	Ohms/square
$\phi$	Spectrometer work function

# List of Contents

---

<b>Copyright Statement</b> .....	<b>ii</b>
<b>Abstract</b> .....	<b>iii</b>
<b>Acknowledgements</b> .....	<b>v</b>
<b>List of Publications</b> .....	<b>vi</b>
<b>List of Abbreviations</b> .....	<b>vii</b>
<b>List of Symbols</b> .....	<b>x</b>
<b>List of Contents</b> .....	<b>xi</b>
<b>List of Figures</b> .....	<b>xv</b>
<b>List of Tables</b> .....	<b>xxii</b>
<b>Chapter 1</b> .....	<b>1</b>
<b>Introduction</b> .....	<b>1</b>
<b>1.1 Introduction</b> .....	<b>1</b>
<b>1.2 Problem definition</b> .....	<b>3</b>
<b>1.3 Project Aim</b> .....	<b>4</b>
<b>1.4 Project Objectives</b> .....	<b>4</b>
<b>1.5 Structure of the Thesis</b> .....	<b>4</b>
<b>Chapter 2</b> .....	<b>7</b>
<b>Background and Literature Review</b> .....	<b>7</b>
<b>2.1 Introduction</b> .....	<b>7</b>
<b>2.2 The basic structure of TFTs and operation theory</b> .....	<b>8</b>
2.2.1 Overview of TFT principles of operation .....	<b>8</b>
2.2.2 Basic structure of TFTs.....	<b>8</b>
2.2.3 Types of thin film transistors TFTs .....	<b>9</b>
2.2.4 The operation theory of TFTs .....	<b>12</b>
<b>2.3 Materials used in TFT devices</b> .....	<b>16</b>
<b>2.4 Density of states (DOS)</b> .....	<b>18</b>

2.4.1	Density of states of amorphous silicon hydrogenated a-Si:H	18
2.4.2	Density of states of amorphous indium gallium zinc oxide a-IGZO	19
<b>2.5</b>	<b>Oxide thin film properties</b>	<b>20</b>
2.5.1	ZnO crystal structure	20
2.5.2	Amorphous structure of IGZO	21
<b>2.6</b>	<b>ZnO and IGZO layer based TFTs</b>	<b>23</b>
2.6.1	Zinc oxide (ZnO) layers based TFTs	23
2.6.2	Multicomponent amorphous oxides of indium gallium zinc oxide (IGZO) based TFTs	29
<b>2.7</b>	<b>Sputtering</b>	<b>34</b>
2.7.1	RF magnetron sputtering	36
<b>2.8</b>	<b>Conclusions</b>	<b>38</b>
<b>Chapter 3</b>		<b>39</b>
<b>Experimental Techniques</b>		<b>39</b>
<b>3.1</b>	<b>Introduction</b>	<b>39</b>
<b>3.2</b>	<b>Thin film deposition</b>	<b>39</b>
3.2.1	High target utilisation sputtering HiTUS	40
3.2.2	RF magnetron sputtering	42
<b>3.3</b>	<b>Excimer laser annealing (ELA)</b>	<b>46</b>
<b>3.4</b>	<b>IGZO-TFT fabrication on silicon</b>	<b>48</b>
<b>3.5</b>	<b>Thin film characterisation and analytical techniques</b>	<b>50</b>
3.5.1	Photoluminescence (PL)	50
3.5.2	Transmission electron microscopy (TEM)	53
3.5.3	X-ray diffraction (XRD)	54
3.5.4	X-ray photoelectron spectroscopy (XPS)	58
3.5.5	Four point probe (4PP) measurements	58
3.5.6	Hall Effect measurements	61
<b>3.6</b>	<b>Conclusion</b>	<b>62</b>
<b>Chapter 4</b>		<b>63</b>
<b>ZnO Thin Films by HiTUS</b>		<b>63</b>
<b>4.1</b>	<b>Introduction</b>	<b>63</b>
<b>4.2</b>	<b>Photoluminescence characterisation</b>	<b>63</b>

4.2.1	Photoluminescence of thermally annealed HiTUS ZnO films .....	64
4.2.2	Photoluminescence of rapidly thermal annealed ZnO films .....	68
4.2.3	Photoluminescence of laser annealed HiTUS ZnO films .....	72
<b>4.3</b>	<b>Transmission electron microscopy (TEM) study .....</b>	<b>78</b>
4.3.1	Transmission electron microscopy (TEM) of laser annealed HiTUS ZnO 41 sccm films .....	78
4.3.2	Transmission electron microscopy (TEM) of laser annealed HiTUS ZnO films (41 sccm 200 nm) .....	81
4.3.3	Transmission electron microscopy (TEM) of HiTUS ZnO films (41 sccm) thermally annealed at 880 °C for 1 hour.....	83
<b>4.4</b>	<b>X- ray diffraction characterisation.....</b>	<b>84</b>
<b>4.5</b>	<b>Discussion.....</b>	<b>87</b>
<b>Chapter 5 .....</b>		<b>89</b>
<b>ZnO Thin Films by RF Magnetron Sputtering .....</b>		<b>89</b>
<b>5.1</b>	<b>Introduction.....</b>	<b>89</b>
<b>5.2</b>	<b>Laser anneal of films deposited at various RF power .....</b>	<b>90</b>
<b>5.3</b>	<b>PL of thermal annealed ZnO films deposited at various substrate temperatures .....</b>	<b>97</b>
<b>5.4</b>	<b>PL of laser annealed ZnO films deposited at various substrate temperatures .....</b>	<b>99</b>
<b>5.5</b>	<b>XRD characterisation of laser annealed ZnO films deposited at various substrate temperatures .....</b>	<b>101</b>
<b>5.6</b>	<b>Transmission electron microscopy (TEM) characterisation.....</b>	<b>106</b>
5.6.1	Transmission electron microscopy (TEM) of ZnO films grown at room temperature .....	107
5.6.2	Transmission electron microscopy (TEM) of ZnO films grown at 300 °C.....	110
<b>5.7</b>	<b>Discussion.....</b>	<b>113</b>
<b>Chapter 6 .....</b>		<b>116</b>
<b>Electrical Characterisation of ZnO and IGZO.....</b>		<b>116</b>
<b>6.1</b>	<b>Introduction.....</b>	<b>116</b>
<b>6.2</b>	<b>Microstructure and electrical properties characterisation of ZnO films deposited on silicon dioxide substrates.....</b>	<b>117</b>
6.2.1	PL characterisation of thermal annealed ZnO films deposited at RT and 400 °C. ....	117
6.2.2	PL characterisation of laser annealed ZnO films deposited at RT, and 400 °C .....	118

6.2.3	X- ray diffraction (XRD) characterisation .....	119
6.2.4	Four point probe measurements (4PP) .....	123
<b>6.3</b>	<b>Electrical properties of laser annealed IGZO thin films.....</b>	<b>124</b>
6.3.1	Electrical properties of laser annealed IGZO (2:2:1) and (1:1:1) films.....	124
6.3.2	Hall Effect characterisation.....	129
<b>6.4</b>	<b>Electrical properties of thermal and laser annealed IGZO–TFTs.....</b>	<b>131</b>
6.4.1	Thermal annealed IGZO–TFTs.....	134
6.4.2	Laser annealed IGZO –TFTs.....	136
<b>6.5</b>	<b>Discussion.....</b>	<b>139</b>
<b>Chapter 7 .....</b>		<b>141</b>
<b>Conclusion and Future Work.....</b>		<b>141</b>
7.1	Introduction.....	141
7.2	Key Outcomes.....	142
7.3	Future work .....	146
<b>List of references .....</b>		<b>148</b>
<b>Appendices.....</b>		<b>160</b>
Appendix A: Derivation of TFT drain current at linear regime .....		160
Appendix B: PL spectra of ZnO deposited at 20% O <sub>2</sub> in Ar, RT, 2 mTorr at various RF powers .....		162

## List of Figures

---

<i>Figure 2.1: Schematic of a bottom gate TFT (a) cross section, (b) top view, (c) 3D view.....</i>	<i>9</i>
<i>Figure 2.2: Types of TFTs (a) staggered top-gate, (b) staggered bottom-gate, (c) coplanar bottom-gate, (d) coplanar top-gate .....</i>	<i>10</i>
<i>Figure 2.3: The structure of etch stopper, and back channel – etched TFTs . .....</i>	<i>11</i>
<i>Figure 2.4: Diagram shows the main types of TFTs. ....</i>	<i>12</i>
<i>Figure 2.5: Shows the <math>I_{DS}</math> vs <math>V_{DS}</math> characteristic curves, for various values of <math>V_{GS}</math> and for n-channel TFTs enhancement type.....</i>	<i>14</i>
<i>Figure 2.6: Shows the non-linear saturation.....</i>	<i>15</i>
<i>Figure 2.7: Transfer characteristics of n-type TFT. ....</i>	<i>16</i>
<i>Figure 2.8: Schematic model of subgap DOS of a-Si:H, adapted from [14] . ....</i>	<i>16</i>
<i>Figure 2.9: Schematic electronic structure of a-IGZO density of states fro as-deposited, adapted from [52]. ....</i>	<i>20</i>
<i>Figure 2.10: Hexagonal wurtzite ZnO structure. Large gray shaded and small black spheres denote O and Zn atoms, respectively .....</i>	<i>21</i>
<i>Figure 2.11: Schematic orbital structure of carrier transport path in: (a) covalent semiconductor "silicon". (b) Post transition metal oxide semiconductor .....</i>	<i>22</i>
<i>Figure 2.12: The concept of crystal grain growth of ZnO films as a function of thermal annealing:(a) as-deposited, (b) thermal annealed above 500 °C, adapted from[65]..</i>	<i>28</i>
<i>Figure 2.13: Sputtering process (adapted from [78]). ....</i>	<i>35</i>
<i>Figure 2.14: Illustration of the phenomena taking place during deposition by RF magnetron sputtering (adapted from [85]) .....</i>	<i>37</i>
<i>Figure 3.1: Schematic diagram of the HiTUS system (adapted from [87]). ....</i>	<i>42</i>
<i>Figure 3.2: Schematic diagram of RF magnetron sputtering system. ....</i>	<i>43</i>
<i>Figure 3.3: Thickness monitoring setup by interferometer. ....</i>	<i>45</i>
<i>Figure 3.4: Schematic diagram of KrF excimer laser setup. ....</i>	<i>48</i>

<i>Figure 3.5: The cross section of IGZO –TFT showing the concept of patterning pre and post laser anneal for the fabrication of TFTs devices.</i>	50
<i>Figure 3.6: Principle of photoluminescence transitions [100].</i>	51
<i>Figure 3.7: Schematic diagram of PL setup.</i>	51
<i>Figure 3.8: PL spectra of ZnO showing peaks of NBE and DLE emissions.</i>	52
<i>Figure 3.9: The supra band gap transitions of ZnO as calculated defects levels, adapted [102].</i>	53
<i>Figure 3.10: Schematic diagram of TEM [105].</i>	54
<i>Figure 3.11: Schematic diagram of X-ray diffraction adapted from [109].</i>	55
<i>Figure 3.12: Illustration of the diffraction of X-ray in crystal (adapted from [109]).</i>	56
<i>Figure 3.13: Schematic diagram of (a) one-point probe, (b) four point probe system.</i>	59
<i>Figure 3.14: Schematic diagram of the Hall Effect concept.</i>	61
<i>Figure 3.15: Layout of experimental setup diagram.</i>	62
<i>Figure 4.1: PL spectra of thermally annealed ZnO (41 sccm) at 700 °C in air, illustrates the effect of annealing duration at 700 °C.</i>	65
<i>Figure 4.2: PL spectra of thermally annealed ZnO (41 sccm sample) at temperatures up to 880 °C in air, showing the effect of increasing the temperature for 1 hour.</i>	66
<i>Figure 4.3: PL of thermal anneal in air of ZnO 41 sccm at 840 °C and various dwell periods.</i>	68
<i>Figure 4.4: PL evolution of 38 sccm samples under rapid thermal annealing (RTA) with Dt=1 s at various temperatures in nitrogen.</i>	69
<i>Figure 4.5: PL of rapid thermal anneal (RTA) in nitrogen (38 sccm sample), at 1000 °C versus dwell time.</i>	70
<i>Figure 4.6: PL spectra of 38 sccm films under RTA in oxygen at Dt=1 s.</i>	71
<i>Figure 4.7: PL spectra of RTA samples at 880 °C with dwell time 1 s in oxygen and nitrogen ambient, comparing samples deposited at various O<sub>2</sub> flow rates. The PL</i>	

<i>spectra of all the as-deposited films did not show any significant PL (they have been omitted from the graph for clarity purpose).</i> .....	72
<i>Figure 4.8: Photoluminescence spectra from 41 sccm samples annealed at various fluences with a single pulse.</i> .....	73
<i>Figure 4.9: Normalized PL peak of NBE and DLE intensity various laser energy densities.</i> .....	74
<i>Figure 4.10: PL emission of samples deposited at oxygen flow rates of 41, 38, 35, 32, and 28 sccm and laser annealed at 220 mJ/cm<sup>2</sup> with a single pulse.</i> .....	75
<i>Figure 4.11: PL spectra of a Zn-rich sample (28 sccm) showing a clear evolution of NBE and no appearance of DLE.</i> .....	76
<i>Figure 4.12: PL spectra from the 41 sccm sample laser annealed at a medium fluence, (235 mJ/cm<sup>2</sup>) but with multiple pulses.</i> .....	77
<i>Figure 4.13: PL spectra from the 41 sccm sample showing the effect of multiple pulse LA at a high fluence of 295 mJ/cm<sup>2</sup>.</i> .....	78
<i>Figure 4.14: TEM images for as-deposited ZnO (41 sccm) film (a): dark field shows the grain size, (b) bright field,(c) dark field shows defects content, and (d) defocused image shows the density of grain boundary.</i> .....	79
<i>Figure 4.15: TEM images of ZnO film (41 sccm) laser treated at 220 mJ/cm<sup>2</sup> single pulse (a) dark field image, (b) defocused image, and (c) magnified dark field image.</i> .....	80
<i>Figure 4.16: TEM images of HiTUS ZnO film (41 sccm) laser annealed at 295 mJ/cm<sup>2</sup> with a single pulse, (a) and (b) dark fields showing grain sizes enlarged, and lower defects, (c) showing the grain boundaries.</i> .....	81
<i>Figure 4.17: TEM images of a 200 nm HiTUS ZnO (41sccm), processed at 295 mJ/cm<sup>2</sup> with a single pulse, (a) bright field image shows bi-layer microstructure (b) grain boundaries channel and (c) shows the in-depth effect of high fluence with crystallisation reaching 135 nm below the surface of a 200 nm film.</i> .....	82

<i>Figure 4.18: TEM images of HiTUS ZnO film (41 sccm) thermally annealed at 880C° for 1hour, (a) defocused image shows thickness variation (b) dark field image the nature of grains (c) higher magnification bright field shows fault formation. ....</i>	<i>84</i>
<i>Figure 4.19: XRD diffraction patterns of thermally annealed ZnO (41 sccm) sample at various temperatures, for 1 hour in air. ....</i>	<i>86</i>
<i>Figure 4.20: XRD diffraction patterns from the 38 sccm ZnO sample after RTA in nitrogen at various temperatures and dwell times. ....</i>	<i>86</i>
<i>Figure 4.21: XRD diffraction patterns from the 41 sccm ZnO sample after single pulse LA at various fluences. ....</i>	<i>87</i>
<i>Figure 5.1: Deposition rate as a function of RF power for ZnO films deposited at oxygen concentrations of 20% O<sub>2</sub> in Ar, and 5% O<sub>2</sub> in Ar. ....</i>	<i>91</i>
<i>Figure 5.2: Evolution of PL spectra of laser annealed ZnO (50 W, 20% O<sub>2</sub> in Ar at RT) films at various energy densities in air at single pulse, results in medium fluences showing development of DLE peak, while at high fluences results show a reduction of DLE peak with evolution of a strong NBE peak. ....</i>	<i>92</i>
<i>Figure 5.3: The development of DLE and NBE intensity peaks as a function of laser energy densities at single pulse extracted from PL spectra of ZnO films deposited at RT, 20% O<sub>2</sub> in Ar, and 50 W (shown in Figure 5.2). ....</i>	<i>93</i>
<i>Figure 5.4: NBE intensity peak versus laser energy density of ZnO deposited at RT and with 20% O<sub>2</sub> in Ar and various RF powers of 50, 100, 200, and 300 W, as a function of laser anneal. ....</i>	<i>94</i>
<i>Figure 5.5: DLE intensity peak versus laser energy density of ZnO deposited at RT with 20% O<sub>2</sub> in Ar and various RF powers (50, 100, 200, and 300 W) as a function of laser anneal. ....</i>	<i>95</i>
<i>Figure 5.6: Evolution of NBE intensity peak versus laser energy density of ZnO grown at 5% O<sub>2</sub> in Ar, RT, 2 mTorr at various RF powers (50, 100, 200, and 300 W) as a function of laser anneal. ....</i>	<i>96</i>

<i>Figure 5.7: Evolution of DLE intensity peak versus laser energy density of ZnO grown at 5% O<sub>2</sub> in Ar, RT, 2 mTorr at various RF powers (50, 100, 200, and 300 W) as a function of laser anneal. ....</i>	<i>97</i>
<i>Figure 5.8: PL spectra of ZnO films deposited at various temperatures of RT, 100 °C, 200 °C, 300 °C, and 400 °C. ....</i>	<i>98</i>
<i>Figure 5.9: PL spectra of thermal annealed (at 700 °C, dwell time 1hour) ZnO films grown at various temperatures. The inset shows the evolution of NBE peak at about 381nm. ....</i>	<i>99</i>
<i>Figure 5.10: NBE peak intensity of laser annealed ZnO films deposited at various substrate temperatures (RT, 100, 200, 300, and 400 °C). As the deposition temperature increased, the NBE peak decreased. ....</i>	<i>100</i>
<i>Figure 5.11: DLE peak intensity of laser annealed ZnO films deposited at various substrate temperatures (RT, 100, 200, 300, and 400 °C). ....</i>	<i>101</i>
<i>Figure 5.12: XRD patterns of ZnO deposited at room temperature following to laser anneal versus laser energy density at single pulse. ....</i>	<i>102</i>
<i>Figure 5.13: XRD spectra of ZnO films deposited at 300 °C following by laser anneal at various fluences. ....</i>	<i>104</i>
<i>Figure 5.14: XRD patterns (thermal annealed at 700 °C for an hour) of ZnO films deposited at various substrate temperatures. The inset shows XRD patterns of films grown at RT, and 100 °C. ....</i>	<i>105</i>
<i>Figure 5.15: TEM images for as-deposited ZnO deposited at room temperature, (a) bright field image, (b) bright field image with higher magnification, (c) dark field image. ....</i>	<i>107</i>
<i>Figure 5.16: TEM images of ZnO film deposited at room temperature and laser annealed at 270 mJ/cm<sup>2</sup>. (a) image of bright field, (b) an image with higher magnification defocus, (c) image of dark field. ....</i>	<i>108</i>

<i>Figure 5.17: TEM images of laser annealed ZnO deposited at room temperature and laser annealed at 315 mJ/cm<sup>2</sup>, (a) high magnification defocus image, (b) dark field image showing the effect of high fluence on grain size. ....</i>	<i>109</i>
<i>Figure 5.18: TEM images of thermal annealed ZnO at 700 °C for 1 hour in air, (a) defocused image with appearance of pores (b) bright field image (c) dark field image showing the nature of grain size. ....</i>	<i>110</i>
<i>Figure 5.19: TEM images of as-grown ZnO film at substrate temperature 300 °C, (a) defocused image (b) bright field image, (c) dark field image. ....</i>	<i>111</i>
<i>Figure 5.20: TEM images of ZnO deposited at a substrate temperature of 300 °C and after laser annealing at fluence 335 mJ/cm<sup>2</sup> with a single pulse, (a) defocused image (b) defocused image at high magnification (c) dark field image. ....</i>	<i>112</i>
<i>Figure 6.1: PL spectra of thermal annealed (700 °C for 1 hour in air) ZnO films grown onto silicon dioxide substrates at RT and 400 °C. ....</i>	<i>117</i>
<i>Figure 6.2: Evolution of NBE and DLE peaks of Laser annealed ZnO deposited on SiO<sub>2</sub> substrate at 400 °C. ....</i>	<i>119</i>
<i>Figure 6.3: XRD patterns of as deposited and thermal annealed ZnO deposited on silicon dioxide substrates at RT and 400 °C. ....</i>	<i>120</i>
<i>Figure 6.4: XRD patterns of laser annealed ZnO films deposited on silicon dioxide substrate at RT. The inset shows XRD spectra of as-deposited film. ....</i>	<i>121</i>
<i>Figure 6.5: XRD patterns of laser annealed ZnO film deposited on SiO<sub>2</sub> substrate at 400°C. ....</i>	<i>122</i>
<i>Figure 6.6: Sheet resistance of laser annealed IGZO (2:2:1) films deposited at 50 W, 5 %, O<sub>2</sub> in Ar, 50 nm, at various deposition pressures (2, 5 and 10 mTorr). ....</i>	<i>126</i>
<i>Figure 6.7: Sheet resistance of laser annealed IGZO (2:2:1) films deposited at 100 W, 2 mTorr, 50 nm, at various oxygen deposition concentrations of 2, 5, 10% O<sub>2</sub> in Ar. ....</i>	<i>127</i>
<i>Figure 6.8: Sheet resistance of laser annealed IGZO (2:2:1) films deposited at 2, and 5% O<sub>2</sub> in Ar, 2 mTorr, 50 nm, at various RF powers (50 W and 100 W). ....</i>	<i>128</i>

<i>Figure 6.9: Sheet resistance of laser annealed IGZO (2:2:1), and (1:1:1) grown at 2% O<sub>2</sub> in Ar, 50 W and 50 nm. ....</i>	<i>129</i>
<i>Figure 6.10: Hall mobilities, carrier concentrations, and resistivities of 50nm thick IGZO (1:1:1) thin films film as a function of laser fluence. ....</i>	<i>130</i>
<i>Figure 6.11: Cross section diagram of IGZO TFTs used for thermal and laser annealing (W/L= 1000 μm/5 μm). ....</i>	<i>132</i>
<i>Figure 6.12: Schematic diagram showing the process sequence of top gate–bottom contacts IGZO-TFT fabrication and the concept of laser annealing pre and post IGZO channel patterning. ....</i>	<i>133</i>
<i>Figure 6.13: Transfer characteristics ON sweep of IGZO-TFTs (W/L= 1000 μm/5 μm) V<sub>DS</sub> =1 V, IGZO 30 nm, pre and post IGZO pattern thermal annealed at 150°C in air for 1 hour. ....</i>	<i>135</i>
<i>Figure 6.14: Transfer characteristics ON sweep IGZO-TFTs (W/L= 1000 μm/5 μm) V<sub>DS</sub> =1, IGZO 30 nm, laser annealed at laser energy density of 75 mJ/cm<sup>2</sup> with a single pulse, pre and post IGZO patterning. ....</i>	<i>136</i>
<i>Figure 6.15: Transfer characteristics of ON sweep IGZO-TFTs (W/L= 1500 μm/5 μm) V<sub>DS</sub> =1 V at laser energy density 75 mJ/cm<sup>2</sup> single pulse post IGZO pattern. ....</i>	<i>138</i>
<i>Figure 6.16: Transfer characteristics of ON sweep IGZO-TFTs (W/L= 1500 μm/5 μm) V<sub>DS</sub> =1 V pre and post IGZO pattern laser at laser energy density 75 mJ/cm<sup>2</sup> single pulse. ....</i>	<i>139</i>
<i>Figure A-1: Cross-sectional view of the channel region of a TFT used to drive gradual channel approximation [7]. ....</i>	<i>160</i>
<i>Figure B-1: Evolution of PL spectra of laser annealed ZnO deposited at 100 W, 20% O<sub>2</sub> in Ar at RT. ....</i>	<i>162</i>
<i>Figure B-2: Evolution of PL spectra of laser annealed ZnO deposited at 200 W, 20% O<sub>2</sub> in Ar at RT. ....</i>	<i>163</i>
<i>Figure B-3: Evolution of PL spectra of laser annealed ZnO deposited at 300 W, 20% O<sub>2</sub> in Ar at RT. ....</i>	<i>164</i>

## List of Tables

---

<i>Table 2.1: Summary of previous work on ZnO-TFTs. TA stands for thermal annealing and LA for laser annealing. ....</i>	<i>27</i>
<i>Table 2.2: Summary of the IGZO-TFTs work presented previously in the literature. TA stands for thermal annealing and LA for laser annealing. ....</i>	<i>33</i>
<i>Table 4.1: XPS showing Zn:O ratio for films deposited at various oxygen flow rates. .</i>	<i>66</i>
<i>Table 4.2: XPS showing Zn:O ratio for films as a function of annealing temperatures. ....</i>	<i>67</i>
<i>Table 5.1: Data from XRD patterns of ZnO films deposited at room temperature (RT) following laser anneal at various energy densities with single pulse irradiation. ....</i>	<i>103</i>
<i>Table 5.2: Data from XRD patterns of ZnO films deposited at 300 °C following laser anneal at various energy density at single pulse. ....</i>	<i>103</i>
<i>Table 5.3: Average grain size calculated from XRD patterns of ZnO films deposited at various substrate temperatures following laser anneal at various energy densities with single pulse irradiation, and also following thermal anneal at 700 °C for 1 hour. Films processed with medium and high fluences exhibit the highest peak of DLE and NBE peaks respectively. ....</i>	<i>106</i>
<i>Table 6.1: Comparison of average grain size calculated from XRD patterns of ZnO films deposited on Si and SiO<sub>2</sub> substrates at RT and 400 °C, following laser anneal at various energy densities with single pulse irradiation, and thermal anneal at 700 °C for 1 hour. ....</i>	<i>123</i>
<i>Table 6.2: Sheet resistance of laser annealed 60 nm thick of ZnO films deposited at 50 W, 20% O<sub>2</sub> in Ar, 2 mTorr on SiO<sub>2</sub> substrates at RT and 400 °C.. ....</i>	<i>135</i>
<i>Table 6.3: Properties of IGZO –TFTs thermally annealed pre and post patterning of the active layer 30 nm thick. ....</i>	<i>135</i>
<i>Table 6.4: Properties of IGZO –TFTs annealed with different laser annealing conditions. ....</i>	<i>137</i>

*Table 6.5: Electrical properties of IGZO –TFTs laser annealed pre and post patterning of the active layer 50 nm thick, at 75 mJ/cm<sup>2</sup> with a single pulse in air. .... 138*

# Chapter 1

## Introduction

---

### 1.1 Introduction

In recent years, there has been a significant research interest in the development of materials fabrication and processing to realise flexible display technologies [1]. High performance thin film transistors (TFTs) are one of the most significant technologies required in active matrix flat panel displays, including active matrix liquid crystal displays (AMLCD) [2], and active matrix organic light emitting diode (AMOLED) displays, to switch the pixels ON and OFF. Transparent thin film transistors (TTFTs) made of transparent oxide semiconductors (TOSs) have attracted considerable attention due to their potential for use in display devices, because the use of transparent active matrix circuits increases the aperture opening ratio (i.e. increases the light emitting area per pixel, and hence pixel brightness) [2].

Amorphous silicon (a-Si) TFTs have been successfully employed in large area display technology, but the major shortcoming is low mobility ( $\sim 1 \text{ cm}^2/\text{Vs}$ ) which limits the device switching speed and ultimate refresh frequency [3]. Alternatively, poly silicon (poly-Si) TFTs demonstrate higher mobility ( $> 50 \text{ cm}^2/\text{Vs}$ ), and are used in smaller area AMLCDs [4]. However, the need for processing at high temperatures makes poly-Si TFTs incompatible with flexible substrates, and it is difficult to grow uniform layers over large areas, hence affecting display sizes attainable [5]. Furthermore, both a-Si and poly-Si are opaque materials with a narrow band gap of 1.1 eV for crystalline silicon or 1.6 eV for a-Si [6], hence their use results in limitations to the pixel aperture ratios, which affects the pixel brightness [7].

There is consequently a significant interest in developing materials technology that offers alternatives to a-Si and poly-Si in order to achieve optimised performance in future displays, and to also offer the potential for new design innovation through the realisation of flexible, and ideally transparent displays and TFT materials. Several metal oxide semiconductor materials have been studied over recent years, both as transparent conducting oxides (TCOs) and as transparent semiconducting oxides (TSOs) for application to electronic devices such as displays. One such oxide material is Zinc oxide (ZnO) which is a material of interest for TFTs because of its wide and direct band gap (3.36 eV) [8]. High processing temperature (deposition or annealing) is typically required to achieve good properties such as to enhance the film crystallinity, reduce the defects, reduce grain boundaries, and control conductivity. Hence deposition and processing of ZnO at low temperatures with good microstructure and electrical properties, to be compatible with flexible substrate is one of the most challenging tasks.

Another material of interest for display applications is amorphous indium gallium zinc oxide, for use in transistor devices a-IGZO TFTs. These devices have attracted considerable attention [9, 10], and have been demonstrated as switching devices in active matrix liquid crystal displays (AMLCD), and organic light emitting diode based displays (OLED) [11, 12]. The a-IGZO based TFTs reported in 2004 by Nomura et al, were fabricated on flexible substrates via pulsed laser deposition (PLD). These devices were investigated as an alternative to a-Si and poly-Si TFTs, because of the high field effect mobility that was demonstrated in the amorphous state ( $>10 \text{ cm}^2/\text{Vs}$ ) [9], which was attributed to the heavy metal cations with  $(n - 1) d^{10} ns^0$   $n \geq 5$  electron configuration [13]. In the past ten years, there has been much work on IGZO devices, with commercial displays now using this material [14-16]. However, there is still a need to optimise low temperature deposition and processing of IGZO for flexible applications, ideally utilising a deposition and processing technique that is suitable for large area at low cost.

For the research presented in this thesis, the combination of low temperature deposition by sputtering (a technique well suited to scale up to large areas) and post deposition by laser annealing has been investigated in order to study the potential for application to the processing of ZnO and IGZO and TSOs. The use of laser processing provides the potential to localise the modification induced by annealing in order to minimise energy deposited into the substrate, hence can be a method suitable for low temperature substrates. The work presented here uses RF magnetron sputtering and High Target Utilisation Sputtering (HiTUS) in combination with subsequent pulsed UV excimer laser treatment, to examine the effect on the thin film structure and properties.

One of the main experimental tools used to investigate the effect of deposition and annealing for this work is photoluminescence (PL). Typical PL emission from ZnO exhibits two significant peaks: a strong narrow ultraviolet (UV) centred at around (381 nm) from near band emission (NBE) associated with free exciton recombination, and a broad visible peak (from 450-750 nm) associated with deep level emission (DLE) [17, 18]. The DLE is attributed to intrinsic or extrinsic defects [18], and to produce ZnO films with good microstructure and electrical properties, the related defects (DLE peak) should be suppressed with a pronounced evolution of NBE intensity. It has been reported that an improvement of NBE intensity is clearly observed after thermal annealing [19]. Hence, for this work, the effect on PL of ZnO thin films processed by low temperature laser annealing is compared with the effect of thermal and rapid thermal annealing. Work on IGZO thin films is also presented, in which the electrical properties of devices utilising IGZO semiconductor layers are studied following laser annealing.

## **1.2 Problem definition**

There is a difficulty in fabricating good quality TFTs materials that are transparent and at the same time fabricated at low temperatures. Also stability of performance is an issue with the channel materials. Laser processing is a technique that has promise for

highly localised film modification. This project consequently addresses this area of materials and device research to investigate the use of laser processing for the optimisation of transparent semiconducting thin films suitable for use in TFTs.

### **1.3 Project Aim**

The project aims to investigate the deposition and processing of oxide semiconductors of zinc oxide (ZnO) and indium gallium zinc oxide (IGZO) in order to understand how to modify and optimise the properties of these transparent semiconducting oxide thin films for use in electronic device applications.

### **1.4 Project Objectives**

The specific objectives of this work are to:

- Undertake background study of TFT devices, ZnO and IGZO thin film deposition and fabrication and characterisation of TCOs in electronic devices.
- Experimental design to investigate the optimisation of TCOs: ZnO and IGZO.
- Investigate the deposition and post processing of ZnO thin films through characterisation of the resultant structural, electrical and defect properties.
- Investigate the deposition and post processing of IGZO thin films through characterisation of the resultant structural, electrical and defect properties.
- Evaluate the effect of excimer laser processing on ZnO and IGZO.
- Investigate the performance of TFT devices comprising IGZO produced in previous objectives.

### **1.5 Structure of the Thesis**

This thesis consists of the following chapters:

Chapter 2: Background and Literature Review

This chapter presents background knowledge and a literature review related to the structure, principle, and theory of the operation of thin film transistors (TFTs). This is followed by a review of semiconductor materials in thin film transistors (TFTs) based on polycrystalline zinc oxide and amorphous IGZO electrical properties, including a discussion of the deposition methods used.

Chapter 3: Experimental Procedures and Techniques

The third chapter provides a description of the experimental systems utilised throughout this research, comprising a description of the two deposition techniques of HiTUS and RF-magnetron sputtering, and of the excimer laser processing system. Also discussed are the characterisation techniques applied to the films following deposition and processing: photoluminescence (PL), X-ray diffraction (XRD), Transmission Electron Microscopy (TEM), Four Point Probe (4PP), and Hall Effect.

Chapter 4: ZnO Thin Films by HiTUS

This chapter presents the results obtained from a study of the photoluminescence of ZnO films deposited at low temperature by the HiTUS technique and followed by different annealing processes: laser, thermal, rapid thermal annealing. The structure of the processed ZnO films is also examined and analysed using Transmission Electron Microscopy (TEM) and X - ray Diffraction (XRD) and their results are correlated to the PL properties.

Chapter 5: ZnO Thin Films by RF Magnetron Sputtering

In this chapter, the effect of laser annealing on PL spectra of ZnO films deposited by RF magnetron sputtering at various RF powers and oxygen concentrations without intentional substrate heating are reported. The effect of varying deposition parameters is compared with the HiTUS results presented in chapter 4, with the PL spectra of laser and thermal annealed ZnO films grown at various substrate temperatures presented.

Further confirmation of film structure as a function of annealing process is examined by cross sectional TEM, and XRD pattern.

#### Chapter 6: Electrical Characterisation of ZnO and IGZO.

This chapter presents a study of the electrical properties of the investigated oxide semiconductor materials and devices. The electrical properties of laser annealed ZnO thin films and IGZO thin films deposited at various deposition parameters from targets with different compositions are discussed, and an evaluation of test TFT devices fabricated with the optimised IGZO thin films is presented.

#### Chapter 7: Conclusion and Further Work

The conclusion chapter provides a combinatorial summary of the research carried out, and the achievements of the work performed, with some possible suggestions for further work.

## Chapter 2

### Background and Literature Review

---

#### 2.1 Introduction

Metal – oxide semiconductor devices, for example thin film transistors (TFTs) play an important role in electronics applications. TFTs are one of the key components in electronics displays in which they are used as switching elements (addressing) for active matrix liquid displays (AMLCD) [20], and as a driver/address device in organic light emitting diode (OLED) displays [11]. In recent years, transparent oxide semiconductors (TOSs) are of interest for application to TFT technology for displays, because of the transparency in the visible part of the spectrum, due to the wide band gap, and due to the potential for low processing temperature, which facilitates processing on substrates such as glass and flexible materials. For example in 2011, Samsung introduced the first commercial 2-inch transparent display using transparent TFTs [21]. Zinc oxide ZnO-TFTs and amorphous indium gallium zinc oxide a-IGZO-TFTs have attracted much attention for the next generation large-area, transparent, and flexible flat panel displays. These semiconducting thin films exhibit various advantages over conventional Si-TFTs, such as high mobility and transparency [9, 22].

ZnO presents a wide band gap of 3.36 eV [23], and IGZO a band gap of ~3 eV [9], hence, when used as channel layers in TFTs, exposure to light will not affect the device performance. Hence, employing ZnO or IGZO TFTs in AMLCDs for switching the pixel display can improve the brightness of pixels.

These features make zinc oxide (ZnO) and amorphous indium gallium zinc oxide (a-IGZO) thin film transistors (TFTs) the subject of vibrant research and devices using these materials have been demonstrated for display technologies such as liquid crystal displays (LCD) and organic light emitting diodes (OLED) displays [24, 25].

## **2.2 The basic structure of TFTs and operation theory**

### **2.2.1 Overview of TFT principles of operation**

The main role of TFT devices is to control the current that passes between source and drain via the medium of a semiconductor thin film layer. This is achieved by an induced accumulation layer in the active layer/dielectric interface as a function of applied voltage on insulated electrodes (gate/drain). TFTs can be classified into two categories: enhancement mode "normally off", and depletion mode "normally on". For example, for n-channel TFTs, a positive threshold voltage ( $V_{th}$ ) is required to turn on an enhancement mode device, while in depletion mode device a negative threshold voltage is required. However, in a depletion mode "normally on" device a voltage on the gate terminal is required to switch off the device, hence enhancement mode is superior in terms of minimizing the power dissipation as no voltage is needed to switch off the device [26].

### **2.2.2 Basic structure of TFTs**

Figure 2.1, shows the simple bottom gate (inverted) structure of TFTs, which consists of three electrodes terminals: source, drain, and gate. The gate is isolated from the semiconductor layer by an insulating material (gate insulator), whereas the source and the drain are in direct contact with the semiconductor film.

Figure 2.1 (a), shows the cross section of a TFT, while Figure 2.1(b), illustrates the top view, with the dimensions  $W$  and  $L$  representing the width and length of the channel layer respectively.

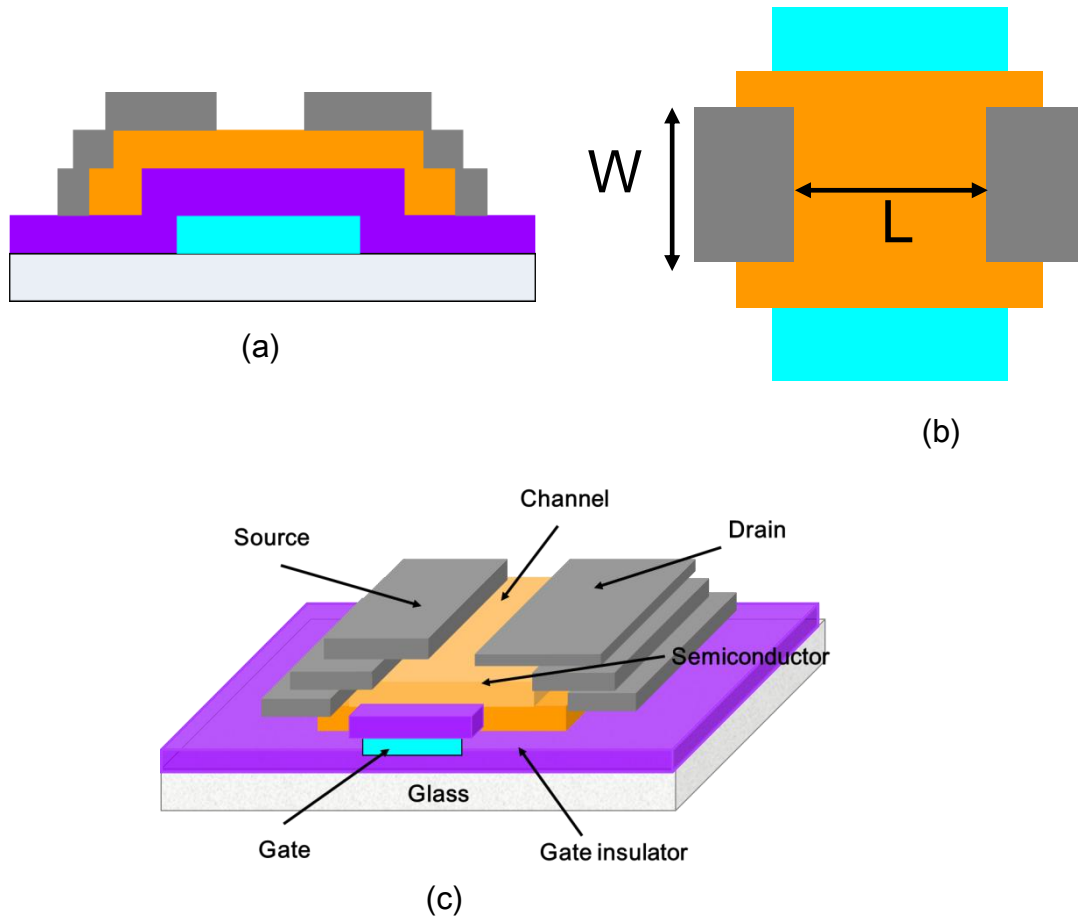


**Figure 2.1:** Schematic of a bottom gate TFT (a) cross section, (b) top view, (c) 3D view.

### 2.2.3 Types of thin film transistors TFTs

Generally, there are four basic possible structures of planar TFT devices, which are classified according to the place of the semiconductor layer, gate terminal, gate insulator, and relative position of source/drain electrodes as depicted in Figure 2.2 [7, 27].

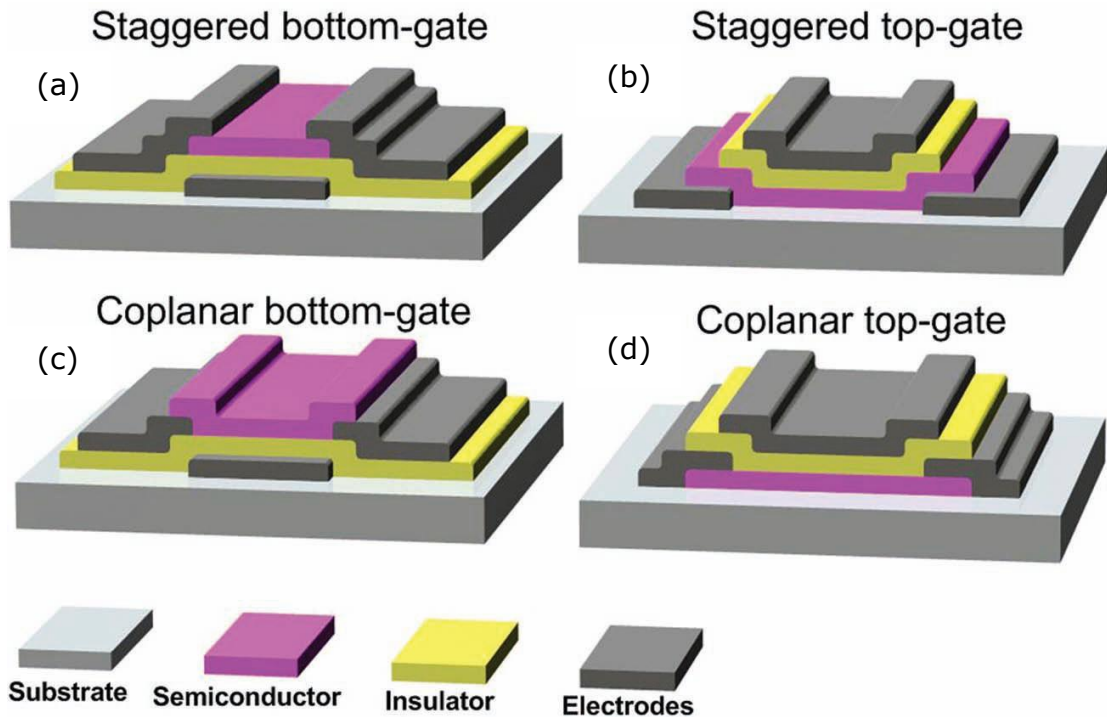


**Figure 2.2:** Types of TFTs (a) staggered bottom-gate, (b) staggered top-gate, (c) coplanar bottom-gate, (d) coplanar top-gate [28].

TFT devices are classified in either staggered or coplanar structures according to Weimer as following:-

1. In staggered configuration: the gate and the source /drain electrodes are on opposite sides of the semiconductor layer, and in such a configuration there is no direct connection with the induced channel. Therefore, the current has to flow vertically to induce the conduction channel before flowing horizontally to reach the drain.
2. Coplanar configuration: the source / drain electrodes and the gate are on the same side of the semiconductor layer. In this case the source / drain electrodes are in direct contact with the induced channel, the current flows in a single plane [29, 30].

As Figure 2.2 shows, the staggered and coplanar configuration can be either bottom gate 'inverted' or top gate devices. This classification is defined by gate electrode location and relative position of the source / drain and the gate terminals. If the gate is on the active layer, the device is in top-gate configuration, whereas, when the gate

electrode is below the active layer, the device is in bottom-gate (inverted) configuration [31].

Finally, the inverted-staggered "bottom gate" a-Si:H TFTs have better device characteristics than the staggered "top gate" structure because in the former the insulator layer is deposited before the active layer, which leads to lower interface density of states [32]. However, inverted staggered TFTs suffer from some drawbacks that may affect TFTs performance such as; the back channel layer being exposed to atmospheric gases, and back channel could be damage from subsequent process patterning of source/drain electrodes [33]. To overcome these issues the TFT structure is specified further according to the structure above the active layer in two ways [7] as illustrated in Figure 2.3. First, the back-channel-etched (BCE) structure, where a thin part of the channel layer is etched together with forming the source and drain electrodes. The second is the etch-stopper (ES) structure, where a protective layer on the top of active layer is formed prior to the source and drain being deposited [34].

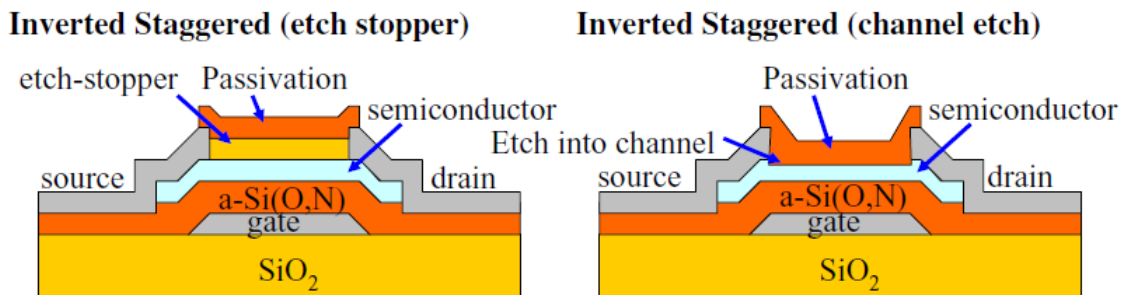


**Figure 2.3:** The structure of etch stopper, and back channel – etched TFTs [14].

The back channel etched (BCE) structure is used widely in the LCD industry to fabricate a-Si:H TFTs, because of its simpler fabrication process and the fact that it saves one photo mask step compared to the etch stopper (ES) structure [7]. However, ES devices exhibit better TFT characteristics, compared to the BCE structure, when under bias stress [35]. Moreover, BCE structures required a thicker channel layer [7, 14]. Figure 2.4 shows classification of main types of TFTs.

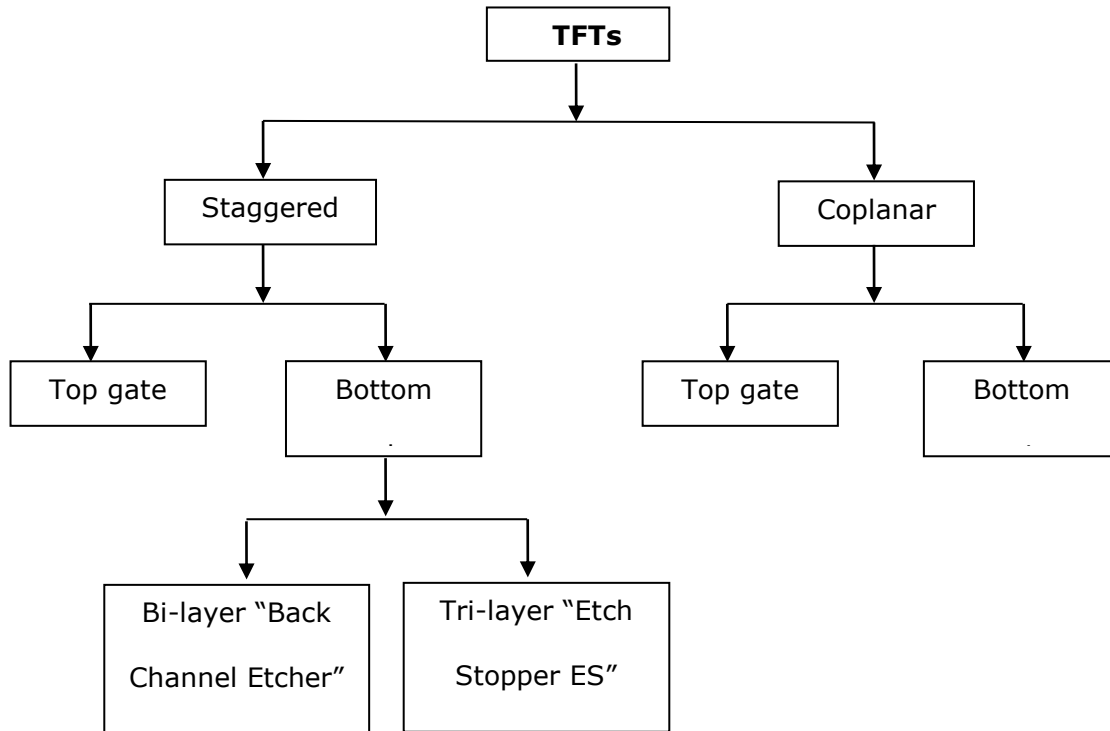


**Figure 2.4:** Diagram shows the main types of TFTs.

### 2.2.4 The operation theory of TFTs

The main principle of operation for TFTs relies on the flow of current in an induced accumulation channel layer in the semiconductor between source/drain electrodes [28]. The TFTs function and theory are similar to the inversion mode of metal – oxide semiconductor field-effect-transistors (MOSFETs). But there is a variance in structure, for example in MOSFETs the current flows following the formation of an inversion layer in the semiconductor layer between source and drain (i.e. in n-channel MOSFET n-type conductive layer generated in p-type substrate), whereas in TFTs, the current flows in an induced charge accumulation layer in the channel/gate dielectric interface. In addition, in silicon based MOSFETs, the silicon is employed as a substrate and active layer, while in TFT devices, a glass substrate is typically used, with the semiconductor layer being deposited as a thin film [28]. Combinations of n-channel TFT, and p-channel TFTs are employed in logic circuits as an inverter, in which switching devices work in different (on/off) states called complementary metal oxide semiconductor (CMOS) as

used in integrated circuits. Oxide CMOS devices have been demonstrated [36], for example in transparent inverter using IGZO TFTs employed in ring oscillator circuits [37].

TFT performance is divided into two main operational regimes: the linear and saturation regimes [7] – as shown in Figure 2.5. When the drain-source voltage,  $V_{DS}$ , is much less than the gate-source voltage,  $V_{GS}$ , minus the threshold voltage  $V_{th}$  ( $V_{DS} \ll V_{GS} - V_{th}$ ), the TFT is operating in the linear regime. When ( $V_{DS} > V_{GS} - V_{th}$ ), the transistor is in saturation, independent of  $V_{DS}$  [7, 38, 39].

For n-channel TFTs, in "normally off" enhancement mode, when the source is grounded and a "positive" voltage is applied on the gate terminal, electrons are attracted towards the gate bias – leading to an accumulation layer at the insulator interface. To pass current through the channel, a positive voltage on the drain must be applied, which causes current to flow along the channel – depending upon the state of the accumulation. When the voltage between gate and source is less than the threshold voltage there is no drain current, because no induced accumulation layer exists. In this case the TFT is in the cut off region [29].

When the gate bias is increased to exceed the threshold voltage level, and a small voltage is applied to the drain i.e ( $V_{DS} < V_{GS} - V_{th}$ ), there will be the appearance of drain current, as the electrons are injected from the source into the lower resistance induced electron accumulation layer creating a path of current. Then they are extracted at the drain contact and as a result drain current is passed in the opposite direction from drain to source [29]. Hence, as in Ohms law, there is a linear of increase drain current with increasing drain voltage; this is the "linear regime".

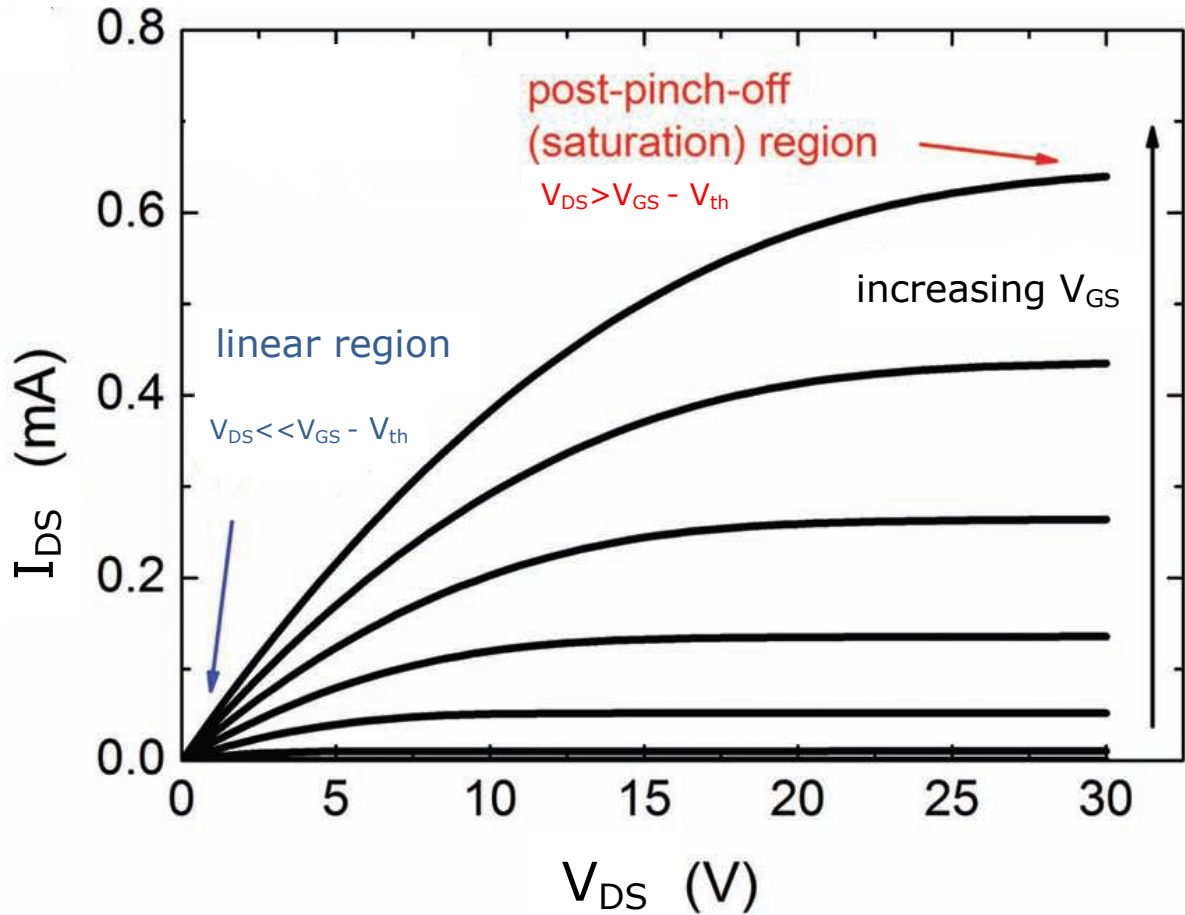


**Figure 2.5:** Shows the  $I_{DS}$  vs  $V_{DS}$  characteristic curves, for various values of  $V_{GS}$  and for n-channel TFTs enhancement type [28].

In linear regime by applying the Gradual Channel Approximation (GCA), the drain current ( $I_{DS}$ ) with respect to gate voltage  $V_{GS}$  given as:

$$I_{DS} = C_O \mu_{ny} \frac{W}{L} \left[ (V_{GS} - V_{th})V_{DS} - \frac{V_{DS}^2}{2} \right] \quad (2.1)$$

where  $W$  and  $L$  width and the length of the channel layer respectively.

When  $V_{DS} \ll V_{GS}$  then the drain current can be written as:

$$I_{DS} = C_O \mu_{ny} \frac{W}{L} [(V_{GS} - V_{th})V_{DS}] \quad (2.2)$$

Further details of deriving equation (2.2) can be found in appendix A, at the end of this thesis

As the applied positive drain voltage increases, the induced carrier density near drain terminal disappears when  $V_{DS} = (V_{GS} - V_{th})$ , resulting in the electron channel becoming pinched off at the drain end, as illustrated in Figure 2.6. The drain current saturates and is no longer Ohmic when  $V_{DS}$  exceed the  $(V_{GS} - V_{th})$  [7, 29].

$$I_{Ds} = C_o \mu_{ny} \frac{W}{2L} [(V_{Gs} - V_{th})^2] \quad (2.3)$$

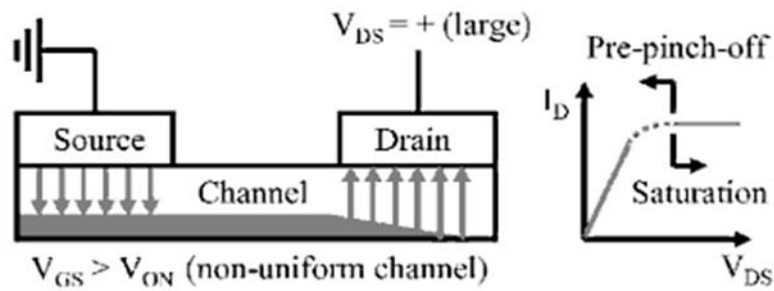


**Figure 2.6:** Shows the non-linear saturation [29].

From equations (2.2),(2.3) we can find the important parameters defining and affecting the TFTs operation, such as the capacitance of the dielectric layer ( $C_o$ ), mobility ( $\mu$ ), threshold voltage ( $V_{th}$ ), and the ratio of width over the length of the semiconductor channel layer. All of these factors must be considered, and this study will be concerned with optimising the mobility of ZnO, and IGZO thin films deposited at low temperature.

Figure 2.7 shows the typical transfer characteristics of n-channel TFTs, from which the key TFT parameters can be extracted, such as threshold voltage ( $V_{th}$ ), drain on-to-off current ratio, field effect mobility, and sub threshold swing ( $S$ ).

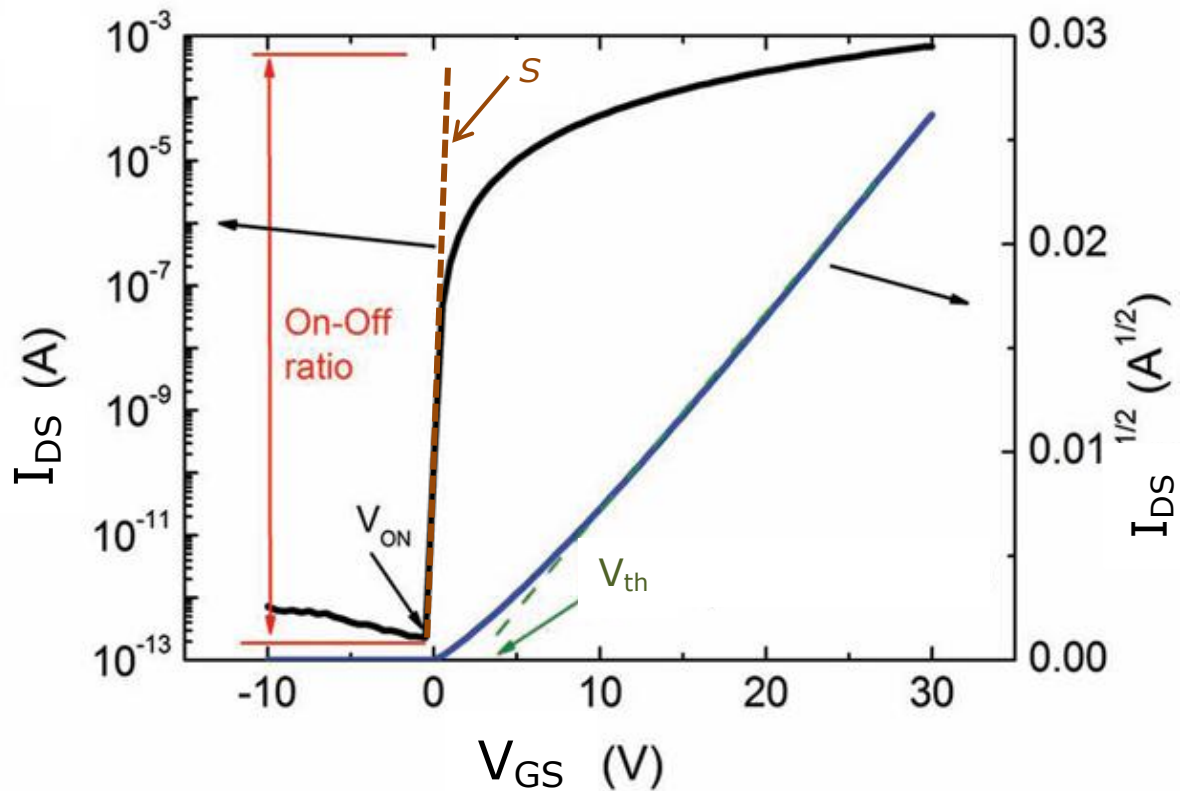


**Figure 2.7:** Transfer characteristics of n-type TFT [28].

The electrical characteristics of TFTs are highly influenced by the materials used in their structure (such as the channel layer material), the deposition techniques, and the parameters employed.

### 2.3 Materials used in TFT devices

The first functional thin film transistor (TFT) was reported in 1962, by P.K.Weimer [7, 40]. They employed a polycrystalline cadmium sulfide (CdS) semiconductor as the active layer and fabrication via vacuum evaporation [40]. In the early 1980s TFTs were fabricated from other semiconductor materials such as CdSe, Te, InSb and Ge [3, 41].

Cadmium sulfide CdSe TFTs were first employed as a switching element in the active matrix liquid crystal display (AMLCD) industry [20]. However, CdSe TFT creates some issues such as large density of interface states in CdSe [3], traps in the CdSe layer or

insulator interface affecting the frequency response of TFTs [42], and traps in the gate insulator leading to instability [43].

An improvement in the LCDs industry was reported by LeComber [44] who employed hydrogenated amorphous silicon (a-Si:H) as a channel layer in TFTs, which achieved good performance in terms of uniformity, low temperature, and capability of fabrication over large area. This was a good fit to the requirements of flat panel display (FPD) addressing [44].

However, the use of conventional amorphous silicon (a-Si) – based TFTs for LCDs displays create some disadvantages. The a-Si opacity leads to blocking the backlight in a FPD, which restricts the pixel brightness (aperture ratio) [7, 45]. Other negative factors are light sensitivity [3, 7], and low mobility ( $\sim 1 \text{ cm}^2/\text{Vs}$ ) which limits the frequency of operation. Hence, alternatives with high mobility are desired in LCDs and OLED displays in order to charge the storage capacitor in less time [28]. An additional factor which must be considered is instability under bias stress which influences the lifetime of the devices [7, 29].

In 1980 Depp et al. reported poly-silicon TFTs with dramatic increase in mobility ( $50 \text{ cm}^2/\text{Vs}$ ), fabricated at growth temperatures of  $625 \text{ }^\circ\text{C}$  and  $1050 \text{ }^\circ\text{C}$  for the poly-Si and gate the insulator respectively [4]. However, poly-Si has some drawbacks associated with the high processing temperature, which makes it unsuitable for flexible substrates. Moreover, poly-Si is difficult to fabricate over large areas [46].

Hence, great interest is shown in replacing the conventional Si TFTs with transparent semiconducting oxide (TSOs) in order to fabricate transparent display devices [22]. The starting of transparent electronics evolution dates to early 2003, with the report of Zinc Oxide (ZnO) thin films in transparent thin film transistors (TTFTs) [22, 26, 47]. Since then, several reports have emerged describing a diversity of TFT channel materials such as: indium gallium zinc oxide (IGZO), tin oxide ( $\text{SnO}_2$ ), indium oxide ( $\text{In}_2\text{O}_3$ ), and zinc tin oxide (ZTO) [48].

These transparent conducting oxides (TCOs) present a combination of two physical properties: good electrical conductivity and high transparency [29]. Transparent semiconducting oxides (TSOs), such as zinc oxide ZnO, are a promising material for the channel layer in TFTs, because they can be grown at room temperature with high electron mobility [49] and exhibit optical transparency in the visible spectrum [47].

In particular, amorphous indium gallium zinc oxide based thin film transistors (a-IGZO TFTs) have attracted considerable attention [9, 10] and have been demonstrated as switching devices in active matrix liquid crystal displays (AMLCD) and light emitting diode based devices (OLED) [11, 12]. Hence, ZnO and a-IGZO thin films are the major interest of this study, which is concerned with the low temperature deposition and the subsequent photonic processing of these materials.

## **2.4 Density of states (DOS)**

### **2.4.1 Density of states of amorphous silicon hydrogenated a-Si:H**

The electronic characteristics of amorphous thin films are strongly dependant on the density of state distribution. Amorphous silicon hydrogenated a-Si:H have no long-range order, the atoms are not periodically located over large distance, but retain short order of Si lattice. Figure 2.8 shows a typical density of states of a-Si:H, the density of states distribution contain the following major parts:

Band tails (tail states): The band tails are due to bonding disorder in amorphous structure, the disorder-induced localisation of states extended near the band edge and decaying exponentially, arising from deviations in length and angle of particular bonds originated from long range structural disorder [3]. The band states below the conduction band minimum (CBM) and above the valence band maximum (VBM),  $E_u$  is the Urbach energy typically  $E_u \sim 25$  meV for conduction band tail and  $E_u \sim 50$  meV for the valence band tail [14].

Dangling bonds (deep defects): are consequences of coordination disorder, and depending on position of the Fermi level. For doped a-Si:H, donor and acceptor levels exist in three charge states, when singly occupied forming neutral defect  $D^0$ , an electron excited out of neutral bond creating positively charged states  $D^+$ , or can be occupied by second electron forming negatively charged states  $D^-$  as depicted in Figure 2.8 [14]. Finally, mobility gap in which separates localized and extended states.

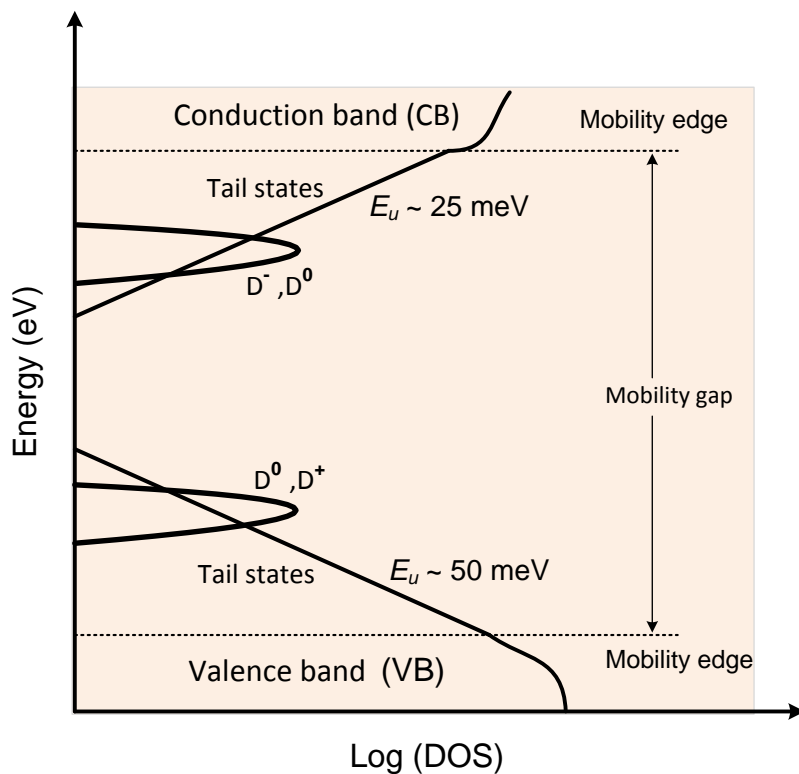


**Figure 2.8:** Schematic model of subgap DOS of a-Si:H, adapted from [14].

#### 2.4.2 Density of states of amorphous indium gallium zinc oxide a-IGZO

Figure 2.9 electronic structure of a-IGZO density of states shows the electronic states that control inversion p-channel TFT operation, n-channel TFT, and Hall effect. a-IGZO presents high density electron traps occupied the states just above the valence band maximum (VBM) with energy range of  $\sim 1.5$  eV which is may the reason a-IGZO TFTs have never achieved to operate in p-channel mode [50]. The un-annealed a-IGZO film grown at room temperature exhibit extra subgap states  $\sim 0.2$  eV below CBM related to

hysteresis in electrical properties of a-IGZO TFT [51]. The subgap DOS in a-IGZO is one – two orders of magnitude smaller than in a-Si:H.

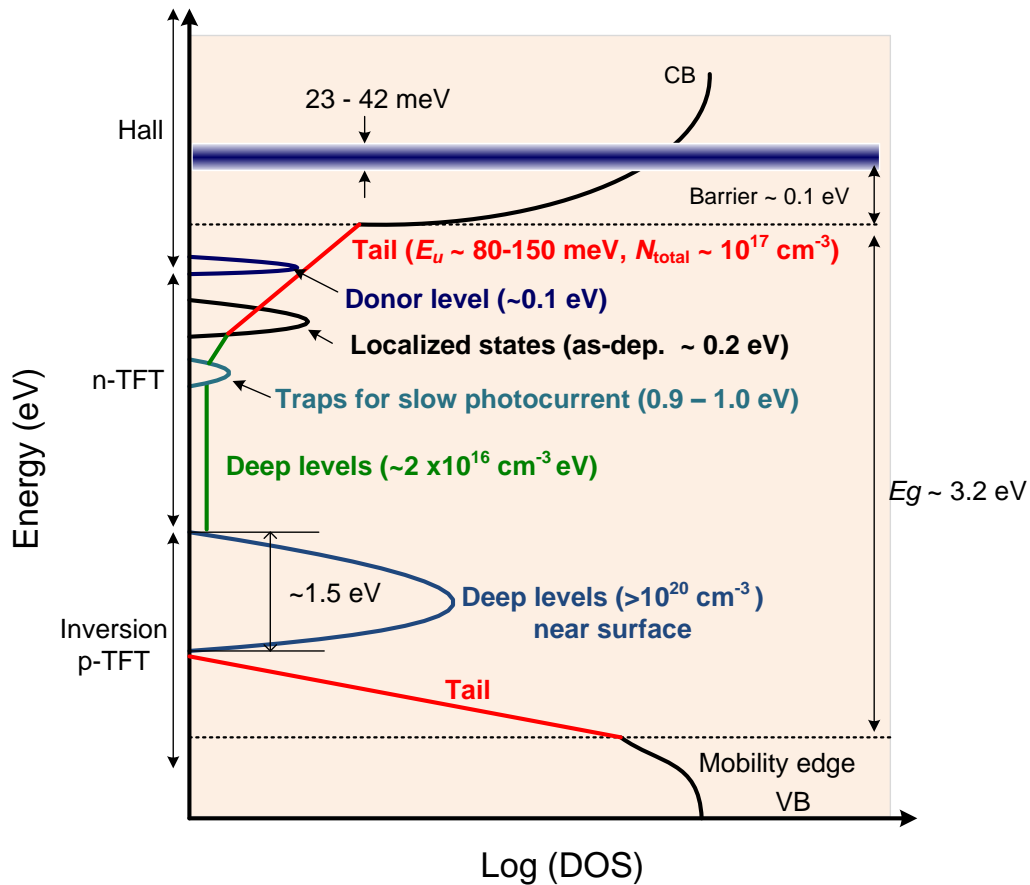


**Figure 2.9:** Schematic electronic structure of a-IGZO density of states for as-deposited adapted from [52].

## 2.5 Oxide thin film properties

### 2.5.1 ZnO crystal structure

ZnO is a wide band gap semiconductor with a direct band-gap of 3.36 eV at room temperature [53], and belongs to the II–VI group of compound semiconductors [54], which have an ionicity at the borderline between covalent and ionic semiconductor [23].

The crystal of ZnO is represented in three kinds of structures, wurtzite (B4), zinc blende (B3), and rocksalt (B1). Under ambient conditions, ZnO crystallizes in the hexagonal

wurtzite symmetry (B4 type), which is the most thermodynamically stable crystal structure [29, 55, 56]. Figure 2.10 shows hexagonal wurtzite ZnO structure.

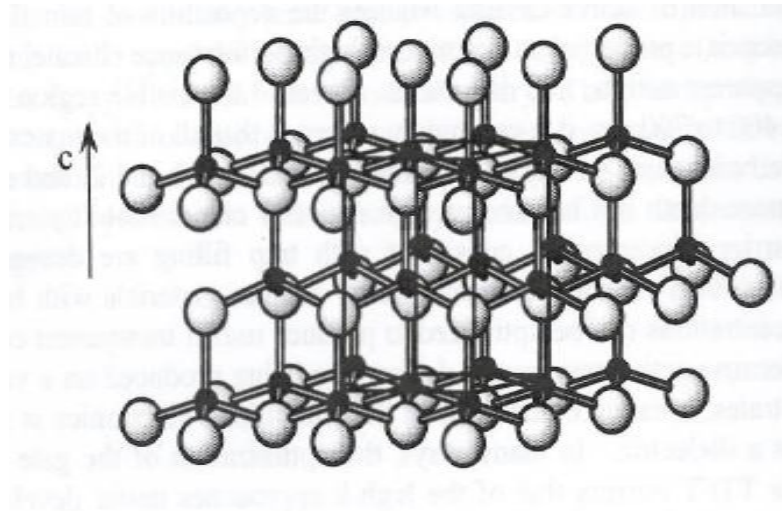


**Figure 2.10:** Hexagonal wurtzite ZnO structure. Large gray shaded and small black spheres denote O and Zn atoms, respectively [29].

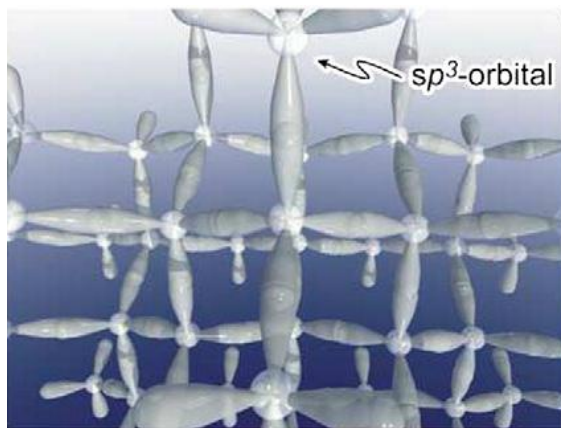
The hexagonal wurtzite lattice of ZnO has a mean lattice constants of  $a = 0.325\text{nm}$ ,  $c = 0.52066\text{nm}$  [56], with the zinc atoms surrounded by oxygen atoms in a nearly tetrahedral arrangement of O atoms [57]. The zinc blende ZnO structure can be stabilized only by growth on cubic substrates, whereas the rocksalt structure is a high pressure metastable phase forming at about 10 GPa, and cannot be epitaxially stabilized [56].

### 2.5.2 Amorphous structure of IGZO

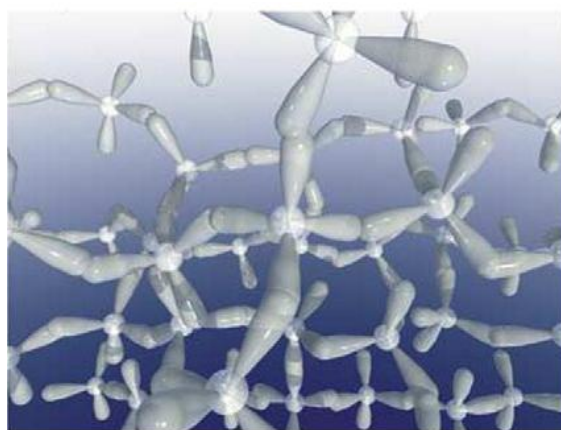
Amorphous oxide semiconductors (AOS), such as indium gallium zinc oxide IGZO, have become one of the most promising materials in flexible TFTs device since first reported in 2004 [9]. The interest is related to the high mobility achieved even in the amorphous phase, which differs from conventional semiconductors where high mobility is achieved in crystalline structures. The amorphous state provides a highly uniform layer, which is important for large area circuit fabrication. The materials exhibit the electric orbital structure and conduction mechanism of carrier transport. For example, in a-IGZO, the conduction band minimum (CBM) consists of unoccupied s-orbitals of metal cations,

and the valence band maximum composed of fully occupied O 2p orbitals [9, 52], with electron conduction through metals ions ns-orbitals. The direct overlap between neighbouring metals ns-orbitals creates a continuous conduction path even in an amorphous structure [9, 33]. Hosono et.al, reported the metal ion should contain heavy post transition metal cations with electric configuration  $(n-1)d^{10} ns^0 n>5$  to achieve high mobility [13, 58]. By contrast, conventional covalent semiconductors such as Si have carrier transport paths composed of  $sp^3$  orbitals with strong spatial directivity [9], and in a-IGZO the conduction band is formed by overlap of the In 5s orbitals [59] as depicted in Figure 2.11.

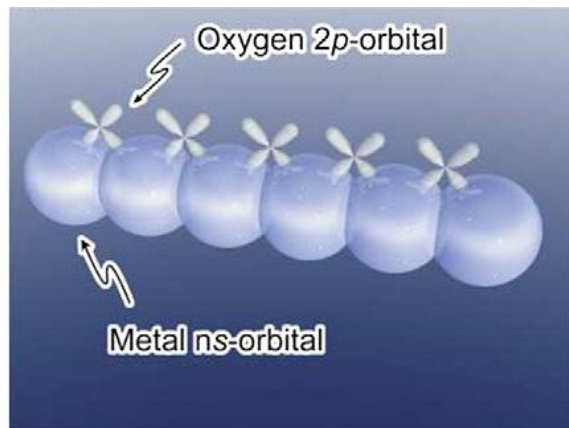
**(a):Covalent semiconductor  
(Silicon crystalline)**



**(amorphous)**



**(b):Post-transition-metal oxide  
semiconductor (crystalline)**



**(amorphous)**

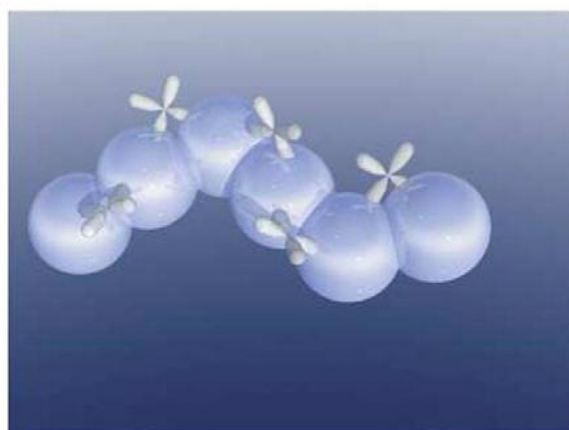


**Figure 2.11:** Schematic orbital structure of carrier transport path in: (a) covalent semiconductor "silicon". (b) Post transition metal oxide semiconductor [9].

## **2.6 ZnO and IGZO layer based TFTs**

### **2.6.1 Zinc oxide (ZnO) layers based TFTs**

The first devices employing fully transparent ZnO-based TFTs were reported in 2003 by three groups: Masuda et. al. Hoffman et. al. and Carcia et. al. [22, 26, 47].

Masuda et.al studied the effect of the double gate insulator layer, with a high carrier concentration layer between the channel layer and source/drain contacts of bottom-gate ZnO-TFTs. Three types of TFTs were investigated: the first devices were fabricated with dual layer gate insulator of SiO<sub>2</sub> and SiN<sub>x</sub>, the second devices were fabricated in the same manner but with high carrier concentration layer between the ZnO layer and source/drain electrodes, and the third set of devices were fabricated with transparent materials. The resultant devices with the high carrier concentration layer presented a high field effect mobility of about 0.97 cm<sup>2</sup>/Vs, and a threshold voltage of -1 V. Conversely, the TFTs without the high carrier concentration layer exhibited a mobility of 0.031 cm<sup>2</sup>/Vs, which was lower than the Hall mobility of the ZnO thin films - at about 0.70 cm<sup>2</sup>/Vs. This reduction was attributed to a reduction in drain current caused by contact resistance between the S/D electrodes and the ZnO layer. TFT devices fabricated on glass substrates demonstrated optical transmittance > 80% in the visible range [22].

Hoffman et.al fabricated bottom-gate highly transparent ZnO-TFTs on glass, with the active layer deposited via ion beam sputtering at room temperature. To functionalise the ZnO film, rapid thermal annealing (RTA) in the range 600-800 °C in oxygen ambient was used. Following the subsequent deposition of the source and drain electrode, RTA was carried out again at 300 °C in an O<sub>2</sub> atmosphere. The devices exhibited channel mobility in the range 0.3 to 2.5 cm<sup>2</sup>/Vs, a threshold voltage of between 10 to 20 V, and a drain current on-to-off ratio ~10<sup>7</sup> [26].

Carcia et. al. demonstrated transparent ZnO-TFTs without post deposition annealing, grown using low temperature processing ( $\sim 120$  °C) via RF magnetron sputtering. The TFTs exhibited a channel mobility of more than  $2 \text{ cm}^2/\text{Vs}$ , a threshold voltage  $\sim 0\text{V}$ , drain current on-to-off ratio of  $>10^6$ , and transparency  $>80\%$  [47].

More recently, Nishii et. al. reported ZnO-TFTs with improved field effect mobility to  $7 \text{ cm}^2/\text{Vs}$ . These devices were fabricated by pulsed laser deposition (PLD) at a substrate temperature in the range of  $150\text{-}300$  °C, and employed a  $\text{CaHfO}_x$  layer between a ZnO active layer and silicon nitride gate insulator [60].

Carcia et. al. studied the influence of different gate dielectric insulators on the performance of ZnO-TFTs. The insulating thin films studied were  $\text{HfO}_2$ ,  $\text{HfSiO}_x$ ,  $\text{SiO}_2$ , and  $\text{Al}_2\text{O}_3$  deposited via atomic layer deposition (ALD) at temperatures  $300$  °C,  $400$  °C,  $\sim 100$  °C, and ( $450$  °C,  $200$  °C,  $150$  °C) respectively. The TFT devices with an alumina dielectric grown at  $125$  °C and  $200$  °C resulted in combination of lower threshold voltage ( $1.1 \text{ V}$ ), and the highest mobility at  $17.6 \text{ cm}^2/\text{Vs}$  [49].

Navamathavan et. al. reported an improvement of ZnO-TFTs characteristics using bottom-gate top-contacts TFTs fabricated with silicon nitride ( $\text{SiN}_x$ ) as the gate dielectric layer grown by plasma enhanced chemical vapour deposition (PECVD) at  $300$  °C, and the active layer grown by RF magnetron sputtering at  $300$  °C. The resultant devices showed field effect mobility at  $31 \text{ cm}^2/\text{Vs}$ , a threshold voltage of  $9 \text{ V}$ , and drain current on/off ratio more than  $10^5$  [61].

Cross et. al. examined the stability of inverted-staggered ZnO-TFTs devices under bias stress. Comparisons were made between the stability of devices fabricated using silicon dioxide ( $\text{SiO}_2$ ) and silicon nitride ( $\text{SiN}$ ) as the gate insulator, deposited via low pressure chemical vapour deposition followed by annealing at  $1000$  °C, with the active layer in both cases grown by RF magnetron sputtering at room temperature. The results demonstrated devices with silicon nitride as gate insulator have slightly better performance than TFTs with silicon dioxide gate dielectric. However, the TFT

parameters achieved were lower than that reported in the literature and were attributed to the influence of grain boundary scattering at the ZnO/insulator layer interface. In terms of stability under bias stress, both sets of devices exhibited a shift in threshold voltage caused by the lattice mismatch between the ZnO/insulator interface [62].

Kim et. al. studied the effect of post deposition laser treatment, thermal anneal, and a combination of thermal anneal with laser anneal on the performance of bottom gate-bottom contacts ZnO-TFTs fabricated at 400 °C, utilizing a KrF excimer laser ( $\lambda = 248$  nm) in air at a fluence of 100 mJ/cm<sup>2</sup> with up to 200 pulses, while thermal annealing was carried out in a furnace in air ambient at a temperature of 400 °C. The result showed improvement in laser annealed devices at 200 pulses compared with un-annealed TFTs with a threshold voltage of 13.4 V, drain current on-to-off ratio of 7.8, and field effect mobility of 0.14 cm<sup>2</sup>/Vs. The devices which were subjected to a combination of thermal and laser annealing exhibited better performance, with the threshold voltage significantly decreased to 0.6 V, field effect mobility increased to 5.08 cm<sup>2</sup>/Vs, and an on-to-off ratio 8.49 [63].

Lim et. al. demonstrated an enhancement in electrical properties of bottom gate ZnO-TFT devices, fabricated at medium temperatures (200 °C), which were subjected to post deposition photonic processing by UV lamp light exposure with wavelength 368 nm for 3 min, 30 min, and 120 min in vacuum. The results exhibit a negative shift in threshold voltage as function of exposure time to 17.8, 1.7, and -6.5 V respectively [64].

Nakata et. al. made a comparative study between thermal and excimer laser annealing of inverted-staggered bottom gate ZnO-TFTs. The active layer was grown via RF magnetron sputtering with no substrate heating. Devices fabricated on silicon substrates were subjected to thermal annealing in air ambient at temperatures from 300 °C to 850 °C for 30 min, while excimer laser processing ( $\lambda=308$  nm) was

conducted for devices on plastic substrates at fluences ranging from 250-450 mJ/cm<sup>2</sup> in air. Results showed that laser annealing was more effective than thermal anneal, with a field effect mobility of 12 cm<sup>2</sup>/Vs achieved at a laser energy density of 350 mJ/cm<sup>2</sup> compared with thermal annealed devices where the equivalent field effect mobility was 6.4 cm<sup>2</sup>/Vs at annealing temperature 850 °C [65].

Ya-Hui yang et. al. reported the influence of laser annealing on solution based ZnO-TFTs with the bottom-gate coplanar structure. The ZnO active layer was deposited by spin-coating and post baked at 95 °C. Subsequently the devices were irradiated by 3<sup>rd</sup> harmonic Nd:YAG laser 355 nm. The resultant as deposited devices demonstrated field effect mobility, threshold voltage; drain current on to off ratio of 0.19 cm<sup>2</sup>/Vs, 3.4 V, and 5.38x10<sup>5</sup> respectively. However, laser irradiated devices show a pronounced improvement in performance, where for example devices processed at a laser dosage of 740mJ (spot size of 2.5x10<sup>-2</sup> cm<sup>2</sup>) exhibited a field effect mobility of 0.49 cm<sup>2</sup>/Vs and drain current on to off ratio 3.19x10<sup>6</sup> [66].

The main results of these studies are presented in Table 2.1. From all reports summarized above we can conclude the electrical characteristics of ZnO TFTs are highly dependent on the deposition techniques employed, and that high deposition temperature or thermal annealing is required to improve the electrical properties of ZnO-TFTs. However, the laser annealing process is a powerful technique to enhance and improve the properties of ZnO-TFTs fabricated at low substrate temperature (<120 °C) compatible with flexible substrates.

Author	Active layer deposition		Post deposition processing	Mobility $\mu$ $\text{cm}^2/\text{Vs}$	$V_{\text{th}}$ (V)	On/Off ratio
	Technique	Temp				
Masuda et.al 2003 [22]	Pulsed laser deposition	450 °C	No	0.97	-1	$\sim 10^5$
Hoffman et.al 2003 [26]	Ion beam sputtering	RT	RTA at 600-800 °C in $\text{O}_2$	2.5	10-2	$\sim 10^7$
Carcia et.al 2003 [47]	RF magnetron sputtering	120 °C	No	2	0	$> 10^6$
Nishii et.al 2003 [60]	PLD	150-300 °C	No	7	N/A	N/A
Carcia et.al 2006 [49]	RF magnetron sputtering	RT	No	17.6	6	N/A
				For $\text{Al}_2\text{O}_3$ at 200 °C		
				3.1	1.1	N/A
				For $\text{Al}_2\text{O}_3$ at 125 °C		
Navamathavan et.al 2008 [61]	RF magnetron sputtering	300 °C	No	31	9	$> 10^5$
Cross et.al 2008 [62]	RF magnetron sputtering	RT	TA at 1000 °C	0.2-0.7	N/A	$10^5$
				With SiN	N/A	$3 \times 10^4$
				0.1-0.25		
				With $\text{SiO}_2$		
Nakata et.al 2009 [65]	RF magnetron sputtering	RT	TA at (300-850 °C) ELA ( $\lambda$ 308nm) 250-450mJ/cm <sup>2</sup>	6.4	N/A	N/A
				12	N/A	N/A
Kim et.al 2010 [63]	RF magnetron sputtering	RT	KrF ELA 248 nm at 100mJ/cm <sup>2</sup> Combination TA at 400 °C +LA at 100 mJ/cm <sup>2</sup> 200 pulses	0.14	13.4	7.8
				5.08	0.6	8.49
Lim et.al 2010 [64]	Plasma enhanced atomic layer deposition PEALD	200 °C	UV lamp 368nm exposure from 3 min 120 min	0.037	17.8	$1.3 \times 10^5$
				0.035	-6.5	$1.4 \times 10^5$
Ya-Hui et.al 2010 [66]	Spin-coating	95 °C	Nd:YAG laser 355nm	0.45	N/A	$3.19 \times 10^6$

**Table 2.1:** Summary of previous work on ZnO-TFTs. TA stands for thermal annealing LA for laser annealing, and Temp for temperature.

Post-deposition processing improved the transfer characteristics of ZnO-TFTs devices by phenomena which occurred when the ZnO films were heated up, indicating possible enhancement mechanisms such as: crystal grain growth caused by Zn atoms gaining higher energy, making Zinc and oxygen atoms well bonded by filling the entire volume within a grain creating a path for current to flow as shown in Figure 2.12 [65, 67]. Hence electrical current increased, and there could be an increase in the carrier concentration by generation of oxygen vacancies or Zn interstitials [64], and a reduction of the concentration of point defects.

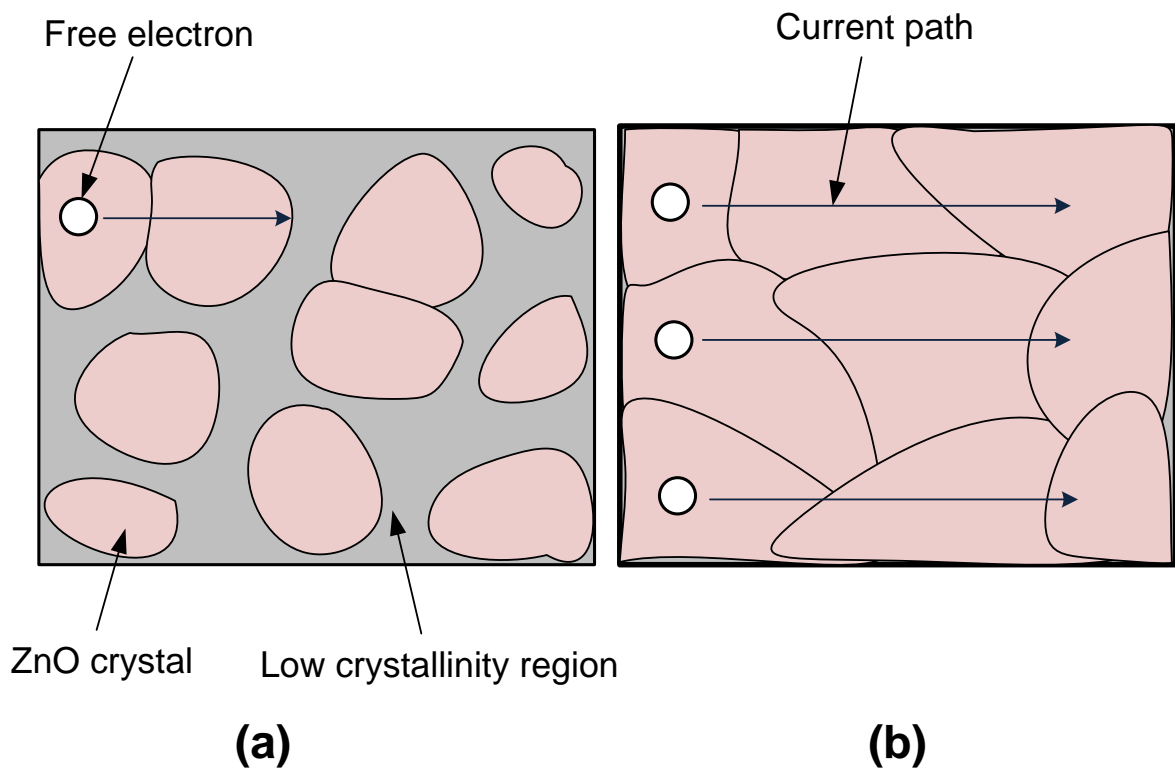


**Figure 2.12:** The concept of crystal grain growth of ZnO films as a function of thermal annealing: (a) as-deposited, (b) thermal annealed above 500 °C, adapted from [65]

To investigate this in detail, the research presented here investigates the effect of laser annealing on the microstructure properties of ZnO thin films grown by two different techniques; high target utilisation system (HiTUS) without intentional substrate heating at various oxygen flow rates to identify the influences of three annealing methods (furnace, rapid thermal, and laser annealing), and RF magnetron sputtering deposition

at various temperatures (from RT to 400 °C) to investigate and compare the effect of a laser and thermal anneal of ZnO grown at various substrate temperatures, and to investigate the nature of point defects developed or suppressed by the annealing processes.

### **2.6.2 Multicomponent amorphous oxides of indium gallium zinc oxide (IGZO) based TFTs**

In 2003 Nomura et. al. reported transparent single crystalline IGZO thin film transistors using the top gate structure, with all TFT layers deposited via pulsed laser deposition (PLD) at room temperature: 120 nm of  $\text{InGaO}_3(\text{ZnO})_5$  (as the active layer) deposited on yttria-stabilized zirconia (YSZ) substrate, followed by thermal annealing at 1400 °C for 30 min, ITO source and drain electrodes grown and patterned on the channel layer, amorphous  $\text{HfO}_2$  80 nm thick deposited as the gate insulator, and finally, an ITO gate electrode on the top. As a result of the high annealing temperature, the devices exhibited high field effect mobility  $\sim 80 \text{ cm}^2/\text{Vs}$ , a drain current on-to-off ratio  $\sim 10^6$ , threshold voltage of 3 V, and an optical transmittance  $> 80\%$  at wavelengths between 390 nm-3200 nm [68].

Amorphous oxide semiconductor (AOS) of indium gallium zinc oxide (IGZO)-based transparent and flexible TFTs was first reported in 2004 by Nomura et. al. who demonstrated a-IGZO based TFTs, coplanar top-gate structure on polyethylene terephthalan (PEN) flexible substrates at room temperature, with all layers grown by pulsed laser deposition (PLD). Yttrium oxide,  $\text{Y}_2\text{O}_3$ , was employed as the gate insulator. The resultant devices exhibited a field effect mobility of  $\sim 8.3 \text{ cm}^2/\text{Vs}$ , drain current on-to-off ratio  $\sim 10^6$ , and threshold voltage of 1.6 V [9].

In early 2006, Yabuta et. al. fabricated staggered top-gate type a-IGZO TFTs, where RF magnetron sputtering was used to deposit the channel layer and gate insulator layers on glass substrates. The electrical properties showed channel mobility, threshold voltage, drain current on-to-off ratio of  $12 \text{ cm}^2/\text{Vs}$ , 1.4 V, and  $\sim 10^8$  respectively [10].

Since the first reports on IGZO TFTs research, there has been interest in studying the effect of post deposition annealing as a mechanism to improve performance and stability of the devices.

Kikunhi et. al. studied the effect of post deposition processing of IGZO-TFTs at temperatures up to 400 °C. Two IGZO films were deposited via pulsed laser deposition (PLD) and RF magnetron sputtering at room temperature. Prior to fabrication, the top-contact bottom-gate TFTs structured a-IGZO films were subjected to a thermal anneal in wet oxygen and dry oxygen atmosphere of 1 atm at various annealing temperatures up to 200 °C. The RF sputtered TFTs annealed in dry oxygen at 150-200 °C exhibited enhanced and improved characteristics, whereas wet annealing enhanced device performance, but caused a large negative shift in threshold voltage. In contrast, PLD devices with wet annealing at 200 °C exhibited improved characteristics with a small negative shift in threshold voltage [69].

Ide et. al. examined the effect of the ozone ( $O_3$ ) annealing technique at temperature <250 °C, on top-contact bottom-gate TFTs with a-IGZO films via RF magnetron sputtering and ozone ( $O_3$ ) annealing. The  $O_3$  annealing improved the performance of TFTs properties, and was more effective than conventional thermal annealing in oxygen or air. The devices exhibited a channel mobility of  $\sim 11.4 \text{ cm}^2/\text{Vs}$ , threshold voltage 0.1 V, and sub threshold swing of 217 mV/decade [70, 71].

Nomura et. al. studied the stability of passivated a-IGZO TFTs against negative bias light illumination stress (NBLS), and constant current stress (CCS). Bottom – gate top contact TFTs were fabricated on Si substrates at room temperature, with the active layer grown via pulsed laser deposition (PLD), and prior to the source and drain contacts formation thermal annealing at 400 °C in wet oxygen with  $H_2O$  vapour was conducted. Then the  $Y_2O_3$  passivation layer was deposited, and the devices were annealed at 350 °C in air for 30 min. The resultant passivated TFTs exhibited a channel mobility  $\sim 12.14 \text{ cm}^2/\text{Vs}$ , threshold voltage  $\sim -1 \text{ V}$ , and sub threshold swing  $\sim 0.14$

V/decade with improvement of the stability against constant current stress, and negative bias light illumination stress compared to un-passivated TFTs [72].

However, post thermal annealing at temperatures higher than the maximum allowable temperature for heat resistance of plastic substrates ( $\sim 150$  °C) is undesirable when considering low cost and flexible substrate applications. So, as an alternative to thermal annealing, photonic processing using UV lamps or laser irradiation is a method of interest for a range of applications where highly localised annealing and surface modification is required [73, 74].

For example, Nakata et. al. reported utilizing excimer laser annealing (ELA) to process 20 nm IGZO thin films for inverted-staggered bottom gate a-IGZO-TFTs deposited via RF magnetron sputtering at room temperature, using a XeCl excimer laser ( $\lambda=308$  nm) at 25 ns, for 2 pulses. The IGZO-TFTs irradiated at laser fluences of  $130 \text{ mJ/cm}^2$  exhibited ON current more than one order of magnitude higher than that of un-annealed devices with a field effect mobility of  $14 \text{ cm}^2/\text{Vs}$  [73].

Subsequently, many researchers have extensively focused on enhancing and improving the properties of a-IGZO – TFTs using different kinds of post deposition photonic processing.

Ahn et. al. fabricated bottom gate a-IGZO-TFTs, using a 50 nm thick channel layer grown by RF magnetron sputtering without intentional substrate heating. The IGZO films were selectively laser processed via a projection mask using a XeCl ( $\lambda=308$  nm) excimer laser in air ambient at ten pulses with a range of laser energy densities from 0 to  $250 \text{ mJ/cm}^2$ . The electrical properties of the devices treated with laser energy density  $130 \text{ mJ/cm}^2$  exhibited a channel mobility of  $21.79 \text{ cm}^2/\text{Vs}$ , on/off ratio of  $1.2 \times 10^8$ , and threshold voltage  $\sim -0.15 \text{ V}$ . As the laser fluences increased to  $130 \text{ mJ/cm}^2$  the resistivity of IGZO film decreased from  $104 \Omega \text{ cm}$  to  $3.2 \times 10^{-3} \Omega \text{ cm}$  with carrier concentration  $1.3 \times 10^{20} \text{ cm}^{-3}$ , and hall mobility  $15 \text{ cm}^2/\text{Vs}$  [74].

It has also been reported by Zan et. al. that the 4<sup>th</sup> harmonic of an Nd:YAG laser (266 nm) or UV lamp irradiation (172 nm) light exposure suppressed the instability of a-IGZO TFTs, and reduced the defects in IGZO film. Tests used a stable bottom-gate top contact a-IGZO-TFT where the active layer was deposited by RF magnetron sputtering and was subjected to the low temperature annealing methods of solid-state Nd:YAG laser processing at 266 nm or UV lamp irradiation (172 nm). The TFT devices annealed by Nd:YAG laser at energy density 10.7 mJ/cm<sup>2</sup> exhibited an improvement in stability with channel mobility of 8 cm<sup>2</sup>/Vs, threshold voltage 0 V, an on/off current ratio larger than 7 order of magnitude, while devices subjected to UV lamp irradiation for 30 min showed a channel mobility of 3 cm<sup>2</sup>/Vs, a threshold voltage 0 V, and on/off current ratio larger than 6 order magnitude [75].

Ya-Hui Yang et. al. studied the effect of the 3<sup>rd</sup> harmonic of the Nd:YAG laser ( $\lambda=355$  nm) on the performance of solution based IGZO-TFTs. 200 nm thick IGZO was the active layer grown by spin-coating, and baked at 95 °C, with the devices subjected to Nd:YAG laser annealing at various energy densities in air. Results demonstrate a clear improvement in device properties as a function of laser processing, with field effect mobility of 7.65 cm<sup>2</sup>/Vs, and drain current on to off ratio  $2.88 \times 10^7$  [76, 77].

Author	IGZO active layer deposition		Post deposition processing	Mobility $\mu$ cm <sup>2</sup> /Vs	V <sub>th</sub> (V)	On/Off ratio
	Technique	Temp				
Nomura et.al 2003 [68]	Pulsed laser Deposition (PLD)	RT	Thermal anneal at 1400°C,3min	80	3	~10 <sup>6</sup>
Nomura et.al 2004 [9]	Pulsed laser Deposition (PLD)	RT	No	8.3	1.6	~10 <sup>6</sup>
Yabuta et.al 2006 [10]	RF magnetron Sputtering	RT	No	12	1.4	10 <sup>8</sup>
Ahn et.al 2009 [74]	RF magnetron Sputtering	RT	XeCl-LA ( $\lambda=308\text{nm}$ ) 0 -250mJ/cm <sup>2</sup>	21.79	-0.1	1.2x10 <sup>8</sup>
Nakata et.al 2009 [73]	RF magnetron Sputtering	RT	XeCl ELA ( $\lambda=308\text{nm}$ ), 130mJ/cm <sup>2</sup> , 2pulses	14	N/A	N/A
Zan et.al 2010 [75]	RF magnetron Sputtering	RT	- Nd:YAG laser 266nm 10-25mJ/cm <sup>2</sup>	8	0	>10 <sup>7</sup>
			-UV lamp irradiation 172nm, 30min	3	0	>10 <sup>6</sup>
Kikunhi et.al 2010 [69]	PLD	RT	-TA in wet O <sub>2</sub> at 200°C	12.6	-1.7	N/A
	RF magnetron Sputtering	RT	-TA in dry O <sub>2</sub> at 150°C	8.9	-5	N/A
Ide et.al 2011 [70]	RF magnetron Sputtering	RT	TA ozone O <sub>3</sub> at 150°C	11.4	0.1	N/A
Nomura et.al 2011 [72]	PLD	RT	TA at 400°C in wet O <sub>2</sub> with H <sub>2</sub> O vapour	12.14	-1	N/A
Ya-Hui Yang 2011 [77]	Spin-coating	95°C	Nd:YAG laser 355nm	7.65	N/A	2.8x10 <sup>7</sup>

**Table 2.2:** Summary of the IGZO-TFTs work presented previously in the literature. TA stands for thermal annealing, LA for laser annealing and Temp for temperature.

In all reports summarized in Table 2.2, RF magnetron sputtering, and pulsed laser deposition (PLD) are the most common techniques used to grow IGZO for a channel layer in TFTs, without intentional heating of the substrate. Overall, devices thermally annealed exhibit reasonable TFTs properties compared with un-annealed devices. However, thermal anneal <200 °C in O<sub>3</sub> is more effective than in O<sub>2</sub> or air because O<sub>3</sub> results in better devices by suppressing the large negative shift in V<sub>th</sub> that is reported when annealing in O<sub>2</sub> was employed. This effect is ascribed to annealing in O<sub>3</sub> being

more effective in reducing the defects in the deep channel region than O<sub>2</sub>. Also the stronger oxidation of O<sub>3</sub> leads to a reduction in electron density [71].

Interestingly, excimer laser annealing of TFTs demonstrated by Ahn et. al. exhibits better performance than thermally annealed devices, with mobility of 21.9 cm<sup>2</sup>/Vs. This is linked to a different possible mechanism that arises from raising the film temperature such as; creating a new equilibrium by removing weakly bonded oxygen atoms [75], reduction in the density of tail states below the conduction band in IGZO film, and reduction in contact resistance between IGZO channel layer and source/drain contacts [74], as well as an increase in the electron density.

Laser annealing is thus a technique that can be used to improve the properties of IGZO TFTs. Further work is presented in this study which investigates the effect of laser annealing on electrical properties of IGZO films grown without intentional substrate heating at various deposition parameters by varying RF power, oxygen concentration, deposition pressure and from targets with two different stoichiometries, (2:2:1) and (1:1:1). The influence of laser annealing before and after IGZO channel layer patterning on the electrical properties of IGZO TFTs is also studied.

## **2.7 Sputtering**

Sputtering is one of the most important deposition methods used to deposit thin films onto substrate surfaces, and is widely used in industrial and microelectronics fabrication [78, 79]. First discovered in 1852 was the dc gas discharge tube by W.R.Grove [80]. This was developed as a thin film deposition technique by Langmuir in the 1920s [81].

Sputtering is a physical vapour deposition technique in which the substrate (anode terminal) is placed in a vacuum system (chamber) opposite the cathode surface which is covered with the target material to be deposited via transfer of target atoms through the sputtering gases [78].

The basic concept of sputtering is that when the gas, typically argon, is introduced to the evacuated chamber, a voltage is applied between the electrodes to create a discharge.  $\text{Ar}^+$  ions are created in the resultant glow discharge phenomenon (plasma), and are accelerated towards the cathode and sputter the target via transfer of kinetic energy, resulting in coating the thin film on the substrate surface [78] as shown in Figure 2.13.

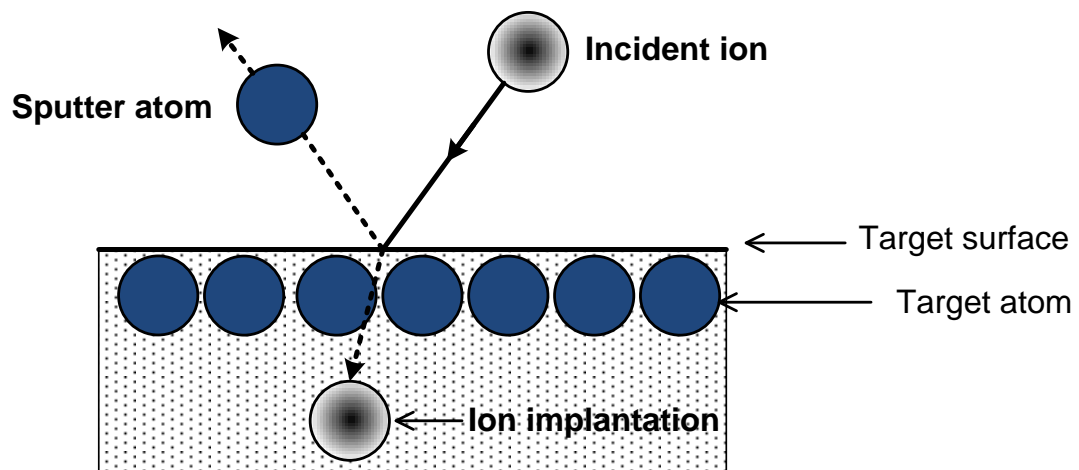


**Figure 2.13:** Sputtering process (adapted from [78]).

However, this technique has some shortcomings which relate to the quality and film properties, such as low deposition rate [57]. In 1970s, Chapin had developed a sputtering system to achieve large area high-rate deposition by inserting a strong magnet below the target in order to generate a magnetic field perpendicular to the electric field between the target and the substrate [82]. This forced the electrons to move close to the target in circular path of the magnetic field lines. Therefore electron motion increases the probability that they will collide with neutral gaseous molecules to generate ions, hence increase the rate of ion bombardment of the target, and prevent ion bombardment occurring at the substrate surface [83].

However, when dc sputtering is used to deposit insulating materials such as silicon dioxide  $\text{SiO}_2$  or yttrium oxide  $\text{Y}_2\text{O}_3$ , the glow discharge phenomenon cannot be sustained because of the build up of a surface charge of positive ions in front of the

target surface leading to the cessation of the sputtering process. For this reason, magnetron sputtering supplied by a radio frequency voltage (13.56 MHz) is used to prevent charge build up on the target [78].

### **2.7.1 RF magnetron sputtering**

A simple RF magnetron sputtering system consists of three main parts; the main sputtering chamber with a substrate holder (anode) and sputtering electrode/ target assembly (cathode), diffusion and rotary pumps, and load lock chamber. For the work presented here, RF magnetron sputtering deposition was undertaken in the system described in detail in Chapter 3. In general, when undertaking RF magnetron sputtering, the substrate and the target are closely placed, often about less than 10 cm [83]. The substrate is ideally inserted inside the chamber from a clean area via a load lock chamber equipped with a transfer arm used to load several substrates without opening the chamber to the atmosphere. The chamber is connected to a pumping system which can also pump down the load lock before the substrate is loaded to the main chamber. The substrate holder can be rotated during sputtering to achieve a uniform deposition over a large area. Inert and/or reactive gases are passed through mass flow controllers (MFC) to allow a certain value of gas flow introduced to the chamber. The gases are usually  $O_2 / Ar + O_2$  with ratio from 0 to 1 at pressure  $10^{-3} - 10^{-2}$  Torr, with  $O_2$  acting as the gas, while Ar is used to enhance the sputtering process [83, 84]. Shutters can be used to shield the substrate during pre-sputtering, or to block other electrodes in a multi electrode system. During the sputtering processing the target electrode (cathode) will become hot from the plasma mechanisms; hence, to avoid excessive heating up of the cathode, the electrode assembly is supplied with cooling water.

Figure 2.14 shows the plasma mechanisms during deposition, with the electric field applied cross the area between target (cathode) and substrate (anode). As the argon gas is introduced to the vacuum chamber, argon atoms will get ionized creating a

plasma (glow discharge) and accelerated causing (ion bombardment) collisions onto the target surface resulting in releasing target atoms and electrons. Ejected target atoms are scattered by argon atoms until they arrive and condense on the substrate surface forming a thin film layer at the substrate, while generated electrons will collide with neutral argon atoms leading to increased ionization of argon atoms, with the magnetic field restricting the movement of electrons near the target surface, to keep them away from bombarding the film surface.

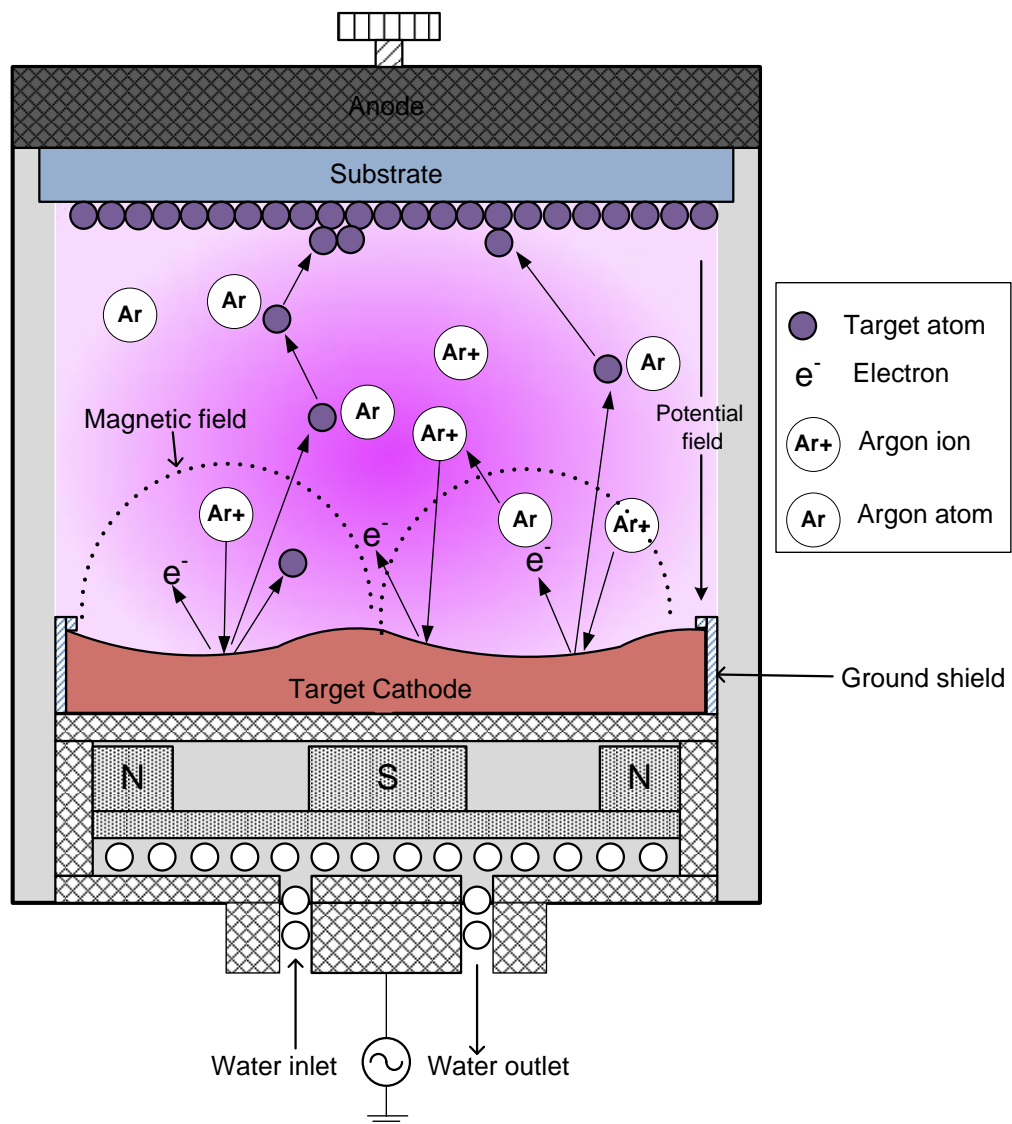


**Figure 2.14:** Illustration of the phenomena taking place during deposition by RF magnetron sputtering adapted from [85].

## 2.8 Conclusions

High performance TFTs for full active matrix display (LCD or OLED) applications should demonstrate the following criteria: low threshold voltage ( $V_{th}$ ), high electron mobility ( $\mu$ ), high current on/off ratio, processing at low temperature to become compatible with plastic substrates, good stability [86], and ideally be transparent. In this study all the above important aspects must be considered for investigating ZnO and a-IGZO thin films, and ZnO, a-IGZO based TFTs. This includes microstructure characterisation of ZnO and a-IGZO to examine the defects, grain size, and crystal structure which influences the electron mobility and the surface uniformity of the film, which is important for channel interface considerations. This work was devoted to investigate the effect of laser processing on microstructure and electrical properties of two oxide semiconductor materials of ZnO and IGZO. The ZnO was deposited using two sputtering techniques HiTUS, and RF magnetron sputtering. HiTUS films were deposited at room temperature with different oxygen flow rates, RF magnetron sputtering films were deposited at various RF power, oxygen concentration and substrate temperatures. IGZO films were also deposited by RF magnetron sputtering, using two targets with two stoichiometries (2:2:1) and (1:1:1), at various conditions to investigate the optimal conditions in terms of conductivity and Hall mobility. IGZO-TFTs were fabricated and subjected to laser and thermal processing to study the effect annealing process on TFT performance.

## Chapter 3

### Experimental Techniques

---

#### 3.1 Introduction

The initial phase of the work was concerned with the deposition of ZnO thin films by using two sputtering deposition techniques: High Target Utilisation Sputtering (HiTUS), and RF magnetron sputtering. A comparative study of post deposition processing was then investigated using three annealing techniques, excimer laser annealing (ELA), rapid thermal anneal (RTA), and thermal anneal (TA). Laser processing of IGZO thin films deposited by RF magnetron sputtering was also investigated for optimization studies. Finally, photoluminescence (PL), X-ray diffraction (XRD), transmission electron microscopy (TEM), four point probe (4PP), and Hall Effect as thin film characterisation techniques have been utilised to investigate the microstructure and electrical properties of processed ZnO and IGZO thin films.

#### 3.2 Thin film deposition

The first phase of this work was undertaken in collaboration with Cambridge University. A series of initial trials involved a study of ZnO films and ZnO TFT devices based on the bottom gate structure. These initial films were deposited at Cambridge University using the High Target Utilisation sputtering (HiTUS) method, which is a technique previously utilised by our group for luminescent materials and which offers high quality thin films deposited at low temperature [87]. To investigate the properties of ZnO grown at room temperature, the first stage of experimental work was the optimisation of the ZnO thin films layer by a comparative study between three annealing techniques: thermal anneal (TA), rapid thermal anneal (RTA), excimer laser anneal (ELA).

The second phase of this work involved ZnO thin films deposited on silicon, and silicon dioxide covered silicon ( $\text{SiO}_2/\text{Si}$ ) substrates, by RF magnetron sputtering at various substrate temperatures up to 400 °C. Following deposition at NTU, ZnO films were subjected to laser annealing in order to study its effect on structure and semiconducting properties.

The third phase of this work was devoted to studying the electrical properties of IGZO thin films deposited by RF magnetron sputtering under various conditions. The optimal conditions of film deposition and laser anneal were determined after electrical characterisation of IGZO layers, and these conditions were used to fabricate test IGZO-TFTs.

There are various techniques employed to grow transparent conducting oxides thin films such as: molecular beam epitaxy [88], chemical vapour deposition [89], pulsed laser deposition [90], atomic layer deposition [91], and RF magnetron sputtering [17]. Among these methods RF magnetron sputtering is the most commonly used technique, and has been used extensively during the last decade, because of advantages such as low operating temperature, uniformity, and reasonable quality of film at low cost [92]. For the research presented here, two sputtering techniques were used – High Target Utilisation Sputtering (HiTUS) and RF-magnetron sputtering, with HiTUS depositions being undertaken via collaboration with Cambridge University, and the RF-magnetron sputtering undertaken at NTU.

### **3.2.1 High target utilisation sputtering HiTUS**

High target utilisation sputtering (HiTUS) is a technique developed by a UK technology company, Plasma Quest Ltd. [93] as an advanced RF sputtering technology, in which a high density plasma is created in a remote chamber, to allow high deposition rates of ~ 50 nm/min while maintaining excellent material properties [94]. Figure 3.1 shows a schematic diagram of the employed HiTUS system. The system consists of a side arm plasma launch system (PLS) connected to the main sputtering chamber. The PLS

contains a quartz tube surrounded by a copper antenna coil. 13.56 MHz RF power is supplied to the side arm to generate highly intense plasma ( $10^{13}$  ions  $\text{cm}^{-3}$ ) away from the substrate. Argon and oxygen are injected into the chamber separately using gas distribution rings, with the argon next to the target for sputtering (of metallic target) and oxygen in close proximity to the substrate for deposition of metal oxide thin films [94]. The electromagnets at the exit of the PLS enhance and steer the plasma onto the target resulting in a high density plasma over the full surface area of the target [87]. The HiTUS technique has been previously reported for the deposition of low temperature metal oxides for transparent conducting electrodes [87, 95], light emitting devices [96], thin film transistors [94], and electroluminescent devices [97].

For this work, several samples of ZnO films were deposited onto 100 mm silicon substrates by using reactive sputtering from a 99.99% purity metallic zinc target. Argon and oxygen were used as sputtering and reactive gases respectively, argon flow rate of 55 sccm, at different oxygen flow rates of 28, 32, 35, 38, and 41 sccm. With RF launch power of 1000 W and target bias power was 800 W. The films were deposited to a thickness of 60 nm, and 200 nm, with no intentional substrate heating (maximum achievable temperature during sputtering about 70 °C). Samples were received from Cambridge University, following deposition by HiTUS in a system as shown in Figure 3.1.

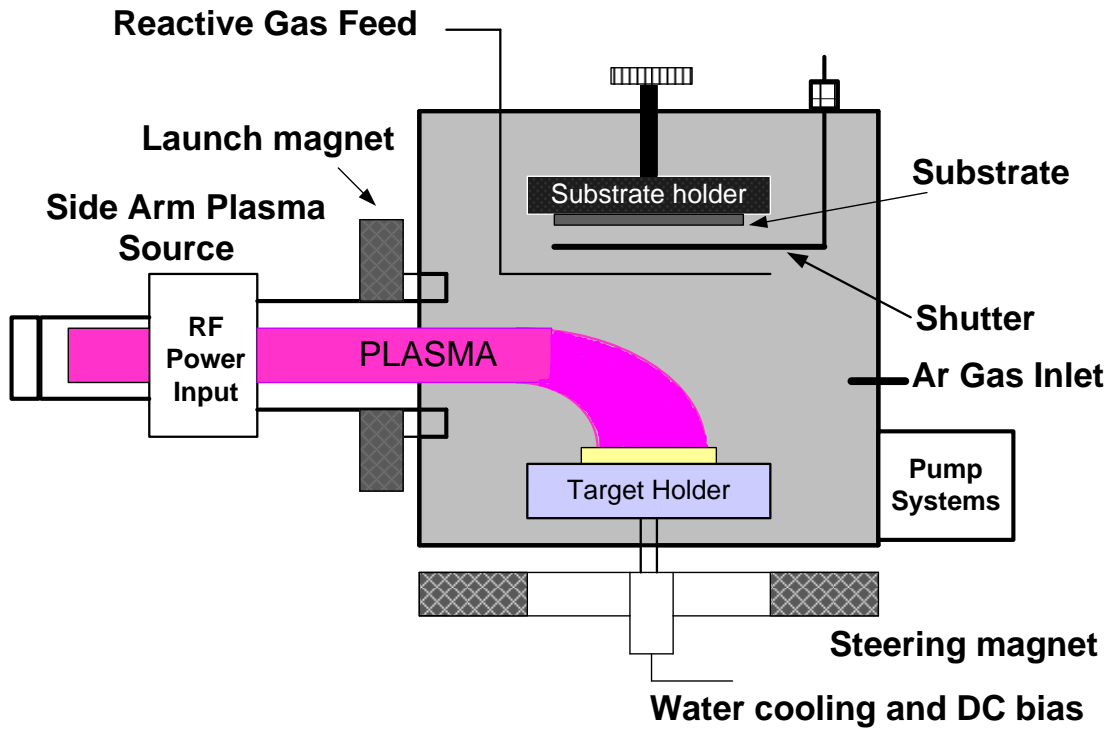


**Figure 3.1:** Schematic diagram of the HiTUS system (adapted from [87]).

### 3.2.2 RF magnetron sputtering

All films deposited by RF magnetron sputtering were grown by the author using the facilities at NTU. Initially, three ceramic targets (purity 99.99%) at 76.2 mm diameter (5 mm thick) of transparent semiconductor oxides materials of zinc oxide (ZnO) and indium gallium zinc oxide (IGZO) with two different stoichiometries (2:2:1) (1:1:1), were loaded in the sputtering system. Figure 3.2 shows a schematic diagram of the RF magnetron sputtering system used in this work.

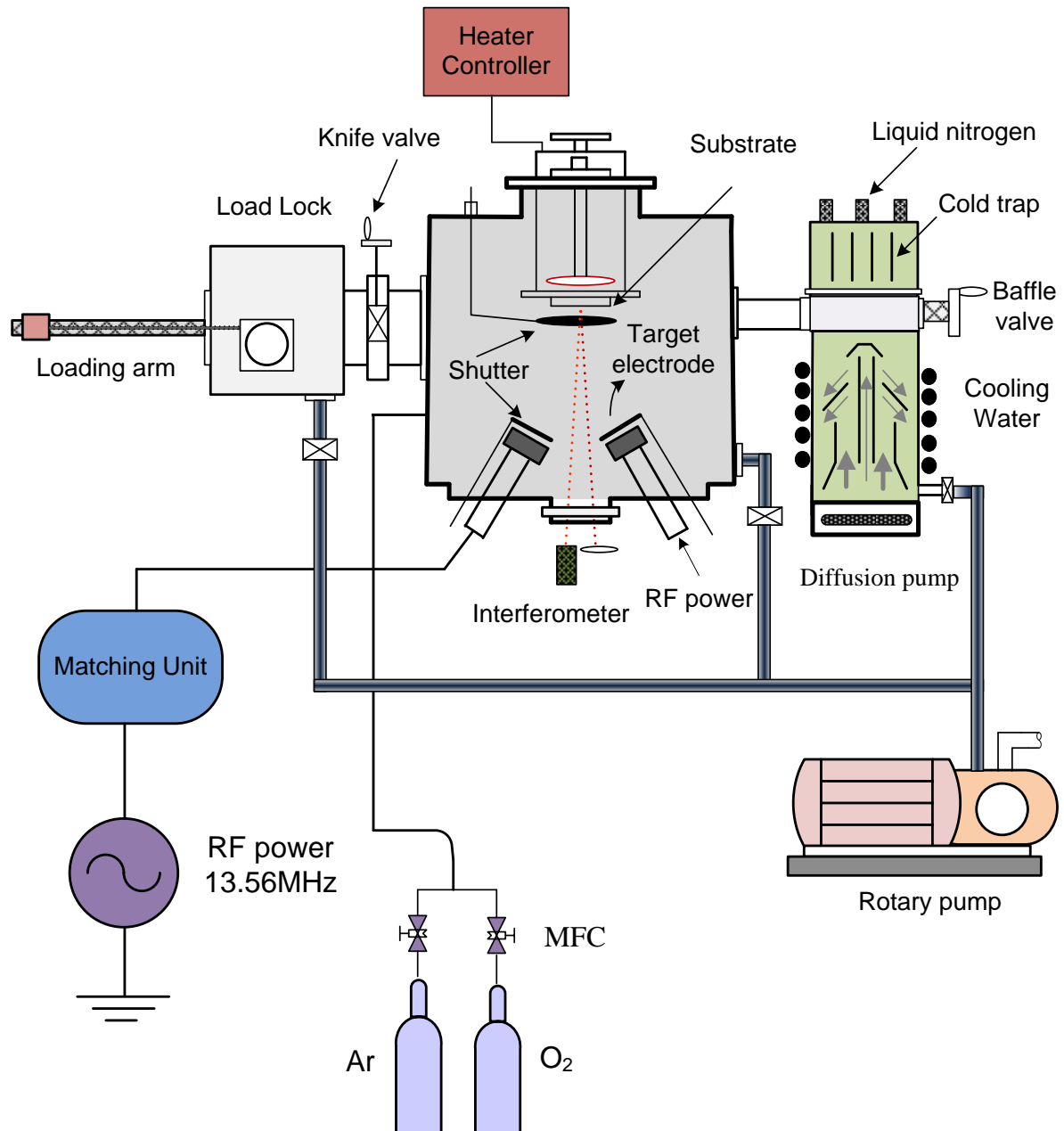


**Figure 3.2:** Schematic diagram of RF magnetron sputtering system.

Before sputtering took place, the deposition chamber was baked at 500 °C for about one hour, in order to remove moisture that comes from the atmosphere following loading the targets. After the chamber had cooled down, its base pressure reduced to  $1.2 \times 10^{-7}$  mbar. To start the deposition, a gas mixture of argon (sputtering) and oxygen (reactive) was introduced to the chamber (at various oxygen concentrations)

controlled by mass flow controllers (MFC). In order to strike plasma the relative chamber pressure was set to about 25 mTorr, while the (13.56 MHz) RF power was set to 40 W. Once the plasma was generated and stabilized, the chamber pressure was reduced to the required deposition pressure by opening the baffle valve gradually. The RF power was also increased gradually in steps of 20 W, until the specific required values of growth pressure and power were reached, and then the substrate shutter was taken out after a 5 minute pre sputtering to clean the target surface. An interferometer was used to monitor the film thickness during the deposition.

The thickness of the deposited films was monitored during growth via an in-situ optical interferometer system at the bottom of the sputtering system, while the laser beam goes through a window and approaches the substrate. A laser beam ( $\lambda=625$  nm) was directed to the sample being deposited (see Figure 3.3), with the incident beam reflected at the film surface ( $x_1$ ), while a part of the incident beam is transmitted through the transparent film and is reflected at the substrate surface ( $x_2$ ). The additional optical path length results in a phase change compared to the reflected incident beam, and leads to interference between the two reflected beams which is related to the film thickness. The interference between reflected beams results in a varying intensity detected by a photodiode, and this intensity variation is monitored via (Picodog Data Acquisition) software and displayed as a series of constructive and destructive interference manifesting in a cyclical manner as the film thickness increases.

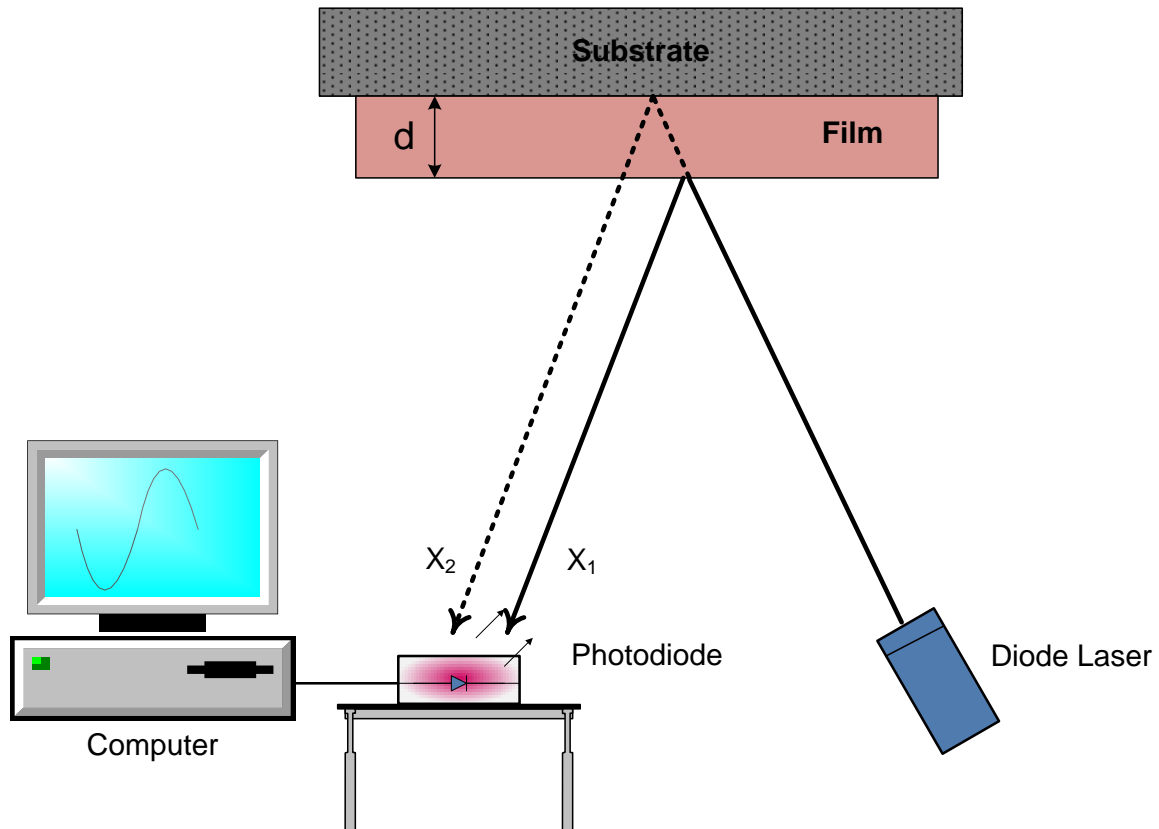


**Figure 3.3:** Thickness monitoring setup by interferometer.

The constructive interference (intensity maximum) occurs when  $m\lambda = 2nd\sin\theta$

where:  $\lambda$ : incident wavelength

$m$ : is an integer

$n$ : refractive index of the film

$d$ : thickness of the film

For thickness calibration prior to deposition on the actual substrate, deposition was carried out on a masked glass wafer in order to have a sharp step edge between the deposited film and the substrate. The film's thickness was then measured by a stylus profilometer (Dektak), and compared to the interferometer trace. Equivalent film thicknesses for one full cycle on the interferometer were found to be 1800 Å, and 1650 Å for ZnO and IGZO films respectively. The refractive index calculated for both materials at laser incident angle of 70° was found to be  $n=1.84$  for ZnO, and  $n=2.01$  for IGZO.

A series of depositions were carried out by RF magnetron sputtering as follows:

- 1- Samples of ZnO films of 60nm thickness, were deposited onto 100 mm silicon (100) substrates at ambient temperatures (with no intentional substrate heating) by varying oxygen concentrations (5% O<sub>2</sub> in Ar-20% O<sub>2</sub> in Ar), and RF power (50, 100, 200, and 300 W) target diameter 76.2 nm with deposition pressure set at 2 mTorr.
- 2- Samples of ZnO films (60 nm thick) were deposited onto silicon (100) substrates, and (111) silicon dioxide coated silicon (SiO<sub>2</sub>/Si) substrates across a range of substrate temperatures (RT, 100 °C, 200 °C, 300 °C, and 400 °C), with oxygen concentrations of 20% O<sub>2</sub> in Ar, RF power 50 W, and deposition pressure of 2 mTorr.
- 3- Samples of IGZO thin films of 30 nm and 50 nm thickness were deposited by RF magnetron sputtering from In<sub>2</sub>O<sub>3</sub>:Ga<sub>2</sub>O<sub>3</sub>:ZnO targets with two different stoichiometries ratios of (2:2:1), and (1:1:1) onto (111) silicon dioxide coated silicon substrates. Deposition was performed at ambient temperature (with no intentional substrate heating) across a range of sputtering conditions by varying oxygen concentrations (2% O<sub>2</sub> in Ar, 5% O<sub>2</sub> in Ar, and 10% O<sub>2</sub> in Ar), and RF power (50 W, 100 W) with target diameter 76.2nm at deposition pressure 2 mTorr to optimise the films for use in TFT device testing.

### **3.3 Excimer laser annealing (ELA)**

The laser annealing process is a highly localised heat treatment technique to modify and improve the properties of transparent conducting thin films. All of ZnO films, IGZO films, and IGZO channel layers for TFTs that were deposited by both HiTUS and RF magnetron sputtering with different growth conditions, were subjected to laser treatment using a KrF excimer laser at NTU. Various fluences (energy density in units of Joules per square centimetre – J/cm<sup>2</sup>) were applied via single or multiple pulses to investigate the optimal conditions.

Laser processing was performed using a Lambda Physic LPX 305i excimer laser with an operating wavelength 248 nm (KrF), at 20 ns pulse width. The pulse frequency varied from 1 to 25 Hz, while a discharge voltage ranging from 14 to 24 kV was used to provide coarse adjustment of the energy density. The ZnO and IGZO thin films were diced onto 11 mm x 11 mm pieces, and processed using a homogenised laser beam spot with an area of 10 mm x 10 mm. Various fluences were used in the range of 0 mJ/cm<sup>2</sup> to 340 mJ/cm<sup>2</sup> ( $\pm 2\%$ ), using single pulse, and multiple pulse irradiation with fine adjustment of fluence provided by a variable attenuator.

Figure 3.4 shows a schematic diagram of the laser beam plan view setup. Initially, the raw beam is directed to a variable attenuator to control the energy density of the beam by tilting the optics, and a UV lens is used to reduce the spot size in order to increase the energy density. The main principle of the beam homogenizer is to divide the laser beam into small sections (beamlets), and recombine them by over lapping in order to produce a highly uniform energy profile over a predefined cross section size at the mask location. This is achieved using two lens arrays and a condenser lens [98]. A mask stage is used to pattern the beam spot to particular features, then the projection lens is used to image the mask features onto the work piece. The distance from projection lens to the sample cell was varied to control the laser spot size at the sample position. Sample positioning was achieved utilising a computer controlled x-y-z translation stage.

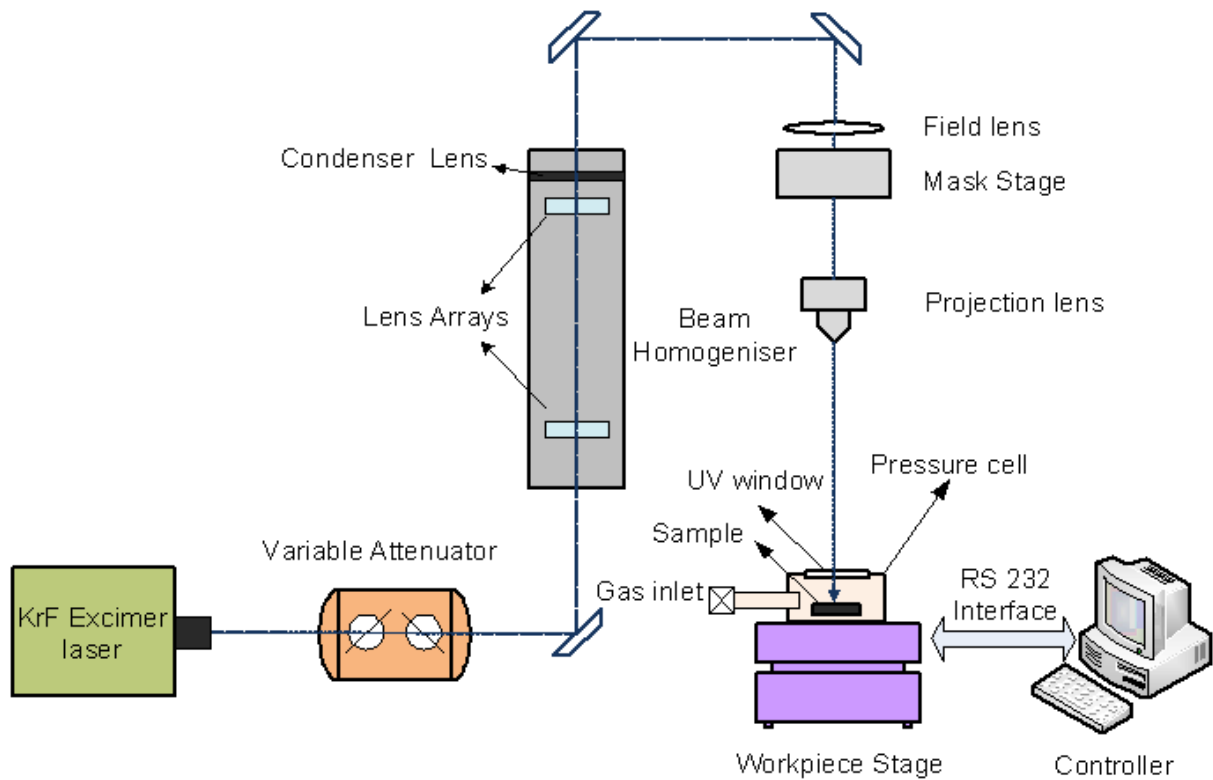


**Figure 3.4:** Schematic diagram of KrF excimer laser setup.

For comparison rapid thermal annealing (RTA) was conducted using Annealsys rapid thermal processor/annealer (model AS-One) at University of Nottingham. Annealing was carried out in an environment of oxygen or nitrogen were injected into annealing chamber with flow rate of 50 sccm at atmospheric pressure, Various temperatures of (600, 740, 880, and 1000 °C) and dwell times at 1000 °C (1-16 s) were used, the temperature ramp rate was 20 °C/s. Thermal annealing was carried out as well at temperatures of 300, 500, 600, 700, 840, and 880 °C with dwell time of 1 hour, and the ramp rate average was 25 °C/min.

### 3.4 IGZO-TFT fabrication on silicon

Figure 3.5: shows a cross section of the type of top gate, bottom contacts IGZO-TFT device fabricated on  $\text{SiO}_2/\text{Si}$  substrates [through the collaboration with Cambridge University] as per the following process:

- (i) Chromium (Cr) and gold (Au) are deposited by evaporation to form the source and drain electrode contacts at 5 nm and 75 nm respectively and patterned by photolithography and lift off.
- (ii) The IGZO active layer is deposited by RF magnetron sputtering with no intentional heating of the substrate, from an IGZO ceramic source target with  $\text{In}_2\text{O}_3:\text{Ga}_2\text{O}_3:\text{ZnO}$  stoichiometry ratio of (1:1:1) (99.9% purity) at RF power of 50W with target diameter 76.2 mm (i.e. power energy density of  $1.1 \text{ W/cm}^2$ ), oxygen concentration 2%  $\text{O}_2$  in Ar, at 2 mTorr working pressure, and thickness 30 nm, or 50 nm .
- (iii) The devices were divided into two sets, one set was laser annealed before IGZO patterning, while the second set was laser annealed after IGZO patterning (in both cases, the samples were laser annealed as described in Section 3.3. prior to the gate dielectric deposition. Comparison devices were fabricated where the wafers underwent thermal anneal at low temperature (150 °C in air for 1 hour) As opposed to laser treatment.
- (iv) The IGZO layer was patterned by photolithography and wet etching as illustrated in Figure 3.5, with channel width (W) and length (L) at 1000  $\mu\text{m}$  and 5  $\mu\text{m}$  respectively.
- (v) Alumina ( $\text{Al}_2\text{O}_3$ ) was deposited as the gate dielectric by atomic layer deposition (ALD) at 120 °C, and patterned by photolithography and lift off.
- (vi) Finally, a bilayer gate electrode (Cr/Au, 5/75 nm) was deposited by evaporation. A cleaning procedure was conducted before each deposition, as follows:
- Sample placed inside spinner
  - Covered with acetone
  - Left for 10 seconds
  - Flushed with IPA
  - Spin at 100 rpm for 2 min
  - Baked at 120 °C for 3 min by hot plate.

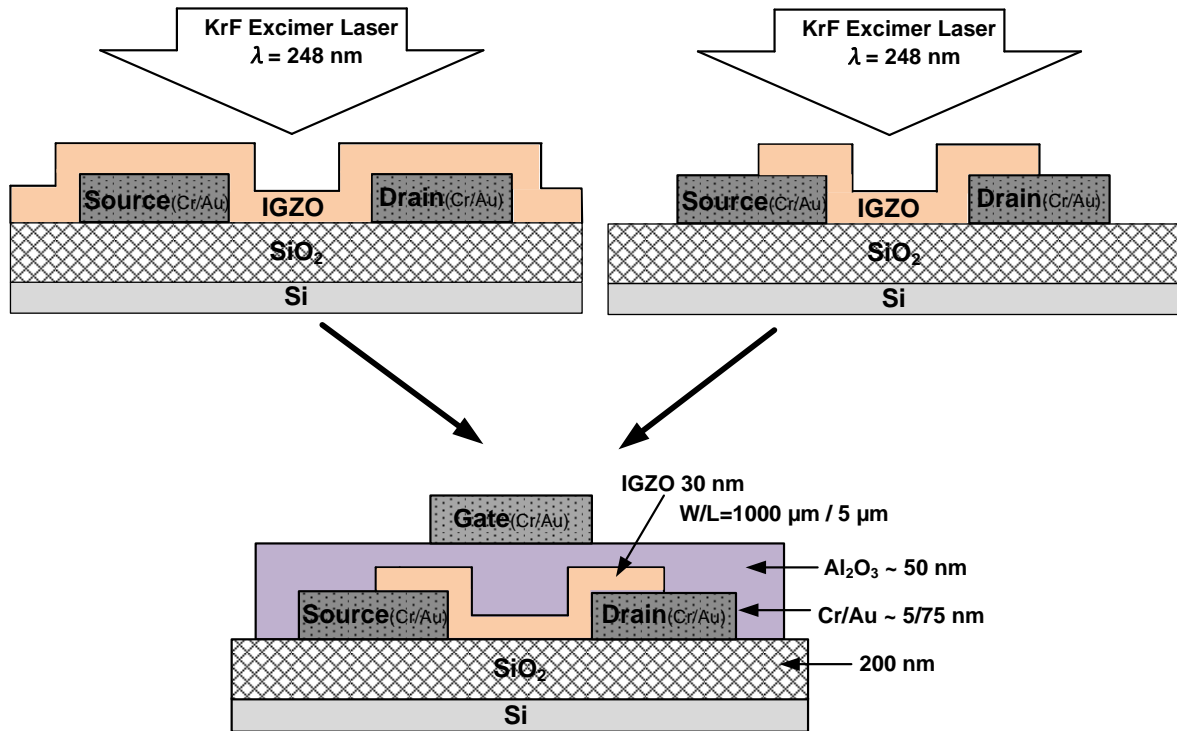
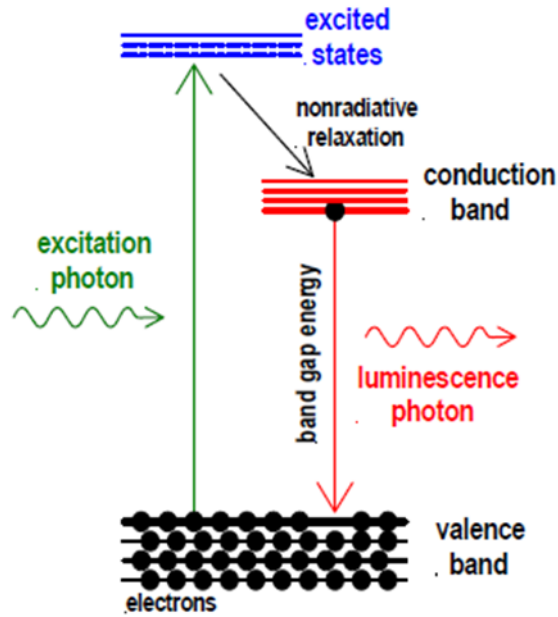


**Figure 3.5:** The cross section of IGZO-TFT showing the concept of patterning pre and post laser anneal for the fabrication of TFTs devices.

### 3.5 Thin film characterisation and analytical techniques

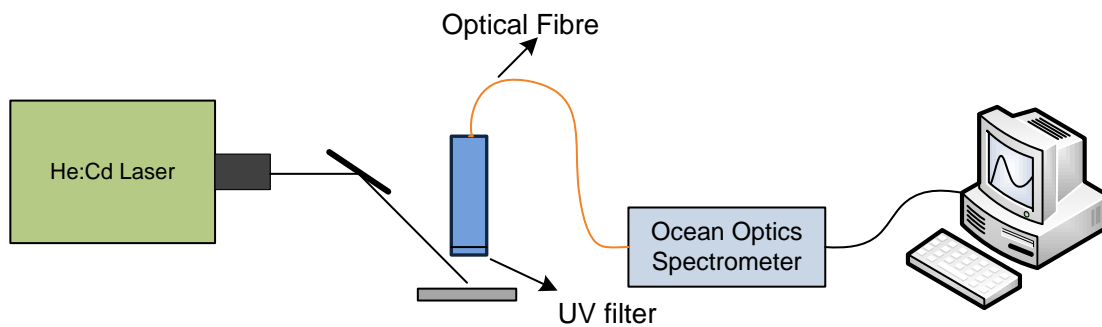
#### 3.5.1 Photoluminescence (PL)

Figure 3.6 describes the mechanism of Photoluminescence. When UV light, with sufficient energy ( $h\nu > E_g$ ) falls on a sample of thin film semiconductor material, the photons will be absorbed, and the excess energy enables the electrons to rise from the top of valence band (VB) up to the conduction band (CB) a process known as "electronic excitation". Then, the electrons will lose part of the gained energy during the jump to cross the band gap ( $E_g$ ) to the lowest energy in the (CB) [99, 100]. Eventually, the electron returns to the valence band (VB) [101], and the resultant photon emission is called Photoluminescence (PL). This emission of light (PL) from a luminescent material originates from a combination of two phenomena: fluorescence and phosphorescence.



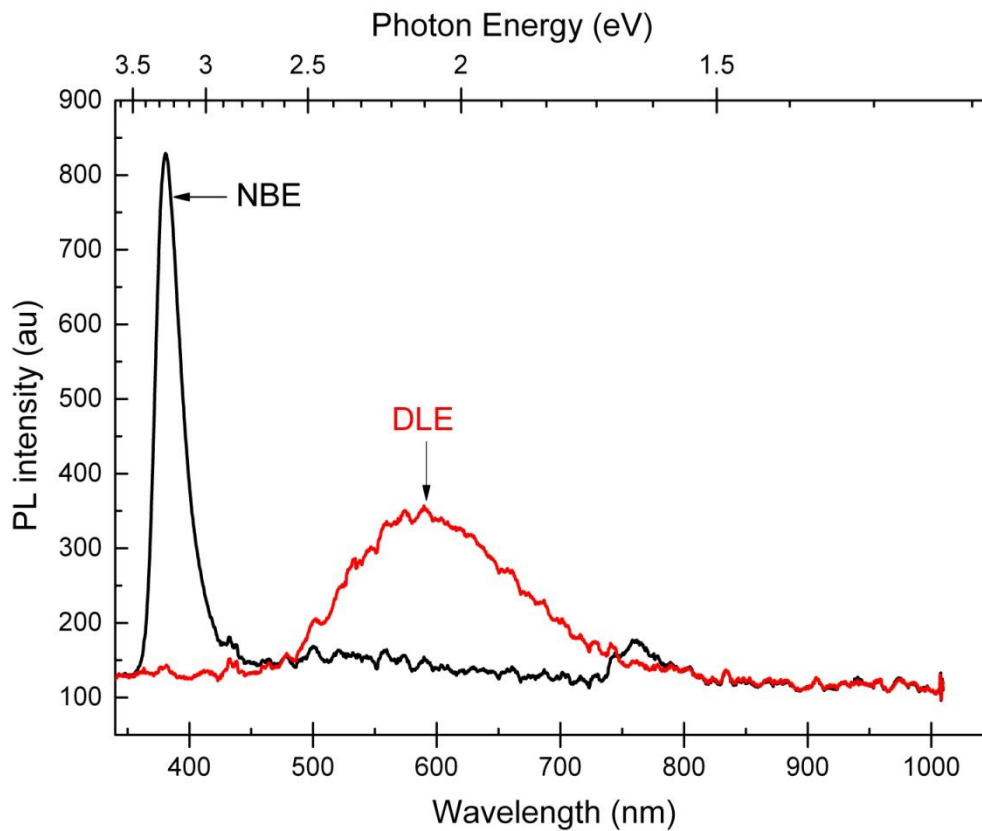
**Figure 3.6:** Principle of photoluminescence transitions [100].

For this work, photoluminescent measurements were performed in a dark room (to improve signal to noise ratio) at room temperature and were enlisted in order to identify the quality of the ZnO films, since point defects can be detected from certain types of PL emission. A He:Cd UV continuous wave laser (with wavelength 325 nm) was used as the excitation source. Figure 3.7 shows a simple schematic of the PL setup.



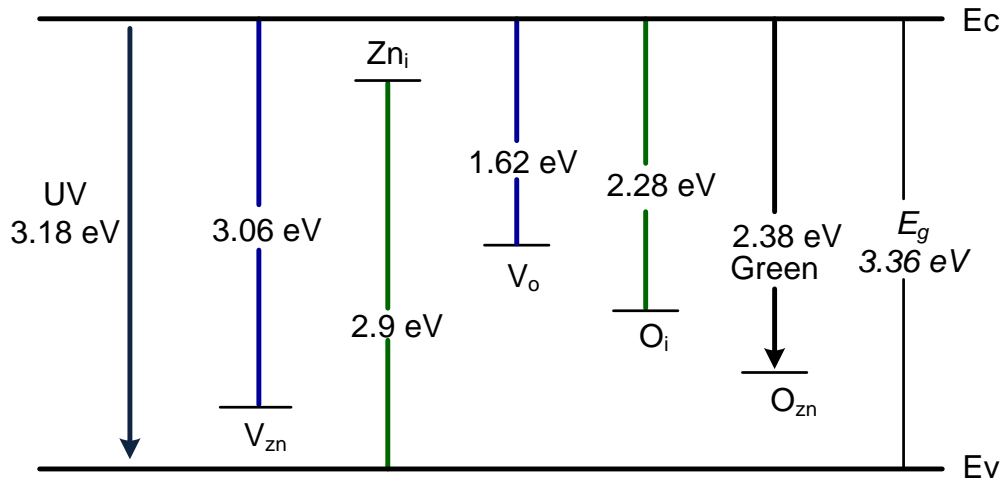
**Figure 3.7:** Schematic diagram of PL setup.

Figure 3.8 shows typical PL emissions from ZnO films, illustrating the two extremes of PL exhibited. Ideally, a good quality ZnO thin film will have a high intensity UV emission, which is due to Near Band Edge emission (NBE), i.e. emits photons of energy close to the band gap, and is an indicator of a good crystalline structure, free of defects. The second case, illustrated in Figure 3.8 shows a broad band visible emission, which is due to photons of lower energy than the band gap that are associated with defects. This is known as Deep Level Emission (DLE), and ideally would be suppressed.



**Figure 3.8:** PL spectra of ZnO showing peaks of NBE and DLE emissions.

Figure 3.9 illustrates the supra band gap excitation of NBE and DLE PL emission, calculated the energy levels of intrinsic point defects in ZnO films such as, zinc vacancy ( $V_{zn}$ ), oxygen vacancy ( $V_o$ ), zinc interstitial ( $Zn_i$ ), oxygen interstitial ( $O_i$ ), and antisite ( $O_{zn}$ ) [102].



**Figure 3.9:** The supra band gap transitions of ZnO calculated defects levels, adapted from [102].

### 3.5.2 Transmission electron microscopy (TEM)

Transmission electron microscopy (TEM) is an excellent tool for thin film microstructure characterisation [103]. The main concept of transmission electron microscopy is the use of a beam of electrons to generate images by transmission (and scattering) through a thin section of the sample – analogous to transmission optical microscopy. Electrons are emitted from an electron gun (highly energetic electron gun) by thermionic emission to form an electron beam that will interact with the sample.

The electron beam is focused on the specimen by a condenser lens system which permits variation of the illumination aperture and the area of the specimen illuminated [104]. After the electrons pass through the sample they are focused by an objective lens into a magnified image [105]. Finally, the image can be further magnified by a projector lens on a fluorescent screen, and the image is recorded by a CCD camera [104] as shown in Figure 3.10. Three types of images can be identified by TEM system: bright field image to determine the film thickness created with transmitted electrons, dark field image to identify the nature of grain size of the film formed by the diffracted beam, and high resolution image [106].

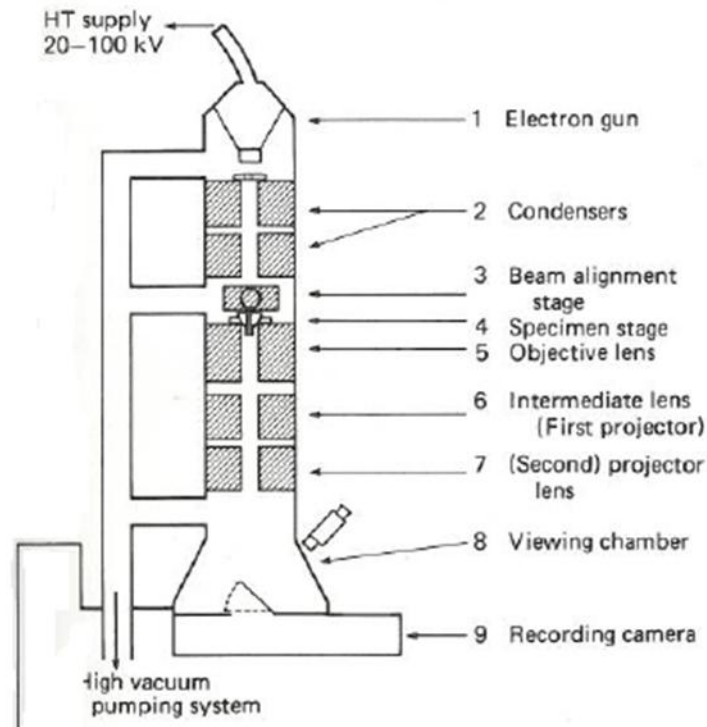


**Figure 3.10:** Schematic diagram of TEM [105].

ZnO films were sent for TEM analysis to Glebe Scientific, Ireland, where cross-sectional view micrographs were obtained to evaluate grain size and microstructure of the ZnO samples, before and after the post deposition treatment investigated in this work.

### 3.5.3 X- ray diffraction (XRD)

X-ray diffraction is a very sensitive structural analysis tool, for examining the nature of crystal structure and its orientation. X-rays are high-energy electromagnetic radiation waves with wavelengths in the range of 0.01-100 Å [107], corresponding to photons with energies ranging from about 200 eV to 1 MeV [108]. When a monochromatic X-ray beam hits a sample, in addition to absorption, it generates scattered X-rays with the same wavelength as the incident beam [107]. The scattered X-rays from a sample are not evenly distributed in space, but are a function of the electron distribution in the sample. Figure 3.11 shows the schematic diagram of a X-ray diffractometer.

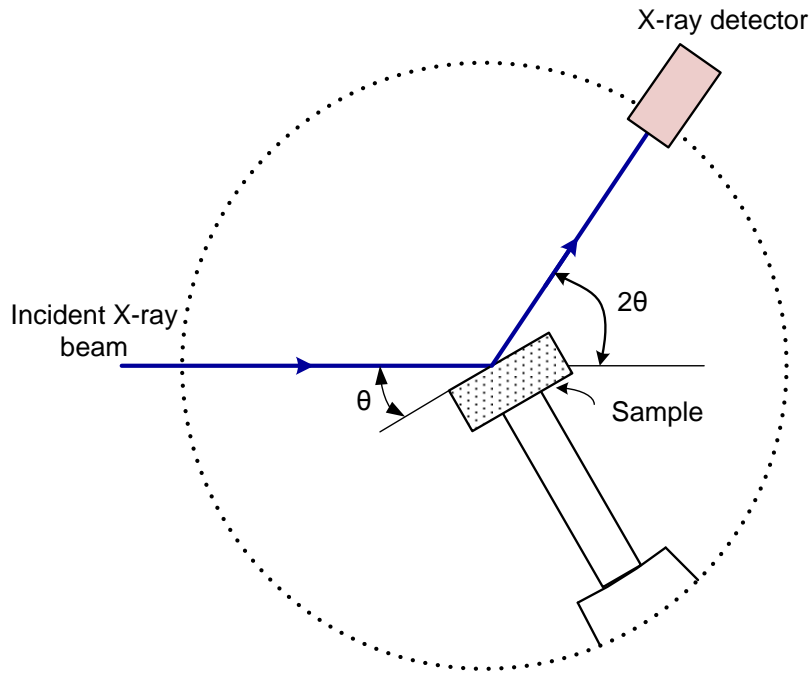


**Figure 3.11:** Schematic diagram of X-ray diffraction adapted from [109].

The principle of x-ray diffraction is based on Bragg diffraction, the theory being developed in 1913, which describes a powerful relationship between the wavelength of the radiation, the inter planar spacing in the specimen ( $d$ ), and the angle of diffraction beam [110].

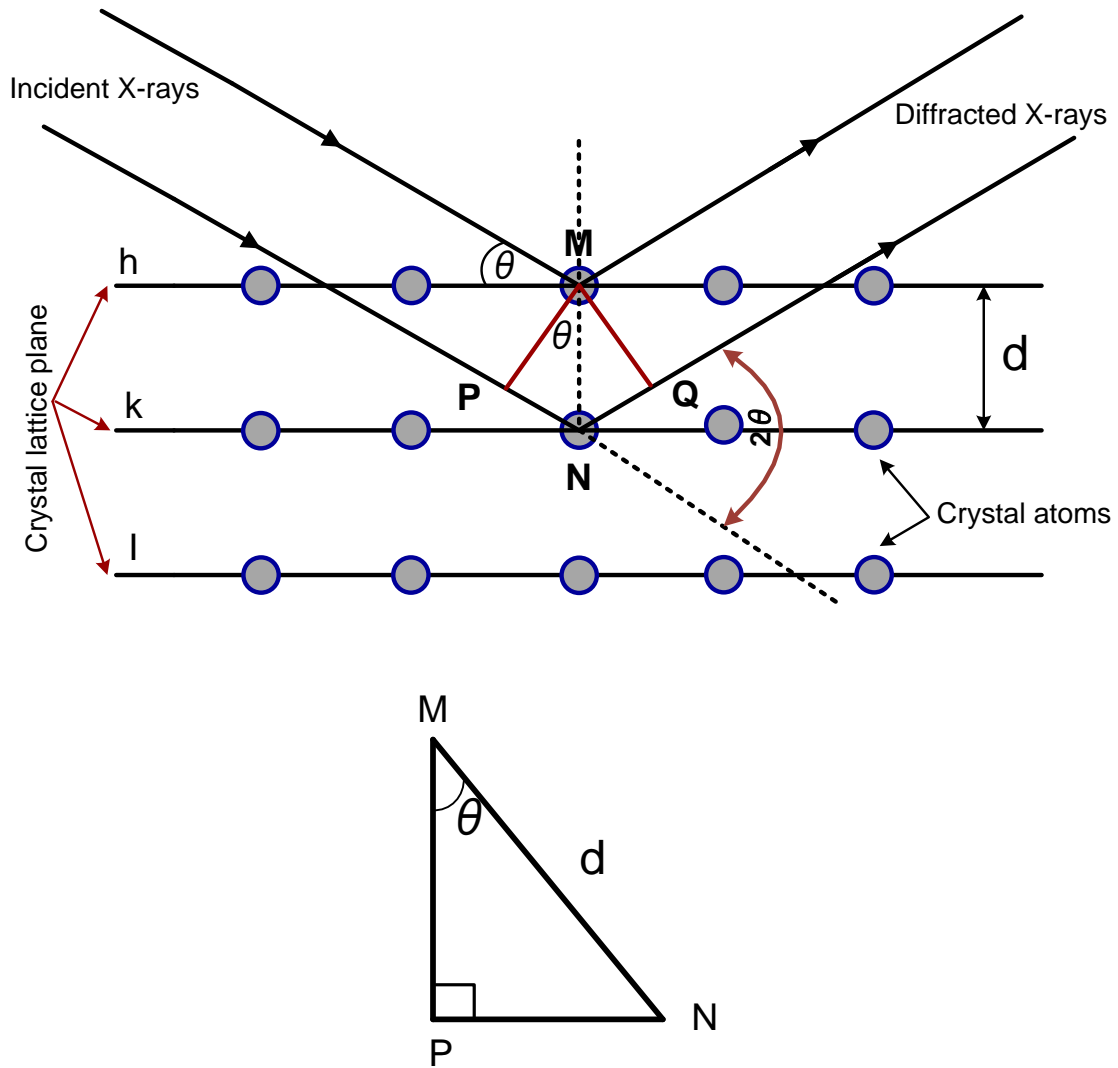


**Figure 3.12:** Illustration of the diffraction of X-ray in crystal (adapted from [109]).

Figure 3.12 illustrates a section of crystal, its atoms arranged on a set of parallel planes separated by a distance  $d$ , the incident X-ray beam with wavelength ( $\lambda$ ) on crystal at angle  $\theta$ , called Bragg angle [109]. Constructive interference occurs only between the scattering waves when the distance  $PN + NQ$  is equal to an integer No. of wavelengths;

$$PN + NQ = m\lambda \tag{3.1}$$

$$m\lambda = d \sin \theta \tag{3.2}$$

Since  $PN=NQ$  ,  $2NP=m\lambda$

$$NP = d \sin \theta \quad (3.3)$$

$$2NP = 2d \sin \theta \quad (3.4)$$

$$m\lambda = 2d \sin \theta \quad (3.5)$$

where:  $\lambda$ : is the wavelength of the incident x-ray beam

$\theta$ : Bragg's angle

$d$ : the distance between adjacent crystallographic planes in specimen.

$m$ : is an integer.

The Scherrer formula was used in this work to estimate crystal domain size of the materials:

$$D = \frac{K\lambda}{B \cos \theta} \quad (3.6)$$

where,  $D$ : Crystallite size of materials

$K$ : constant

$\lambda$ : X-ray wavelength

$B$ : full width at half maximum (FWHM) of the peak being investigated

$\theta$ : Bragg diffraction angle

For this work, X-ray diffraction measurements were performed for ZnO, and IGZO films on silicon substrates using a Phillips PANalytical X-Pert PRO system operated in Bragg-Brentano configuration with a monochromated Cu-K $\alpha$  radiation source ( $\lambda = 1.54056 \text{ \AA}$ ) -to identify the crystalline changes induced by excimer laser annealing (ELA), and thermal annealing. A bracket flat stage was used to hold the films, and the scanning parameters were controlled via X-Pert Data Collector software.

### 3.5.4 X-ray photoelectron spectroscopy (XPS)

X-ray photoelectron spectroscopy (XPS) is known as Electron Spectroscopy for Chemical Analysis (ESCA). XPS is a surface analytical techniques in which identifying the elemental and chemical species information arising from the top surface of the sample. XPS is a photoelectron effect was observed in 1887 by Hertz [106]. The basic principle of XPS is when a monochromatic X-ray emitted from X-ray source and directed to the sample placed in high vacuum environment to achieve the analysis without interference from gas phase collisions, as the photons hit the sample cause direct transfer of energy from photon to core-level electron and photoelectrons are ejected from irradiated atoms [111]. The energy of ejected electron measured by a spectrometer, in which related to the binding energy of atom from which electron is ejected. The basic of this process can be stated as

$$BE = h\nu - KE - \phi \quad (3.7)$$

where, BE is the binding energy of the electron in the atom,  $h\nu$  is the photon energy of X-ray source, KE is the kinetic energy of the emitted electron, and  $\phi$  is the spectrometer work function.

For this research work XPS measurements were carried out at University of Nottingham, to investigate the stoichiometry of as-deposited and thermally annealed HiTUS ZnO films deposited at various oxygen flow rates.

### 3.5.5 Four point probe (4PP) measurements

A four point probe measurements system was used in order to determine the sheet resistance (and resistivity) of the thin film [112]. The main concept of the in-line four point probe is having four equally spaced probes placed on the semiconductor film (sample under test) and applying a current through the outer two probes in order to measure a potential drop (voltage) between the two inner probes as shown in Figure 3.13. In a four point probe measurement, the impact of resistance in the voltage

measuring probes is negligible because the use of a high input impedance voltmeter leads to low current flow through voltage line [106].

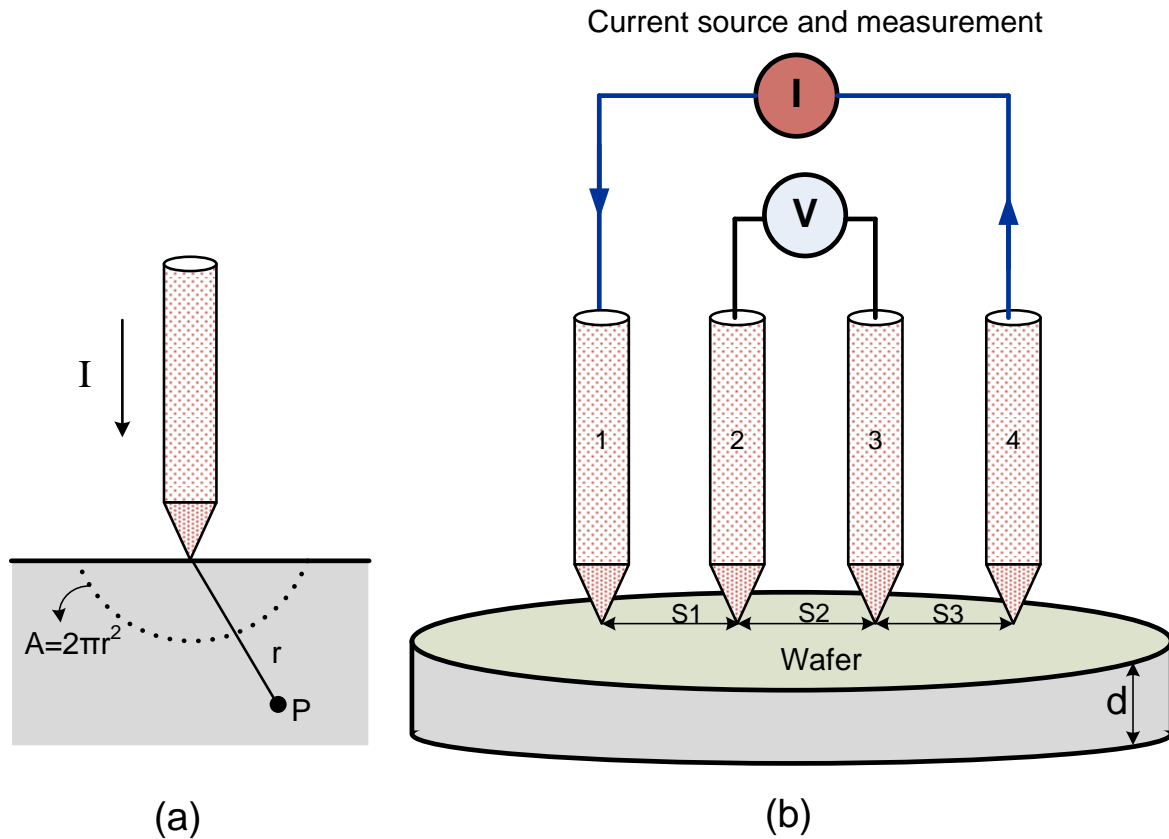


**Figure 3.13:** Schematic diagram of (a) one-point probe, (b) four point probe system.

Figure 3.13(a) start to derive the voltage at single probe. The electric field  $\mathcal{E}$  is related to the current density  $J$ , voltage  $V$ , and the resistivity  $\rho$ .

$$\mathcal{E} = J\rho = -\frac{dV}{dr} \quad (3.8)$$

$$J = \frac{I}{A} = \frac{I}{2\pi r^2} \quad (3.9)$$

The voltage at point P with distance  $r$  from the probe given as:

$$-\frac{dV}{dr} = \frac{\rho I}{2\pi r^2} \quad (3.10)$$

Multiply both sides by  $dr$

$$-dV = \frac{\rho I}{2\pi r^2} dr \quad (3.11)$$

By taking the integration for both sides

$$\int_0^V = -\frac{\rho I}{2\pi} \int_0^r \frac{dr}{r^2} \quad (3.12)$$

$$V = -\frac{\rho I}{2\pi} \int_0^r r^{-2} dr \quad (3.13)$$

$$V = -\frac{\rho I}{2\pi} \left[ \frac{1}{r} - 0 \right] = \frac{I\rho}{2\pi r} \quad (3.14)$$

As depicted in Figure 3.13(b), four point probe placed on a semi-infinite film the cross voltage measured between two inner probes "probes 2 and 3", so the voltage at probe 2 ( $V_2$ ) and probe 3 ( $V_3$ ) with  $S_1$ ,  $S_2$ , and  $S_3$  the distance between the probes given as:

$$V_2 = \frac{I\rho}{2\pi} \left( \frac{1}{S_1} - \frac{1}{S_2+S_3} \right) \quad (3.15)$$

$$V_3 = \frac{I\rho}{2\pi} \left( \frac{1}{S_1+S_2} - \frac{1}{S_3} \right) \quad (3.16)$$

The total voltage between probe 2 and 3  $V = V_2 - V_3$  given as:

$$V = \frac{I\rho}{2\pi} \left( \frac{1}{S_1} - \frac{1}{S_2+S_3} - \frac{1}{S_1+S_2} + \frac{1}{S_3} \right) \quad (3.17)$$

Then the resistivity  $\rho$  is given by

$$\rho = \frac{2\pi}{\left( \frac{1}{S_1} - \frac{1}{S_1+S_2} - \frac{1}{S_2+S_3} + \frac{1}{S_3} \right)} * \frac{V}{I} \quad (3.18)$$

When the probe spacing  $S_1=S_2=S_3=S$

$$\rho = \frac{V}{I} \frac{2\pi}{1/S} = \frac{V}{I} (2\pi S) \quad (3.19)$$

For infinite thin film equation (3.19) becomes

$$\rho = \frac{V}{I} \frac{\pi t}{\ln 2} \quad (3.20)$$

Sheet resistance  $R_{sh} = \rho/t$ , where  $t$ : is the film thickness

$$R_{sh} = \frac{\rho}{t} = 4.532 \frac{V}{It} \quad (\text{Ohm/sq}) \quad (3.21)$$

### 3.5.6 Hall Effect measurements

A Hall Effect system is the most common tool used to determine the behaviour of carrier transport in semiconductor thin films and is based on the effect discovered in 1879 by Hall [113]. As depicted in Figure 3.14, when a magnetic field ( $B$ ) is applied perpendicular to a rectangular (specimen) conductor carrying current ( $I$ ), an electric field ( $E$ ) is induced perpendicular to both current ( $I$ ), and magnetic field. In the case of an n-type semiconductor, electrons will be deflected towards the front surface of the sample making it negatively charged with respect to the back surface. In the steady state the magnetic and electrostatic force will balance, and the voltmeter will measure a 'Hall voltage' indicating the negative sign of the electrons [106, 114].

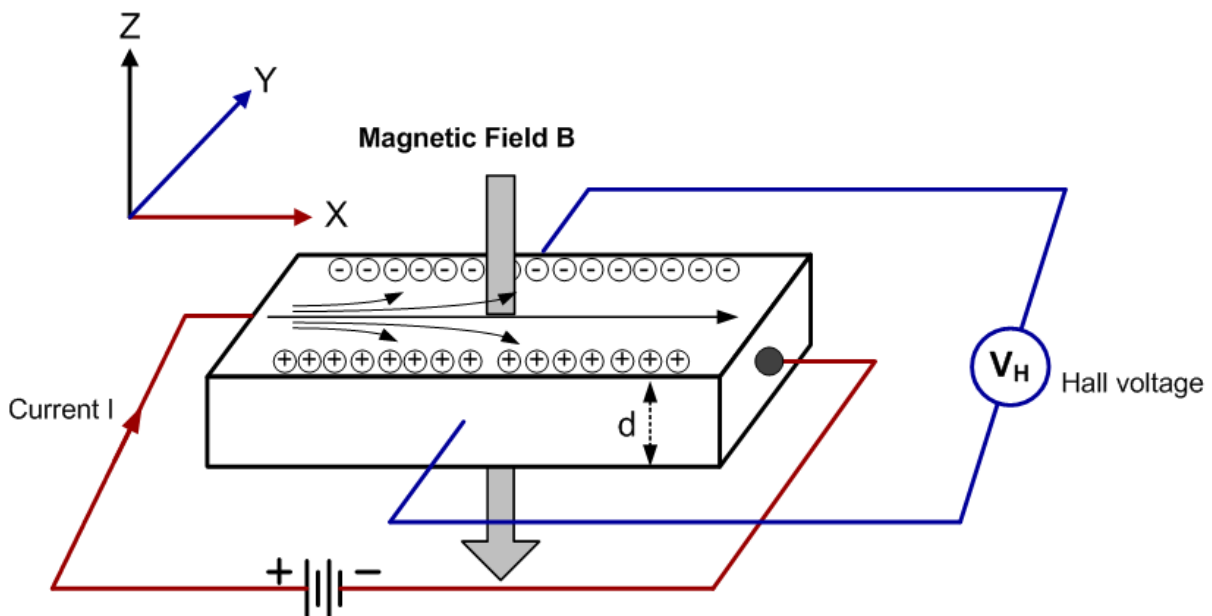


**Figure 3.14:** Schematic diagram of the Hall Effect concept.

Figure 3.15 illustrates experimental diagram setup, with a square sample placed in a Van de Pauw configuration, the current passes through two opposing electrodes while magnetic field is applied perpendicular to the sample surface. Assuming the carriers

only flow along the x-direction, the electric field ( $E_y$ ) will balance the resultant electrostatic forces.

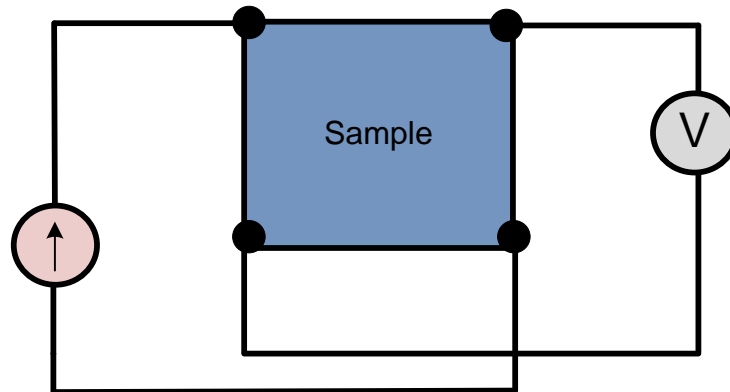


**Figure 3.15:** Layout of experimental setup diagram.

In this work room temperature Hall Effect were measured by Van de Pauw system at PragmaIC Printing Ltd at Cambridge University.

### 3.6 Conclusion

In summary, this chapter has provided a general description of the experimental equipment and techniques employed in this project. This includes: ZnO, and IGZO thin film deposition (by HiTUS, and RF-magnetron sputtering); post deposition laser processing by excimer laser; and thin film microstructure characterisation techniques such as photoluminescence (PL), X-ray diffraction (XRD), transmission electron microscopy (TEM), and X-ray photoelectron spectroscopy (XPS). The electrical properties of films were examined by Hall Effect, and by four point probe.

## Chapter 4

### ZnO Thin Films by HiTUS

---

#### 4.1 Introduction

This chapter presents the results from a microstructure characterisation of the ZnO thin films deposited at room temperature by the HiTUS method followed by post deposition annealing studies which were undertaken by the author using thermal annealing (TA), rapid thermal annealing (RTA), and laser annealing (LA). Five 60 nm thick HiTUS ZnO samples deposited on Si at various oxygen flow rates: 41, 38, 35, 32 and 28 sccm. Section 4.2 presents room temperature photoluminescence characterisation results for the thermally annealed, rapid thermal anneal, excimer laser annealed films respectively. Section 4.3 presents the corresponding cross sectional of TEM images of the films, and section 4.4 presents XRD structure patterns of the films following the three annealing methods investigated. Finally, section 4.5 summaries the finding related to HiTUS grown ZnO.

#### 4.2 Photoluminescence characterisation

Photoluminescence (PL) spectrometry is a powerful tool for characterizing the optical quality of semiconductor materials such as the metal oxide thin films investigated here. The PL intensity is related directly to the defect densities in materials [115], and so is a useful indicator of film quality. Specifically for the films studied here, it is well known that the PL characteristics of ZnO are generally influenced by the deposition method and preparation conditions [116], and are representative of film quality [67]. This work is focused on two different deposition techniques: HiTUS and RF magnetron sputtering, hence comparison of the resultant film quality via these two techniques is of interest. In particular, the PL properties of ZnO films in the UV and visible part of the spectrum are known to be closely related to microstructure [117, 118]. In undoped ZnO (intrinsic)

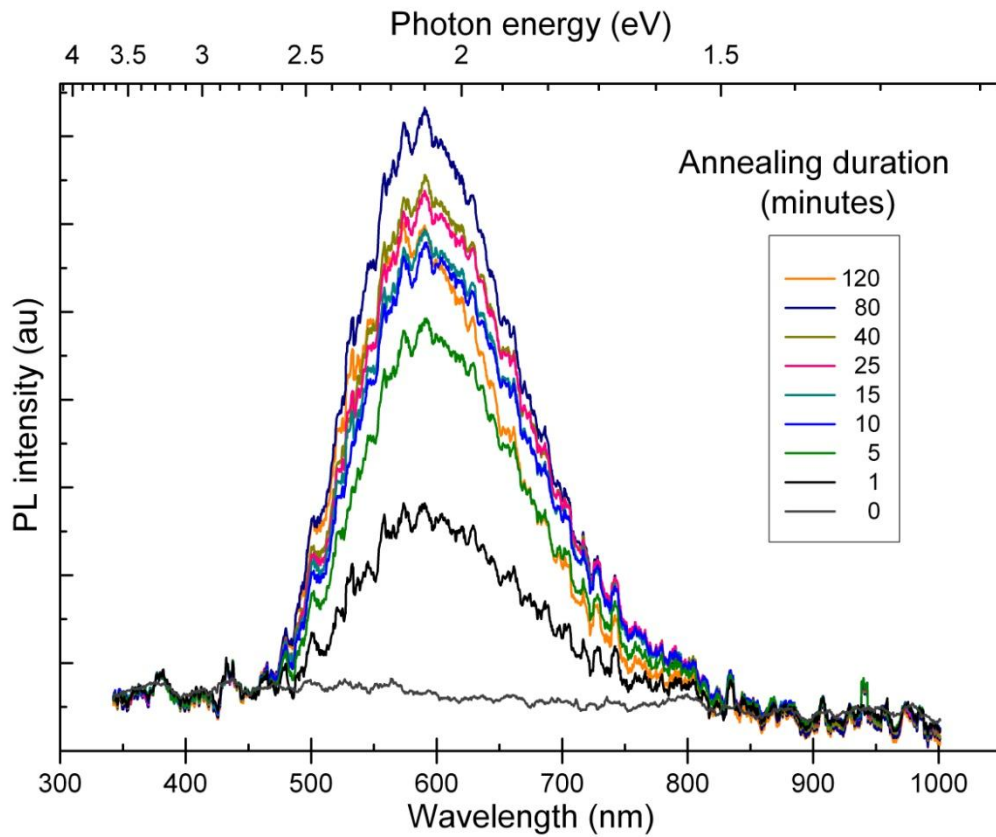
films the UV "Near Band emission"(NBE) at around 380nm (3.2 eV) is attributed to excitonic recombination, and the broad visible peak known as "Deep Level Emission"(DLE) which ranges from 450 nm to 750 nm (2.7 eV to 1.65 eV) is correlated directly with the intrinsic defects and defect complexes in the materials [84, 115, 119]. It has been reported that an improvement of NBE intensity is clearly observed after thermal annealing with increase annealing temperatures [19, 115, 116]. Hence, the intensity ratio of NBE over DLE is usually taken as an indication of the degree of crystallinity improvement [120].

For the work presented in this chapter, the main objective is to investigate the deposition and to perform a comparative study of the effect of post processing techniques on ZnO thin films thermal annealing TA, rapid thermal annealing RTA, and laser annealing LA. Hence a study of the resultant film properties has been undertaken using PL spectrometry, where a particular interest is directed at how the NBE and DLE are affected.

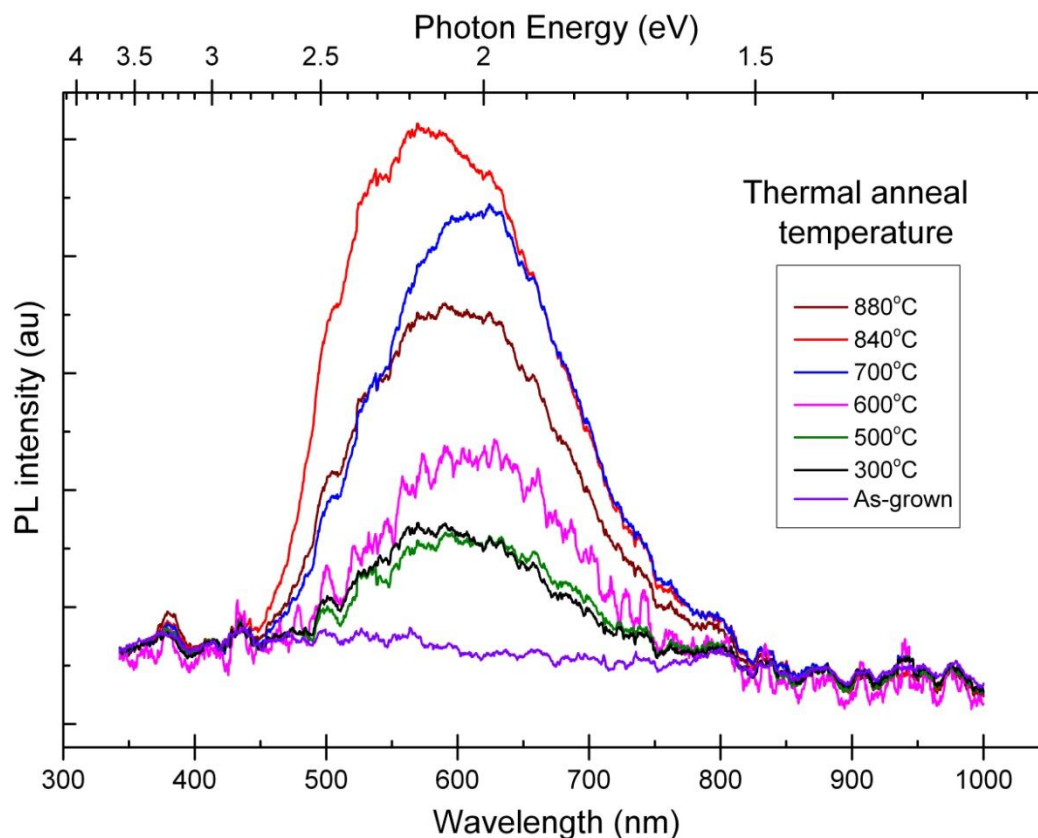
#### **4.2.1 Photoluminescence of thermally annealed HiTUS ZnO films**

Figure 4.1 illustrates the room temperature photoluminescence spectra of the 41 sccm ZnO thin films, following an annealing process in a furnace at temperatures up to 700 °C and at various dwell times up to 2 hours. The PL spectra shows a strong broad visible emission peak, associated with deep level emission (DLE), consisting of orange/red emissions which has been shown to be attributed to radiative transitions from defect sites associated with excess oxygen [121]. As shown in Figure 4.2 the DLE PL increases significantly with increasing temperature up to 840 °C, whereas there is negligible appearance of ultra-violet near band edge emission (NBE), even at high temperatures. In this case, the dwell time is kept constant at 1 hour and the temperature reaches 880 °C. The 840 °C were clearly producing the highest DLE emission, however processing at longer periods results in film ablation, since temperature at 700 °C was investigated by means of dwell time (Figure 4.1). It is

shown that the DLE emission increases as the dwell time increases to 80 minutes, but further annealing results in a DLE reduction.



**Figure 4.1:** PL spectra of thermally annealed ZnO (41 sccm) at 700 °C in air, illustrates the effect of annealing duration at 700 °C.



**Figure 4.2:** PL spectra of thermally annealed ZnO (41 sccm sample) at temperatures up to 880 °C in air, showing the effect of increasing the temperature for 1 hour.

XPS measurements of ZnO samples deposited at various oxygen flow rates illustrated an improvement of film Zn:O stoichiometry as the oxygen flow rates increased as shown in Table 4.1. Also thermally annealed samples (41 sccm) at various temperatures were examined via XPS indicating as the annealing temperature increases led to decrease of Zn:O ratio as shown in Table 4.2. (i.e. the film surface becomes increasingly oxygen rich as the annealing temperature increased above 700 °C).

Oxygen flow rate (sccm)	28	32	35	38	41
Zn:O ratio	1.36±0.13	1.23±0.04	1.20±0.02	1.18±0.06	0.94±0.05

**Table 4.1:** XPS showing Zn:O ratio for films deposited at various oxygen flow rates.

Annealing condition	As-grown	300 °C	500 °C	700 °C	840 °C	880 °C
Zn:O ratio	0.94±0.05	0.99±0.03	0.99±0.05	0.87±0.16	0.84±0.05	0.79±0.07

**Table 4.2:** XPS showing Zn:O ratio for films as a function of annealing temperatures.

To identify the effect of annealing time on the evolution of the PL spectra, annealing for various times was conducted. For annealing at a temperature lower than 700 °C, the PL did not improve significantly beyond an annealing time of 15 min. However, annealing at higher temperature (840 °C) led to a dramatic change in PL spectra. Increasing dwell time caused a shift in the dominant DLE from an orange to a green emission, and further dwell with time increases caused a gradual reduction of green PL most probably due to loss of film materials.

Regarding a progressive loss of film material evidenced at high annealing temperature, thicker samples of ZnO films (200 nm – 41 sccm) were also studied in order to investigate the development of PL emission at the high temperature (840 °C) as a function of annealing times. The samples were introduced to the furnace after the temperature had reached 840 °C and were taken out promptly at the end of each annealing period. Figure 4.3 illustrates the development of PL emission as a function of dwell time. A broad visible orange/red peak (2.10 eV and 1.85 eV) appeared after the first 30 s of annealing, and as the dwell time increased beyond 2 min its intensity started to decrease. At longer annealing times a strong green/yellow emission peak at about 530 nm (2.34 eV) developed from 11 min. Then the orange/red peak is significantly reduced after about 16 min, while the green/yellow emission reaches the highest peak intensity at 22 min. After 43 min the green/yellow emission ultimately is reduced in intensity due to excessive loss of material. It has been reported that the orange/red DLE emission is usually associated with radiative transitions related to excess of oxygen [122] - potentially interstitial ( $O_i$ ), i.e. the increase of orange/red emission with annealing temperature could be attributed to the removal of non-

radiative defects during annealing and enhancing radiative transition related to excess oxygen defects. However, the subsequent decrease of orange/red emission with shift to strong green/yellow DLE with increasing dwell time could be attributed to a change of dominant defects from oxygen interstitial ( $O_i$ ) defects to zinc vacancy ( $V_{zn}$ ) defects, as  $V_{zn}$  are forms at lower energy [123]. Hence, a clear effect of annealing temperature was observed above 700 °C with negligible appearance of NBE.

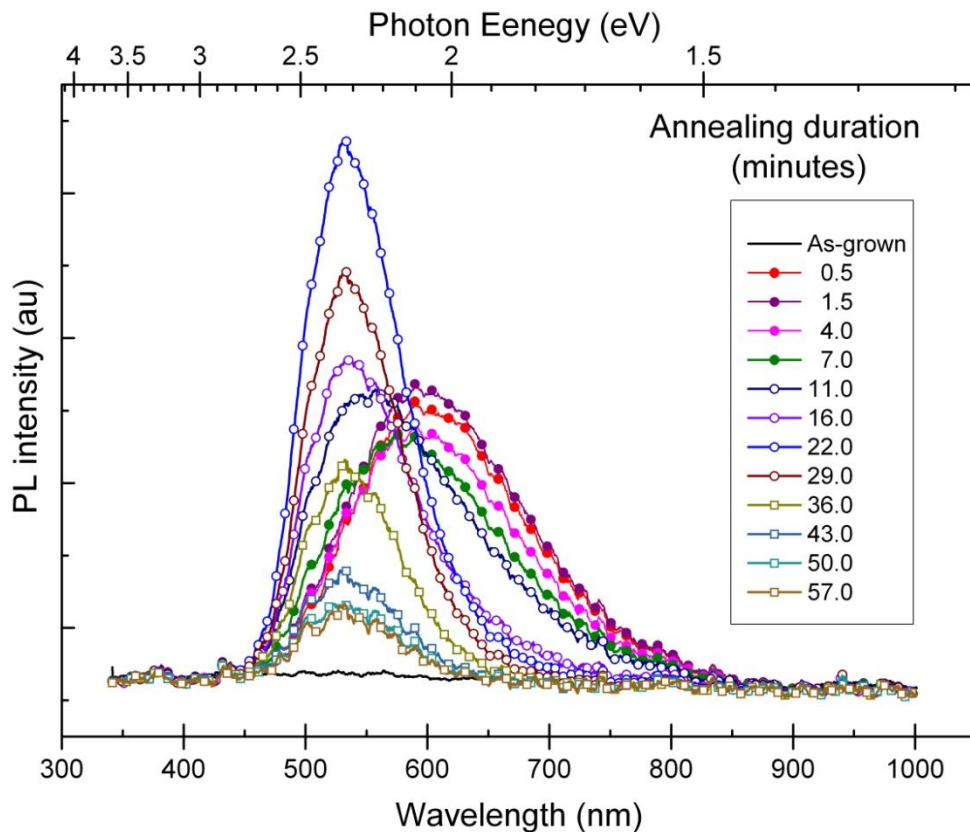


**Figure 4.3:** PL of thermal anneal in air of ZnO 41 sccm at 840 °C and various dwell periods.

#### 4.2.2 Photoluminescence of rapidly thermal annealed ZnO films

Rapid thermal annealing (RTA) has been carried out on ZnO films grown at oxygen flow rates of 38 sccm, using a range of annealing environments: nitrogen, and oxygen, at various temperatures from 600 to 1000 °C. At dwell times of 1 s, the NBE appears at temperatures >800 °C but significant loss of material was observed at final temperatures > 800 °C. Figure 4.4 presents the PL spectra of ZnO films annealed in

nitrogen ambient. There is an evolution of an orange/red peak emission as the temperature is increased. When the temperature was further increased to the highest value of 1000 °C, a transition of the PL to a broad visible emission occurred which is a combination of both green and orange/red emissions. In addition, a weak NBE peak appears at temperatures higher than 800 °C, but with significant loss of material.

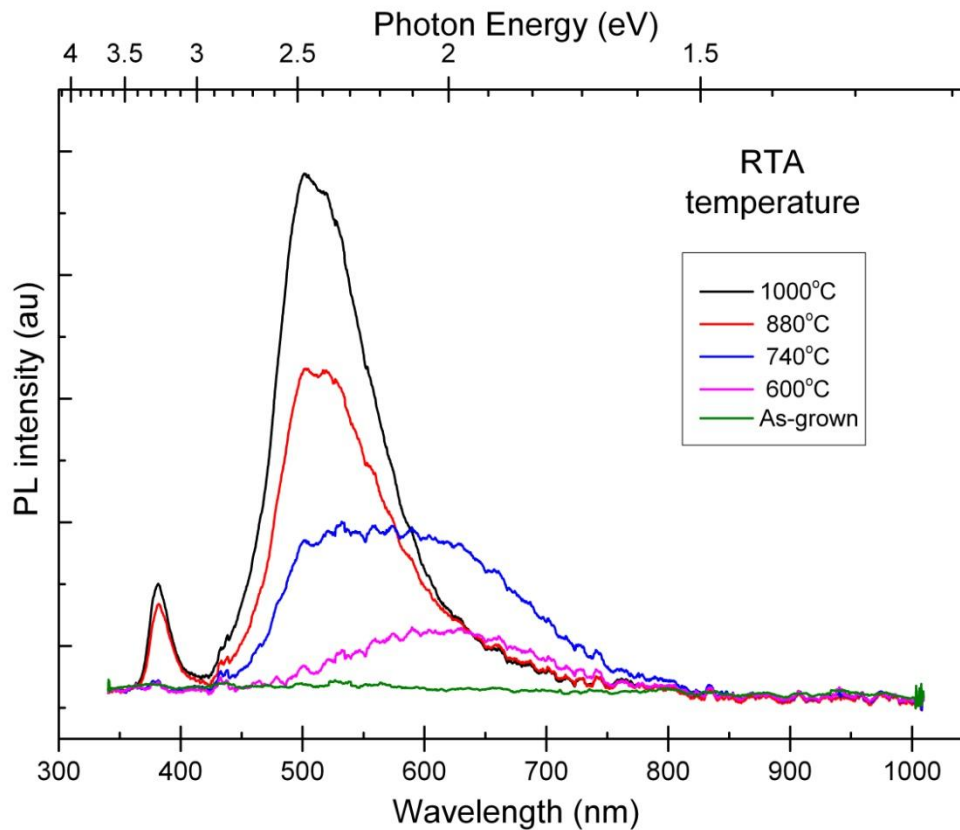


**Figure 4.4:** PL evolution of 38 sccm samples under rapid thermal annealing (RTA) with  $Dt=1$  s at various temperatures in nitrogen.

Annealing at 1000 °C with various dwell times was conducted to investigate the behaviour of the NBE emission as shown in Figure 4.5. When the dwell time increased from 1 s to 6 s the NBE intensity increased significantly, and reached the maximum at 6 s. A further increase of dwell time up to 16 s resulted in reduction of NBE intensity because the film has lost most of its materials. Hence, from the PL characteristics presented, the NBE emission has a clear dependence on the final temperature and

dwell period. However, the NBE emission has a much stronger dependence on final temperature than dwell time.

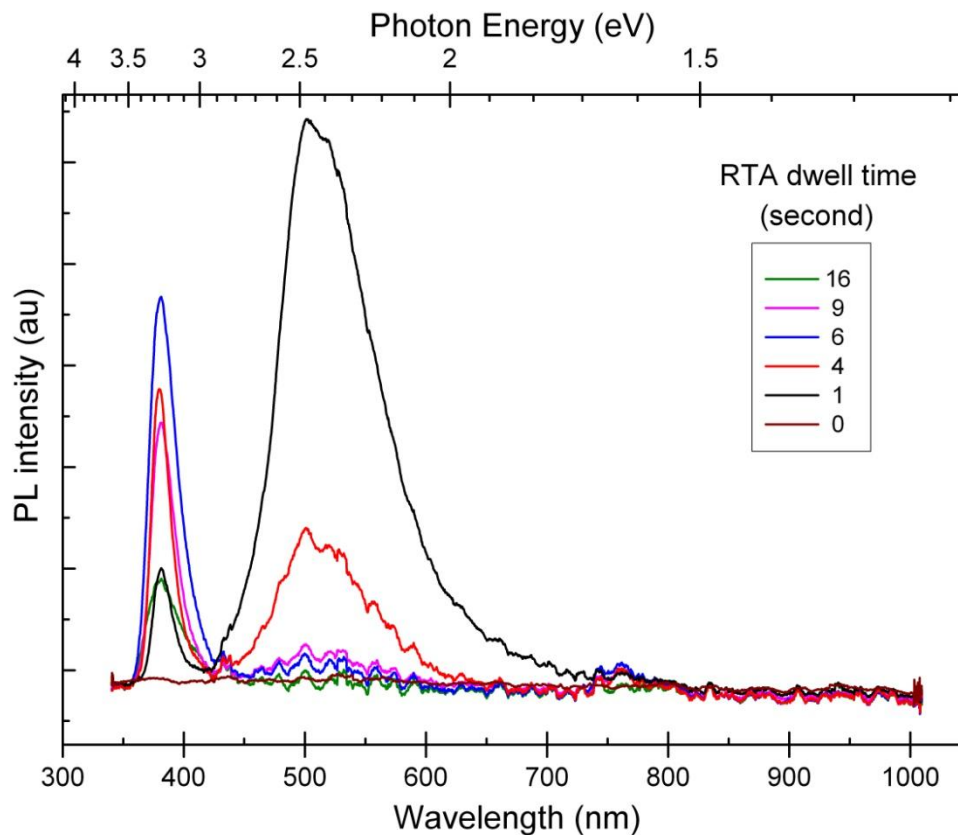


**Figure 4.5:** PL of rapid thermal anneal (RTA) in nitrogen (38 sccm sample), at 1000 °C versus dwell time.

Figure 4.6 shows the PL spectra of ZnO samples from the same wafer (38 sccm) that were annealed using a similar process (RTA) but in oxygen environment. Predominantly there was an evolution of an orange/red peak. The intensity decreased as the annealing temperature increased up to higher than >800 °C because of significant loss of material at RTA temperature of >800 °C. A small increase in NBE was also observed at 1000 °C. The evolution of only the orange/red peak would be consistent with the emission being attributed to defects related to excess oxygen, while the evolution of the green/yellow peak for RTA in nitrogen ambient is most likely to be a result of change in Zn:O ratio of the films and the balance of resultant intrinsic defects.

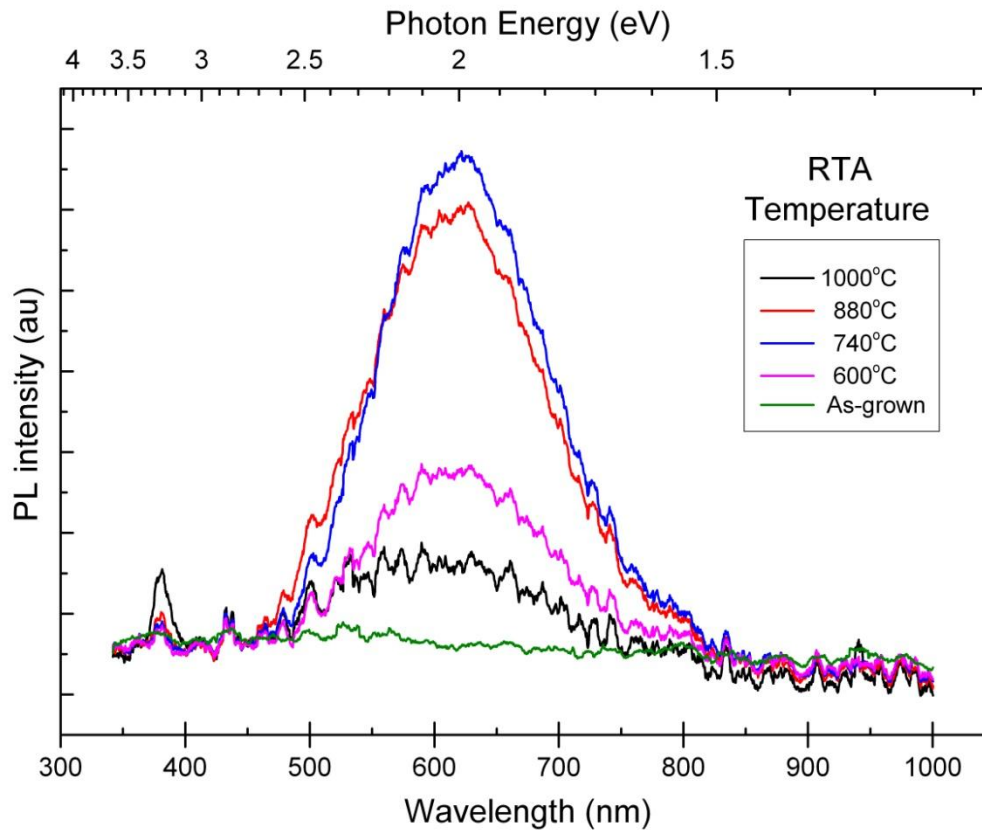


**Figure 4.6:** PL spectra of 38 sccm films under RTA in oxygen at  $Dt=1$  s.

Further investigation has been carried out to study the influence of annealing for samples deposited at various oxygen concentrations (41, 35, and 28 sccm), for this purpose rapid thermal annealing in oxygen and nitrogen ambient at 880 °C for a dwell time of 1 s was performed. PL spectra depicted in Figure 4.7 show that a green/yellow emission is observed for all samples annealed in nitrogen, and also that the intensity has a clear dependence on the initial film stoichiometry: as the oxygen flow rate during deposition decreased, the intensity of green/yellow decreased.

No appearance of green/yellow emission occurring for samples annealed in the oxygen ambient, which could be attributed to an increased oxygen adsorption that occurs at the grain boundaries in polycrystalline ZnO films [124], which could combine with the ZnO matrix as oxygen interstitials and antisites with reduction of oxygen vacancies. In addition, the results show a negligible appearance of the NBE peak for films processed

in oxygen, indicates an increase of defects acting as non-radiative recombination centres.

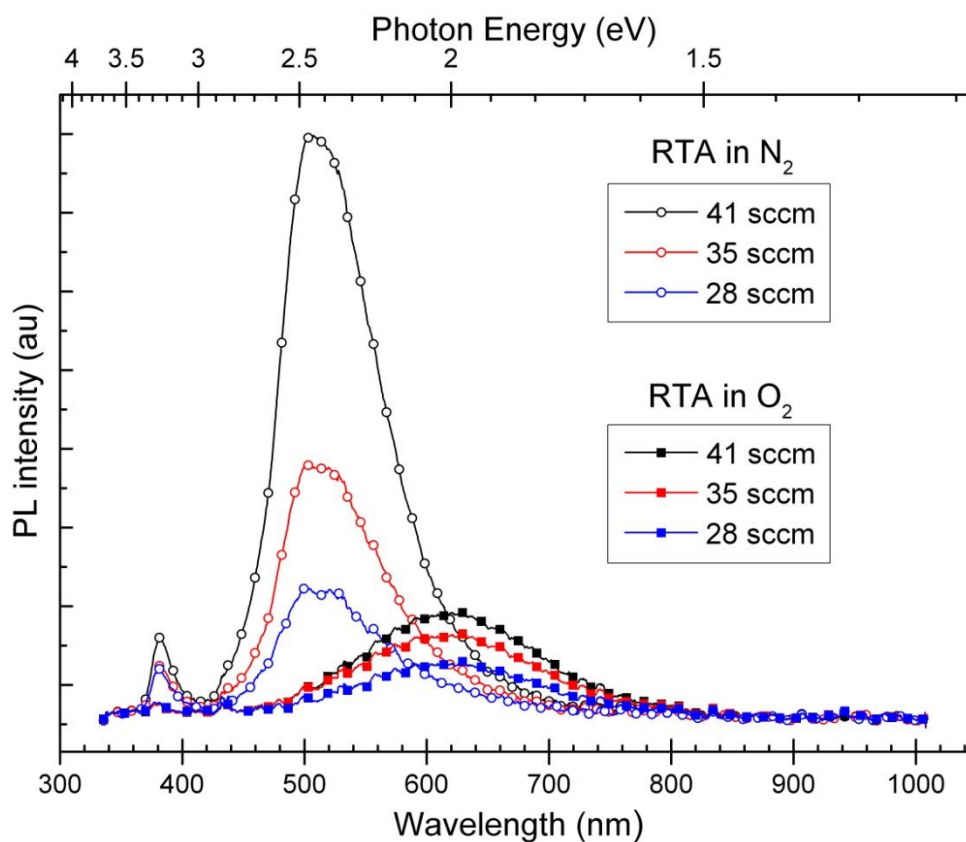


**Figure 4.7:** PL spectra of RTA samples at 880 °C with dwell time 1 s in oxygen and nitrogen ambient, comparing samples deposited at various O<sub>2</sub> flow rates. The PL spectra of all the as-deposited films did not show any significant PL (they have been omitted from the graph for clarity).

### 4.2.3 Photoluminescence of laser annealed HiTUS ZnO films

Figure 4.8 shows the PL spectra of as grown films and laser annealed HiTUS ZnO 41 sccm, 60 nm films, as a function of applied laser irradiation dose at one pulse. As the laser fluence increases to medium values, a broad visible peak (440-800 nm) appears and increases with fluence up to 220 mJ/cm<sup>2</sup>. This peak is related to the deep level emission (DLE). Further increase of laser fluences result in the DLE decreasing and at 244 mJ/cm<sup>2</sup> a sharp UV emission (the Near Band Emission) starts to appear. This indicates that the crystal quality of the film has been improved – since a strong NBE is

only emitted by highly ordered films [115]. At higher fluences the NBE intensity reaches the maximum at 295 mJ/cm<sup>2</sup> and exhibits only a very weak DLE peak. When the laser fluence is further increased, the UV peak is eliminated – probably due to film damage.

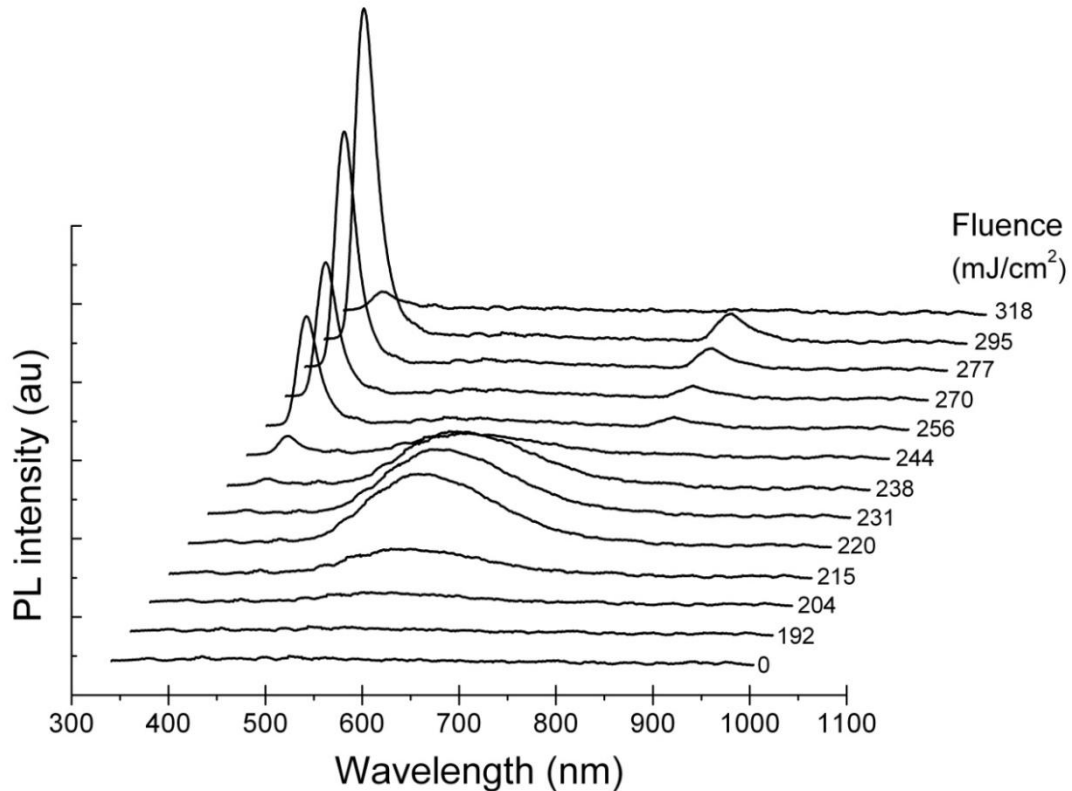


**Figure 4.8:** Photoluminescence spectra from 41 sccm samples annealed at various fluences with a single pulse. (The small peaks at  $\sim 760$  nm are the second harmonic of UV peaks at  $\sim 381$  nm).

The evolution of the two significant emission peaks observed can be classified into five process regimes which are strongly dependent upon laser fluences applied, as illustrated in Figure 4.9. (1) The as-deposited sample shows negligible NBE emission, and very weak DLE. This is most likely related to non-radiative recombination centres, that are expected to exist in the vicinity grain boundaries, with the absorbed energy released as heat instead of light [125]; (2) for samples laser annealed at low fluences (up to 220 mJ/cm<sup>2</sup>) the results show an increase in DLE intensity with a weak evolution of the NBE peak. In this case, the density of non-radiative centres at the grain boundaries can be considered to have been reduced, along with some crystallinity

improvements observed; (3) at fluences in the range of 220-244 mJ/cm<sup>2</sup> the DLE starts decreasing and at 244 mJ/cm<sup>2</sup> the NBE becomes more dominant at  $\lambda=381$  nm, indicating a reduction in point defects; (4) at higher fluences investigated up to 295 mJ/cm<sup>2</sup> the NBE intensity increases sharply and there is only a very weak DLE present, associated with improved ZnO film crystallinity [120]; (5) at a very high energy density of 315 mJ/cm<sup>2</sup> there is a dramatic decrease of the NBE peak is observed, associated with observed material loss from the film surface.

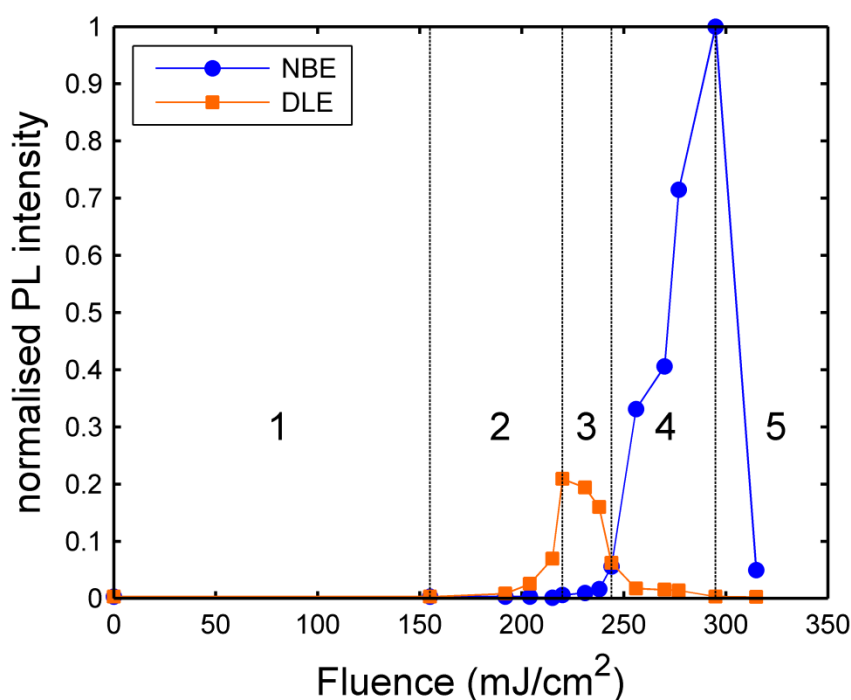


**Figure 4.9:** Normalized PL peak of NBE and DLE intensity various laser energy densities.

Laser annealing of ZnO films grown without intentional substrate heating at various oxygen flow rates (41, 38, 35, 32 and 28 sccm) was conducted to investigate the origin of the two significant PL peaks of DLE and the NBE emissions. Figure 4.10 shows the PL spectra of samples laser annealed at a medium fluence of 220 mJ/cm<sup>2</sup> at single pulse, demonstrating a dramatic drop in the broad visible peak emission occurring consistently with a lower oxygen flow rate. Simultaneously, the near band edge emission appears stronger for lower oxygen flow rates, indicating that the magnitude of DLE is related to

higher initial oxygen concentrations, which can be also confirmed by laser annealing of Zn-rich film (28 sccm) at various fluences with single pulse as shown in Figure 4.11, i.e. no appearance of DLE consistent with lack of excess oxygen related defects, with strong evolution of NBE.

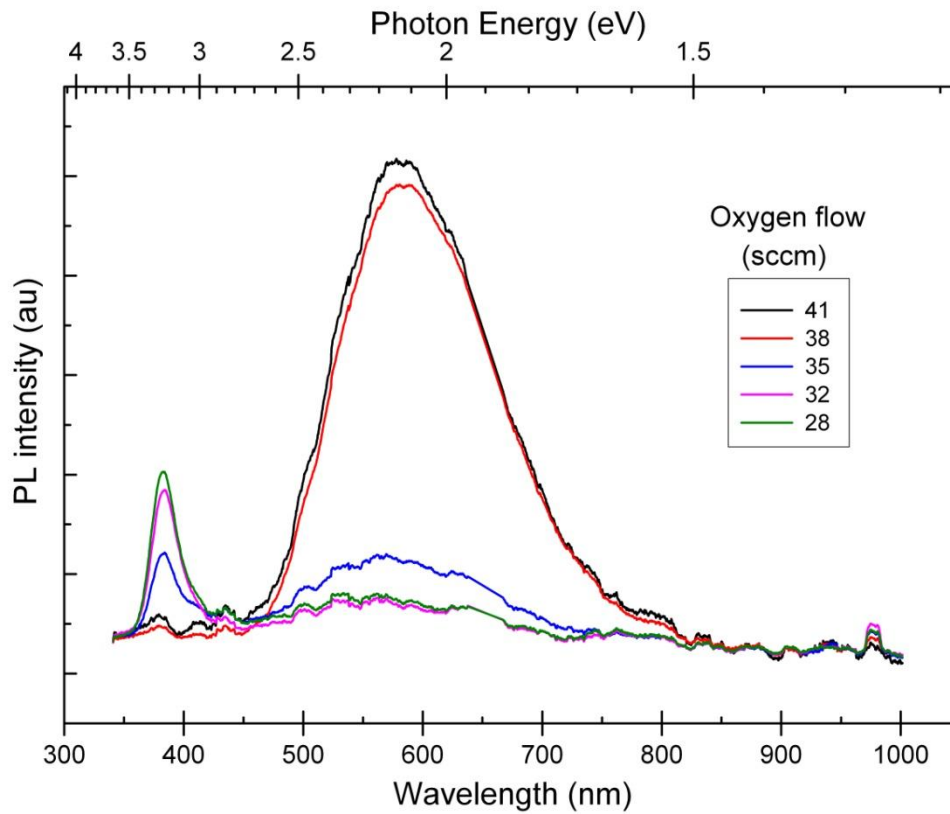


**Figure 4.10:** PL emission of samples deposited at oxygen flow rates of 41, 38, 35, 32, and 28 sccm and laser annealed at  $220 \text{ mJ/cm}^2$  with a single pulse.

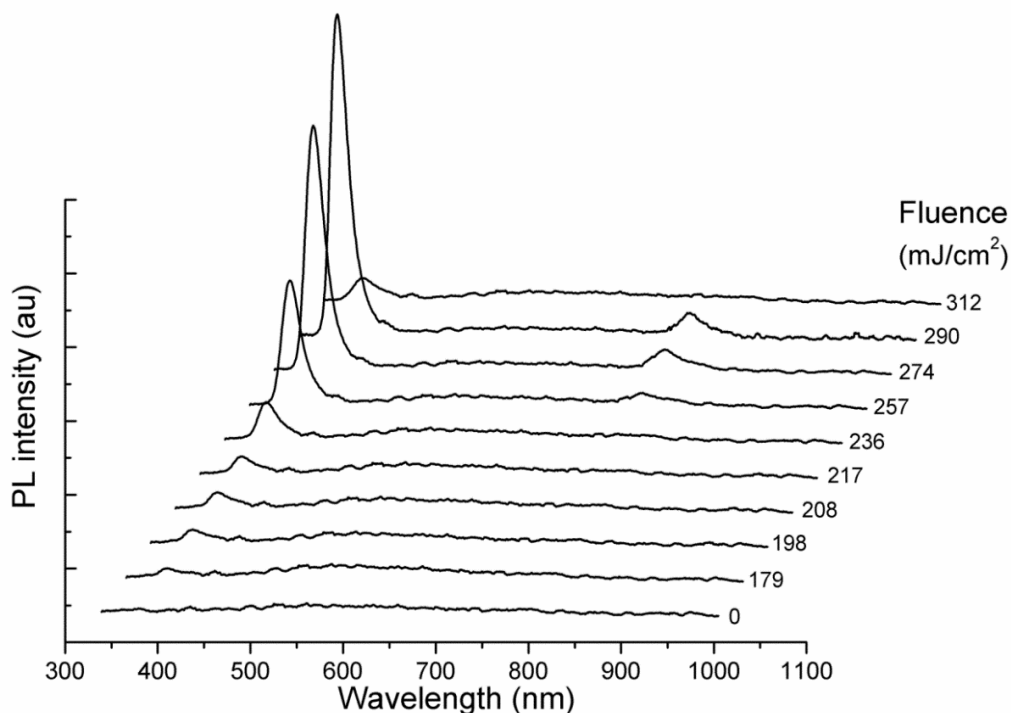


**Figure 4.11:** PL spectra of a Zn-rich sample (28 sccm) showing a clear evolution of NBE and no appearance of DLE.

The developments of PL spectra as a function of multiple laser pulses at various fluences were studied for ZnO grown at 41 sccm of oxygen. (1): at low fluences ( $<170 \text{ mJ/cm}^2$ ) no PL was observed up to 100 pulses, (2): at medium fluences ( $<260 \text{ mJ/cm}^2$ ) an increase of NBE intensity is observed as the number of pulses was increased up to an optimum number of pulses, which is related to the fluence applied. As shown in Figure 4.12, the PL of multiple pulses of laser energy density  $235 \text{ mJ/cm}^2$ , create a clear evolution of NBE as the number of pulses increases up to 37 pulses, demonstrating that laser annealing causes a reduction of defects as a function of total delivered pulses, with additional pulses resulting to a subsequent decrease of NBE intensity. (3): at high fluences, as the number of pulses is increased, the NBE emission decreased. This behaviour was observed as of the second pulse. An example of multiple pulses of high fluence was conducted on energy density of  $295 \text{ mJ/cm}^2$  is shown in Figure 4.13. The intensity of NBE peak observed at high fluence of  $295 \text{ mJ/cm}^2$  with a

single pulse relatively higher than that achieved via medium fluences of  $235 \text{ mJ/cm}^2$  at 37 pulses.

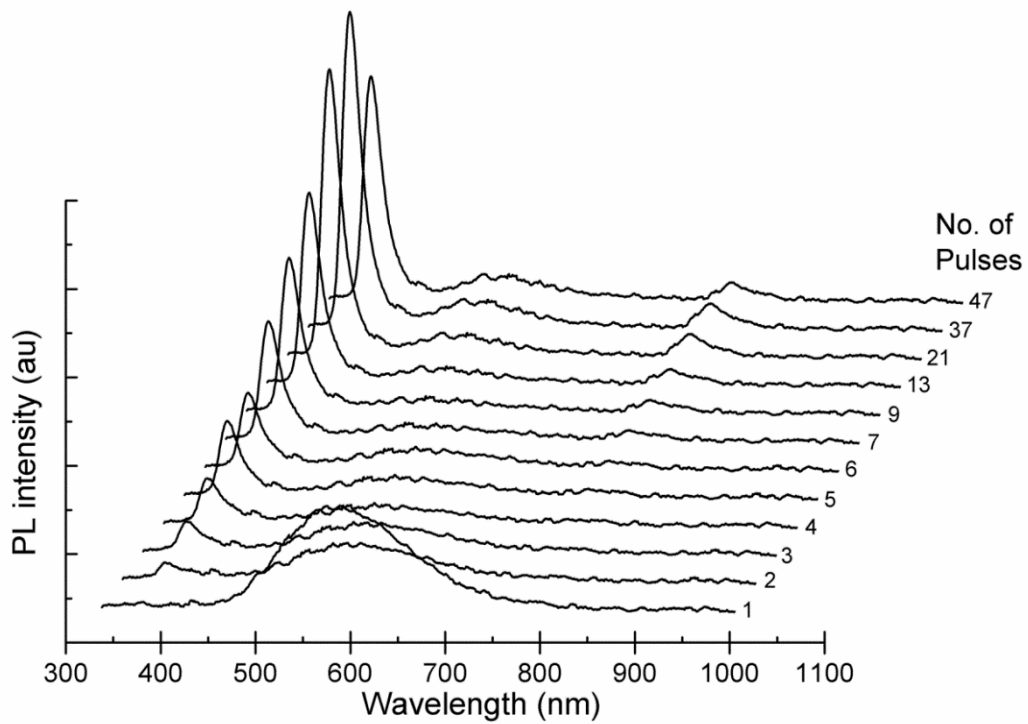


**Figure 4.12:** PL spectra from the 41 sccm sample laser annealed at a medium fluence, ( $235 \text{ mJ/cm}^2$ ) but with multiple pulses.

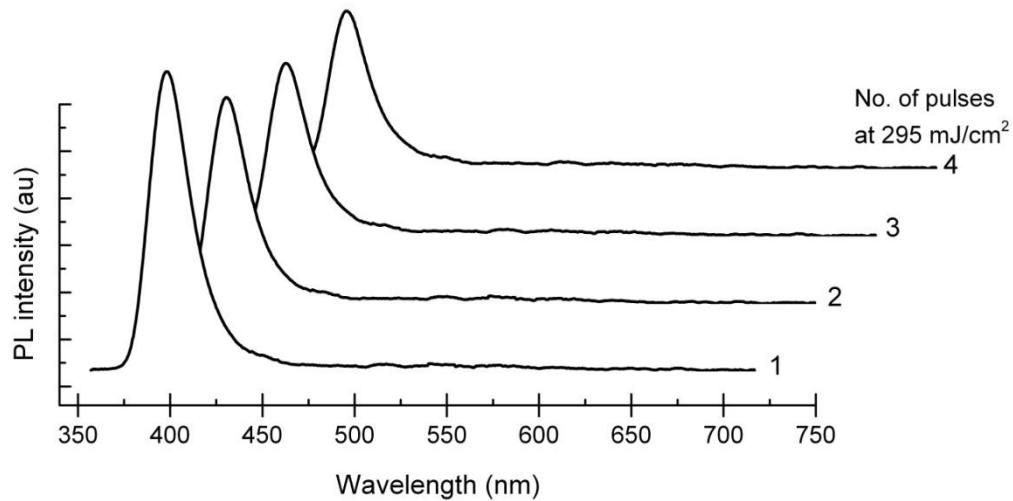


**Figure 4.13:** PL spectra from the 41 sccm sample showing the effect of multiple pulses LA at a high fluence of  $295 \text{ mJ/cm}^2$ .

### 4.3 Transmission electron microscopy (TEM) study

Cross sectional transmission electron microscopy (TEM) was performed to determine the form of any grain size changes caused by laser irradiation treatments, and to identify any other significant features. The study was focused on HiTUS ZnO film grown at 41 sccm of  $\text{O}_2$  (60 nm), as-deposited film, and laser annealed film at fluences of  $220 \text{ mJ/cm}^2$  and  $295 \text{ mJ/cm}^2$  (where the highest intensity of DLE and NBE were observed respectively in the PL spectra), and a sample that had been thermally annealed at  $880^\circ\text{C}$ . TEM characterisation was performed by Glebe Scientific, Ireland.

#### 4.3.1 Transmission electron microscopy (TEM) of laser annealed HiTUS ZnO 41 sccm films

Figure 4.14 shows the cross-sectional TEM images for the as-deposited ZnO film. Figure 4.14 (a), is a dark field image showing the polycrystalline nature of the film with

columnar shaped grain growth having mid-height grain width variation from 10 nm to 15 nm. Figure 4.14 (b) illustrates the expected presence of a thin layer of amorphous oxide at upper surface of Si. Figure 4.14 (c), shows that the film contains a high defect and fault content, while (d) in the defocused image; low density grain boundary channels are observed.

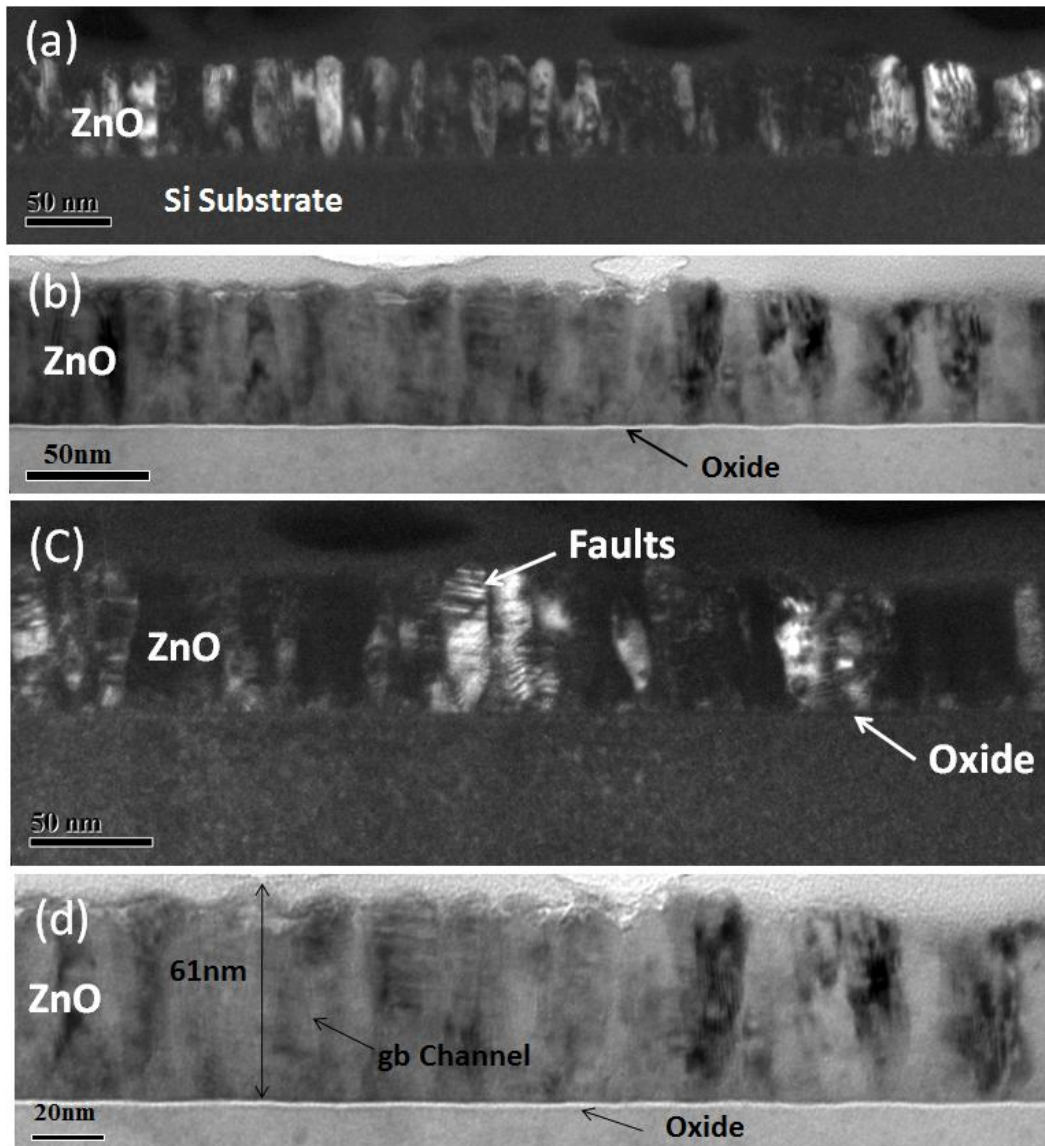


**Figure 4.14:** TEM images for as-deposited ZnO (41 sccm) film (a): dark field shows the grain size, (b) bright field, (c) dark field shows defects content, and (d) defocused image shows the density of grain boundary.

Cross sectional TEM images for ZnO annealed at laser fluence of  $220 \text{ mJ/cm}^2$  with a single pulse, which produced the highest DLE PL, are shown in Figure 4.15. Strong c-

axis preferred growth is observed (via electron diffraction – which is consistent with the XRD results shown in section 4.4). In Figure 4.15 (a), the dark field image shows the disrupted nature of ZnO grains and the typical grain diameters vary from 10 to 40 nm, with a few grains extending through the full thickness of the layer. In Figure 4.15 (b), the defocused image shows an absence of the type of grain boundary channels compared to the as deposited film (see Figure 4.14(d)). Figure 4.15 (c), shows the defect content remaining high but a less evident presence of faults.

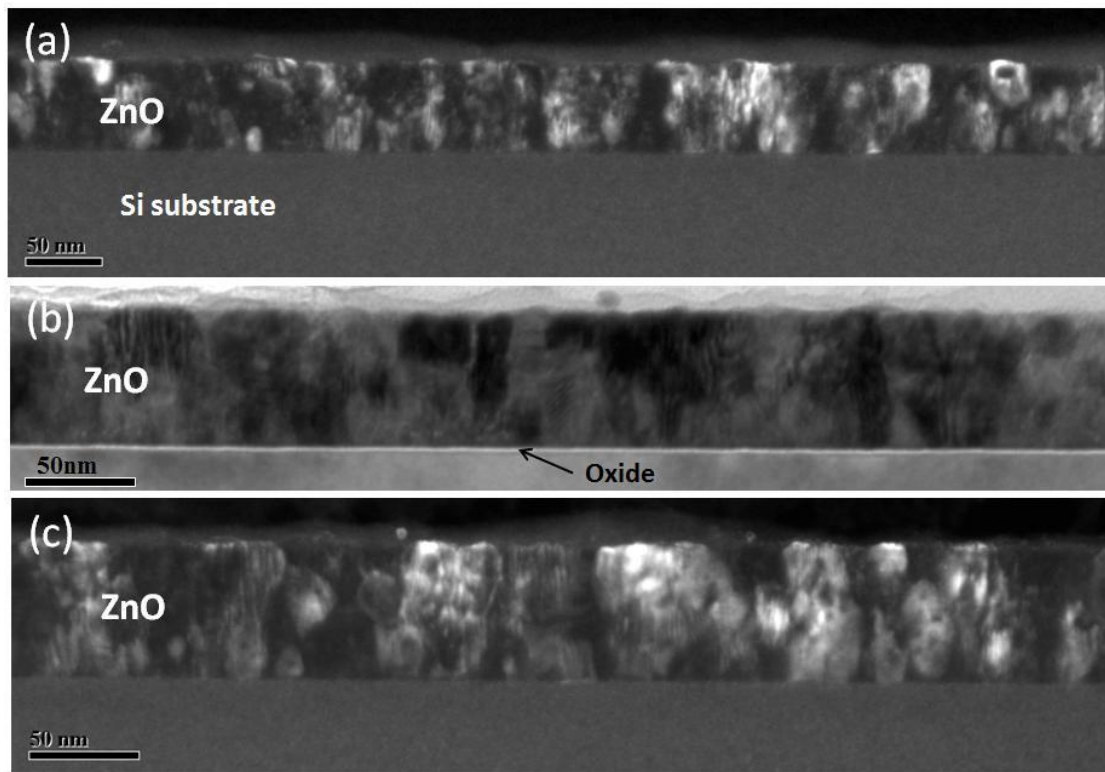


**Figure 4.15:** TEM images of ZnO film (41 sccm) laser treated at  $220 \text{ mJ/cm}^2$  single pulse (a) dark field image, (b) defocused image, and (c) magnified dark field image.

Shown in Figure 4.16 are cross sectional TEM images of the ZnO film (41 sccm) laser annealed at  $295 \text{ mJ/cm}^2$ , which demonstrate the coarse grained morphology of the layer. Here the mid-height widths of the columnar grains size are typically 15 to 25 nm (as opposed to the as-deposited film of 10 to 15 nm), which gives an indication that the grain size is enlarged, and the film has a significantly lower defect content than the as-deposited ZnO film shown in Figure 4.16 (a) and (b) from different area from the

same sample. It is also observed and shown in Figure 4.16 (c) that the grain boundary channels are rather clearer than in the as-deposited film.

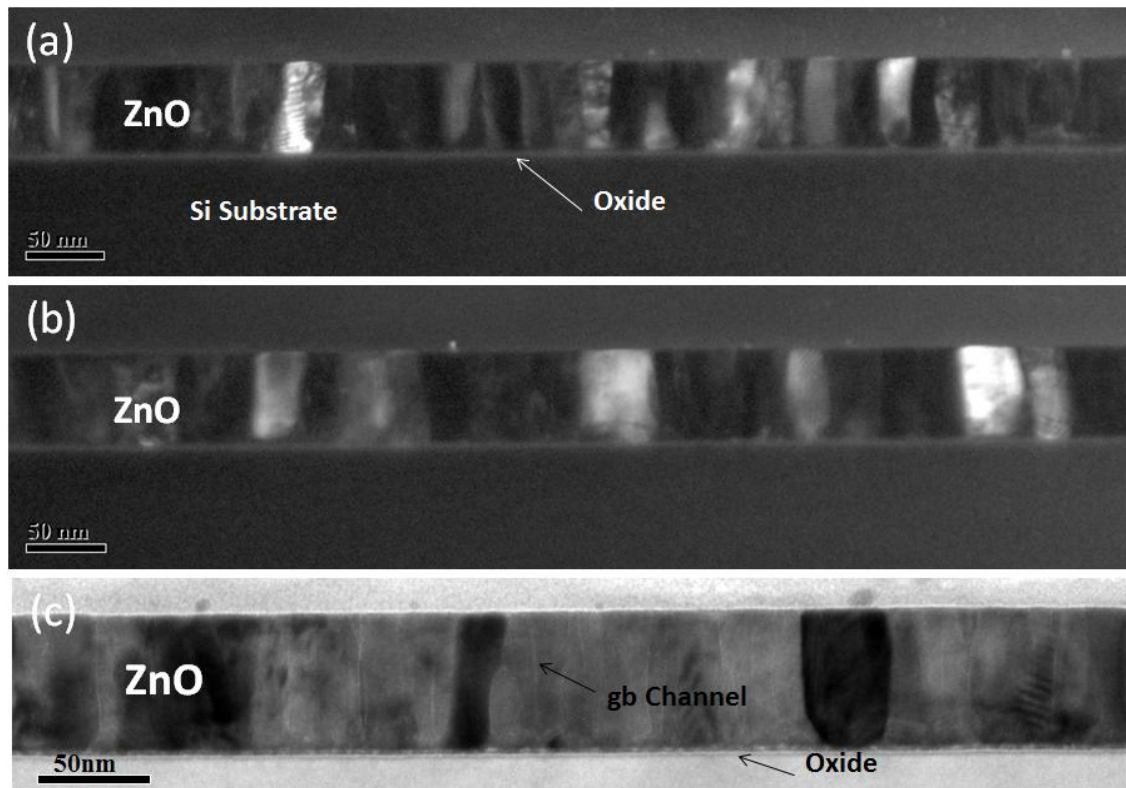


**Figure 4.16:** TEM images of HiTUS ZnO film (41 sccm) laser annealed at  $295 \text{ mJ/cm}^2$  with a single pulse, (a) and (b) dark fields showing grain sizes enlarged, and lower defects, (c) showing the grain boundaries.

### 4.3.2 Transmission electron microscopy (TEM) of laser annealed HiTUS ZnO films (41 sccm 200 nm)

Figure 4.17 illustrates cross sectional TEM images of the 41 sccm ZnO, 200 nm thick sample deposited at room temperature and laser annealed at  $295 \text{ mJ/cm}^2$  with a single pulse. This was considered appropriate in order to identify the extent of the in-depth crystallisation due to finite absorption of laser energy. Figure 4.17 (a), shows a bi-layer microstructure coarse grain at region A, whereas a finer grained material exists at region marked B, and a delaminated zone marked as region C. In Figure 4.17 (b), the marked areas indicate improvements of grain boundary channels. In figure 4.17 (c) the dark field image shows the thickness of an upper crystalline layer and a lower more

amorphous layer, with thicknesses 135 nm and 70 nm respectively. The upper layer contains ZnO grains with typical width of 25-40 nm by comparison to the 10-15 nm grains contained in the lower layer.

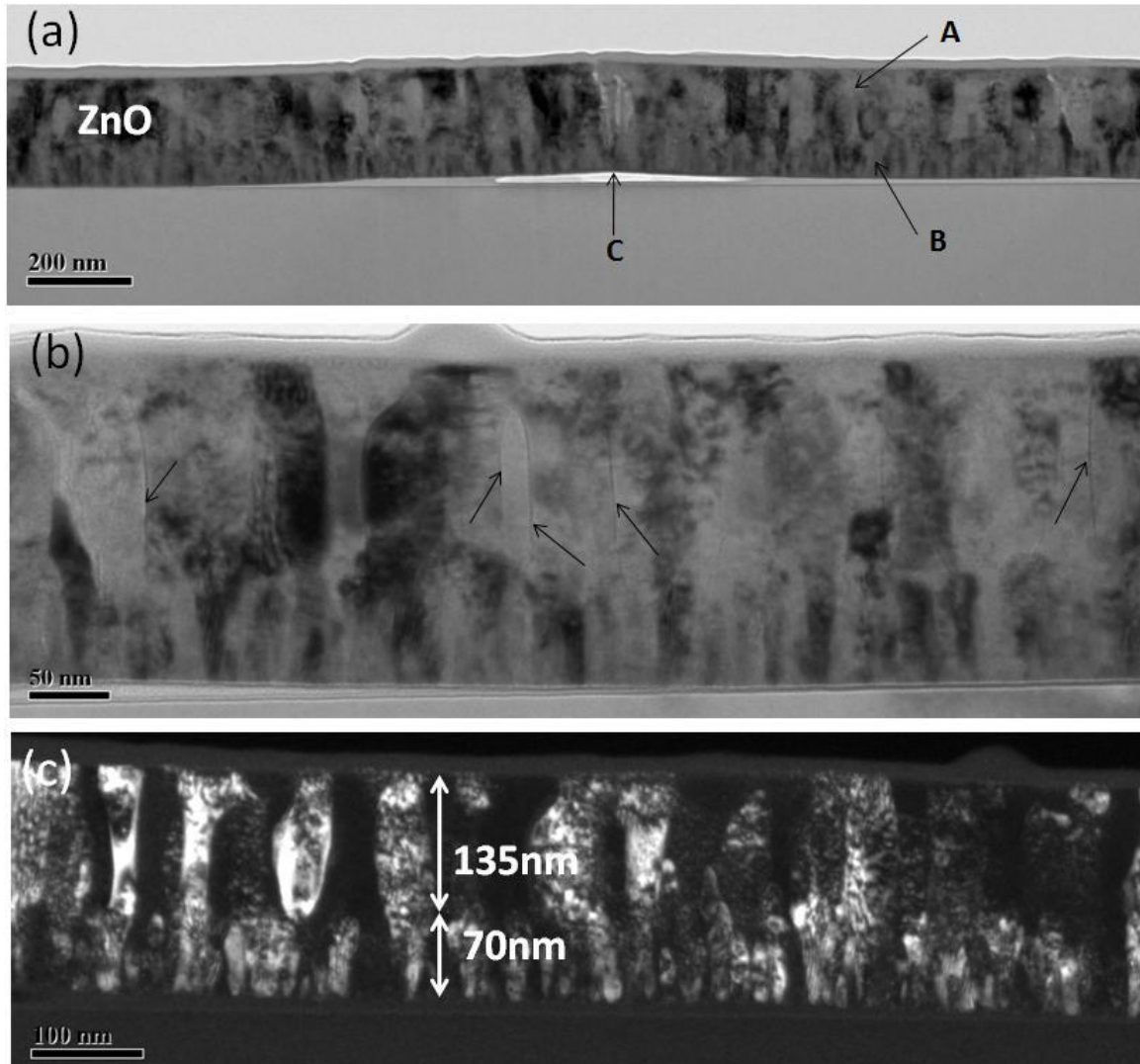


**Figure 4.17:** TEM images of a 200 nm HiTUS ZnO (41 sccm), processed at  $295 \text{ mJ/cm}^2$  with a single pulse, (a) bright field image shows bi-layer microstructure (b) grain boundaries channel and (c) shows the in-depth effect of high fluence with crystallisation reaching 135 nm below the surface of a 200 nm film. "The rising in Figure 4.17 (c) is related to the capping layer not to the film".

### **4.3.3 Transmission electron microscopy (TEM) of HiTUS ZnO films (41 sccm) thermally annealed at 880 °C for 1 hour**

Figure 4.18, shows TEM images of HiTUS ZnO film (41 sccm) thermally annealed at 880 °C for 1 hour in air (for which the corresponding PL shows only DLE and very small NBE). In Figure 4.18 (a), the defocused image shows a thin layer of amorphous oxide at the interface of Si with ZnO (expected) and a ZnO thickness from about 52 nm to 65 nm, thermal anneal has also effected the surface rough comparable to the as-deposited sample. In figure 4.18 (b), the dark field image shows the coarse grain in the upper part of the ZnO film and the heavily faulted finer grain in the lower part of the film marked as A. The ZnO grains typically vary in width from 25-50 nm. Figure 4.18 (c), a higher magnification bright field image shows characteristic fault formation in the coarse grained ZnO film.

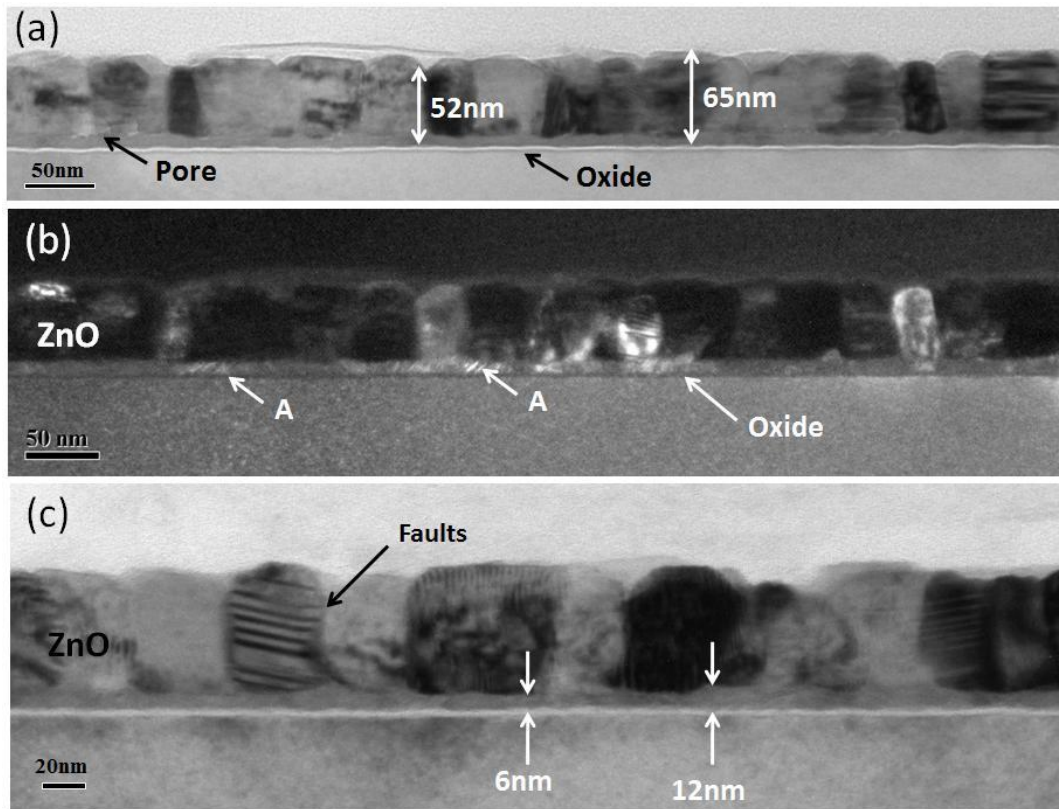


**Figure 4.18:** TEM images of HiTUS ZnO film (41 sccm) thermally annealed at 880 C° for 1 hour, (a) defocused image shows thickness variation (b) dark field image the nature of grains (c) higher magnification bright field shows fault formation.

#### 4.4 X- ray diffraction characterisation

The crystalline characteristics of selected ZnO samples, for the three annealing methods used, were investigated by XRD using the X-Pert Panalytical system operated in Bragg- Brentano mode. The results indicate that the as-deposited films are under compressive stress with a polycrystalline structure. However, the annealing processes resulted in a shift of the (002) peak to higher diffraction angles, consistent with a modification of the films stress as a function of annealing, leading to improved crystal structure, and causing modification of the films stress to tensile. In all cases samples exhibited c-axis preferred orientation as represented by the (002) diffraction peak, and stress changed from compressive to tensile stress.

The XRD patterns of thermally annealed ZnO films for 1 hour are illustrated in Figure 4.19. As the annealing temperature increases, the (002) peak is shifted to higher angles, and the diffraction peak becomes more intense up to the annealing temperature of 840 °C indicating an increase of grain size. For samples which had experienced a further increase of the annealing temperature to 880 °C a further shift in diffraction angle was observed but with no further improvement of grain size. In the rapid thermal annealed samples, similar stress transitions were observed as shown in Figure 4.20.

Figure 4.21, shows the XRD patterns of the as-deposited and single pulse laser annealed ZnO films at various laser fluences. The as-grown film is under compressive stress, but as the laser fluence is increased the (002) peak is shifted to higher angles, indicating a modification of the film stress to tensile, as for TA and RTA. The (002) diffraction peaks become more intense and sharper as the laser fluence reaches 256 mJ/cm<sup>2</sup> and 270 mJ/cm<sup>2</sup>. A subsequent decrease of the (002) peak is observed as the laser fluence is increased to 295 mJ/cm<sup>2</sup>, where the intensity is similar to that produced by a film processed at 277 mJ/cm<sup>2</sup>, this decrease in the (002) peak may be related to loss of c-axis texturing. The reason for the 295 mJ/cm<sup>2</sup> and 277 mJ/cm<sup>2</sup> laser annealed samples to present similar XRD results, whereas in terms of PL the 295 mJ/cm<sup>2</sup> presents highest NBE is still a matter under investigation. The FWHM of the as-deposited film is 0.338°, and the processed at 295 mJ/cm<sup>2</sup> film 0.221°, which gives an indication that the grain size increases with LA. Thermal annealing at 840 °C and RTA at 880 °C produce sharper and more shifted XRD peaks than the laser annealed at 295 mJ/cm<sup>2</sup>. For laser annealed samples the corresponding lattice constant as determined by (002) peak range from c=5.234 Å (for as-deposited) to c=5.158 Å (laser processed at 295 mJ/cm<sup>2</sup>) as the internal stress changes from compressive to tensile stress.

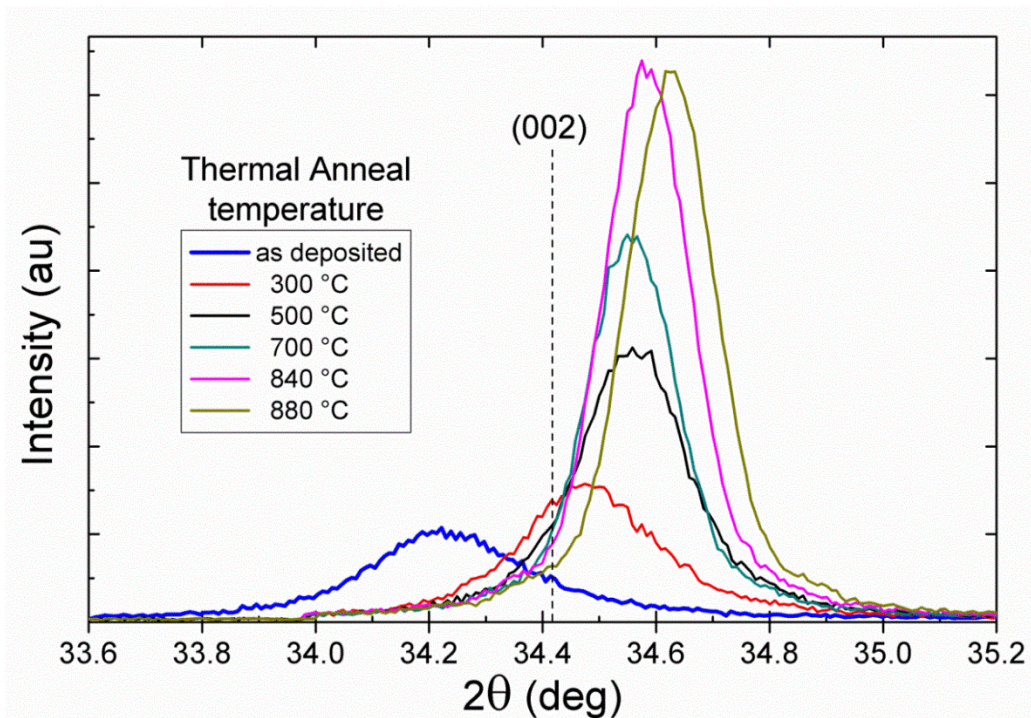


**Figure 4.19:** XRD diffraction patterns of thermally annealed ZnO (41 sccm) sample at various temperatures, for 1 hour in air.

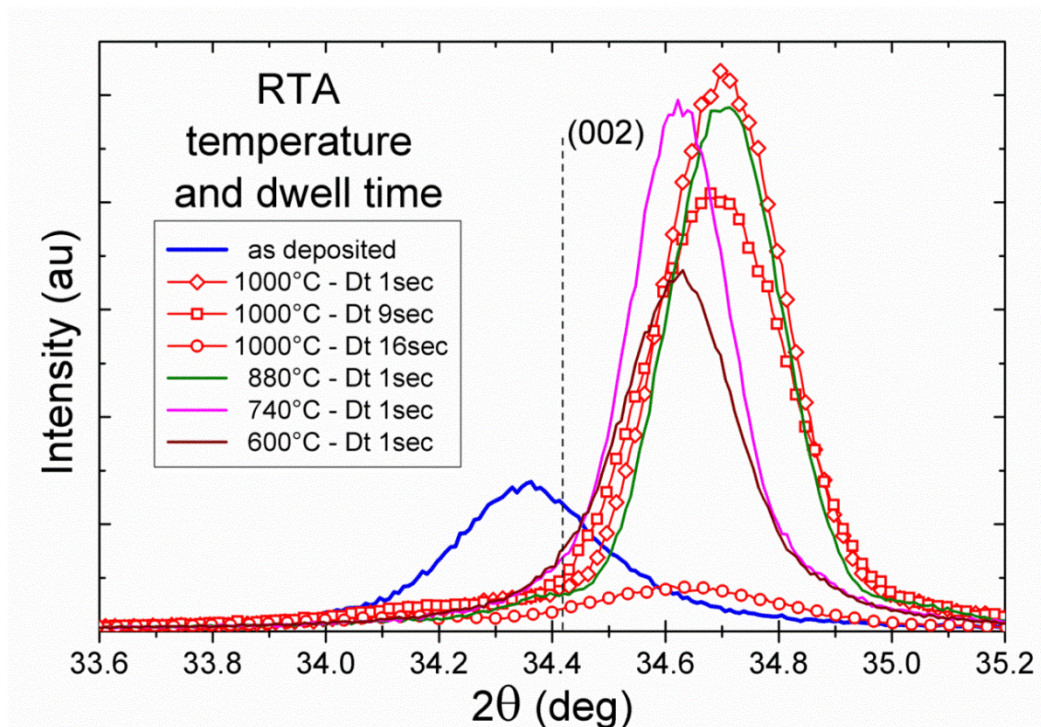


**Figure 4.20:** XRD diffraction patterns from the 38 sccm ZnO sample after RTA in nitrogen at various temperatures and dwell times.

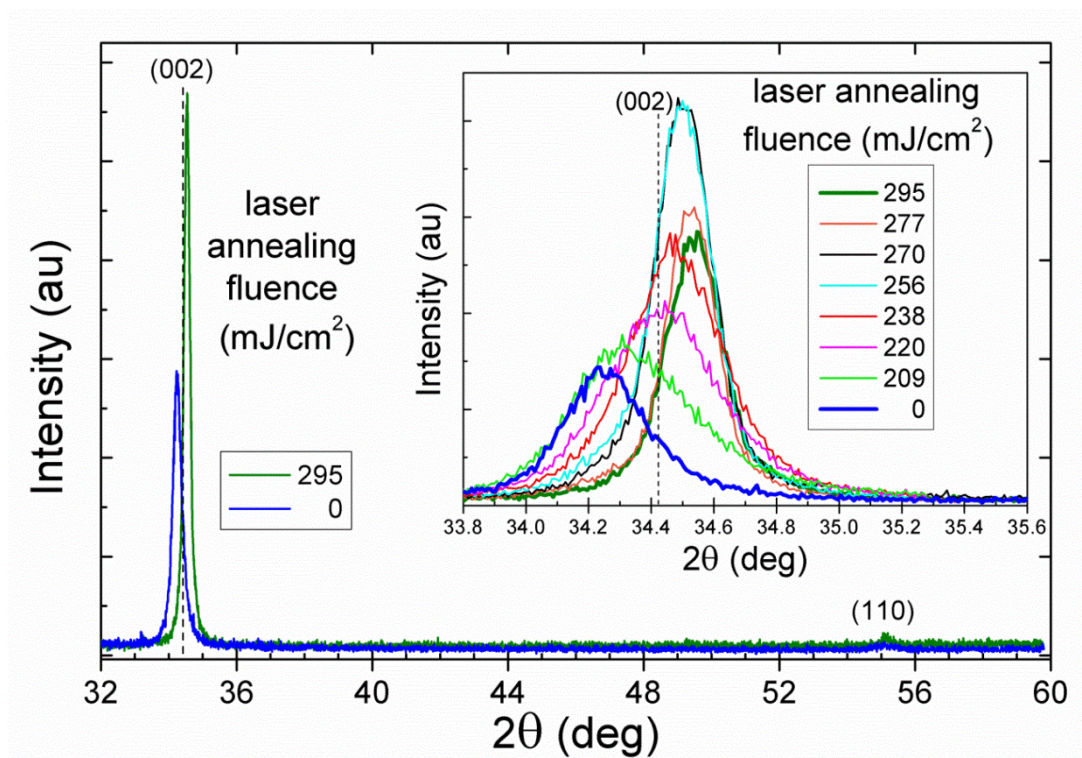


**Figure 4.21:** XRD diffraction patterns from the 41 sccm ZnO sample after single pulse LA at various fluences.

## 4.5 Discussion

ZnO films were deposited by the HiTUS (a high rate deposition technique) at low temperatures on silicon substrates, after which post deposition annealing using three different annealing methods have been studied. The microstructure of the ZnO films was characterised by photoluminescence (PL), X-ray diffraction (XRD), and transmission electron microscopy (TEM). PL results of thermal and rapid thermal annealing exhibit a development of strong visible (DLE) orange/red emission related to defects, and was further enhanced when processed in oxygen, hence confirming that excess oxygen dominated these defects.

High temperature RTA resulted in a component of green/yellow emission with the resultant PL, centred at about 505 nm that is not seen following a thermal anneal. The lowest PL peak of DLE was observed from the films deposited at lower oxygen flow rates (i.e. more zinc) giving a clear indication of the potential domination of  $V_{zn}$  defects

rather than  $V_o$ , which would be consistent with the lower energy formation of  $V_{zn}$  defects [123]. RTA at even higher temperature demonstrates a significant development of the NBE peak (crystallinity related PL). This is potentially indicating a reduction of defects at grain boundaries. However, higher temperatures cause film degradation and material loss for both TA and RTA.

Important results were demonstrated by laser annealing, where it was proven possible to modify the internal properties of the ZnO films with a grain re-growth, crystallinity improvement, and a dramatic reduction of point defect density (as indicated by the NBE to DLE ratio [120] ), and without any film degradation or material loss that occurs in high temperature thermal and rapid thermal annealing. Laser annealing is a highly localised technique with a controlled in-depth crystallisation and modification of the films was demonstrated by cross sectional TEM images (as shown in Figure 4.15 (c)). At the same time it was clearly shown that LA offers an enlargement of grain size, with XRD analysis giving further confirmation evidence for crystal structure improvement with increasing laser fluence. This demonstrates that laser processing is a useful method to control the in-depth modification of the thin film sample, gaining a benefit from isolating the processed region from the substrate, and hence being compatible of processing films on flexible substrates without any damage to the film or the substrate.

## Chapter 5

### ZnO Thin Films by RF Magnetron Sputtering

---

#### 5.1 Introduction

This chapter deals with results of microstructure characterisation of ZnO thin films deposited by RF magnetron sputtering and subsequently processed by excimer laser annealing (ELA). The initial phase of this work was focused on characterisation of ZnO semiconductor layers grown under various conditions (RF power and oxygen concentration) followed by laser annealing to identify optimised conditions in term of the effect on the emitted PL spectra compared with the HiTUS ZnO films presented in Chapter 4. The next phase was concerned with a comparative study of the effect of laser annealing on the properties of ZnO thin films grown by RF magnetron sputtering at room temperature (RT), as well as at various substrate temperatures from 100 °C to 400 °C. Section 5.2 presents room temperature photoluminescence spectra results for excimer laser annealed ZnO deposited at various RF powers. Sections 5.3 and 5.4 present PL characterisation of laser and thermal annealing of ZnO deposited at various substrate temperatures. Section 5.5 presents X-ray diffraction pattern of films subsequent to treatments using the laser and thermal annealing methods studied. Section 5.6 presents cross sectional transmission electron microscopy (TEM) images of selected ZnO films

In recent years there have been reported studies dealing with the influence of laser annealing on the properties and microstructure of ZnO thin films deposited by RF magnetron sputtering [126], pulsed laser deposition [127], and other deposition techniques [128, 129]. However, the work to date has not included a detailed study of the effect of laser anneal on PL properties of ZnO deposited at various substrate temperatures. In particular, the main objective of the work presented here is a

comparative study to investigate the influence of excimer laser anneal on the intrinsic PL characteristics of ZnO films grown at various substrate temperatures from RT to 400 °C, and at various RF powers.

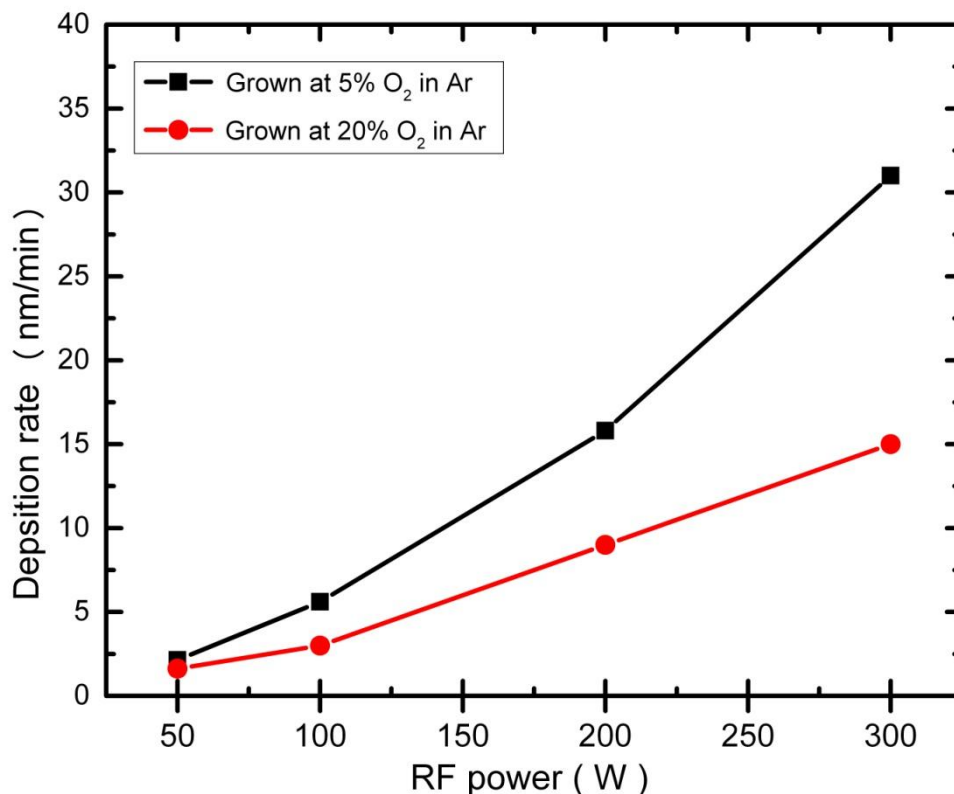
## **5.2 Laser anneal of films deposited at various RF power**

Initially, two sets of ZnO films were deposited on silicon substrates at oxygen concentrations of 5% O<sub>2</sub> in Ar and 20% O<sub>2</sub> in Ar, at various RF powers of: 50, 100, 200, and 300 W respectively. The sputtering electrode used are a 3" Torus by Kurt Lesker, without intentional substrate heating and at a deposition pressure of 2 mTorr. Subsequently, laser annealing was used to process all films at various conditions as explained in Chapter 3.

The deposition rate of sputtered ZnO films is strongly dependent on deposition conditions. As shown in Figure 5.1, the RF power affects the growth rate of ZnO films. As the RF power increases, the deposition rate increases significantly, which can be attributed to the increasing electric field between the cathode (target) and anode (substrate) resulting in the density of sputter gas ions increasing, which in turn leads to enhanced sputtering of the target surface resulting in an increase in the number of sputtered species arriving at the substrate surface.

Oxygen is typically mixed with the argon ambient during the deposition to ensure films with better control stoichiometry [130], and to influence the resultant electrical and optical properties of the films [47, 131, 132]. However, from results presented here, it can be seen that the oxygen percentage also affects the growth rate. As the oxygen percentage is increased, the deposition rate decreases significantly across all RF powers tested. Sputtering at high oxygen content leads to re-sputtering of the growing film on the substrate by bombardment of highly energetic oxygen ions [55]. With increasing the oxygen content, the target surface will become more oxidized leading to high emission of secondary electrons (i.e. electrons produced from ejected target materials

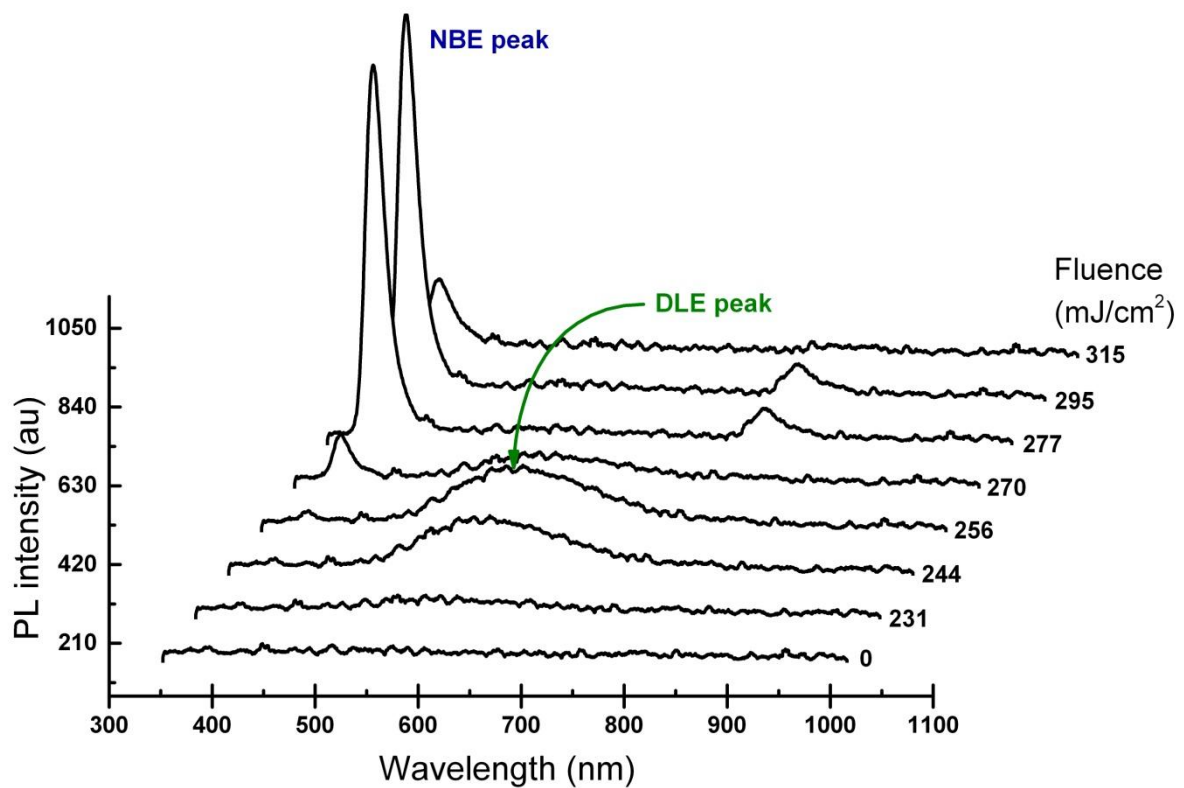
when argon ions hit the target) resulting in a decrease of growth rate [92]. Increasing oxygen content at low RF power showed negligible influences on deposition rate.



**Figure 5.1:** Deposition rate as a function of RF power for ZnO films deposited at oxygen concentrations of 20% O<sub>2</sub> in Ar, and 5% O<sub>2</sub> in Ar.

Figure 5.2 shows the room temperature PL spectra evolution of ZnO films deposited (to 60 nm thickness) with 20% O<sub>2</sub> in Ar, RT, at RF power of 50 W, as a function of laser annealing in air ambient with single pulses. No luminescence peak was observed for as deposited films and films irradiated at low fluences (<244 mJ/cm<sup>2</sup>), which is likely to be due to the dominance of non-radiative recombination centres created by lattice and surface defects in sputtered ZnO films [133]. As the laser energy density of the laser treatment is increased up to medium fluences (244 – 256 mJ/cm<sup>2</sup>), a deep level emission peak (DLE) ranging from 450 nm-750 nm starts developing as a function of fluence and reaches the highest intensity (correlating with a very weak appearance of an NBE peak at around 381 nm) at fluence of 256 mJ/cm<sup>2</sup>.

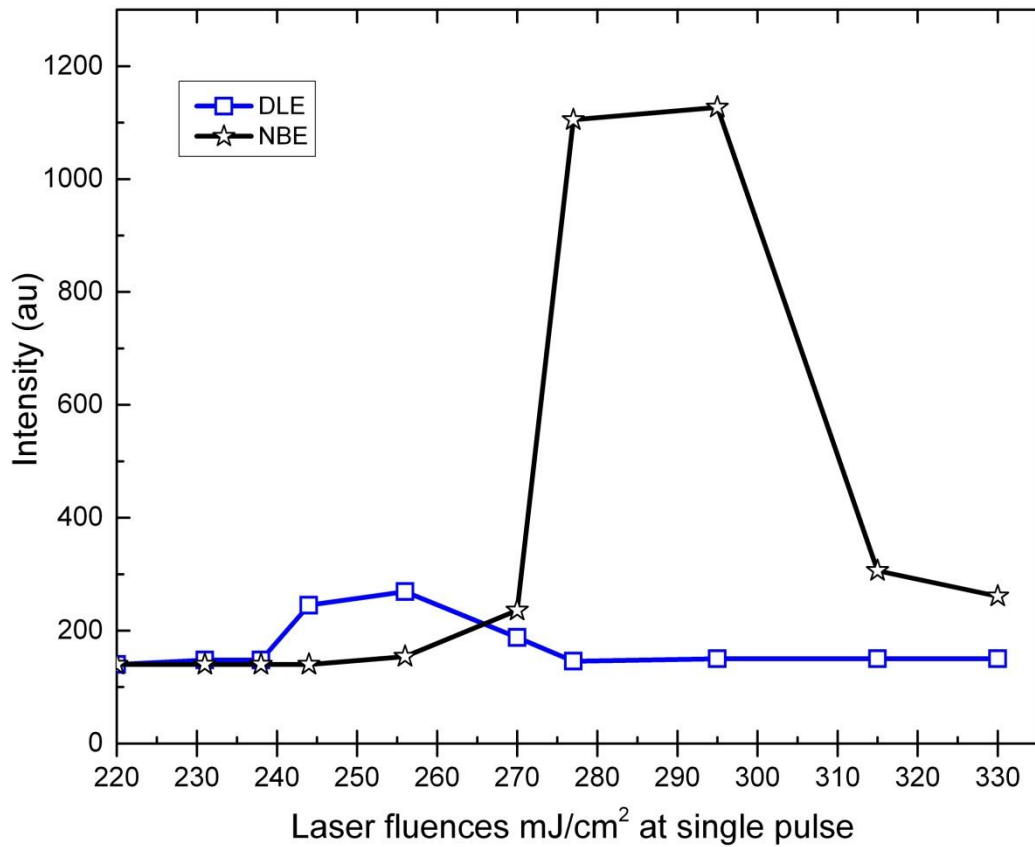
Further increase in fluences ( $270 - 295 \text{ mJ/cm}^2$ ) causes an increase in the NBE intensity with a gradual decrease in DLE intensity until the DLE emission disappears at higher fluences. A reduction in the DLE peak with increasing NBE peak is usually associated with an increase of the grain size [134, 135]. Similar PL spectra trends were observed for films deposited at RF power of 100, 200, and 300 W but with a significant drop in NBE peak as the sputtering RF power increased, as a function of laser processing (PL spectra of these films are shown in appendix B).



**Figure 5.2:** Evolution of PL spectra of laser annealed ZnO (50 W, 20% O<sub>2</sub> in Ar at RT) films at various energy densities in air at single pulse, results in medium fluences showing development of DLE peak, while at high fluences results show a reduction of DLE peak with evolution of a strong NBE peak. (The small peaks at  $\sim 760\text{nm}$  are the second harmonic of the UV peaks at  $\sim 381\text{nm}$ ).

Figure 5.3 shows the development of the NBE and DLE peaks intensity at about 381 nm (NBE) and 450 to 750 nm (DLE) as a function of laser fluence. These data were

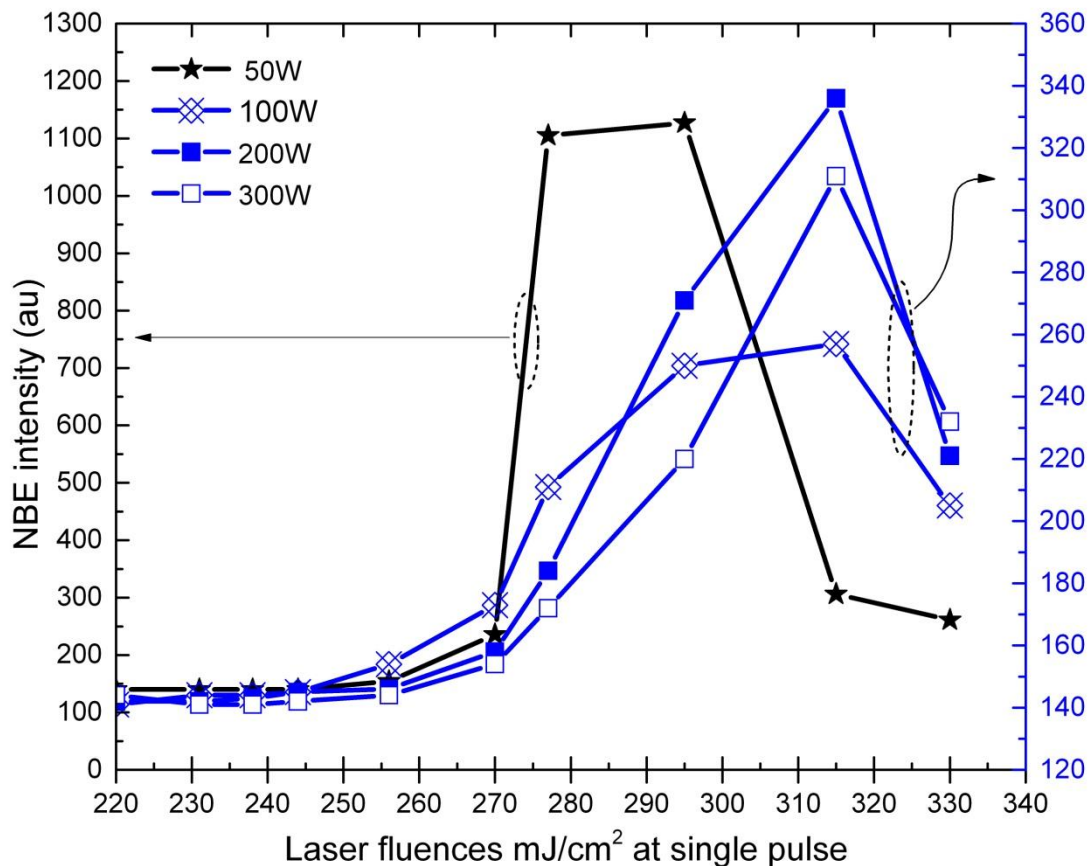
extracted from PL spectra of ZnO films shown in Figure 5.2. Note that the trends for both peaks remains unchanged and flat for laser fluences lower than  $220 \text{ mJ/cm}^2$ .



**Figure 5.3:** The intensity development of DLE and NBE peaks as a function of laser energy densities for the same ZnO films shown in Figure 5.2 are plotted for clarity.

For comparison, the NBE and DLE peak intensity as a function of laser fluences for all the films (grown at various RF powers) were extracted from the PL spectra and are presented in Figures 5.4 and 5.5 respectively. It can be clearly seen that as the RF power is increased the intensity of NBE decreases after laser treatment (note the two different vertical scales denoted with different colours). In addition, the intensity of visible light emission associated to defect centres DLE of laser annealed ZnO film grown at 50 W is higher than films deposited at 100 W, 200 W, and 300 W (Figure 5.5). This effect is suppressed after a laser anneal at high fluence of  $295 \text{ mJ/cm}^2$  with stronger UV emission intensity, which is consistent with the PL of HiTUS ZnO reported in Chapter 4. The intensity ratio of NBE over DLE can be classified as a degree of the film quality

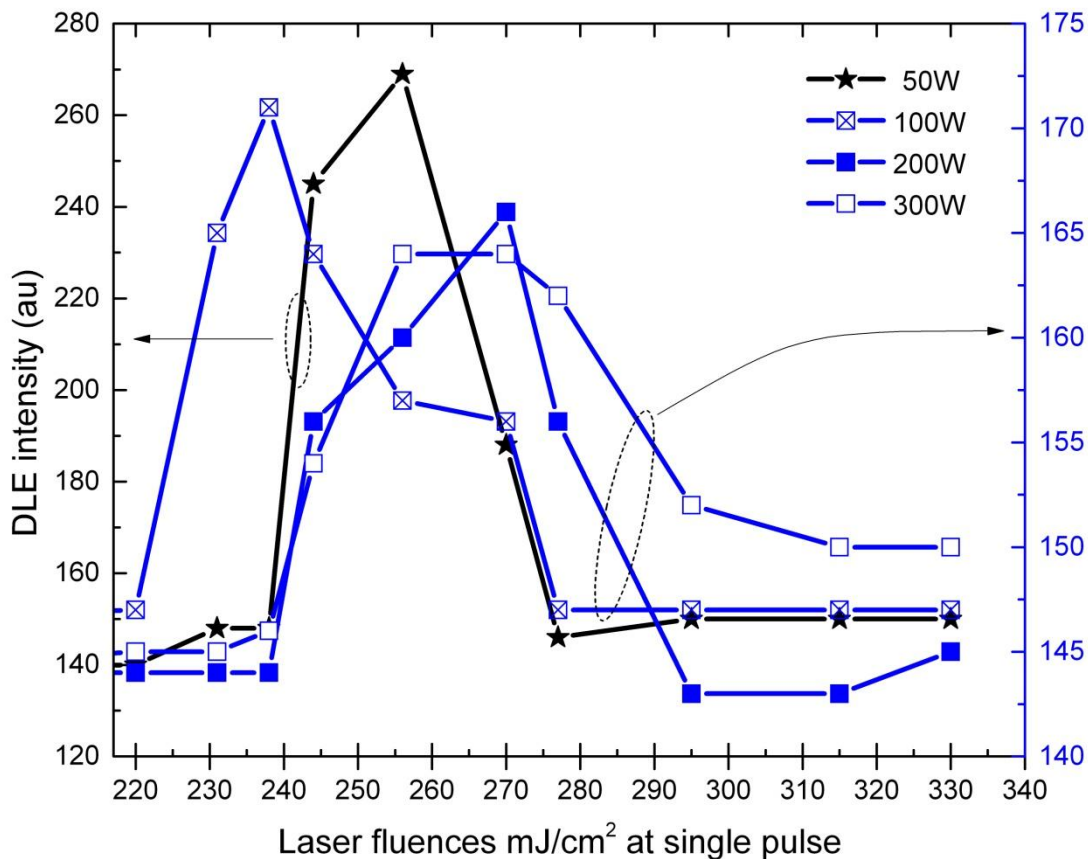
[136] hence from the PL spectra of laser processed ZnO films deposited at various RF powers. It is inferred that the films grown at an RF power of 50 W demonstrate an NBE: DLE ratio that indicates better crystallinity and potentially a larger grain size.



**Figure 5.4:** NBE intensity peak versus laser energy density of ZnO deposited at RT and with 20% O<sub>2</sub> in Ar and various RF powers of 50, 100, 200, and 300 W, as a function of laser anneal.

As shown by the results presented here, with increasing the RF power, the UV emission peak decreased drastically, which implies that the film quality deteriorated. This could be linked to crystallinity of lower quality, which can be attributed to three possible factors that influence the film structural order when sputtering at high RF power: (i) high energetic ion bombardment causing faster reaction and particles with high energy bombarding the film, and introduce defects [134, 137]. (ii) Linear increase of the deposition rate with increasing the RF power giving less time to newly arrived species to move to their stable sites [138]. (iii) With increasing the RF power the relative

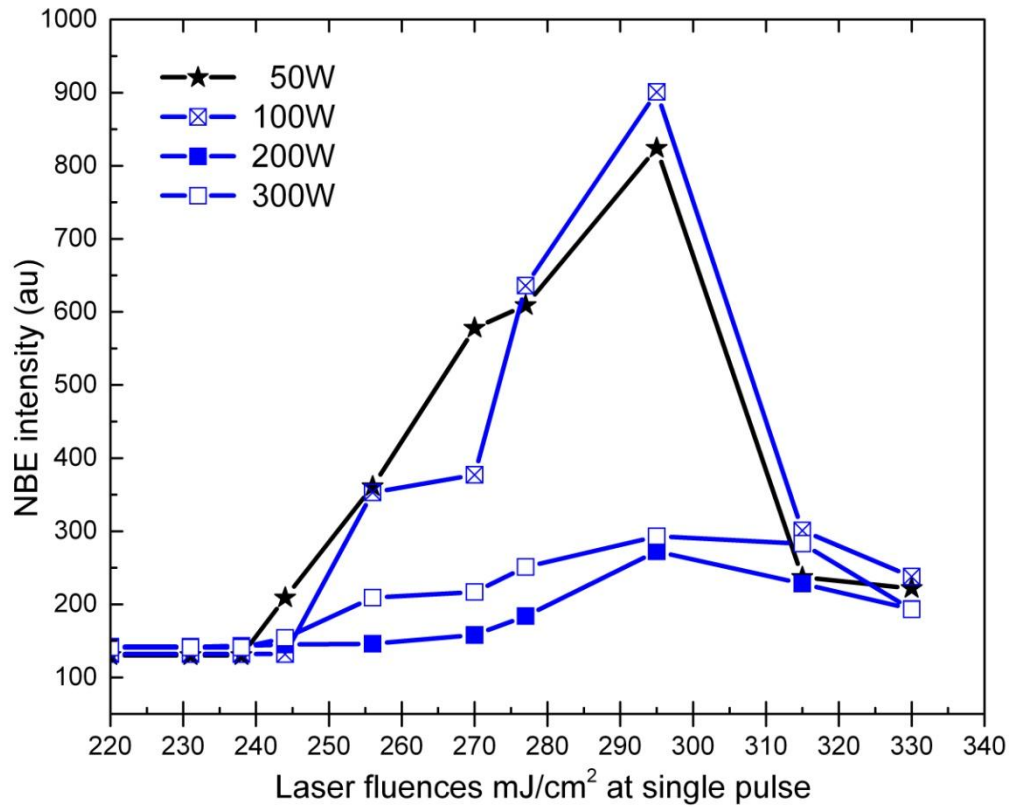
number of Zn to ZnO condensing on the substrate increased leading to forming an oxide at the substrate in which result in films with more crystal structure disorder than if arrived particles were already in oxide form [139].



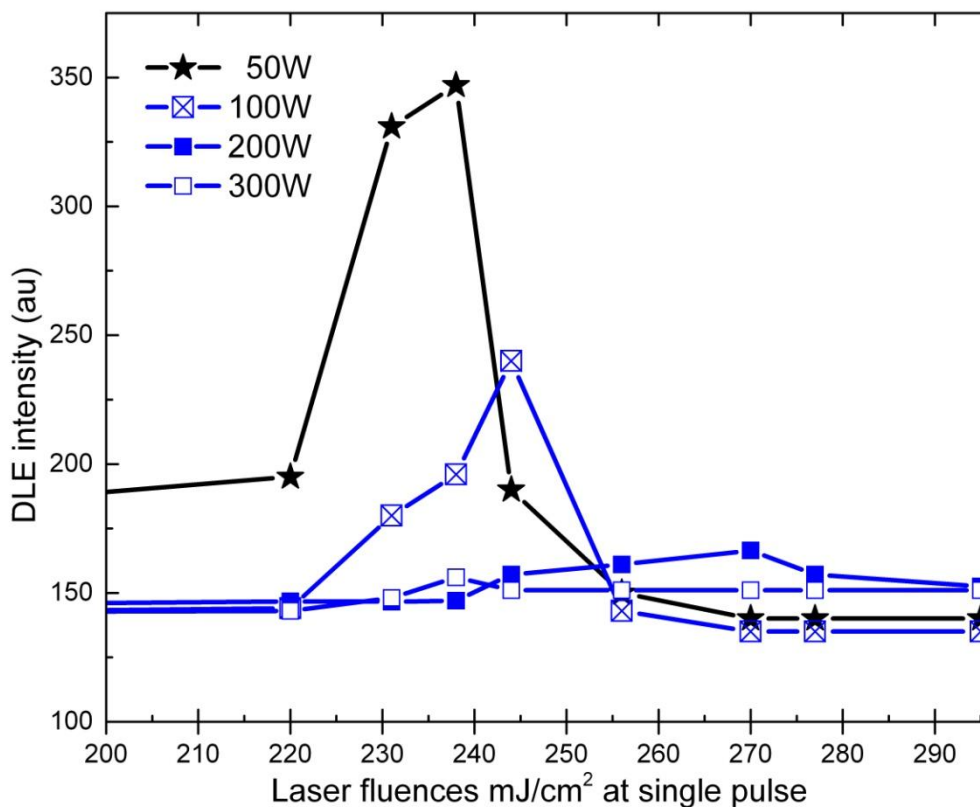
**Figure 5.5:** DLE intensity peak versus laser energy density of ZnO deposited at RT with 20% O<sub>2</sub> in Ar and various RF powers (50, 100, 200, and 300 W) as a function of laser anneal.

Figures 5.6 and 5.7 show the evolution of NBE and DLE peaks respectively, extracted from PL spectra of a second set of ZnO films grown at lower oxygen concentration of 5% O<sub>2</sub> in Ar with various RF powers. Following the post deposition laser anneal, the development of visible emission (450 nm-750 nm) DLE peak at medium fluences shows a similar trend to films grown at 20% O<sub>2</sub> in Ar, but with slightly lower intensity. The intensity of NBE increased gradually at high fluences and was at the highest intensity for the film deposited at 100 W. However, in comparison with the set grown at 20% O<sub>2</sub> in Ar, the strongest UV emission peaks were when the oxygen concentration was 20%

O<sub>2</sub> in Ar, and RF power was 50 W. This is comparable with the HiTUS ZnO film reported in Chapter 4, which is similar to that reported by Hsieh et.al in which the optimal oxygen concentration on intensity of UV of 21% for ZnO grown at 500 °C without an annealing process [134].



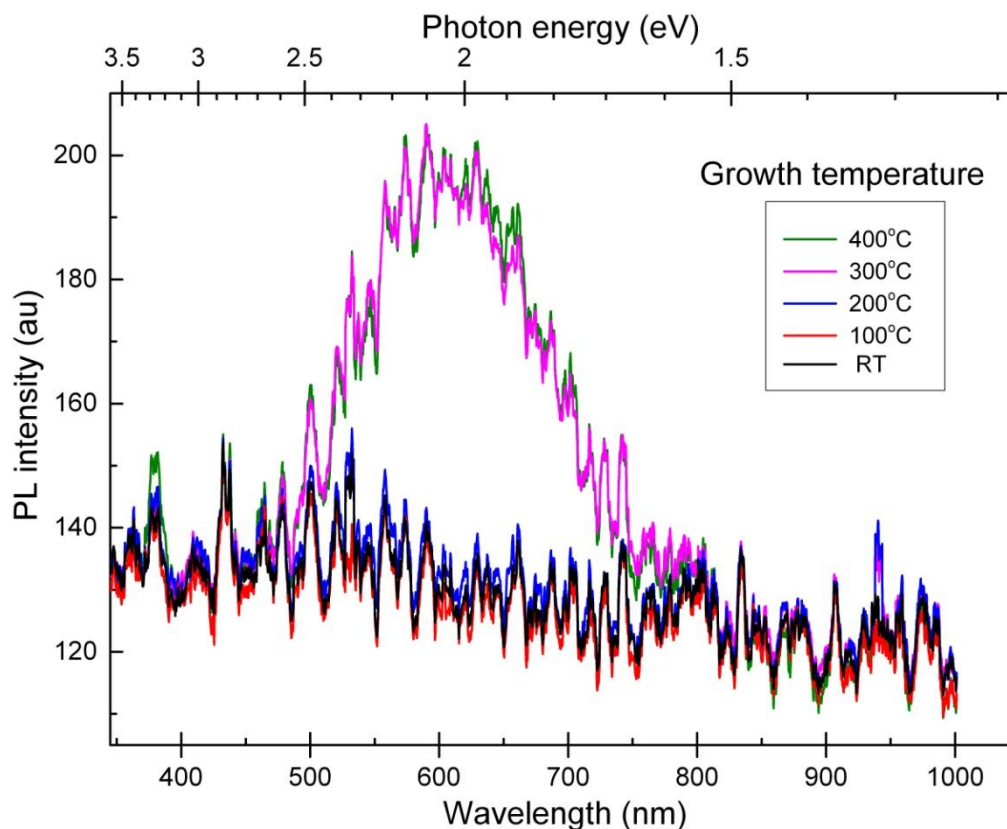
**Figure 5.6:** Evolution of NBE intensity peak versus laser energy density of ZnO grown at 5% O<sub>2</sub> in Ar, RT, 2 mTorr at various RF powers (50, 100, 200, and 300 W) as a function of laser anneal.



**Figure 5.7:** Evolution of DLE intensity peak versus laser energy density of ZnO grown at 5% O<sub>2</sub> in Ar, RT, 2 mTorr at various RF powers (50, 100, 200, and 300 W) as a function of laser anneal.

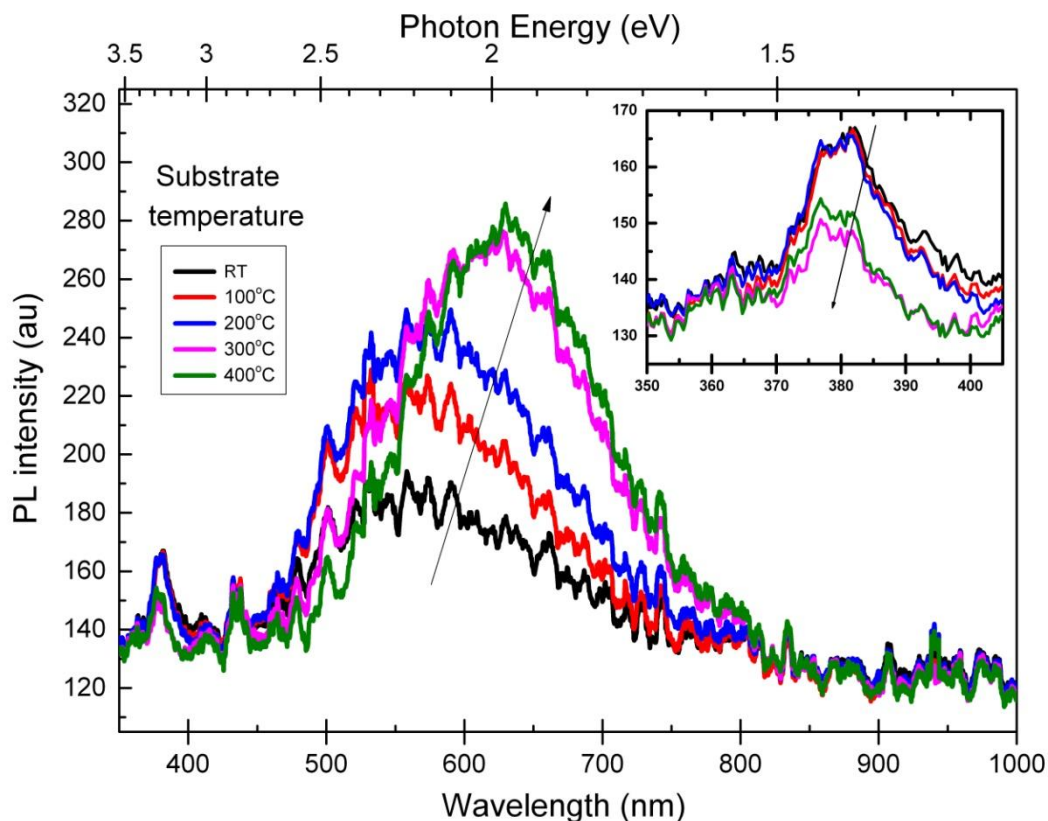
### 5.3 PL of thermal annealed ZnO films deposited at various substrate temperatures

Figure 5.8 shows the PL spectra of ZnO films (50 W, 20% O<sub>2</sub> in Ar) deposited at temperatures from RT to 400 °C. For the as-deposited ZnO films (i.e. prior to annealing) at 100 °C and 200 °C there is a negligible appearance of UV NBE, and visible light DLE, similar to the PL of the as-deposited film at room temperature (assumed to be associated with non-radiative recombination centres). For the films grown at higher substrate temperatures of 300 °C and 400 °C a small DLE peak with a very weak NBE peak were observed, indicating a reduction in defects acting as non-radiative recombination centres as the growth temperature increased.



**Figure 5.8:** PL spectra of ZnO films deposited at various temperatures of RT, 100 °C, 200 °C, 300 °C, and 400 °C.

For comparison with the laser annealed results, Figure 5.9 illustrates the PL characteristics measured at room temperature of ZnO films produced at various substrate temperatures (RT, 100 °C, 200 °C, 300 °C, and 400 °C), followed by thermal annealing at 700 °C in air for a dwell time of 1 hour, (all films were introduced into the furnace after the temperature had reached 700 °C, and then were taken out immediately after an hour). The PL spectra show development of the DLE broad visible emission (450-750 nm) related to defects, which increased significantly as the film growth temperatures were increased up to 200 °C, with just a weak NBE. The effect of annealing on films deposited at 300 °C, and 400 °C lead to a prominent increase and shift of the DLE peak, with a simultaneous reduction of the NBE peak. A subsequent increase of DLE peak with a shift to orange/red emission at (630 nm) is indicative of radiative transitions from defects associated with excess oxygen [121], potentially interstitial ( $O_i$ ) defects [140].



**Figure 5.9:** PL spectra of thermal annealed (at 700 °C, dwell time 1 hour) ZnO films grown at various temperatures. The inset shows the evolution of NBE peak at about 381 nm.

#### 5.4 PL of laser annealed ZnO films deposited at various substrate temperatures

The development of PL as a function of single pulse laser treatment was investigated for ZnO (50 W, 20% O<sub>2</sub> in Ar) films grown at various temperatures from RT to 400 °C. Figures 5.10 and 5.11 show the evolution of NBE and DLE peaks respectively, extracted from PL spectra of ZnO films deposited at various temperatures. Following laser annealing at various fluences, an evolution of the two main peaks were observed for all five deposition temperatures, with the strong narrow UV emission centred at 381 nm, and the broad visible emission DLE peak at 440-750 nm. Interestingly, the effect of the laser anneal at high fluences is that a significant reduction in intensity of the NBE peak is observed (Figure 5.8) as the film growth temperature is increased. Moreover, the DLE is not completely suppressed for the samples deposited at higher temperature (as it

happens for lower deposition temperatures). Hence, ZnO crystal quality deteriorated after laser annealing as the deposition temperatures were increased.

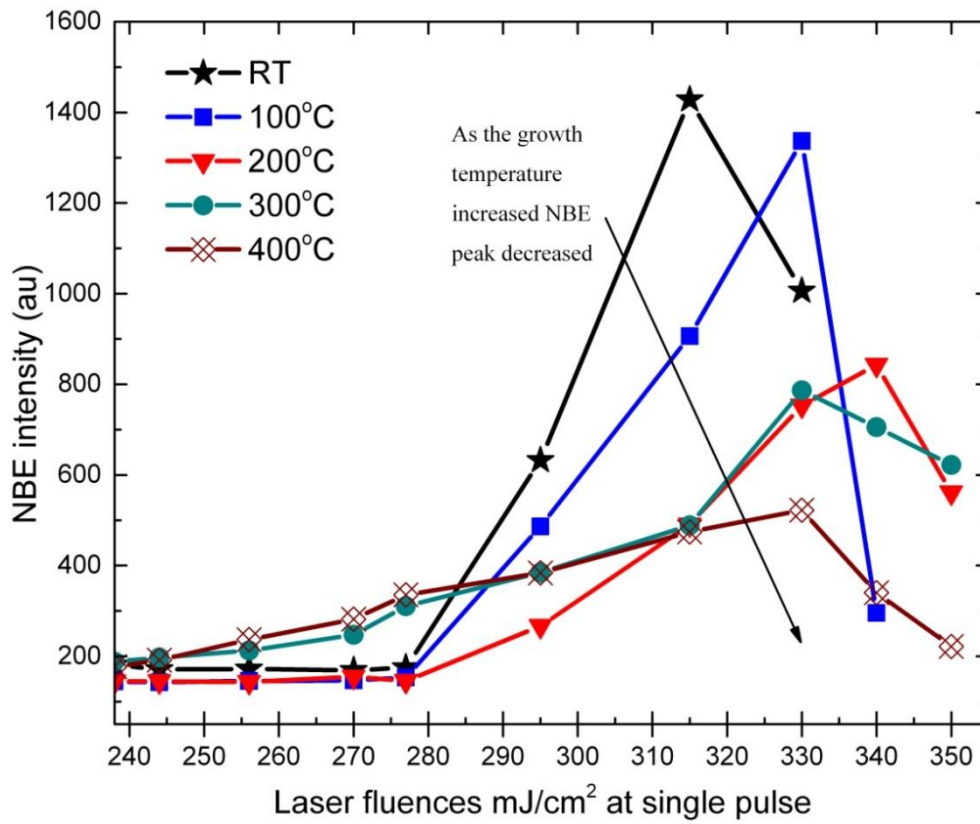


**Figure 5.10:** NBE peak intensity of laser annealed ZnO films deposited at various substrate temperatures (RT, 100, 200, 300, and 400 °C). As the deposition temperature increased, the NBE peak decreased.

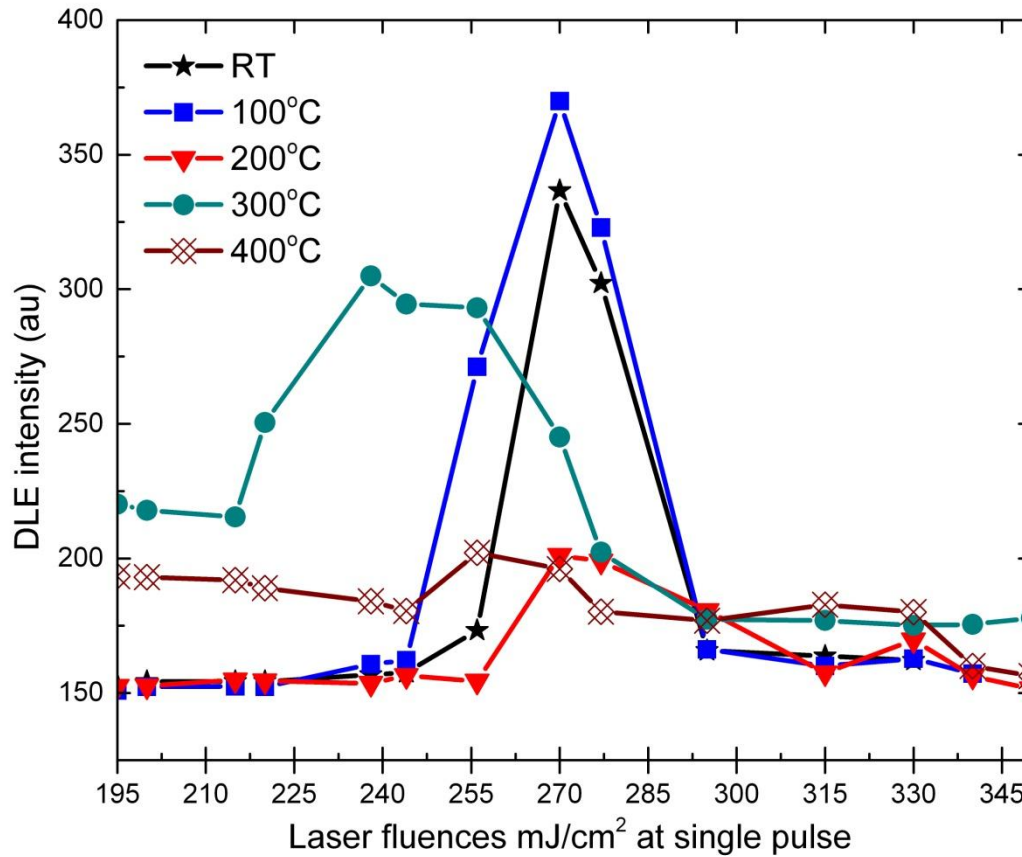


**Figure 5.11:** DLE peak intensity of laser annealed ZnO films deposited at various substrate temperatures (RT, 100, 200, 300, and 400 °C).

### 5.5 XRD characterisation of laser annealed ZnO films deposited at various substrate temperatures

Figure 5.12 shows the XRD patterns from as-grown and laser annealed ZnO films deposited without intentional substrate heating at RF power of 50 W. All samples exhibit a significant (002) diffraction peak, indicating that the preferred orientation is along the c-axis, perpendicular to the substrate plane. The XRD patterns reveal the strong effect of excimer laser annealing on the crystal microstructure of ZnO thin films grown at room temperature, as the laser fluence is increased. The effect is a prominent increase in the (002) peak height, a reduction in the peak width and a shift of  $2\theta$  to higher angles which indicates a transition from compressive to tensile stress. The average crystallite domain sizes for all samples were estimated and are listed in Table

5.1, by Scherrer's formula:  $D = 0.9\lambda / B \cos \theta$ , where  $\lambda$ ,  $B$ , and  $\theta$  are X-ray wavelength, full width at half maximum (FWHM) of (002) peak, and Bragg diffraction angle respectively. The average crystallite domain size of the as-grown film of 19.16 nm increases to about 31.18 nm after laser annealing at a fluence of 315 mJ/cm<sup>2</sup>. The highest XRD peak intensity was achieved at this laser energy density which is consistent with the highest intensity of NBE peak observed from the PL spectra, and indicates that laser annealing is a powerful process to improve the crystal structure of ZnO thin films when deposited at low temperatures.

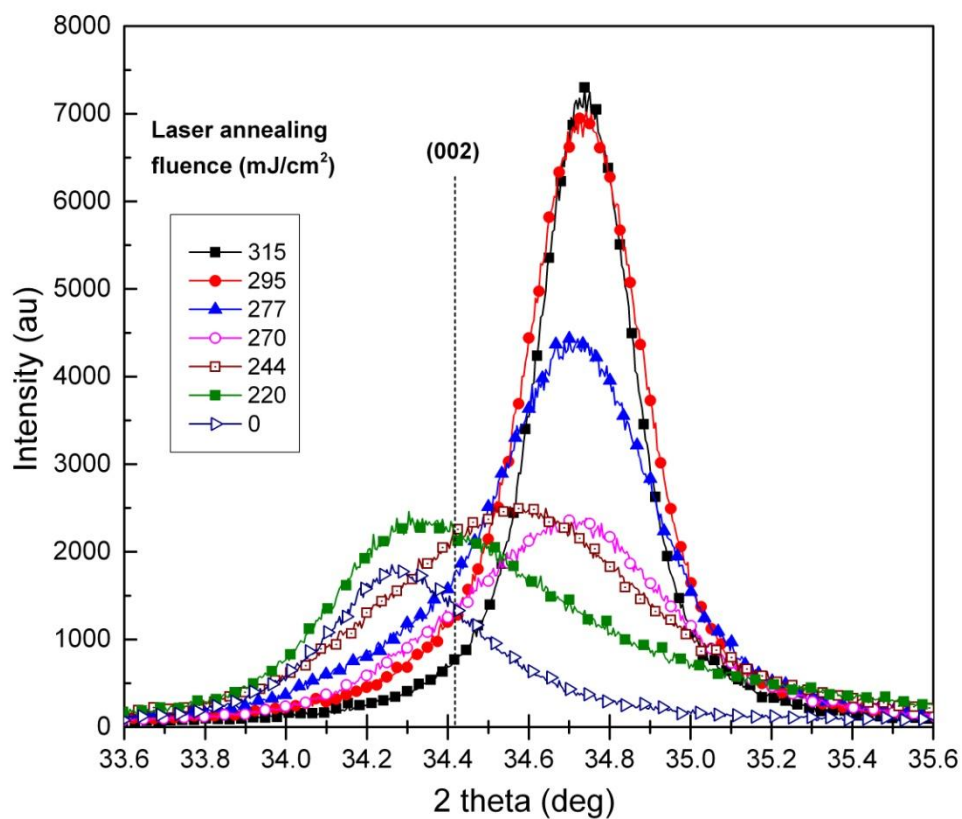


**Figure 5.12:** XRD patterns of ZnO deposited at room temperature following to laser anneal versus laser energy density at single pulse.

Laser fluence (mJ/cm <sup>2</sup> )	0	220	244	270	277	295	315
FWHM (deg)	0.434	0.676	0.735	0.618	0.463	0.359	0.267
2 theta (deg)	34.26	34.30	34.59	34.74	34.70	34.74	34.73
Crystallite domain size (nm)	19.16	12.30	11.32	13.47	17.98	23.19	31.18

**Table 5.1:** Data from XRD patterns of ZnO films deposited at room temperature (RT) following laser anneal at various energy densities with single pulse irradiation.

Figure 5.13 shows the XRD spectra of as-grown and laser annealed films deposited at a substrate temperature of 300 °C. All films exhibit the (002) diffraction peak. As the laser energy density increases from 220-315 mJ/cm<sup>2</sup> the effect is a decrease in the (002) peak intensity, with a broadening of the peak and a concomitant shift to higher diffraction angles. As the fluence is increased up to 335 mJ/cm<sup>2</sup>, the effect is a prominent shift to higher angles with a significant decrease in peak height, and increase the peak broadening. Using Scherrer's formula, the average crystallite domain size is evaluated and presented in Table 5.2. It can be seen that the grain domain size decreased as the laser fluence increased up to 340 mJ/cm<sup>2</sup>, indicating that the laser process deteriorates the microstructure of ZnO deposited at 300 °C.

Laser fluence (mJ/cm <sup>2</sup> )	0	220	238	295	315	335	340
FWHM (deg)	0.234	0.271	0.342	0.376	0.356	0.363	0.363
2 theta (deg)	34.66	34.72	34.71	34.77	34.75	34.79	34.78
Crystallite domain size (nm)	35.58	30.72	24.30	22.14	23.39	22.94	22.94

**Table 5.2:** Data from XRD patterns of ZnO films deposited at 300 °C following laser anneal at various energy density at single pulse.

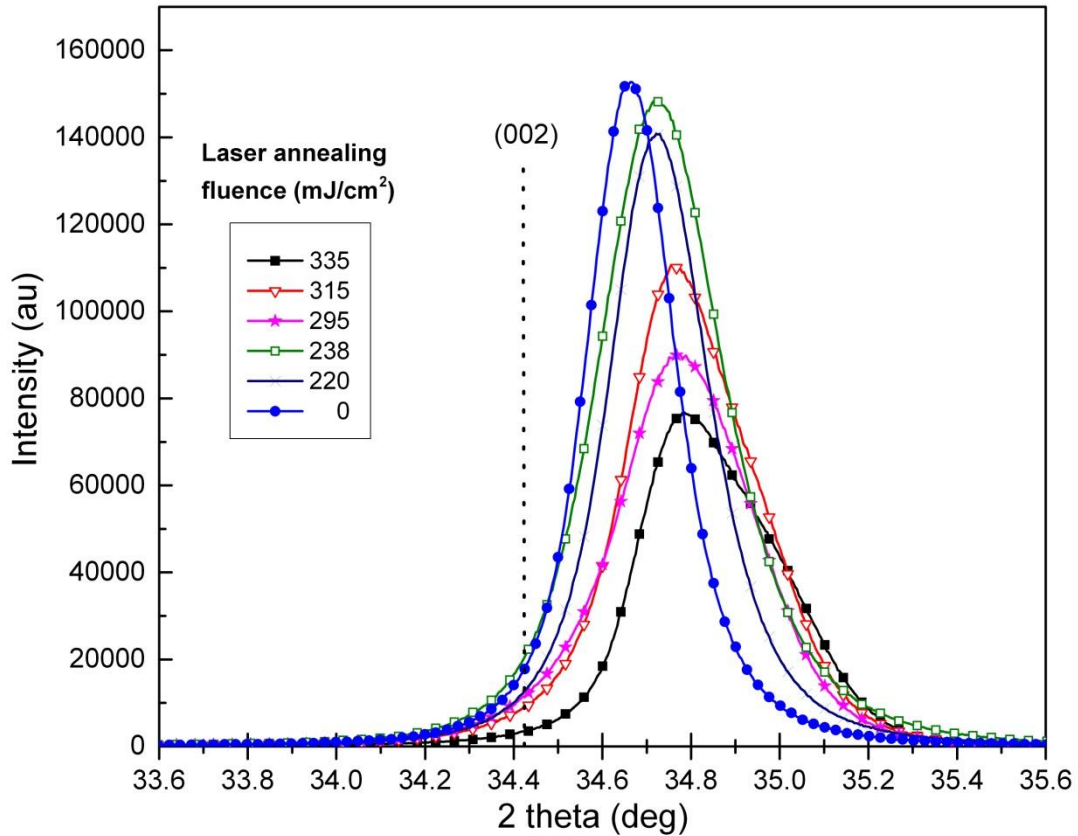


**Figure 5.13:** XRD patterns of ZnO films deposited at 300 °C following by laser anneal at various fluences.

XRD patterns of ZnO films deposited at various substrate temperatures followed by thermal annealing in a furnace at 700 °C for 1 hour are shown in Figure 5.14. For the films deposited at various temperatures as the growth temperature increased, a shift in  $2\theta$  to higher angles occurs, with increasing crystallite domain size (see Table 5.3). Subsequent to the thermal anneal at 700 °C, the peak intensity increased rapidly as a function of the growth temperature up to 300 °C, with a slight shift in  $2\theta$  angle, and an increase the grain domain size. Further increase in growth temperature up to 400 °C results in a significant drop in XRD peak intensity. For comparison, the average grain size of thermal and laser annealed ZnO deposited at various substrate temperatures are listed in Table 5.3. The average domain size as a function of laser processing for films deposited at RT, and 100 °C increased significantly, while decreased dramatically for films grown at 200 °C, 300 °C, and 400 °C.

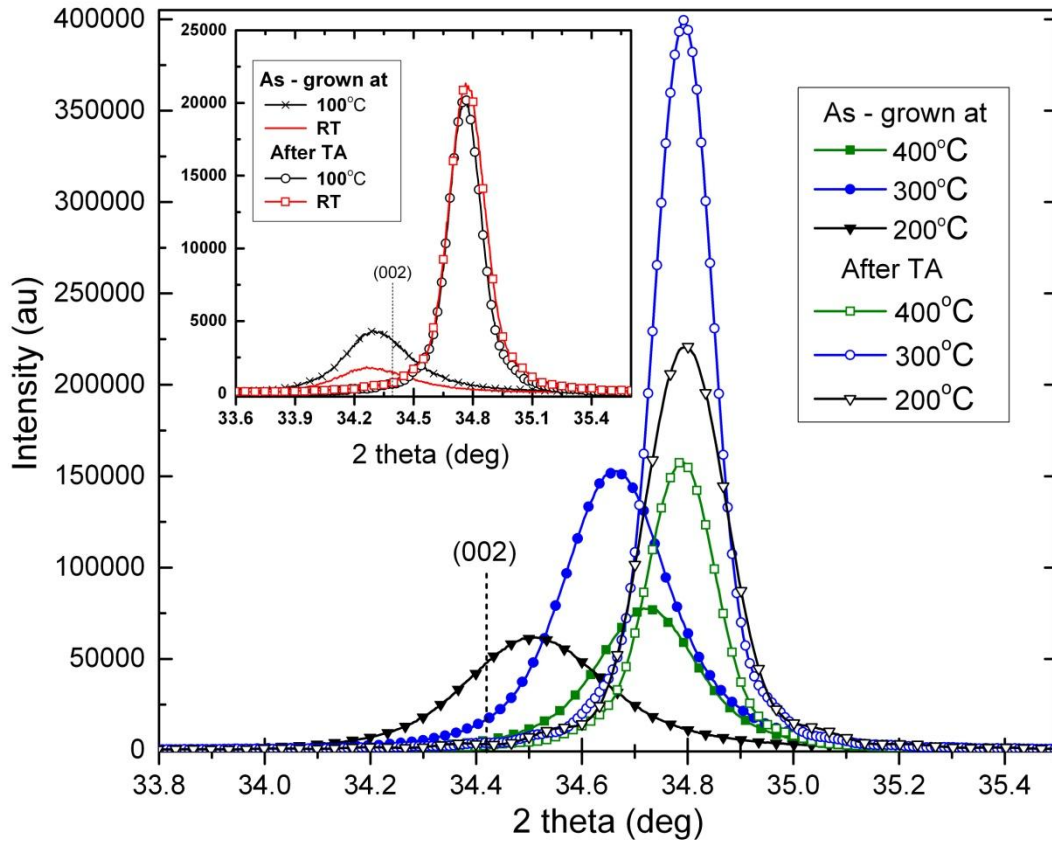


**Figure 5.14:** XRD patterns (thermal annealed at 700 °C for an hour) of ZnO films deposited at various substrate temperatures, showing that the films reach thermodynamic equilibrium after TA. The inset shows XRD patterns of films grown at RT, and 100 °C.

Growth temperature	Average crystal domain size (nm)			
	As-grown	LA at medium fluence	LA at high fluence	TA at 700 °C
Room temperature	19.16	13.47	31.18	37.01
100 °C	21.43	18.01	37.85	41.43
200 °C	25.30	18.00	23.00	45.51
300 °C	35.58	24.30	22.94	64.56
400 °C	38.37	35.60	28.06	55.52

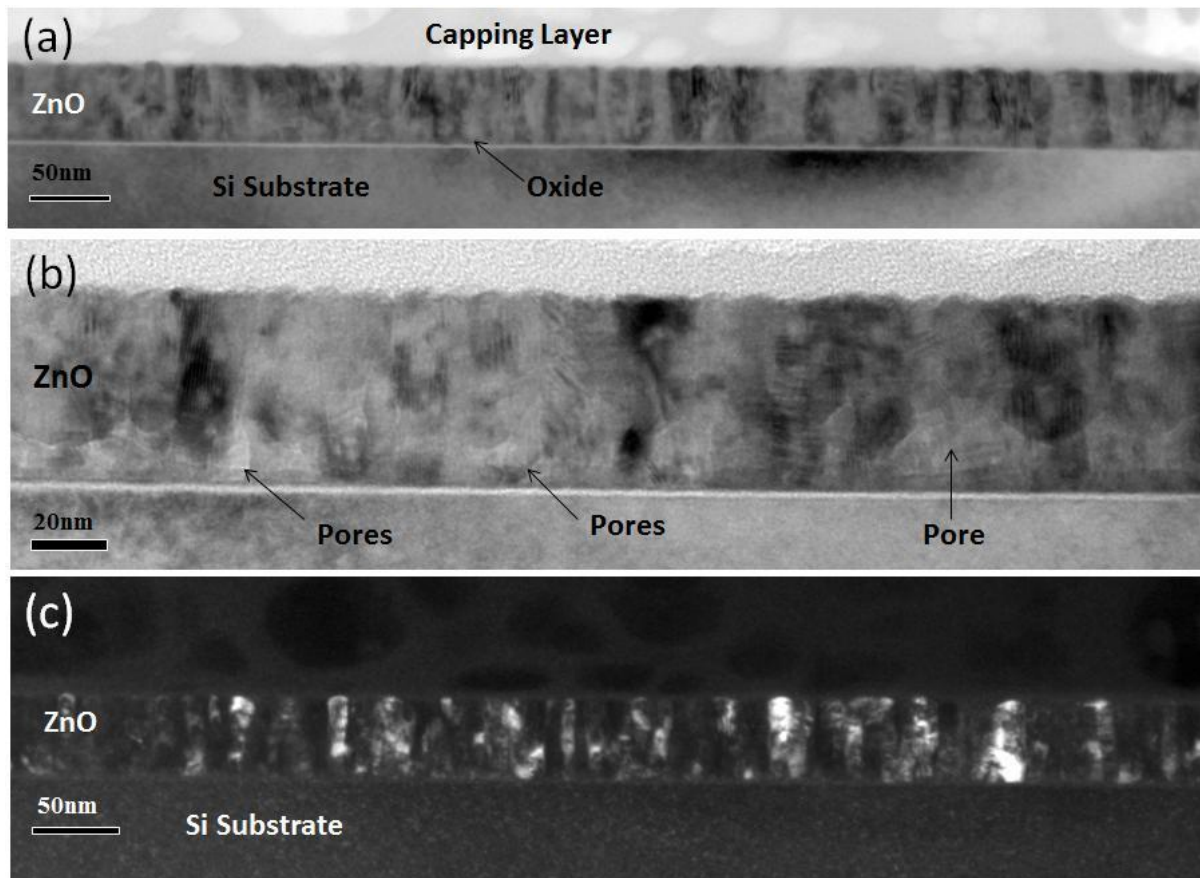
**Table 5.3:** Average grain domain size calculated from XRD patterns of ZnO films deposited at various substrate temperatures following laser anneal at various energy densities with single pulse irradiation, and also following thermal anneal at 700 °C for 1 hour. Films processed with medium fluences (230 – 270 mJ/cm<sup>2</sup>) and high fluences (>285 mJ/cm<sup>2</sup>) exhibit the highest peak of DLE and NBE peaks respectively.

## 5.6 Transmission electron microscopy (TEM) characterisation

Cross sectional transmission electron microscopy (TEM) was carried out to investigate the microstructure of ZnO films deposited by RF magnetron sputtering at various substrate temperatures (from RT to 400 °C), before and after laser treatment. The results presented here are focused on two sets of ZnO films: (i) ZnO deposited at RT, as-deposited film and laser annealed at fluences at 270 mJ/cm<sup>2</sup> and 315 mJ/cm<sup>2</sup> (where the highest intensity of DLE and NBE were observed respectively), as well as thermally annealed sample in a furnace at 700 °C for 1 hour. (ii) ZnO grown at 300 °C, as deposited, and laser annealed at 335 mJ/cm<sup>2</sup> corresponding to highest peak of NBE. The absorption coefficient at 248 nm was calculated by Ellipsometer measurements for ZnO films grown at RT and 300 °C, were found to be about 0.021 nm<sup>-1</sup>, 0.023 nm<sup>-1</sup> respectively, imply that the thickness of UV beam inside the sample about 47.61 nm, 43.47 nm for films deposited at RT and 300 °C respectively.

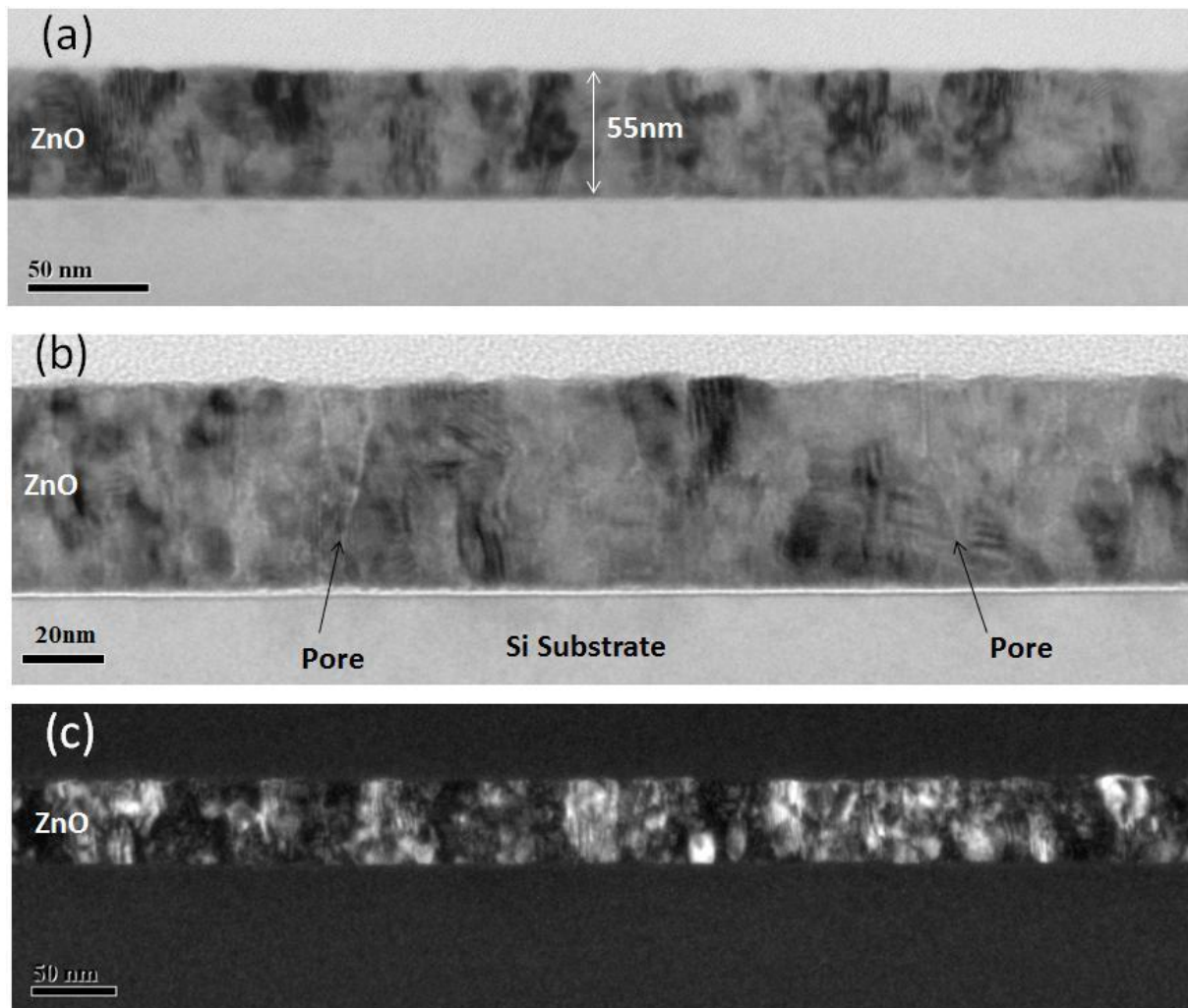
### 5.6.1 Transmission electron microscopy (TEM) of ZnO films grown at room temperature

Figure 5.15, shows cross sectional TEM images of as-deposited ZnO film. The samples exhibit c-axis growth texture. Figure 5.15 (a) is a bright field image of the lower part of the 50 nm of ZnO layer, indicating the film contains coarse pores. Figure 5.15 (b) is the higher magnification image which confirms that the film contains large pores located in the lower part of ZnO layer, and (c) dark field image showing columnar grain microstructure varying from about 8 to 20 nm.



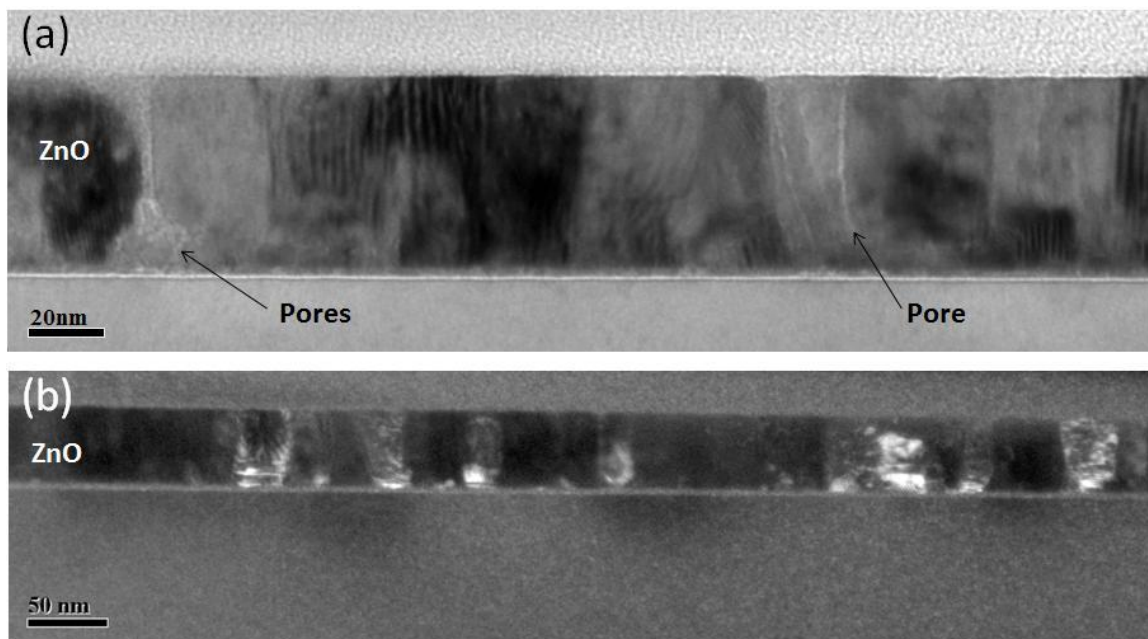
**Figure 5.15:** TEM images for as-deposited ZnO deposited at room temperature, (a) bright field image, (b) bright field image with higher magnification, (c) dark field image.

TEM images of laser annealed ZnO film at  $270 \text{ mJ/cm}^2$  are shown in Figure 5.16. A high magnification defocused image is shown in Figure 5.16 (a) showing a presence of vertical porosity, and removal of the coarse pores observed in the as-deposited film near the lower surface. Figure 5.16 (b) shows the ZnO layer exhibiting a less columnar grain to that of the as-grown film. Figure 5.16 (c) is a dark field image showing an irregular grain morphology of the ZnO layer, with grain size varying from about 13 to 15 nm according to XRD analysis.



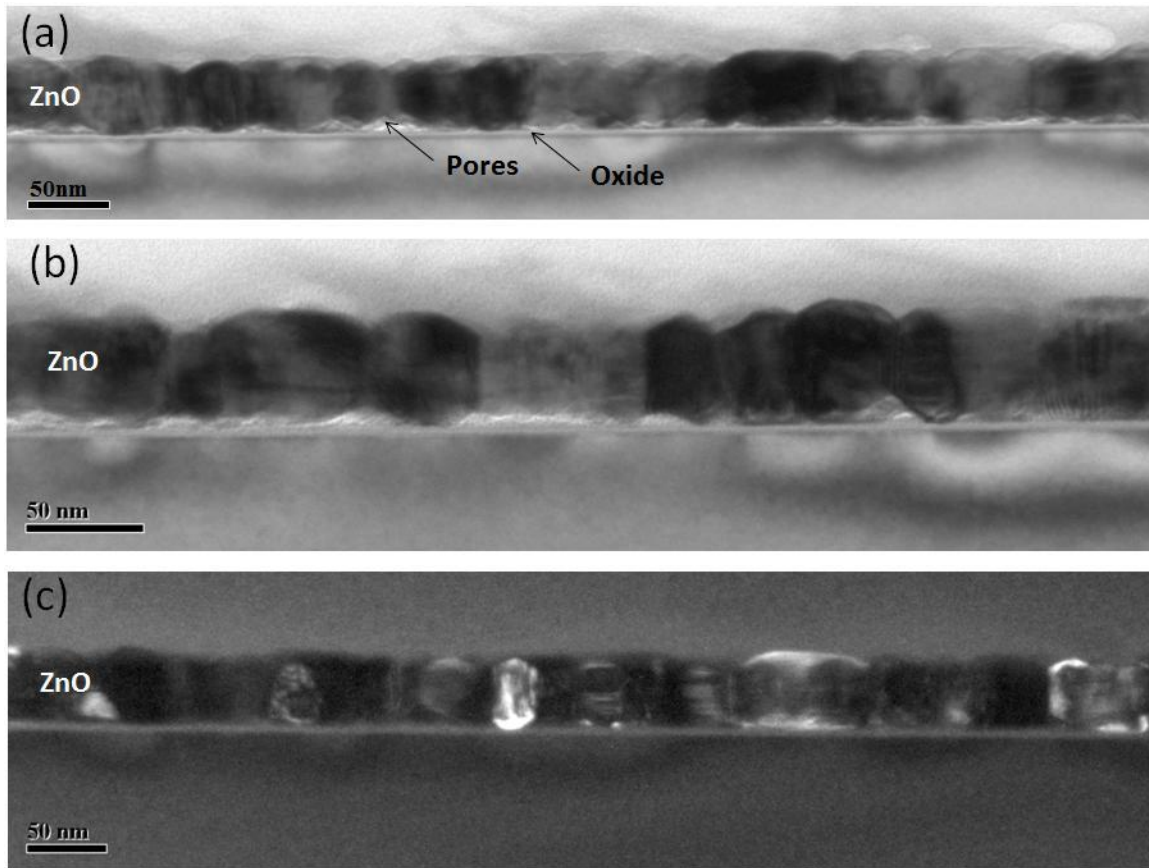
**Figure 5.16:** TEM images of ZnO film deposited at room temperature and laser annealed at  $270 \text{ mJ/cm}^2$ . (a) image of bright field, (b) an image with higher magnification defocus, (c) image of dark field.

Figure 5.17 shows TEM images of a ZnO film laser annealed at  $315 \text{ mJ/cm}^2$ , which is the fluence at which the highest NBE peak was observed by PL spectra. The higher magnification defocused image of Figure 5.17 (a) shows the vertical pore structure of the ZnO layer. Figure 5.17 (b) is a dark field image showing the columnar grain structure, where the grain size is larger than any previous samples, in which approximately 31 nm according to XRD results, also showed that the laser beam penetrate cross the film thickness (with no appearance of bi-layer microstructure seen in thicker film in Chapter 4 Figure 4.17).



**Figure 5.17:** TEM images of laser annealed ZnO deposited at room temperature and laser annealed at  $315 \text{ mJ/cm}^2$ , (a) high magnification defocus image, (b) dark field image showing the effect of high fluence on grain size.

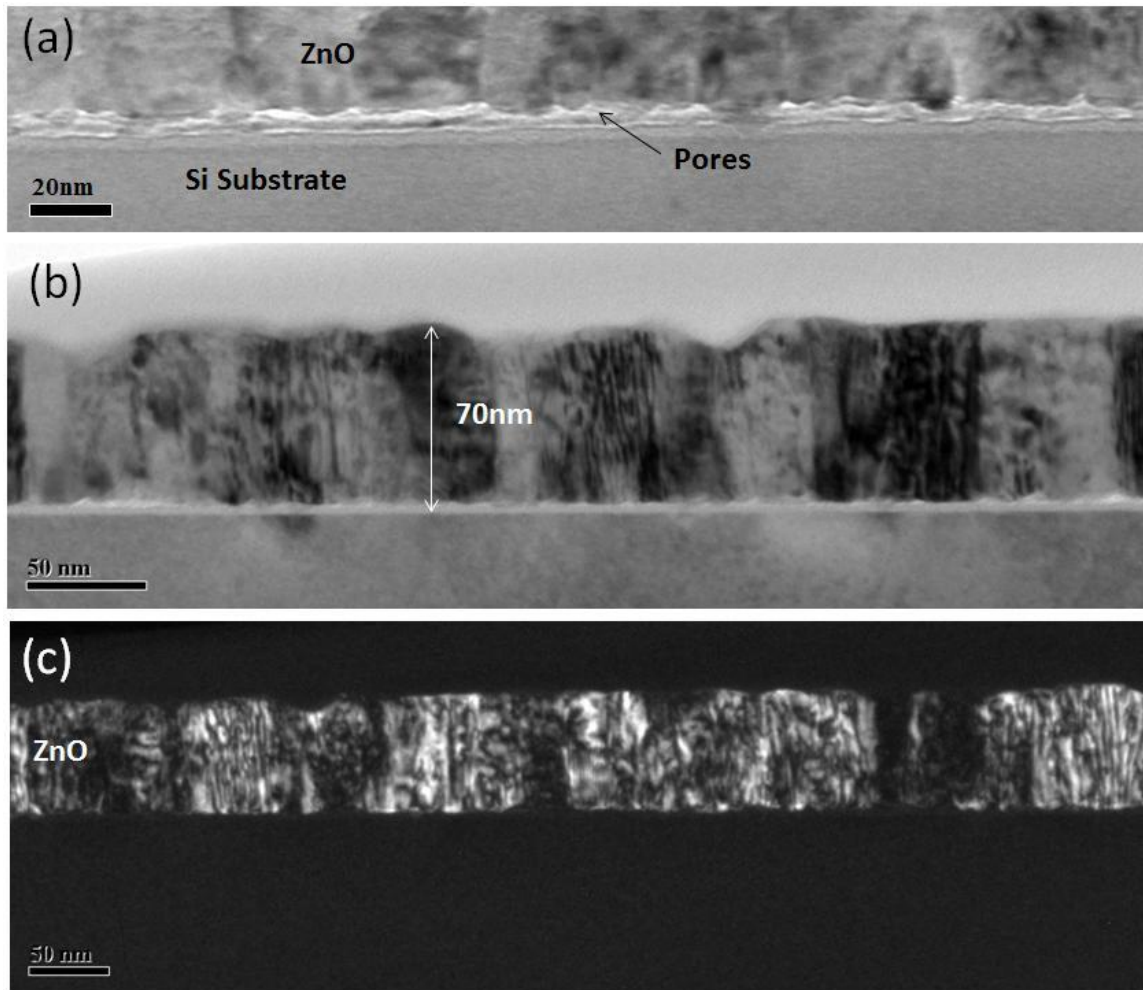
TEM images of thermal annealed at  $700 \text{ }^\circ\text{C}$  ZnO deposited at room temperature are illustrated in Figure 5.18. Figure 5.18 (a) shows a defocused image exhibiting a distribution of irregular pores at the lower surface of ZnO layer. Figure 5.18 (b) shows a clearly visible uneven nature of the upper and lower surface of the ZnO layer, whereas Figure 5.18 (c) shows grained layer with grain size varying from about 30 to 60 nm.



**Figure 5.18:** TEM images of thermal annealed ZnO at 700 °C for 1 hour in air, (a) defocused image with appearance of pores (b) bright field image (c) dark field image showing the nature of grain size.

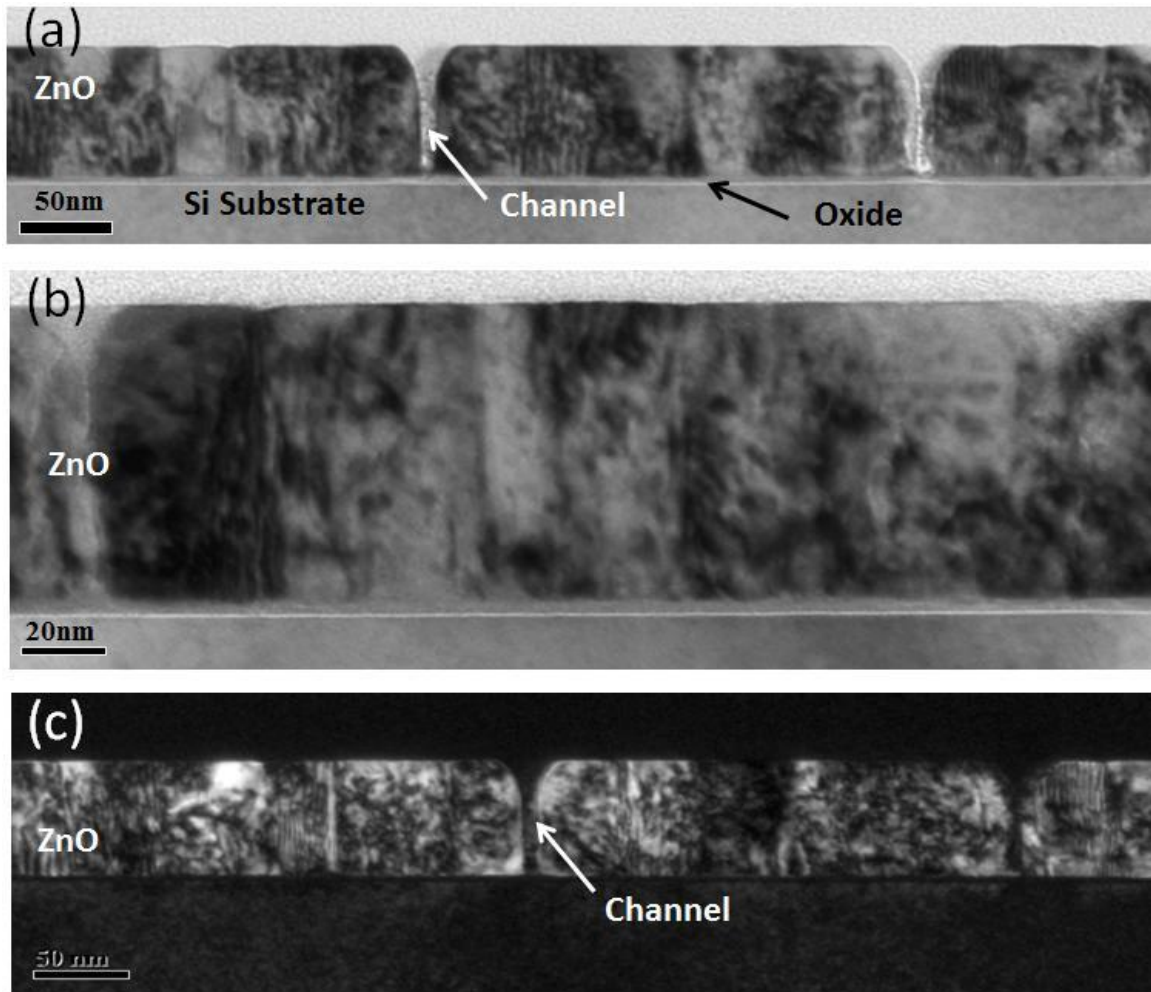
### 5.6.2 Transmission electron microscopy (TEM) of ZnO films grown at 300 °C

Figure 5.19 presents TEM images of as-deposited ZnO grown at 300 °C. Figure 5.19 (a) is a defocus image indicating a high pore density located at the lower surface of ZnO layer, and Figure 5.19 (b) is a bright field image showing the coarse grain morphology of ZnO. In Figure 5.19 (c) the dark field image provides evidence of highly textured nature of ZnO layer with high defect content.



**Figure 5.19:** TEM images of as-grown ZnO film at substrate temperature 300 °C, (a) defocused image (b) bright field image, (c) dark field image.

Figure 5.20 presents the TEM images of ZnO film deposited at 300 °C after laser annealing at 335 mJ/cm<sup>2</sup> with a single pulse. Figure 5.20 (a) is a defocused image showing the appearance of coarse channels in the ZnO film. Figure 5.20 (b) is a defocused image with higher magnification showing an absence of vertical porosity that had developed after laser annealing of ZnO films deposited at room temperature (see Figure 5.17 (a)). Figure 5.20 (c) is a dark field image confirming high defect content.



**Figure 5.20:** TEM images of ZnO deposited at a substrate temperature of 300 °C and after laser annealing at fluence 335 mJ/cm<sup>2</sup> with a single pulse, (a) defocused image (b) defocused image at high magnification (c) dark field image.

Cross sectional TEM images for all of the samples examined provide clear evidence that laser annealing has consistently improved the microstructure properties ZnO films. For samples deposited at room temperature, laser anneal leads to a reduction in coarse pores at the lower surface of ZnO and a reduction of defect density, along with a pronounced increase of grain size. Thermal annealing at 700 °C leads to a high pore content at the lower surface of the film (Figure 5.18 (a)), with a defect content lower than that of the as-deposited sample. However the laser annealed sample at 335 mJ/cm<sup>2</sup> and deposited at 300 °C, exhibits a number of coarse channels, and high defect content (Figure 5.20 (a)).

## 5.7 Discussion

The effect of post-deposition annealing on the PL performance as well as on the microstructure properties of RF magnetron sputtered ZnO films grown at various RF powers and various substrate temperatures was studied. In terms of ZnO films grown at various RF powers using PL results as a measure of film quality, after employing laser processing of ZnO films deposited at room temperature demonstrate that the RF power affected the film structure. As the RF power was increased, the film quality deteriorated. Hence low RF power and laser annealing is required to produce higher quality ZnO films when deposited without any intentional substrate heating an excessive RF power leads to faster sputter causing severe surface damage [141, 142].

PL of laser annealed films deposited at lower oxygen concentration (5% O<sub>2</sub> in Ar) showed the DLE peak at medium fluences. For comparison, the DLE peak was not observed for films deposited at an oxygen flow rate of 28 sccm by high target utilisation sputtering (HiTUS) as we reported in Chapter 4 which is consistent with the lack of excess oxygen related defects, while laser annealing at high fluence results in evolution of a strong NBE peak, which decreased as the RF power increased.

For films deposited at different substrate temperatures (20% O<sub>2</sub> in Ar, 50 W), the as-deposited samples show an increase of average grain domain size from 19.16 nm to 38.37 nm as the growth temperature is increased from RT to 400 °C, which is similar to that reported in reference [143]. Also, the (002) peak height increased and shifted to higher diffraction angles as the substrate temperature increased up to 300 °C. A further increase of growth temperature resulted in a decrease of the (002) peak, which is attributed to the high temperature breaking the bonding of Zn-O and re-evaporating the deposited film, instead of allowing the atoms to move to their stable sites [138]. This can be linked to the result that shows the average grain domain size after thermal annealing at 700 °C increasing to 64.56 nm as the growth temperature is increased up to 300 °C while for films deposited at 400 °C, the grain domain size increase is less

significant, to 55.52 nm, as shown in Table 5.3. Also, in terms of PL characterisation, the thermally annealed samples at 700 °C deposited at substrate temperature of 300 °C and 400 °C exhibit a subsequent increase of DLE peak with a significant shift to orange/red emission, and a slight reduction of NBE peak. The increase of green/yellow DLE emission (peaking at about 570 nm) following thermal annealing for samples with growth temperatures up to 200 °C indicates an increase of radiative defects as the film growth temperature is increased, which is likely to be related to  $V_{zn}$  defects, because Zn vacancies are formed at a lower energy [123]. With increasing the film growth temperature, up to 400 °C, there is a shift to orange/red DLE emission centred at about 640 nm. This indicates a change of the dominant nature of point defects from  $V_{zn}$  to excess oxygen related defects.

PL from the laser annealed samples demonstrates encouraging results in terms of the effect of laser processing of films deposited at low temperatures. Samples deposited on an unheated substrates show the development of a strong UV NBE emission peak at high laser fluences, with the defect related DLE completely suppressed. The NBE intensity was greatly influenced by the substrate temperature at deposition. As the growth temperature was increased beyond ambient, the intensity of the resultant NBE peak following laser annealing, decreased as a function laser fluence. This reduction in NBE emission can be attributed to effects related to improved films fabricated at higher deposition temperatures – resulting in denser films [144]. Also, at higher deposition temperature the defective layer between the film and the substrate becomes slightly thicker. This affects subsequent structural and morphology changes as a result of the laser processing. A decrease in deposition rate as the substrate temperature increased was observed, from  $8.4 \text{ \AA min}^{-1}$  to  $6.7 \text{ \AA min}^{-1}$  at substrate temperatures 100 °C and 300 °C respectively. This is attributed to the vapour pressure of Zn increasing with increasing temperature, leading to re-evaporation of zinc atoms before oxidation [55].

Further structural investigation confirmed deterioration of the ZnO structure deposited at a substrate temperature of 300 °C as a function of laser processing, as observed by

XRD and TEM studies, in which the grain domain size was found to decrease from about 35.58 nm to 22.94 nm for as-grown and laser annealed samples at high fluences ( $335\text{mJ}/\text{cm}^2$ ) respectively. Dark field TEM images demonstrate a high content of defects for both samples, with coarse channels across the film surface affecting surface morphology. In contrast, laser annealed ZnO films grown at room temperature showed a pronounced grain re-growth with a reduction of defect content, and an improved film quality. Moreover, XRD showed that in RF magnetron sputtered films the development of the (002) peak develops as the laser fluence is increased, (similar to the thermal annealed samples). In contrast, the HiTUS films demonstrated a concurrent shift together with a development of the (002) peak, as the laser fluence increased, potentially indicating a slight tilt of the crystal orientation. However, room temperature HiTUS ZnO films showed slightly larger grain domain size pre and post laser processing (24.60 nm and 37.56 nm respectively) compared to RF sputtered ZnO film grown at RT. Results give a clear indication that laser processing is a powerful tool to improve the microstructure properties of ZnO film grown on unheated substrates rather than deposited at high temperatures.

## Chapter 6

### Electrical Characterisation of ZnO and IGZO

---

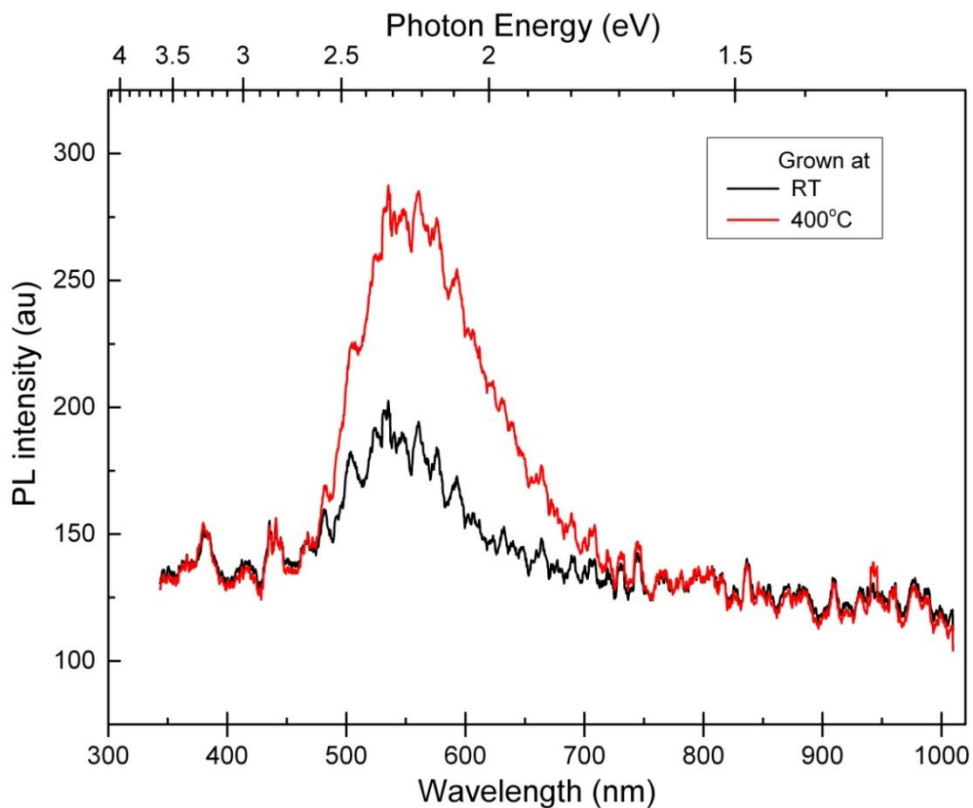
#### 6.1 Introduction

The work presented in this chapter concerns the influence of laser processing on the microstructure and electrical properties of ZnO and IGZO films deposited on top of 200nm thick dielectric layers of silicon dioxide on silicon substrates. The aim of this work was to investigate the optimal conditions of deposition and annealing for semiconductor layers in TFTs. The use of SiO<sub>2</sub>/Si substrates allows for comparative thermal and laser treatments to be studied (as well as comparing with the films deposited onto Si), and also the measurement of electrical conductivity of the films. The effect of laser and thermal annealing on the electrical properties of ZnO layers and on IGZO-TFTs was studied. Section 6.2 presents the microstructure and electrical characterisation of ZnO films grown at room temperature and at 400 °C, with the same deposition conditions used in Chapter 5 (50 W, 20% O<sub>2</sub> in Ar, 2 mTorr, 60 nm), and the results are compared with the microstructure properties of ZnO deposited on silicon substrates. Section 6.3 presents electrical characterisation of laser annealed IGZO thin films deposited at various conditions from targets with two different stoichiometries (2:2:1), and (1:1:1). Section 6.4 presents results of laser and thermal annealing of IGZO films used as the channel layers in TFT test devices, including an examination of the effect of processing pre and post IGZO layer patterning.

## 6.2 Microstructure and electrical properties characterisation of ZnO films deposited on silicon dioxide substrates

### 6.2.1 PL characterisation of thermal annealed ZnO films deposited at RT and 400 °C.

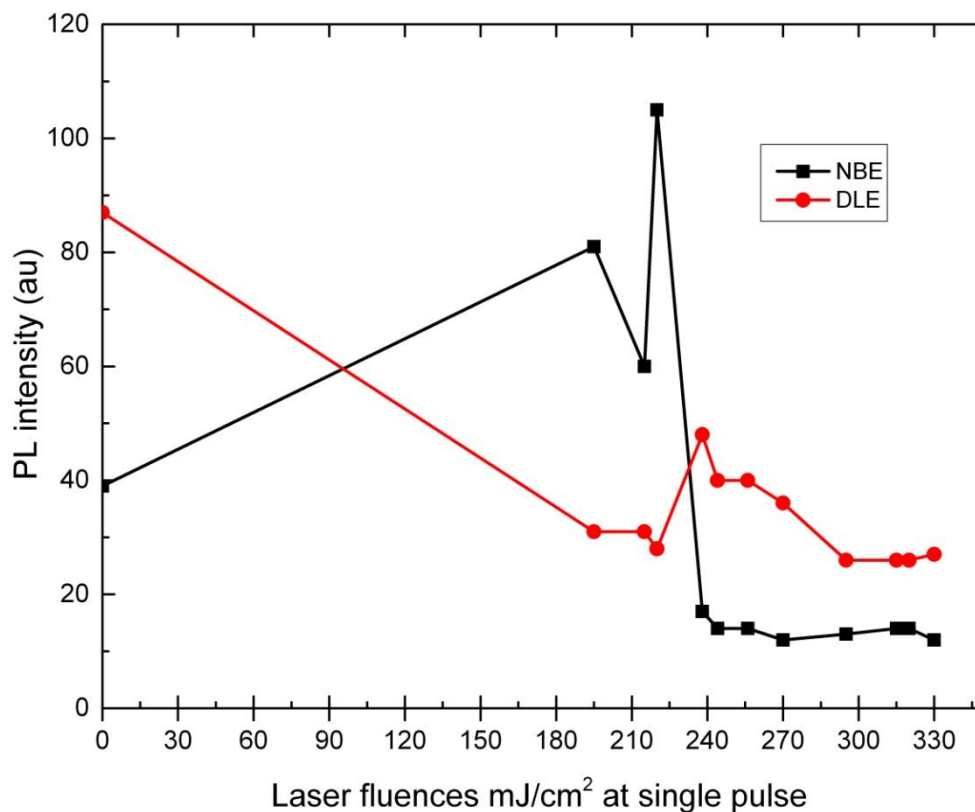
The crystal structure of ZnO films is highly affected by the surface crystallinity and morphology of the substrate [145, 146]. Figure 6.1 shows the PL spectra of films thermally annealed at 700 °C for 1 hour in air, following deposition on silicon dioxide substrates at RT and 400 °C. The results show a weak appearance of an NBE peak for both films, with significant evolution of a broad visible DLE emission (450-750 nm) green/yellow emission, peaking at about 560 nm. An increase in intensity for films deposited at 400 °C is shown, indicating an increase of radiative recombination related defects.



**Figure 6.1:** PL spectra of thermal annealed (700 °C for 1 hour in air) ZnO films grown onto silicon dioxide substrates at RT and 400 °C.

### **6.2.2 PL characterisation of laser annealed ZnO films deposited at RT, and 400 °C**

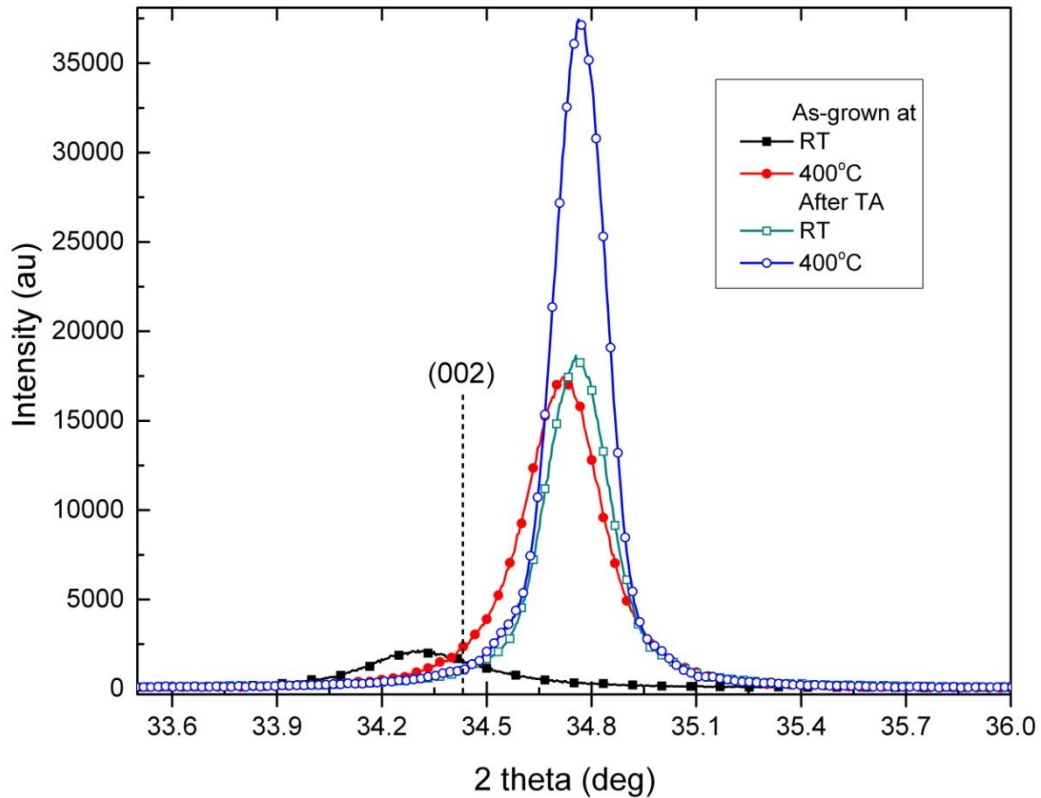
Figure 6.2 shows the NBE and DLE peak intensity of ZnO films grown on an insulating silicon dioxide covered silicon ( $\text{SiO}_2/\text{Si}$ ) substrate at 400 °C (50 W, 20%  $\text{O}_2$  in Ar), as extracted from the PL spectra. The results for the films deposited onto  $\text{SiO}_2$  on Si were very different to those for films deposited directly onto Si. Here, no PL was observed for pre and post laser anneal of ZnO films deposited at RT, while a slight development of NBE and DLE peaks is observed for films grown at 400 °C as a function of laser anneal. For the as deposited film the intensity of DLE is higher than NBE, and as the laser energy density increased up to 220  $\text{mJ}/\text{cm}^2$ , the intensity of NBE peak increased significantly with a reduction in the DLE peak. Further increase of laser fluence causes a decrease in the NBE peak. Therefore, post laser annealing films deposited at 400 °C exhibit better PL spectra than films grown at RT. This contrasts significantly with the results for films deposited at the same conditions on silicon substrates, where the intensity of NBE post laser treatment decreased dramatically as the deposition temperature increased. This difference when the films are on silicon substrates or silicon dioxide coated silicon ( $\text{SiO}_2/\text{Si}$ ) substrates is probably due to thermal insulation provided by the silicon dioxide. In the absence of this thermal insulation the silicon substrate acts as a heat sink.



**Figure 6.2:** Evolution of NBE and DLE peaks of Laser annealed ZnO deposited on SiO<sub>2</sub> substrate at 400 °C.

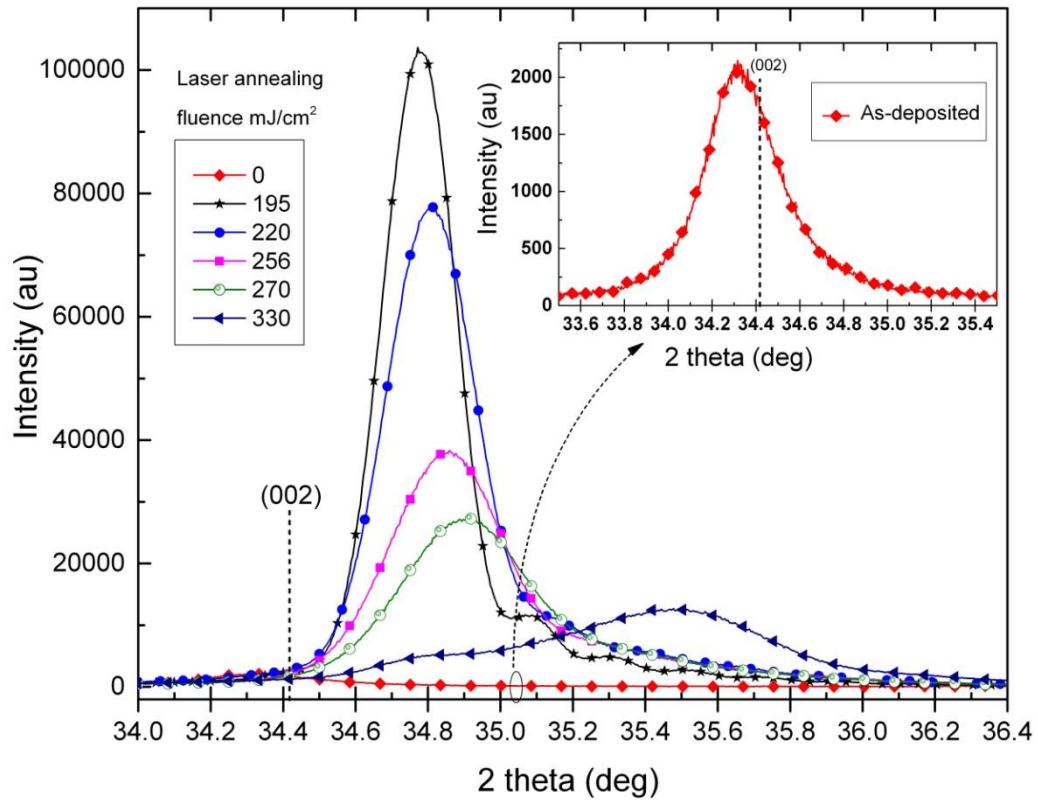
### 6.2.3 X- ray diffraction (XRD) characterisation

Figure 6.3 shows XRD patterns of thermally annealed samples at 700 °C with a dwell time of 1 hour in air for ZnO films deposited on SiO<sub>2</sub> substrates at RT, and 400 °C. For films deposited at RT, the thermal anneal causes a transition from compressive to tensile stress as observed by a shift to higher 2θ angles for the (002) peak and a concurrent crystallinity improvement as observed by a significant increase of the (002) peak height. The films grown at 400 °C exhibit a higher intensity in the (002) peak with a shift to higher angles compared with films deposited at RT, and a prominent increase in the (002) peak with slight shift to higher angle observed after annealing.



**Figure 6.3:** XRD patterns of as deposited and thermal annealed ZnO deposited on silicon dioxide substrates at RT and 400 °C.

Figures 6.4 and 6.5 show XRD patterns of laser annealed samples at various fluences with a single pulse for ZnO deposited on silicon dioxide at RT and 400 °C respectively. Laser processing leads to a shift of the c-axis (002) peak to the higher angles as the fluence is increased up to medium fluence (195 – 220 mJ/cm<sup>2</sup>) as well as an increase of peak intensity. Further increase of the laser fluence up to high fluences (270 – 330 mJ/cm<sup>2</sup>) causes a decrease of the peak intensity. Although no PL spectra was observed for films grown at RT, the XRD spectra indicate that laser annealing influences the microstructure of the ZnO films, and enlarges the crystal size.



**Figure 6.4:** XRD patterns of laser annealed ZnO films deposited on silicon dioxide substrate at RT. The inset shows XRD spectra of as-deposited film.

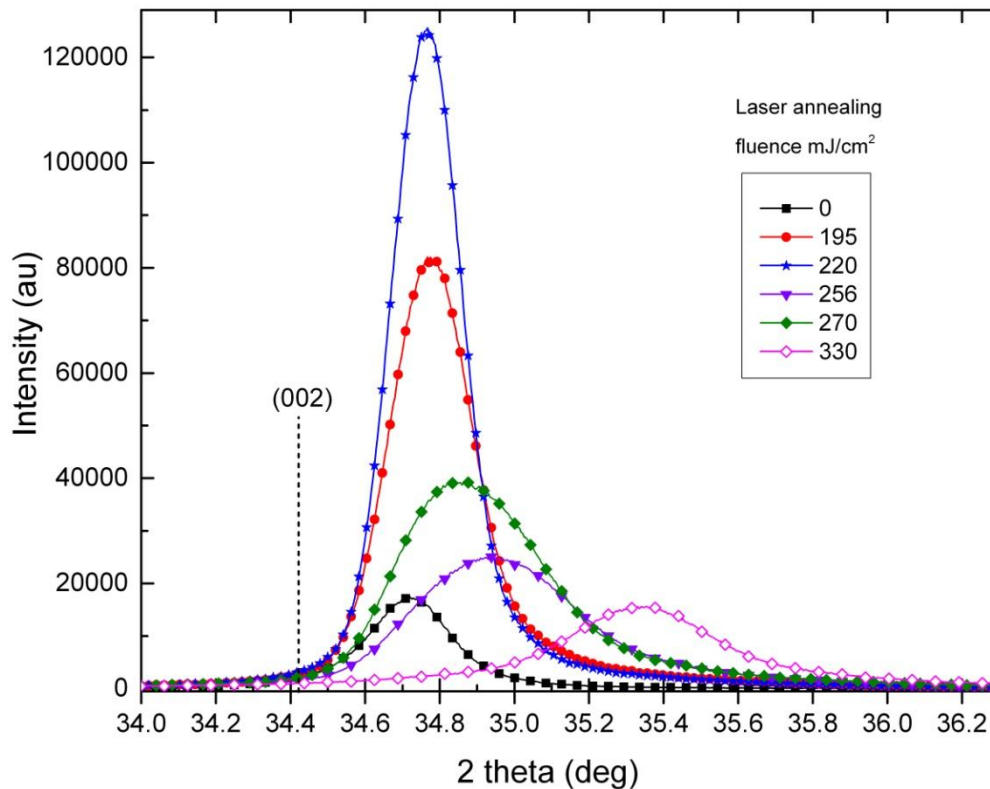


**Figure 6.5:** XRD patterns of laser annealed ZnO films deposited on SiO<sub>2</sub> substrate at 400 °C.

Also, it was found that for films deposited at 400 °C, the highest (002) peak observed for laser energy density of 220 mJ/cm<sup>2</sup> is consistent with the PL results shown in Figure 6.2 in which the highest NBE peak was observed at 220 mJ/cm<sup>2</sup>.

Table 6.1 illustrates a comparison of average grain domain size of ZnO grown on Si and SiO<sub>2</sub> substrates at RT and 400 °C. The average grain domain size for as-deposited films grown at RT from both wafers is similar at approximately 20 nm, in which post to the laser annealing increased to 31 nm for films on Si and to 34 nm for films on SiO<sub>2</sub>.

For ZnO films grown at a substrate temperature of 400 °C on Si and SiO<sub>2</sub> substrates, For as-deposited films the larger average grain domain size is achieved on the silicon substrate, this decreased after laser annealing. However, the average grain domain size increased slightly after laser processing for films grown on SiO<sub>2</sub> substrates at medium laser energy density. Further increase of the laser fluence caused a decrease of average

grain domain size. Hence laser anneal improved the grain domain size as a function of laser annealing for films deposited at 400 °C on SiO<sub>2</sub> substrates, but decreased when grown on silicon substrates. Thermal anneal at 700 °C result in larger average grain domain size.

Average grain domain size (nm)					
Substrate	Temperature	As-grown	LA at medium fluence	LA at high fluence	TA at 700°C
Si	RT	19.16	13.47	31.18	37.01
SiO <sub>2</sub>	RT	21.18	34.37	10.85	38.32
Si	400 °C	38.37	35.60	28.06	55.52
SiO <sub>2</sub>	400 °C	33.21	38.34	17.35	45.31

**Table 6.1:** Comparison of average grain domain size calculated from XRD patterns of ZnO films deposited on Si and SiO<sub>2</sub> substrates at RT and 400 °C, following laser anneal at various energy densities with single pulse irradiation (medium fluence (210-270 mJ/cm<sup>2</sup>), high fluence (>290 mJ/cm<sup>2</sup>)), and thermal anneal at 700 °C for 1 hour.

#### 6.2.4 Four point probe measurements (4PP)

Table 6.2 illustrates the comparison in sheet resistance of laser annealed films deposited at RT and 400 °C on silicon dioxide covered silicon (SiO<sub>2</sub>/Si) substrates. As-deposited films and films processed at fluence less than 295 mJ/cm<sup>2</sup> were highly resistive and not measurable using the four point probe system (i.e. they had sheet resistance > 5 MΩ/sq). However, XRD shows that the conductive films which had been laser annealed at high fluence exhibit an average grain size that is smaller than for films processed at low fluences where the film was highly resistive. The drop in sheet resistance of laser irradiated films could be ascribed to the phenomenon that arises when sufficient energy of photons breaks Zn-O bonds (dissociation) causing Zn-rich or oxygen deficient surface by evaporation of oxygen atoms resulting in oxygen vacancy (V<sub>o</sub>) or zinc interstitial (Z<sub>ni</sub>) domination as a donor [53, 147]. Excimer laser annealing

contributes to an increase in the carrier density of the film [73]. Sheet resistance as a function of thermal anneal at 700 °C for 1 hour for films deposited at RT was found to be less than that grown at 400 °C, with values being  $5976 \pm 150 \text{ } \Omega/\text{sq}$  and  $276241 \pm 200 \text{ } \Omega/\text{sq}$  respectively.

Sheet resistance $\Omega/\text{sq}$			
Growth temperature	295 mJ/cm <sup>2</sup>	315 mJ/cm <sup>2</sup>	295 mJ/cm <sup>2</sup>
RT	943 $\pm$ 100	864 $\pm$ 80	1744 $\pm$ 90
400 °C	492 $\pm$ 90	860 $\pm$ 75	595 $\pm$ 100

**Table 6.2:** Sheet resistance of laser annealed 60nm thick of ZnO films deposited at 50 W, 20% O<sub>2</sub> in Ar, 2 mTorr, on SiO<sub>2</sub> substrate at RT and 400 °C.

### 6.3 Electrical properties of laser annealed IGZO thin films

The main purpose of this section is to study the effect of laser annealing on electrical properties of multicomponent oxide semiconductor IGZO thin films, deposited under various conditions without intentional substrate heating, for application as an active layer in TFTs. When sputtering IGZO, deposition conditions influence the deposition rate which reflects the nature of the sputtering mechanism of material particles and plasma arrivals on the substrate surface creating a thin film. For example, in sputtered IGZO, a high deposition rate results in a lack of zinc content [148], because ZnO has a low deposition rate, while gallium and indium have high deposition rates, hence the latter cations will compensate the zinc deficiency [149].

#### 6.3.1 Electrical properties of laser annealed IGZO (2:2:1) and (1:1:1) films

Initially, three wafers of IGZO were deposited on silicon dioxide covered silicon (SiO<sub>2</sub>/Si) at RF power 50 W, oxygen concentration 5% O<sub>2</sub> in Ar, 50 nm thick, and various deposition pressures (2, 5, 10 mTorr) without intentional substrate heating. The

films were then laser annealed as explained in Chapter 3, to examine the optimal growth pressure in terms of resistivity. Figure 6.6 shows the sheet resistance as determined by the four point probe technique. The as-deposited films and films treated at fluences less than  $75 \text{ mJ/cm}^2$  were not measurable (i.e. films too resistive). However, when treated at fluence  $\geq 75 \text{ mJ/cm}^2$  with a single pulse a dramatic drop in sheet resistance is achieved for all films. The lowest sheet resistance was observed for a film grown at 2 mTorr and processed at laser fluence of  $125 \text{ mJ/cm}^2$  ( $1064 \pm 65 \text{ } \Omega/\text{sq}$ ). Increase in laser energy density beyond the  $150 \text{ mJ/cm}^2$  shown in figures causes a significant increase in sheet resistance for all films, which is attributed to visible surface damage of the films.

Hence, films grown at low deposition pressure of 2 mTorr exhibit the lowest sheet resistance as a function of laser annealing. As the deposition pressure increased from 2 to 10 mTorr, the deposition rate decreased from  $4.47 \text{ nm/min}$  to  $1.3 \text{ nm/min}$ , which can be attributed to the low pressure increasing the mean free path of the sputtered species, and hence the sputtered species arrive to the substrate surface with enough surface mobility creating a dense and compact film with low resistivity [92, 150]. Conversely, when the deposition pressure is increased, the surface of the target will oxidize leading to increased emission of secondary electrons increasing the number of collisions resulting in condensation of sputtered particles on the substrate with low energy, forming a less compact film with an increased resistivity [92].

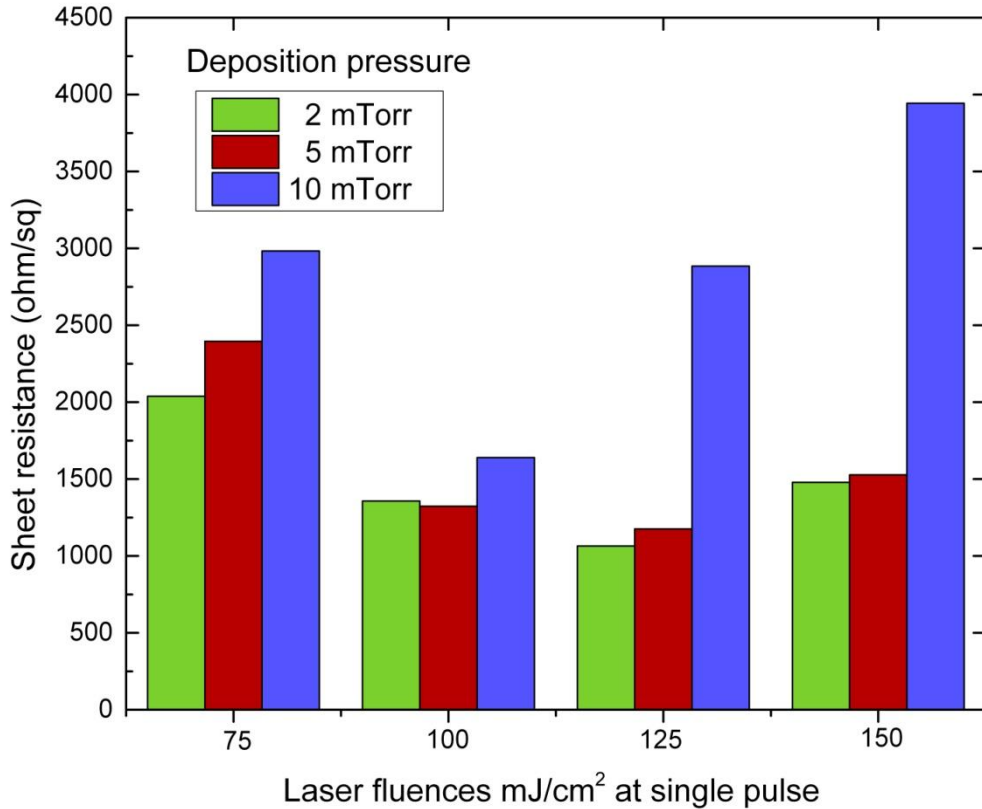


**Figure 6.6:** Sheet resistance of laser annealed IGZO (2:2:1) films deposited at 50 W, 5%, O<sub>2</sub> in Ar, 50 nm, at various deposition pressures (2, 5 and 10 mTorr).

Figure 6.7, shows sheet resistance as a function of laser annealing for single pulse treatment of IGZO thin films deposited at various oxygen concentration (2%, 5% and 10% O<sub>2</sub> in Ar), 50 nm, with RF power of 100 W and deposition pressure 2 mTorr. Laser annealing causes a dramatic drop in sheet resistance for all films processed at laser energy density from 75 to 150 mJ/cm<sup>2</sup>. The film grown at low oxygen concentration of 2% O<sub>2</sub> in Ar exhibits a relatively lower sheet resistance compared with the films deposited at 5 and 10% O<sub>2</sub> in Ar, which relates to the oxygen deficiency leading to enhanced conductivity [47]. When films are grown at low oxygen content, oxygen vacancies form shallow electron donor levels near the conduction band (CB) which are ionized at room temperature, creating free electrons [151]. As the oxygen content is increased during sputtering, oxygen atoms will start filling the oxygen vacancies forming a film close to stoichiometry with high resistivity [47, 131]. Also, the increase of sheet resistance could be linked to re-sputtering that could occur by bombardment of

highly energetic oxygen ions forming more defects. Further increase of laser fluence caused a significant increase in sheet resistance coincident with visible damage of film surface.

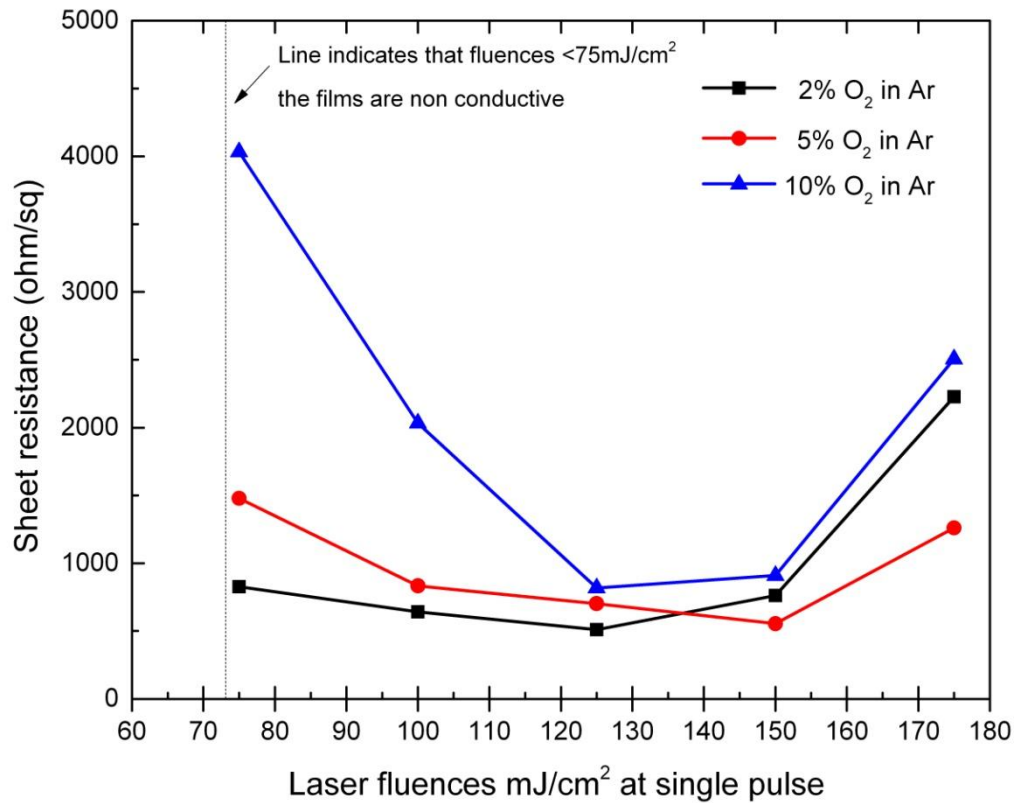


**Figure 6.7:** Sheet resistance of laser annealed IGZO (2:2:1) films deposited at 100 W, 2 mTorr, 50 nm, at various oxygen deposition concentrations of 2, 5, 10% O<sub>2</sub> in Ar.

Figure 6.8 shows the influence of sputtering RF power on the electrical properties of IGZO (2:2:1) films deposited at 2% O<sub>2</sub> in Ar, and 5% O<sub>2</sub> in Ar respectively. The RF powers tested were 50 W and 100 W while the post deposition treatment was laser annealing with a single pulse in air. In both cases an increase of RF power contributes to a significant drop in sheet resistance which would be attributed to the effect of more particles being sputtered from the target (i.e. growth rate increasing), and that indium has a higher sputtering rate than zinc [148] which in this case could lead to an increase of indium content in particles contributing to the film being deposited and resulting in a lower sheet resistance. It could be also linked to oxygen deficiency of sputtered

particles contributing to the film being deposited, where at high RF powers more sputtered species are struck away from the target, leading to insufficient amount of oxygen used to oxidize particles and the target [152].

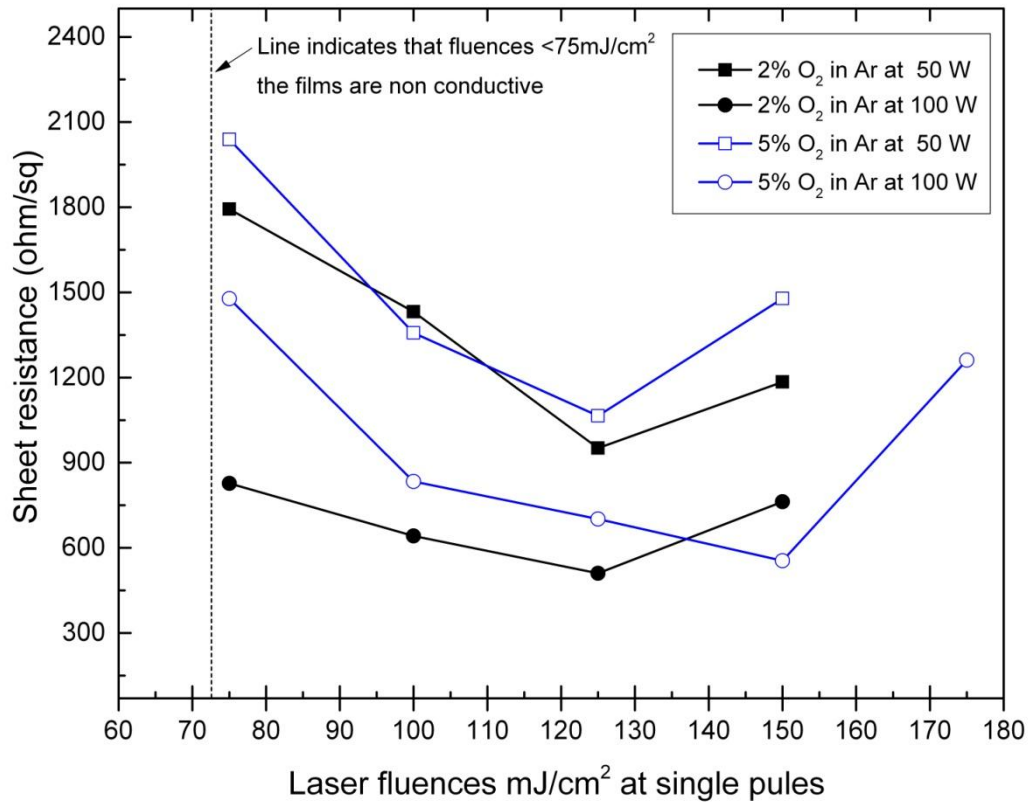


**Figure 6.8:** Sheet resistance of laser annealed IGZO (2:2:1) films deposited at 2, and 5% O<sub>2</sub> in Ar, 2 mTorr, 50 nm, at various RF powers (50 W and 100 W).

A similar trend was observed for laser processed films deposited from a target with a stoichiometry of (1:1:1) at various RF powers and oxygen concentrations.

Figure 6.9 illustrates sheet resistance comparison between films grown from two different stoichiometries of (2:2:1) and (1:1:1) deposited under the same growth conditions of 2% O<sub>2</sub> in Ar, 2 mTorr, RT, and at 50 or 100 W RF power. Results show that films deposited from the (1:1:1) target demonstrate higher sheet resistance than films from (2:2:1) target, which is associated with higher indium content.

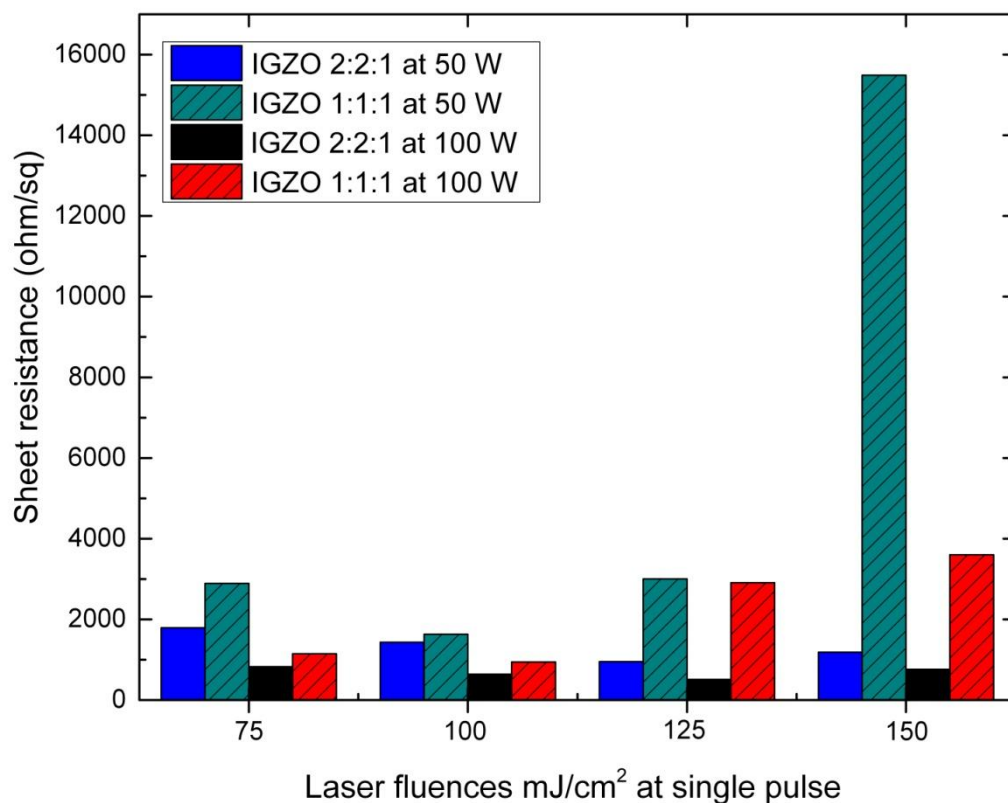


**Figure 6.9:** Sheet resistance of laser annealed IGZO (2:2:1), and (1:1:1) grown at 2% O<sub>2</sub> in Ar, 50 W and 50 nm.

As-deposited films at various deposition parameters, and target compositions were highly resistive (i.e. they had sheet resistance >5 MΩ/sq) for all deposition conditions examined. Laser annealing resulted in a significant reduction in sheet resistance. However, the effect of laser processing on electrical properties is dependant on the deposition conditions and the compositions of the films.

### 6.3.2 Hall Effect characterisation

Figure 6.10 shows the electrical characteristics as determined via room temperature Hall Effect measurement of the laser processed IGZO (1:1:1) thin films (50 W RF power, 2% O<sub>2</sub> in Ar, 50 nm) as a function of laser fluence. The untreated film and also the ones irradiated at laser fluences of 25 mJ/cm<sup>2</sup> and 50 mJ/cm<sup>2</sup> were too resistive to be measured, consistent with the four point probe measurements. At higher fluences of 75 mJ/cm<sup>2</sup> and 100 mJ/cm<sup>2</sup>, results were obtained indicating an increase in Hall

Mobility with increasing fluence - from  $11.1 \text{ cm}^2/\text{Vs}$  to  $13.9 \text{ cm}^2/\text{Vs}$ . At  $175 \text{ mJ}/\text{cm}^2$  the mobility dropped to  $1.67 \text{ cm}^2/\text{Vs}$ , which again coincides with visible surface damage to the films. The corresponding values of resistivity determined via Hall Effect measurement decreased from  $5.92 \times 10^{-2}$  to  $9.7 \times 10^{-3} \text{ } \Omega \text{ cm}$  with fluence increasing from 75 to  $125 \text{ mJ}/\text{cm}^2$ , due to a steady increase in carrier concentration, dropping at higher fluences. In all cases, the thermally annealed samples were not measurable due to their high resistance, but were suitable as the semiconducting channel layer in TFT fabrication, the results of which are described in section 6.4. Similarly, for TFT channel layer fabrication, the laser annealing fluences that produced functional TFT test devices were the lower fluence/higher resistance films processed at  $\leq 75 \text{ mJ}/\text{cm}^2$ .

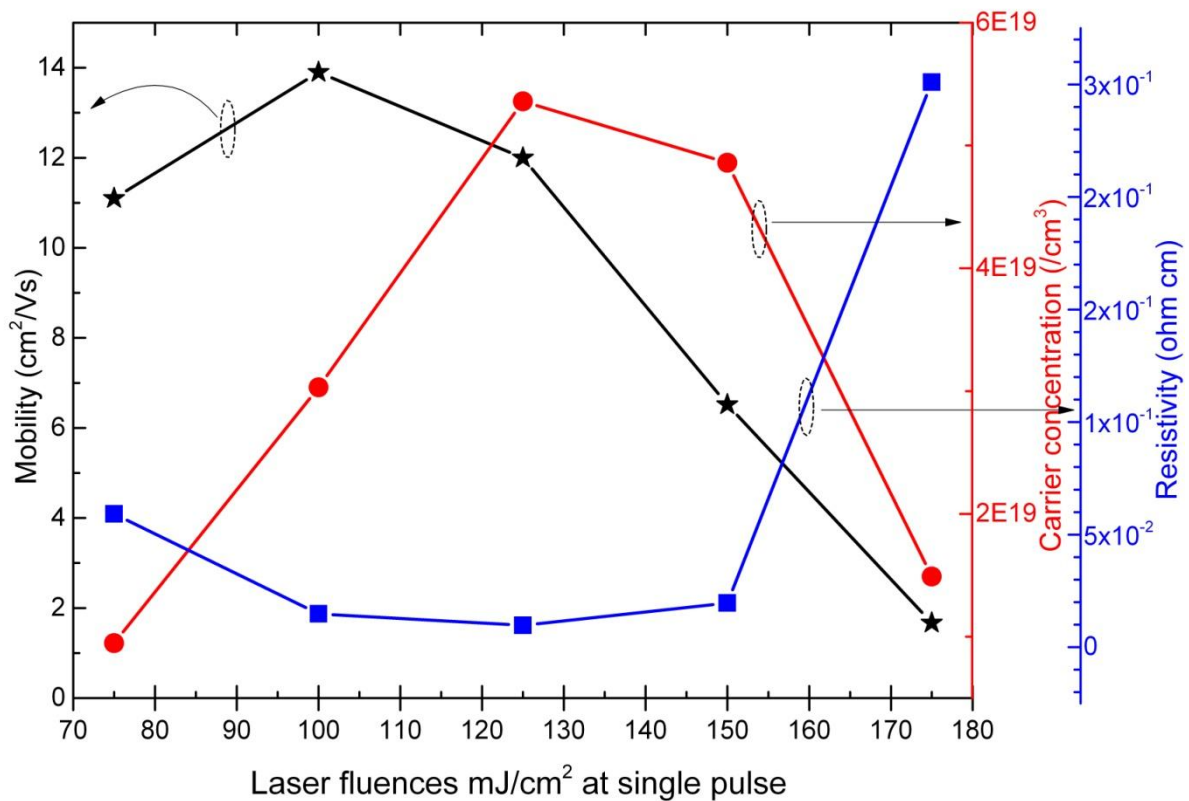


**Figure 6.10:** Hall mobilities, carrier concentrations, and resistivities of 50 nm thick IGZO (1:1:1) thin films film as a function of laser fluence.

For IGZO films with thickness 30 nm, no Hall mobility or conductivity could be detected for as-deposited films and laser irradiated films at various fluences. However, for 50 nm

thick films no measurements were observed for as-grown films, and post laser annealing for applied fluence below  $75 \text{ mJ/cm}^2$ , coincident with 4PP measurements. As the laser energy density increased from  $75 \text{ mJ/cm}^2$  to  $100 \text{ mJ/cm}^2$  with a single pulse the Hall mobility increased significantly from  $11.1 \text{ cm}^2/\text{Vs}$  to  $13.9 \text{ cm}^2/\text{Vs}$  respectively, with a further increase of laser fluence causing a dramatic drop in Hall mobility. The high resistivity of laser annealed 30 nm film could be linked to the surface of the film being affected by atmospheric oxygen and changing the film properties, and is still a matter for investigation. However, it was reported by Nakata et.al in a comparison study, that the dependence of Hall mobility measurements and carrier density on laser fluence of laser annealed IGZO film by XeCl excimer laser ( $\lambda=308 \text{ nm}$ ) deposited at 20 nm and 50 nm where the highest Hall mobility achieved was  $\sim 17 \text{ cm}^2/\text{Vs}$  at laser energy density of about  $180 \text{ mJ/cm}^2$  and  $330 \text{ mJ/cm}^2$  respectively [153]. Hence, the laser annealing is at 248 nm (KrF) and the highest mobility appeared at  $100 \text{ mJ/cm}^2$  ( $13.9 \text{ cm}^2/\text{Vs}$ ).

#### **6.4 Electrical properties of thermal and laser annealed IGZO-TFTs**

IGZO-TFTs devices were subjected to thermal and laser processing pre and post IGZO layer patterning before dielectric layer and gate electrode being deposited as shown in figure 6.11 which is the top gate-bottom contacts structure. IGZO channel layers were deposited by RF magnetron sputtering from the target with stoichiometry of (1:1:1) using the conditions of 50 W, 2%  $\text{O}_2$  in Ar, 2 mTorr with no intentional substrate heating for all wafers. Thermal annealing was carried out on a hotplate in air at  $150 \text{ }^\circ\text{C}$ . From work carried out previously with our collaborator, laser annealing of IGZO-TFTs pre and post IGZO channel patterning resulted in devices with different electrical properties. Each wafer was diced into 3 pieces for annealing purpose of as-deposited, pre IGZO pattern anneal, and post IGZO pattern anneal, then all samples were finalised with dielectric layer and gate electrode deposition in the same run. Laser annealing was

conducted selectively on the wafer at fluences from 0 to 75 mJ/cm<sup>2</sup> for both pre-and post-IGZO pattern.

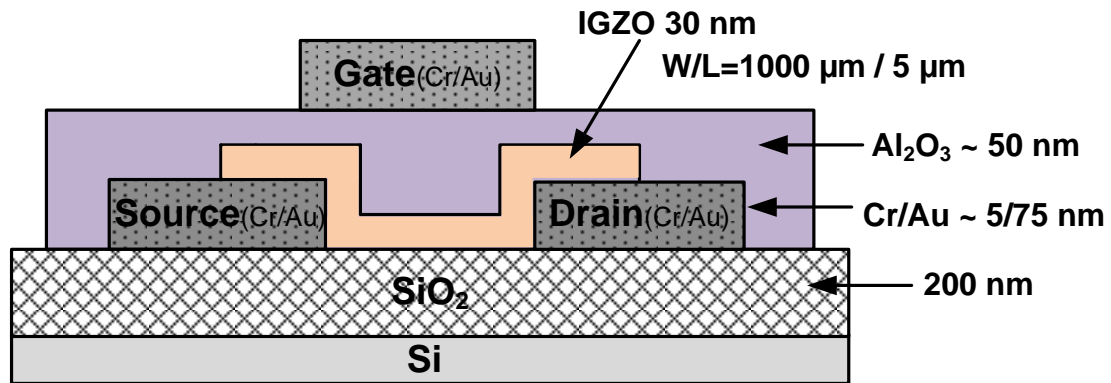


**Figure 6.11:** Cross section diagram of IGZO TFTs used for thermal and laser annealing (W/L= 1000 μm/5 μm).

Figure 6.12 shows the process sequence of top gate-bottom contacts IGZO-TFT fabrication undertaken via collaboration with Cambridge University, with the IGZO channel deposition, and laser processing carried out at NTU.

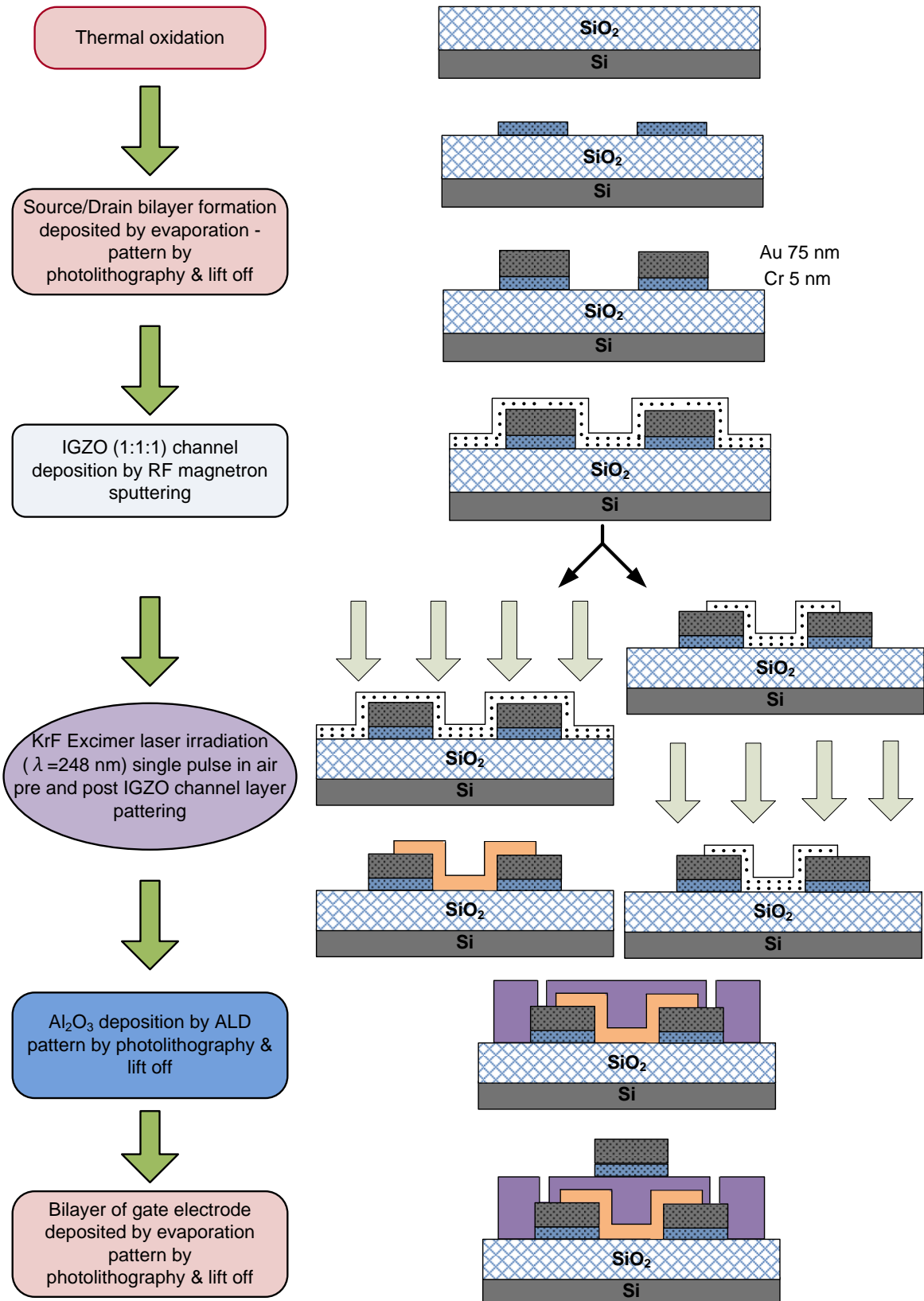


**Figure 6.12:** Schematic diagram showing the process sequence of top gate-bottom contacts IGZO-TFT fabrication and the concept of laser annealing pre and post IGZO channel patterning.

### **6.4.1 Thermal annealed IGZO–TFTs**

Figure 6.13 shows the transfer characteristics of IGZO-TFTs (IGZO 30 nm) thermally annealed at 150 °C in air for 1 hour, where the annealing was undertaken before and after the channel layer patterning. The results are summarised in Table 6.3 as compared to the non-annealed device. There was a slight improvement in electrical performance of IGZO TFT thermal annealed pre IGZO pattern but with an increased off current, whereas post thermal annealed IGZO pattern devices show significant improvement of transfer characteristics. In both cases there is a negative shift in the threshold voltage, an improvement in the ON current, and a significant improvement in the On/Off current ratio for the post pattern annealed sample. In general, for the thermally annealed devices, the improvement in performance was better when annealed post IGZO patterning. Similar result trends were observed upon repetition of this exercise. Results indicated that thermal annealing at low temperature after IGZO channel layer patterning is more effective than before, which could be attributed to the effect on the interface between the IGZO layer and the dielectric layer by the photoresist heat treatment at 100 °C for 1 min and 20 s, since this would be a different effect when the photoresist is heated pre and post thermal anneal.

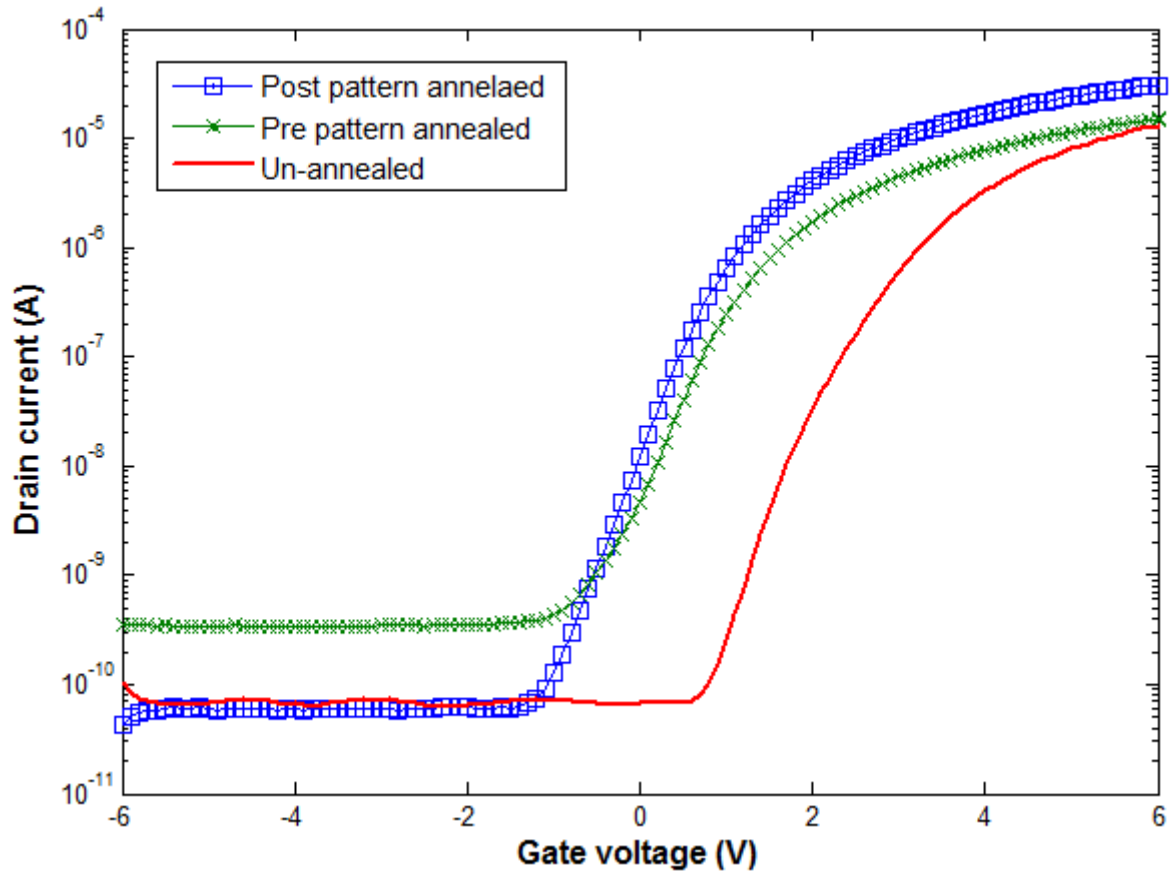


**Figure 6.13:** Transfer characteristics ON sweep of IGZO-TFTs ( $W/L= 1000 \mu\text{m}/5 \mu\text{m}$ )  $V_{DS} = 1 \text{ V}$ , IGZO 30 nm, pre and post IGZO pattern thermal annealed at  $150 \text{ }^\circ\text{C}$  in air for 1 hour.

Sample	$V_{th}$ (V)	$\mu_{FE}$ ( $\text{cm}^2/\text{Vs}$ )	$S$ (V/decade)	$I_D$ Max (A)	$I_{ON}/I_{OFF}$ ratio (average)
Un-annealed	$3.52 \pm 0.14$	$0.14 \pm 0.04$	$0.41 \pm 0.14$	$1.36 \times 10^{-5}$	$1.48 \times 10^5$
150°C pre pattern	$1.65 \pm 0.28$	$0.10 \pm 0.03$	$0.64 \pm 0.11$	$1.54 \times 10^{-5}$	$7.46 \times 10^4$
150°C post pattern	$1.60 \pm 0.23$	$0.16 \pm 0.09$	$0.52 \pm 0.08$	$2.75 \times 10^{-5}$	$0.78 \times 10^6$

**Table 6.3:** Properties of IGZO -TFTs thermally annealed pre and post patterning of the active layer 30 nm thick.

### 6.4.2 Laser annealed IGZO –TFTs

The TFT results for the laser processed samples are shown in Figure 6.14 which represents the characteristics from devices fabricated on the same substrate. As with the thermally annealed samples, the laser treated films at laser energy density of 75 mJ/cm<sup>2</sup> with single pulse show a negative shift in threshold voltage and an increase of ON current. However, devices laser annealed pre IGZO pattern demonstrate higher ON and OFF current than the devices processed post to IGZO pattern. The electrical properties of these devices are summarized in Table 6.4.

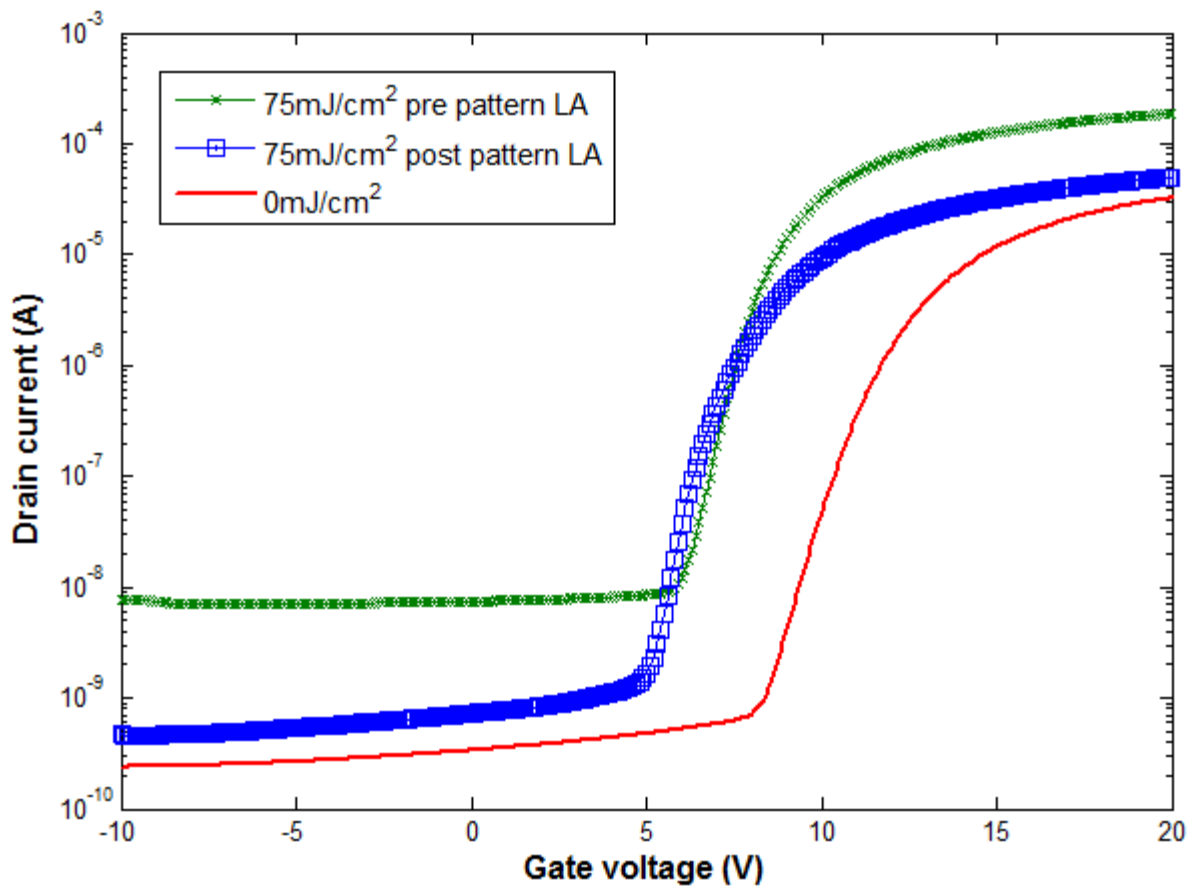


**Figure 6.14:** Transfer characteristics ON sweep IGZO-TFTs ( $W/L = 1000 \mu\text{m}/5 \mu\text{m}$ )  $V_{DS} = 1 \text{ V}$ , IGZO 30 nm, laser annealed at laser energy density of 75 mJ/cm<sup>2</sup> with a single pulse, pre and post IGZO patterning.

Laser annealed IGZO-TFT devices with a channel layer 30nm thick demonstrating very low field effect mobility, as well as no Hall Effect was observed for 30 nm thick films as

a function of laser energy density, while laser processed 50 nm thick film result in Hall mobility as high as 13.9 cm<sup>2</sup>/Vs.

Sample	V <sub>th</sub> (V)	μ <sub>FE</sub> (cm <sup>2</sup> /Vs)	S (V/decade)	I <sub>D</sub> Max (A)	I <sub>ON</sub> /I <sub>OFF</sub> (average)
Un- annealed	12.1±0.7	0.003±0.005	0.70±0.04	3.25x10 <sup>-5</sup>	1.58x10 <sup>5</sup>
75mJ/cm <sup>2</sup> pre pattern	8.15±0.5	0.64±0.69	0.71±0.07	2.00 x10 <sup>-4</sup>	8.47x10 <sup>7</sup>
75mJ/cm <sup>2</sup> post pattern	7.93±0.5	0.25±0.21	0.61±0.17	5.01x10 <sup>-5</sup>	3.38x10 <sup>6</sup>

**Table 6.4:** Properties of IGZO –TFTs annealed with different laser annealing conditions.

Figure 6.15 shows the transfer characteristics of IGZO-TFTs devices with a 50 nm IGZO channel that has been laser treated post IGZO patterning and using the same structure of device as shown in Figure 6.14. I<sub>ON</sub> increased slightly as the laser fluence increased up to 25 mJ/cm<sup>2</sup>, and as the laser fluence increased up to 75 mJ/cm<sup>2</sup> the I<sub>ON</sub> current increased significantly with a pronounced negative shift of threshold voltage. For devices from the same wafer as above but laser treated pre IGZO patterning the I<sub>ON</sub> was not affected by laser fluence at 25 and 50 mJ/cm<sup>2</sup>, while laser annealing at an energy density of 75 mJ/cm<sup>2</sup> caused an increase of the I<sub>ON</sub> current, and is relatively higher than post IGZO pattern treated devices as depicted in Figure 6.16. The electrical properties of these devices are summarized in Table 6.5. Laser anneal at 75 mJ/cm<sup>2</sup> pre IGZO channel layer patterns result in higher I<sub>ON</sub> current and mobility, similar trends were observed for devices with active layer 30 nm thick ( presented in Table 6.4).

Sample	$V_{th}$ (V)	$\mu_{FE}$ (cm <sup>2</sup> /Vs)	$S$ (V/decade)	$I_D$ Max (A)	$I_{ON}/I_{OFF}$ (average)
Un-annealed	2.0±0.2	0.2	0.51	7.9 ×10 <sup>-5</sup>	8.0×10 <sup>5</sup>
75mJ/cm <sup>2</sup> pre pattern	1.2±0.07	1.9	0.75	7.5 ×10 <sup>-4</sup>	8.8×10 <sup>6</sup>
75mJ/cm <sup>2</sup> post pattern	1.3±0.06	1.6	0.66	6.5 ×10 <sup>-4</sup>	7.4×10 <sup>6</sup>

**Table 6.5:** Electrical properties of IGZO-TFTs laser annealed pre and post patterning of the active layer 50 nm thick, at 75 mJ/cm<sup>2</sup> with a single pulse in air.

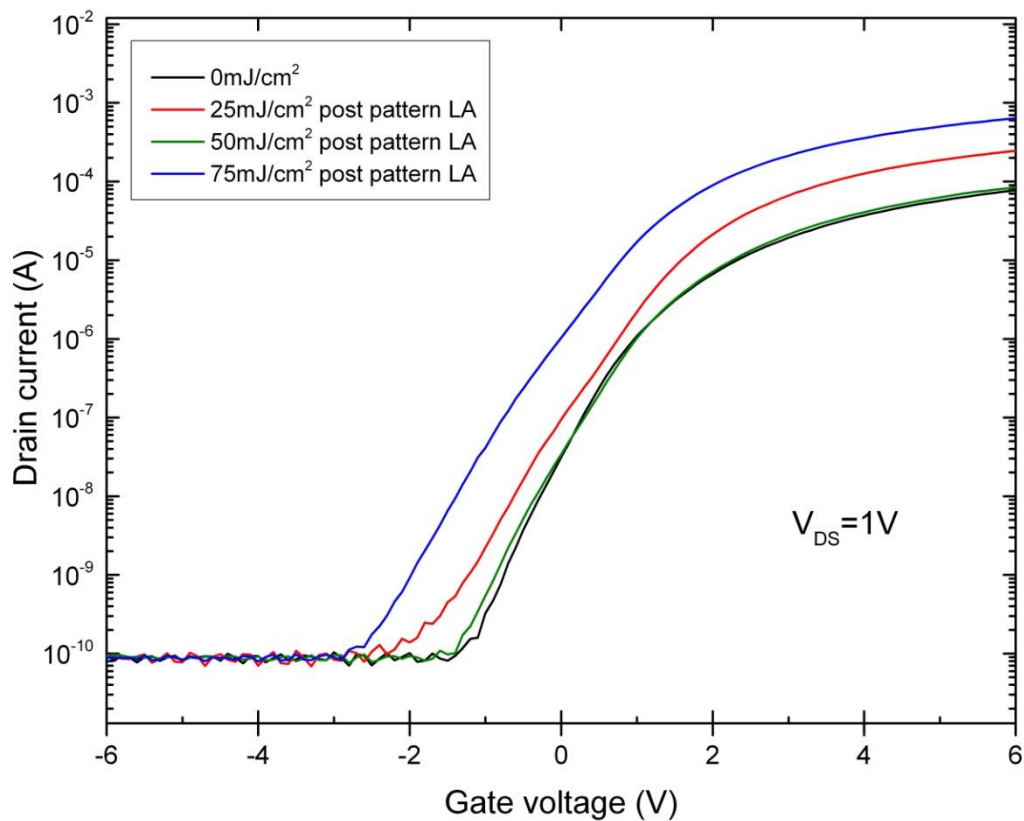


**Figure 6.15:** Transfer characteristics of ON sweep IGZO-TFTs ( $W/L= 1500 \mu\text{m}/ 5 \mu\text{m}$ )  $V_{DS} =1 \text{ V}$  at laser energy density 75 mJ/cm<sup>2</sup> single pulse post IGZO pattern.

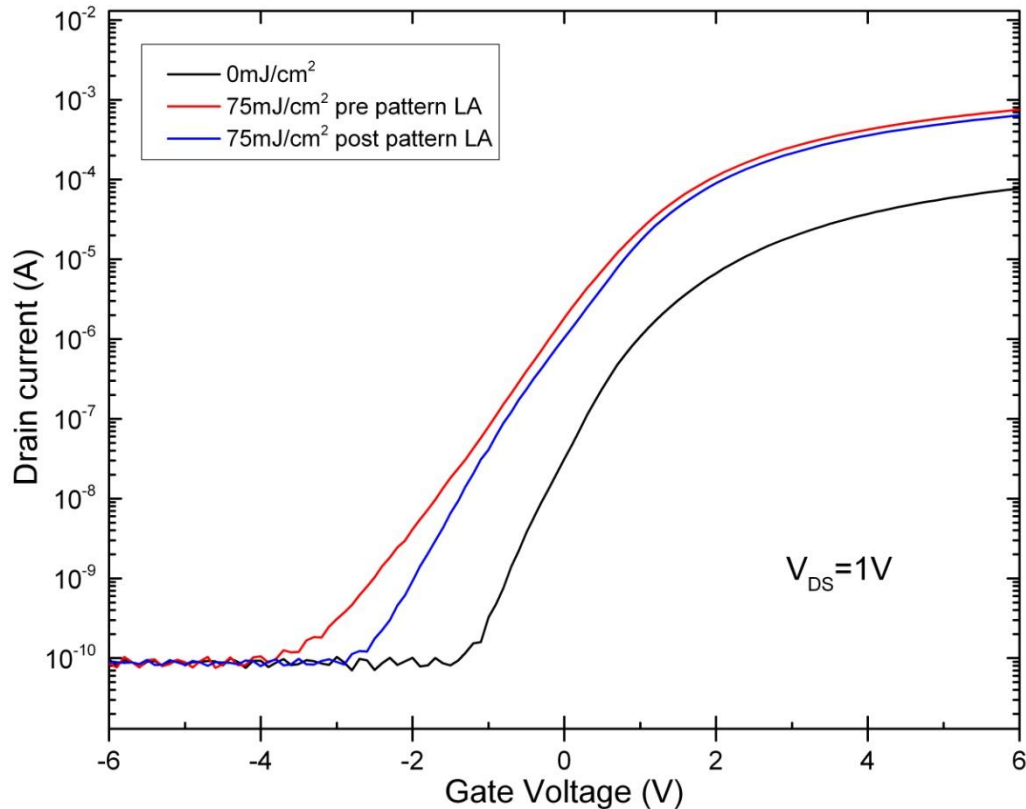


**Figure 6.16:** Transfer characteristics of ON sweep IGZO-TFTs ( $W/L = 1500 \mu\text{m} / 5 \mu\text{m}$ )  $V_{DS} = 1 \text{ V}$  pre and post IGZO pattern laser at laser energy density  $75 \text{ mJ/cm}^2$  single pulse.

## 6.5 Discussion

In oxide semiconductors, the electrical conduction arises by intrinsic defects (that donate free electrons) such as interstitials or oxygen vacancies. It is shown in this chapter that Laser annealing by KrF excimer laser ( $\lambda = 248 \text{ nm}$ ) at single pulse in air results in a significant reduction in resistivity of ZnO and IGZO thin films.

For ZnO films, laser irradiation causes a breaking of the Zn-O bond which results in oxygen vacancies ( $V_o$ ) or zinc interstitial ( $Zn_i$ ) predominantly contributing as a donor. A dramatic reduction in sheet resistance of laser processed ZnO films was observed at high fluences, dropping to about  $864 \Omega/\text{sq}$  at  $315 \text{ mJ/cm}^2$  for films deposited at RT and  $400 \text{ }^\circ\text{C}$ . No PL was observed as a function of laser anneal for films deposited on  $\text{SiO}_2$  at RT. However, the influence on the microstructure of ZnO films was demonstrated by

XRD patterns which shows a shift of the preferred (002) peak as a function of laser fluence. The reason behind no PL being observed for ZnO on SiO<sub>2</sub> grown at RT is still a matter of investigation.

Post deposition annealing of IGZO films leads to removal of weakly bonded oxygen atoms or oxygen combination contributing to a new equilibrium changing the electrical properties of IGZO films [75, 132]. A significant drop in sheet resistance of IGZO thin films deposited without intentional substrate heating as a function of laser energy density for a single pulse is observed with a strong dependence on deposition parameters. The lowest sheet resistance post laser processing was observed at deposition conditions of low deposition pressure, low oxygen concentration, and high RF power. In addition the Hall Effect mobility increased as a function of laser fluence to 13.9 cm<sup>2</sup>/Vs.

For IGZO-TFT devices, thermal and laser annealing pre and post IGZO channel layer patterns result in negative shift in threshold voltage which could be attributed to the high defects density in the subgap density of states (DOS) pins the Fermi level, so no mobile holes. TFTs devices demonstrate high values of sub-threshold swing  $S$  in which related to trap density in the subgap. High sub-threshold swing  $S$  result in poor electrical properties such as, low speed and higher power consumption. Laser annealed devices was unstable under bias stress in which demonstrate positive shift in threshold voltage. laser irradiation is expected to reduce the contact resistance between the IGZO channel layer and the source/drain electrodes by increasing the carrier concentration [74].

## Chapter 7

### Conclusion and Future Work

---

#### 7.1 Introduction

The main aim of this project was to investigate the feasibility of using excimer laser processing as an alternative technique to conventional thermal annealing to improve the microstructure and electrical properties of sputtered ZnO and IGZO thin films for use in electronic devices. Initially, a comparative study was conducted into the effect of post deposition processing using thermal annealing, rapid thermal annealing, and laser annealing on the microstructure properties of ZnO thin films. The films were deposited (via collaboration with Cambridge University) without intentional substrate heating using the HiTUS technique. Oxygen flow rates of 28, 32, 35, 38, and 41 sccm were used to produce films of varying stoichiometry in order to examine the effect of post deposition processing on the properties, and to help in the study of intrinsic defects and the modification of defect type and density as a function of the annealing process used. The effect of post deposition processing was also investigated for ZnO films deposited by RF magnetron sputtering at NTU, as a function of varying deposition conditions: RF power, oxygen content in the sputtering gas, and substrate temperature from RT to 400 °C. Finally, the feasibility of using laser annealing to improve the electrical properties of IGZO films grown via RF magnetron sputtering at room temperature was investigated. IGZO thin films were deposited at various conditions to study the effect of growth and post deposition annealing on the properties, with the optimised films used in TFT test devices. This chapter presents an overview of the major outcomes from this work and discusses aspects that would be suitable for further investigation.

## 7.2 Key Outcomes

The results from this research demonstrate that laser processing is a technique that can be used for controlled modification of the internal properties of low temperature deposited ZnO films. Optimised processing leads to grain re-growth, crystallinity improvement and a dramatic reduction of point defects, without the associated film degradation or loss that occurs when using high temperature thermal and rapid thermal annealing. The results consequently provide evidence for the potential of this technique to be used with the application of ZnO films for use on flexible substrates. The main research findings are summarised as the following:

- A comparative study has been presented into the effect of three annealing methods using a comprehensive range of processing parameters applied to ZnO thin films. The results demonstrate that laser annealing is a powerful technique to control the modification of sputtered ZnO thin films grown at low temperature. The effect is a reduction of intrinsic defects without film degradation or materials loss that is observed for thermal and rapid thermal annealing at high temperatures concomitantly with generation of new defects. The resultant PL spectra exhibit the development of two main peaks: a strong narrow NBE peak centred at 381 nm, and a broad visible emission DLE (440-800 nm). The evolution of these peaks is strongly dependent on the laser energy density applied, with five process regimes observed for various fluence ranges applied at single or multiples pulses. In intrinsic ZnO the nature of point defects considered to be responsible for typical DLE is still a matter of debate [84]. However, the results presented here demonstrate that the DLE peak is related to excess oxygen defects. This is evidenced by the fact that no appearance of a DLE peak was observed as a function of laser fluence for films grown at an oxygen flow rate of 28 sccm (Zn-rich), but there is a pronounced development of NBE peak with fluence increase, indicating that the DLE observed for films

deposited at oxygen flow rate  $> 28$  sccm is related to excess oxygen defects. This is further evidenced when the effect of laser anneal as a function of as-grown stoichiometry is examined; indicating that as the growth oxygen flow rate is increased, the intensity of the DLE is increased consistent with excess oxygen concentration, similar to the trend also observed for the RTA samples.

- The research presents more detailed analyses of point defects generated (defects related to the DLE) by TA and RTA than previously reported. Rapid thermal annealing of low temperature deposited HiTUS ZnO films demonstrate the development of a strong deep level emission (DLE), classified as an orange/red emission, which is further enhanced when annealing is carried out in an oxygen containing environment. This gives the indication that excess oxygen dominates defect activation, which is likely to be through the mechanism of oxygen absorption as oxygen interstitials and antisites. In comparison, thermal annealing in air at high temperature as a function of annealing time demonstrates a reduction in the orange/red emission peak with shift to a sharper green/yellow emission. This could be ascribed to a change in the nature of activated dominant DLE defects from oxygen interstitial ( $O_i$ ) defects to zinc vacancies ( $V_{zn}$ ). This shift is confirmed via XPS characterisation in which the corresponding deviation of film stoichiometry is observed as the temperature is increased up to 700 °C. The effect of film stoichiometry is also presented by the results of the RTA processing, with the films exhibiting a green/yellow DLE for all samples annealed in nitrogen ambient, which is not observed for samples processed in oxygen. The intensity of DLE for all samples has a dependence on the film stoichiometry, with a higher DLE intensity consistent with samples grown at higher oxygen flow rates.
- In terms of the deposition parameters, the research has demonstrated that as a function of laser annealing, a low sputtering RF power is required to produce better quality ZnO films when grown at room temperature. From the resultant PL, the results show that as the growth RF power is increased, the intensity of

the NBE peak is decreased significantly. This could be linked to the fact that at the higher RF powers used for deposition, highly energetic ion bombardment leads to surface damage, and defects are introduced to the film [116]. However, it has been reported elsewhere that for as-deposited films without intentional substrate heating, the grain size increased as the RF power increased [142], while for the as-deposited films investigated here there is an observed reduction in the average grain size as the RF power is increased. This discrepancy could be ascribed to the films being deposited at different parameters, therefore the actual threshold of RF power may differ.

- The intensity of the NBE peak is shown to be strongly influenced by the film growth temperature, with encouraging PL results demonstrated by samples deposited on unheated substrates showing subsequent evolution of strong NBE emission peak at high laser energy density, whilst eliminating the defects related to the DLE peak. As the growth temperature is increased beyond ambient, the NBE intensity peak following laser processing decreased as a function of laser fluence. This effect could be attributed to improved film quality when deposited at higher temperatures, or it might be related to the thickness of the defective layer between the substrate and the film being increased as the growth temperature is increased. However, the exact reason stills a matter of investigation.
- XRD characterisation shows that the average grain domain size for as-grown films is increased as the growth temperature is increased, and following laser processing, the average grain domain size increased significantly for films grown at RT, and 100 °C, whereas this dramatically decreased for films deposited at 200 °C, 300 °C, and 400 °C. Following thermal annealing at 700 °C, XRD demonstrates that for samples where the growth temperature was increased up to 300 °C, there is a significant increase in the (002) peak intensity, compared to the effect on films deposited at 400 °C where there was a dramatic decrease in (002) peak following annealing, similar to results reported previously [138].

Further confirmation of the effect on crystal structure is evidenced by TEM images, where dark field images of laser annealed ZnO films grown on unheated substrates exhibit a pronounced substantial grain growth and crystal improvement.

- One of the most significant results of this work is that laser processing is shown to produce a controlled in-depth crystallisation and modification of ZnO films, which would facilitate the use of the technique to isolate the modified region from the substrate, or any sensitive underlying layers.
- Additional output from this research relates to investigations into the deposition and processing of IGZO for potential use in electronic devices. The results show that to produce IGZO thin films without intentional substrate heating with lowest ultimate sheet resistance as a function of post deposition laser processing the parameters of choice should be low deposition pressure, low oxygen concentration, and high RF power. Similar conditions were observed elsewhere as a function of thermal annealing [154] which could be attributed to deposition mechanisms which affect the sputtered particles arriving on substrate with surface mobility resulting in dense and compact films with low resistivity [92]. The electrical characteristics of laser annealed IGZO thin films deposited at various depositions parameters on unheated substrate demonstrate a significant drop in sheet resistance as a function of laser fluence applied. The as-deposited films were highly resistive (i.e. they had sheet resistance  $> 5 \text{ M}\Omega/\text{sq}$ ) which dropped to about  $500 \pm 10\% \Omega/\text{sq}$  post laser anneal which can be used as metal oxide for electroluminescence devices application. The electrical properties of IGZO films are shown to be strongly dependent on the film growth conditions and target stoichiometry. The sheet resistance of laser processed IGZO films deposited from a target with the stoichiometry of (1:1:1) is relatively higher than films from a (2:2:1) target, which would be attributed to a higher indium content. It was suggested that annealing processes contribute to the removal of weak bonded oxygen atoms or oxygen incorporation which leads to a new

equilibrium resulting in increased film conductivity [75]. For the results presented here, the room temperature Hall Effect mobility of IGZO (50 nm thick) increased significantly as the laser fluence was increased from 75 mJ/cm<sup>2</sup> to 100 mJ/cm<sup>2</sup> (single pulse) reaching values of 11.1 cm<sup>2</sup>/Vs and 13.9 cm<sup>2</sup>/Vs respectively. Hence, results demonstrate that laser annealing is a powerful techniques to modify the electrical properties of IGZO films grown at room temperature.

- Laser annealing of IGZO-TFT pre IGZO channel patterns result in relatively higher ON current than post pattern while thermally annealing post IGZO pattern demonstrate higher ON current. Laser and thermal annealing result in negative shift in threshold voltage, the trap density in the subgap DOS cause high sub-threshold swing in which affect the speed of the devices and increase the power consumption.

### **7.3 Future work**

Following the outcomes of this research project, it is suggested that further work would be beneficial in terms of investigating the microstructure and electrical properties of oxide semiconductors studied here, and into the processing of IGZO-TFTs devices as described below:

- The electrical properties of HiTUS ZnO films, and ZnO grown by RF magnetron sputtering, as a function of laser processing to be characterised via Hall Effect, and then the optimised functional films to be used as a channel layer for ZnO-TFTs fabrication. Another interesting study would be to investigate the effect laser and thermal anneal of ZnO channel layers as a function of pre and post channel layer patterning, since the results with the IGZO devices showed that the sequence is important.
- More microstructure investigation via PL of the effect of laser processing of ZnO deposited by RF magnetron sputtering at higher oxygen concentrations by

varying RF power, and substrate temperature – to further study the nature of defects.

- Temperature dependant PL of laser and thermal annealed ZnO films deposited by HiTUS and RF magnetron sputtering.
- Fabrication of IGZO-TFT devices on flexible substrates to study the effect of ON current as a function of laser fluence, and to deposit alumina layer ( $\text{Al}_2\text{O}_3$ ) on the top of IGZO layer before laser processing as a protection layer from atmospheric contamination during laser processing and before the source/drain has been deposited.
- Study of the effect of a combination of laser annealing and thermal annealing onto microstructure and electrical properties of both ZnO and IGZO thin films.

## List of references

---

- [1] G. P. Crawford, *Flexible Flat Panel Displays*, John Wiley and Sons Ltd , pp. 1-9, 2005.
- [2] T. Hirao, M. Furuta, H. Furuta, T. Matsuda, T. Hiramatsu, H. Hokari, M. Yoshida, H. Ishii and M. Kakegawa, "Novel top-gate zinc oxide thin-film transistors (ZnO TFTs) for AMLCDs," *Journal of the Society for Information Display*, vol. 15, pp. 17-22, 2007.
- [3] Y. Kuo, *Thin Film Transistors: Materials and Processes, Amorphous Silicon Thin Film Transistors, Vol. 1*. Boston, Mass. ; London: Kluwer Academic Publishers, 2004.
- [4] S. Depp, A. Juliana and B. Huth, "Polysilicon FET devices for large area input/output applications," in *Electron Devices Meeting, 1980 International*, 1980, pp. 703-706.
- [5] T. Sameshima, "Status of Si thin film transistors," *J. Non Cryst. Solids*, vol. 227, pp. 1196-1201, 1998.
- [6] N. Park, T. Kim and S. Park, "Band gap engineering of amorphous silicon quantum dots for light-emitting diodes," *Appl. Phys. Lett.*, vol. 78, pp. 2575-2577, 2001.
- [7] C. R. Kagan and P. Andry, *Thin-Film Transistors*. New York: Marcel Dekker, 2003.
- [8] U. Ozgur, Y. I. Alivov, C. Liu, A. Teke, M. Reshchikov, S. Dogan, V. Avrutin, S. Cho and H. Morkoc, "A comprehensive review of ZnO materials and devices," *J. Appl. Phys.*, vol. 98, pp. 041301-041301-103, 2005.
- [9] K. Nomura, H. Ohta, A. Takagi, T. Kamiya, M. Hirano and H. Hosono, "Room-temperature fabrication of transparent flexible thin-film transistors using amorphous oxide semiconductors," *Nature*, vol. 432, pp. 488-492, 2004.
- [10] H. Yabuta, M. Sano, K. Abe, T. Aiba, T. Den, H. Kumomi, K. Nomura, T. Kamiya and H. Hosono, "High-mobility thin-film transistor with amorphous InGaZnO channel fabricated by room temperature rf-magnetron sputtering," *Appl. Phys. Lett.*, vol. 89, pp. 112123, 2006.
- [11] J. Y. Kwon, K. S. Son, J. S. Jung, T. S. Kim, M. K. Ryu, K. B. Park, B. W. Yoo, J. W. Kim, Y. G. Lee and K. C. Park, "Bottom-gate gallium indium zinc oxide thin-film transistor array for high-resolution AMOLED display," *Electron Device Letters, IEEE*, vol. 29, pp. 1309-1311, 2008.
- [12] C. J. Kim, D. Kang, I. Song, J. C. Park, H. Lim, S. Kim, E. Lee, R. Chung, J. C. Lee and Y. Park, "Highly stable Ga<sub>2</sub>O<sub>3</sub>-In<sub>2</sub>O<sub>3</sub>-ZnO TFT for active-matrix organic light-emitting diode display application," in *Electron Devices Meeting, 2006. IEDM'06. International*, 2006, pp. 1-4.

## List of references

- [13] H. Hosono, K. Nomura, Y. Ogo, T. Uruga and T. Kamiya, "Factors controlling electron transport properties in transparent amorphous oxide semiconductors," *J. Non Cryst. Solids*, vol. 354, pp. 2796-2800, 5/1, 2008.
- [14] T. Kamiya, K. Nomura and H. Hosono, "Present status of amorphous In-Ga-Zn-O thin-film transistors," *Science and Technology of Advanced Materials*, vol. 11, pp. 044305, 2010.
- [15] H. Hsieh, T. Tsai, C. Chang, S. Hsu, C. Chuang and Y. Lin, "Active-matrix organic light-emitting diode displays with indium gallium zinc oxide thin-film transistors and normal, inverted, and transparent organic light-emitting diodes," *Journal of the Society for Information Display*, vol. 19, pp. 323-328, 2011.
- [16] T. Arai, "Oxide-TFT technologies for next-generation AMOLED displays," *Journal of the Society for Information Display*, vol. 20, pp. 156-161, 2012.
- [17] S. Jeong, B. Kim and B. Lee, "Photoluminescence dependence of ZnO films grown on Si (100) by radio-frequency magnetron sputtering on the growth ambient," *Appl. Phys. Lett.*, vol. 82, pp. 2625-2627, 2003.
- [18] A. Djurišić, W. C. Choy, V. A. L. Roy, Y. H. Leung, C. Y. Kwong, K. W. Cheah, T. Gundu Rao, W. K. Chan, H. Fei Lui and C. Surya, "Photoluminescence and electron paramagnetic resonance of ZnO tetrapod structures," *Advanced Functional Materials*, vol. 14, pp. 856-864, 2004.
- [19] P. T. Hsieh, Y. C. Chen, C. M. Wang, Y. Z. Tsai and C. C. Hu, "Structural and photoluminescence characteristics of ZnO films by room temperature sputtering and rapid thermal annealing process," *Appl. Phys. A*, vol. 84, pp. 345-349, 2006.
- [20] T. Brody, J. A. Asars and G. D. Dixon, "A 6× 6 inch 20 lines-per-inch liquid-crystal display panel," *Electron Devices, IEEE Transactions on*, vol. 20, pp. 995-1001, 1973.
- [21] <http://www.gizmag.com/samsungs-transparent-lcd-display/18283/>.
- [22] S. Masuda, K. Kitamura, Y. Okumura, S. Miyatake, H. Tabata and T. Kawai, "Transparent thin film transistors using ZnO as an active channel layer and their electrical properties," *J. Appl. Phys.*, vol. 93, pp. 1624, 2003.
- [23] Ü. Özgür, Y. I. Alivov, C. Liu, A. Teke, M. Reshchikov, S. Doğan, V. Avrutin, S. J. Cho and H. Morkoc, "A comprehensive review of ZnO materials and devices," *J. Appl. Phys.*, vol. 98, pp. 041301, 2005.
- [24] J. K. Jeong, J. H. Jeong, J. H. Choi, J. S. Im, S. H. Kim, H. W. Yang, K. N. Kang, K. S. Kim, T. K. Ahn and H. Chung, "3.1: Distinguished paper: 12.1-Inch WXGA AMOLED display driven by Indium-Gallium-Zinc oxide TFTs array," in *SID Symposium Digest of Technical Papers*, 2008, pp. 1-4.
- [25] M. Ito, M. Kon, C. Miyazaki, N. Ikeda, M. Ishizaki, Y. Ugajin and N. Sekine, ""Front Drive" Display Structure for Color Electronic Paper Using Fully Transparent Amorphous Oxide TFT Array," *IEICE Trans. Electron.*, vol. 90, pp. 2105-2111, 2007.

## List of references

- [26] R. Hoffman, B. J. Norris and J. Wager, "ZnO-based transparent thin-film transistors," *Appl. Phys. Lett.*, vol. 82, pp. 733-735, 2003.
- [27] J. T. Wallmark and H. Johnson, *Field-Effect Transistors: Physics, Technology and Applications*. Prentice-Hall, 1966.
- [28] E. Fortunato, P. Barquinha and R. Martins, "Oxide Semiconductor Thin-Film Transistors: A Review of Recent Advances," *Adv Mater*, 2012.
- [29] J. F. Wager, *Transparent Electronics*. New York ; London: Springer, 2008.
- [30] D. Hong, G. Yerubandi, H. Chiang, M. Spiegelberg and J. Wager, "Electrical modeling of thin-film transistors," *Critical Reviews in Solid State and Material Sciences*, vol. 33, pp. 101-132, 2008.
- [31] K. Hoshino, "Instability and temperature-dependence assessment of IGZO TFTs," 2008.
- [32] T. Hirao, M. Furuta, H. Furuta, T. Matsuda, T. Hiramatsu, H. Hokari and M. Yoshida, "4.1: Distinguished paper: High mobility Top-Gate zinc oxide Thin-Film transistors (ZnO-TFTs) for Active-Matrix liquid crystal displays," in *SID Symposium Digest of Technical Papers*, 2006, pp. 18-20.
- [33] J. S. Park, W. J. Maeng, H. S. Kim and J. S. Park, "Review of recent developments in amorphous oxide semiconductor thin-film transistor devices," *Thin Solid Films*, vol. 520, pp. 1679-1693, 2012.
- [34] M. Kim, J. H. Jeong, H. J. Lee, T. K. Ahn, H. S. Shin, J. S. Park, J. K. Jeong, Y. G. Mo and H. D. Kim, "High mobility bottom gate InGaZnO thin film transistors with SiO<sub>x</sub> etch stopper," *Appl. Phys. Lett.*, vol. 90, pp. 212114-212114-3, 2007.
- [35] J. Y. Kwon, K. S. Son, J. S. Jung, K. H. Lee, J. S. Park, T. S. Kim, K. H. Ji, R. Choi, J. K. Jeong and B. Koo, "The impact of device configuration on the photon-enhanced negative bias thermal instability of GaInZnO thin film transistors," *Electrochemical and Solid-State Letters*, vol. 13, pp. H213-H215, 2010.
- [36] D. P. Heineck, B. R. McFarlane and J. F. Wager, "Zinc tin oxide thin-film-transistor enhancement/depletion inverter," *Electron Device Letters, IEEE*, vol. 30, pp. 514-516, 2009.
- [37] R. Presley, D. Hong, H. Chiang, C. Hung, R. Hoffman and J. Wager, "Transparent ring oscillator based on indium gallium oxide thin-film transistors," *Solid-State Electronics*, vol. 50, pp. 500-503, 2006.
- [38] A. C. Tickle, *Thin-Film Transistors*. John Wiley, 1969.
- [39] K. H. Cherenack, "Fabricating silicon thin-film transistors on plastic at 300 °C" Princeton University 2009.
- [40] P. K. Weimer, "The TFT a new thin-film transistor," *Proceedings of the IRE*, vol. 50, pp. 1462-1469, 1962.

## List of references

- [41] E. Lueder, "Processing of thin-film transistors with photolithography and application for displays," in *Digest 1980 SID Intl. Symp.(Soc. for Information Displays)*, 1980, pp. 118-122.
- [42] R. Haering, "Theory of thin film transistor operation," *Solid-State Electronics*, vol. 7, pp. 31-38, 1964.
- [43] H. Koelmans and H. De Graaff, "Drift phenomena in CdSe thin film FET's," *Solid-State Electronics*, vol. 10, pp. 997-1005, 1967.
- [44] P. Le Comber, W. Spear and A. Ghaith, "Amorphous-silicon field-effect device and possible application," *Electron. Lett.*, vol. 15, pp. 179-181, 1979.
- [45] R. Navamathavan, J. Lim, D. Hwang, B. Kim, J. Oh, J. Yang, H. Kim, S. Park and J. Jang, "Thin-Film Transistors Based on ZnO Fabricated by Using Radio-Frequency Magnetron Sputtering," *JOURNAL-KOREAN PHYSICAL SOCIETY*, vol. 48, pp. 271, 2006.
- [46] R. Cross and M. De Souza, "Investigating the stability of zinc oxide thin film transistors," *Appl. Phys. Lett.*, vol. 89, pp. 263513, 2006.
- [47] P. Carcia, R. McLean, M. Reilly and G. Nunes, "Transparent ZnO thin-film transistor fabricated by rf magnetron sputtering," *Appl. Phys. Lett.*, vol. 82, pp. 1117-1119, 2003.
- [48] J. F. Wager, "68.1: Invited paper: Transparent Electronics—Display applications" in 2007.
- [49] P. Carcia, R. McLean and M. Reilly, "High-performance ZnO thin-film transistors on gate dielectrics grown by atomic layer deposition," *Appl. Phys. Lett.*, vol. 88, pp. 123509-123509-3, 2006.
- [50] K. Nomura, T. Kamiya, H. Yanagi, E. Ikenaga, K. Yang, K. Kobayashi, M. Hirano and H. Hosono, "Subgap states in transparent amorphous oxide semiconductor, In-Ga-Zn-O, observed by bulk sensitive X-ray photoelectron spectroscopy," *Appl. Phys. Lett.*, vol. 92, pp. 202117, 2008.
- [51] M. Kimura, T. Nakanishi, K. Nomura, T. Kamiya and H. Hosono, "Trap densities in amorphous-InGaZnO<sub>4</sub> thin-film transistors," *Appl. Phys. Lett.*, vol. 92, pp. 133512, 2008.
- [52] T. Kamiya, K. Nomura and H. Hosono, "Origins of High Mobility and Low Operation Voltage of Amorphous Oxide TFTs: Electronic Structure, Electron Transport, Defects and Doping\*," *Journal of Display Technology*, vol. 5, pp. 468-483, 2009.
- [53] Y. Zhao and Y. Jiang, "Investigation of room temperature UV emission of ZnO films with different defect densities induced by laser irradiation," *Spectrochimica Acta Part A: Molecular and Biomolecular Spectroscopy*, vol. 76, pp. 336-340, 2010.

## List of references

- [54] H. Lu, Y. Tu, X. Lin, B. Fang, D. Luo and A. Laaksonen, "Effects of laser irradiation on the structure and optical properties of ZnO thin films," *Mater Lett*, 2010.
- [55] H. Hartnagel, A. Dawar, A. Jain and C. Jagadish, *Semiconducting Transparent Thin Films*. Institute of Physics Pub. Bristol [England], 1995.
- [56] C. Jagadish, and S. J. Pearton, *Zinc Oxide Bulk, Thin Films and Nanostructures Electronic Resource : Processing, Properties and Applications*. Amsterdam ; London: Elsevier, 2006.
- [57] K. Ellmer, A. Klein Dr., B. Rech, *Transparent Conductive Zinc Oxide : Basics and Applications in Thin Film Solar Cells*. Berlin: Springer, 2008.
- [58] H. Hosono, "Ionic amorphous oxide semiconductors: Material design, carrier transport, and device application," *J. Non Cryst. Solids*, vol. 352, pp. 851-858, 2006.
- [59] K. Nomura, T. Kamiya, H. Ohta, T. Uruga, M. Hirano and H. Hosono, "Local coordination structure and electronic structure of the large electron mobility amorphous oxide semiconductor In-Ga-Zn-O: Experiment and ab initio calculations," *Physical Review B*, vol. 75, pp. 035212, 2007.
- [60] J. Nishii, F. M. Hossain, S. Takagi, T. Aita, K. Saikusa, Y. Ohmaki, I. Ohkubo, S. KSISHIMOTO, A. Ohtomo and T. Fukumura, "High mobility thin film transistors with transparent ZnO channels," *Japanese Journal of Applied Physics*, vol. 42, pp. L347-L349, 2003.
- [61] R. Navamathavan, C. Choi, E. Yang, J. Lim, D. Hwang, and S. Park "Fabrication and characterizations of ZnO thin film transistors prepared by using radio frequency magnetron sputtering," *Solid-State Electronics*, vol. 52, pp. 813-816, 2008.
- [62] R. Cross, M. M. De Souza, S. C. Deane and N. D. Young, "A comparison of the performance and stability of ZnO-TFTs with silicon dioxide and nitride as gate insulators," *Electron Devices, IEEE Transactions on*, vol. 55, pp. 1109-1115, 2008.
- [63] J. J. Kim, J. Y. Bak, J. H. Lee, H. S. Kim, N. W. Jang, Y. Yun and W. J. Lee, "Characteristics of laser-annealed ZnO thin film transistors," *Thin Solid Films*, vol. 518, pp. 3022-3025, 2010.
- [64] S. Lim, J. M. Kim, D. Kim, C. Lee, J. S. Park and H. Kim, "The Effects of UV Exposure on Plasma-Enhanced Atomic Layer Deposition ZnO Thin Film Transistor," *Electrochemical and Solid-State Letters*, vol. 13, pp. H151-H154, 2010.
- [65] M. Nakata, K. Takechi, T. Eguchi, E. Tokumitsu, H. Yamaguchi and S. Kaneko, "Effects of thermal annealing on ZnO thin-film transistor characteristics and the application of excimer laser annealing in plastic-based ZnO thin-film transistors," *Japanese Journal of Applied Physics*, vol. 48, pp. 1608, 2009.

## List of references

- [66] Y. Yang, S. S. Yang and K. Chou, "Laser-irradiated zinc oxide thin-film transistors fabricated by solution processing," *Journal of the Society for Information Display*, vol. 18, pp. 745-748, 2010.
- [67] P. T. Hsieh, Y. C. Chen, K. S. Kao and C. M. Wang, "Structural and luminescent characteristics of non-stoichiometric ZnO films by various sputtering and annealing temperatures," *Physica B: Condensed Matter*, vol. 403, pp. 178-183, 2008.
- [68] K. Nomura, H. Ohta, K. Ueda, T. Kamiya, M. Hirano and H. Hosono, "Thin-film transistor fabricated in single-crystalline transparent oxide semiconductor," *Science*, vol. 300, pp. 1269-1272, 2003.
- [69] Y. Kikuchi, K. Nomura, H. Yanagi, T. Kamiya, M. Hirano and H. Hosono, "Device characteristics improvement of a-In-Ga-Zn-O TFTs by low-temperature annealing," *Thin Solid Films*, vol. 518, pp. 3017-3021, 2010.
- [70] K. Ide, Y. Kikuchi, K. Nomura, M. Kimura, T. Kamiya and H. Hosono, "Effects of excess oxygen on operation characteristics of amorphous In-Ga-Zn-O thin-film transistors," *Appl. Phys. Lett.*, vol. 99, pp. 093507-093507-3, 2011.
- [71] K. Ide, Y. Kikuchi, K. Nomura and T. K. Hosono, "Effects of low-temperature ozone annealing on operation characteristics of amorphous In-Ga-Zn-O thin-film transistors," *Thin Solid Films*, 2012.
- [72] K. Nomura, T. Kamiya and H. Hosono, "Highly stable amorphous In-Ga-Zn-O thin-film transistors produced by eliminating deep subgap defects," *Appl. Phys. Lett.*, vol. 99, pp. 053505-053505-3, 2011.
- [73] M. Nakata, K. Takechi, K. Azuma, E. Tokumitsu, H. Yamaguchi and S. Kaneko, "Improvement of InGaZnO<sub>4</sub> thin film transistors characteristics utilizing excimer laser annealing," *Applied Physics Express*, vol. 2, pp. 1102, 2009.
- [74] B. Du Ahn, W. H. Jeong, H. S. Shin, D. L. Kim, H. J. Kim, J. K. Jeong, S. H. Choi and M. K. Han, "Effect of excimer laser annealing on the performance of amorphous indium gallium zinc oxide thin-film transistors," *Electrochemical and Solid-State Letters*, vol. 12, pp. H430-H432, 2009.
- [75] H. W. Zan, W. T. Chen, C. W. Chou, C. C. Tsai, C. N. Huang and H. W. Hsueh, "Low temperature annealing with solid-state laser or UV lamp irradiation on amorphous IGZO thin-film transistors," *Electrochemical and Solid-State Letters*, vol. 13, pp. H144-H146, 2010.
- [76] Y. Yang, S. S. Yang and K. Chou, "Characteristic Enhancement of Solution-Processed In-Ga-Zn Oxide Thin-Film Transistors by Laser Annealing," *Electron Device Letters, IEEE*, vol. 31, pp. 969-971, 2010.
- [77] Y. Yang, S. S. Yang and K. Chou, "Performance improvements of IGZO and ZnO thin-film transistors by laser-irradiation treatment," *Journal of the Society for Information Display*, vol. 19, pp. 247-252, 2011.
- [78] K. Wasa, M. Kitabatake and H. Adachi, *Thin Film Materials Technology: Sputtering of Compound Materials*. William Andrew, 2004.

## List of references

- [79] M. Maqbool. Growth, characterization and luminescence and optical properties of rare-earth elements and transition metals doped in wide bandgap nitride semiconductors. Ohio University, 2005.
- [80] W. R. Grove, "On the electro-chemical polarity of gases," *Philosophical Transactions of the Royal Society of London*, vol. 142, pp. 87-101, 1852.
- [81] I. Langmuir, "The mechanism of the surface phenomena of flotation," *Transactions of the Faraday Society*, vol. 15, pp. 62-74, 1920.
- [82] J. S. Chapin, "PLANAR MAGNETRON," *Research-Development*, vol. 25, pp. 37, 1974.
- [83] S. Campbell, "The Science Engineering of Microelectronic Fabrication". Oxford University press, 2001.
- [84] H. Morkoç and Ü. Özgür, *Zinc Oxide: Fundamentals, Materials and Device Technology*. Vch Verlagsgesellschaft Mbh, 2009.
- [85] D. Song, "Effects of rf power on surface-morphological, structural and electrical properties of aluminium-doped zinc oxide films by magnetron sputtering," *Appl. Surf. Sci.*, vol. 254, pp. 4171-4178, 2008.
- [86] E. Fortunato, P. Barquinha, A. Pimentel, L. Pereira, G. Goncalves and R. Martins, "Amorphous IZO TFTs with saturation mobilities exceeding 100 cm<sup>2</sup>/Vs," *Physica Status Solidi (RRL)–Rapid Research Letters*, vol. 1, pp. R34-R36, 2007.
- [87] S. Wakeham, M. Thwaites, B. Holton, C. Tsakonas, W. Cranton, D. Koutsogeorgis and R. Ranson, "Low temperature remote plasma sputtering of indium tin oxide for flexible display applications," *Thin Solid Films*, vol. 518, pp. 1355-1358, 2009.
- [88] D. C. Look, D. Reynolds, C. Litton, R. Jones, D. Eason and G. Cantwell, "Characterization of homoepitaxial p-type ZnO grown by molecular beam epitaxy," *Appl. Phys. Lett.*, vol. 81, pp. 1830, 2002.
- [89] M. Purica, E. Budianu, E. Rusu, M. Danila and R. Gavrilă, "Optical and structural investigation of ZnO thin films prepared by chemical vapor deposition (CVD)," *Thin Solid Films*, vol. 403, pp. 485-488, 2002.
- [90] X. Sun and H. Kwok, "Optical properties of epitaxially grown zinc oxide films on sapphire by pulsed laser deposition," *J. Appl. Phys.*, vol. 86, pp. 408-411, 1999.
- [91] E. Przeździecka, W. Paszkowicz, E. Łusakowska, T. Krajewski, G. Łuka, E. Guziewicz and M. Godlewski, "Photoluminescence, electrical and structural properties of ZnO films, grown by ALD at low temperature," *Semiconductor Science and Technology*, vol. 24, pp. 105014, 2009.
- [92] K. Ellmer, "Magnetron sputtering of transparent conductive zinc oxide: relation between the sputtering parameters and the electronic properties," *J. Phys. D*, vol. 33, pp. R17, 2000.
- [93] E. Valeron, "Sputtering Advance Reaches the Target," *Vacuum Solutions (IOP Publishing Ltd., 2000)*, pp. 23, 2000.

## List of references

- [94] A. Flewitt, J. Dutson, P. Beecher, D. Paul, S. Wakeham, M. Vickers, C. Ducati, S. Speakman, W. Milne and M. Thwaites, "Stability of thin film transistors incorporating a zinc oxide or indium zinc oxide channel deposited by a high rate sputtering process," *Semiconductor Science and Technology*, vol. 24, pp. 085002, 2009.
- [95] A. Yeadon, S. Wakeham, H. Brown, M. Thwaites, M. Whiting and M. Baker, "Remote plasma sputtering of indium tin oxide thin films for large area flexible electronics," *Thin Solid Films*, vol. 520, pp. 1207-1211, 2011.
- [96] S. Wakeham, M. Thwaites, C. Tsakonas, W. Cranton, R. Ranson, G. Boutaud and D. Koutsogeorgis, "A new reactive sputtering technique for the low temperature deposition of transparent light emitting ZnS: Mn thin films," *Physica Status Solidi (a)*, vol. 207, pp. 1614-1618, 2010.
- [97] S. Wakeham, C. Tsakonas, W. Cranton, M. Thwaites, G. Boutaud and D. Koutsogeorgis, "Laser annealing of thin film electroluminescent devices deposited at a high rate using high target utilization sputtering," *Semiconductor Science and Technology*, vol. 26, pp. 045016, 2011.
- [98] D. Basting and G. Marowsky, *Excimer Laser Technology*. Berlin ; London: Springer/Praxis, 2005.
- [99] R. M. Ranson, *Investigation into Thermographic Phosphors*. Nottingham Trent University, 1999.
- [100] D. Heiman, "Photoluminescence spectroscopy," Northeastern University, 2004.
- [101] T. H. Gfroerer, "Photoluminescence in analysis of surfaces and interfaces," 2006.
- [102] B. Lin, Z. Fu and Y. Jia, "Green luminescent center in undoped zinc oxide films deposited on silicon substrates," *Appl. Phys. Lett.*, vol. 79, pp. 943-945, 2001.
- [103] B. Fultz and J. M. Howe, *Transmission Electron Microscopy and Diffractometry of Materials*. Springer Verlag, 2007.
- [104] L. Reimer and H. Kohl, *Transmission Electron Microscopy: Physics of Image Formation*. Springer Verlag, 2008.
- [105] I. M. Watt, *The Principles and Practice of Electron Microscopy*. Cambridge. A: Cambridge Univ. Press, 1989.
- [106] D. K. Schroder, *Semiconductor Material and Device Characterization*. John Wiley & Sons, 2006.
- [107] B. B. He, *Two-Dimensional X-Ray Diffraction*. John Wiley & Sons Inc, 2009.
- [108] C. Suryanarayana and M. G. Norton, "X-ray diffraction: a practical approach," *Microscopy and Microanalysis*, vol. 4, pp. 513-515, 1998.
- [109] B. D. Cullity and S. Stock, *Elements of X-Ray Diffraction*. Prentice Hall, 2002.
- [110] C. HAMMOND, "The basics of crystallography & diffraction (Paper)," 2009.

## List of references

- [111] J. C. Vickerman and I. S. Gilmore, *Surface Analysis: The Principal Techniques*. Wiley Online Library, 2009.
- [112] L. B. Valdes, "Resistivity measurements on germanium for transistors," *Proceedings of the IRE*, vol. 42, pp. 420-427, 1954.
- [113] E. H. Hall, "On a new action of the magnet on electric currents," *American Journal of Mathematics*, vol. 2, pp. 287-292, 1879.
- [114] D. S. Ginley, *Handbook of Transparent Conductors*. Springer, 2010.
- [115] Y. Wang, S. Lau, X. Zhang, H. Hng, H. Lee, S. Yu and B. Tay, "Enhancement of near-band-edge photoluminescence from ZnO films by face-to-face annealing," *J. Cryst. Growth*, vol. 259, pp. 335-342, 2003.
- [116] P. Hsieh, Y. Chen, K. Kao and C. Wang, "Structural effect on UV emission properties of high-quality ZnO thin films deposited by RF magnetron sputtering," *Physica B: Condensed Matter*, vol. 392, pp. 332-336, 2007.
- [117] K. K. Kim, J. H. Song, H. J. Jung, W. K. Choib, S. J. Park and J. H. Song, "The grain size effects on the photoluminescence of ZnO-Al<sub>2</sub>O<sub>3</sub> grown by radio-frequency magnetron sputtering," *J. Appl. Phys.*, vol. 87, 2000.
- [118] T. Matsumoto, H. Kato, K. Miyamoto, M. Sano, E. A. Zhukov and T. Yao, "Correlation between grain size and optical properties in zinc oxide thin films," *Appl. Phys. Lett.*, vol. 81, pp. 1231, 2002.
- [119] H. Ong, A. Li and G. Du, "Depth profiling of ZnO thin films by cathodoluminescence," *Appl. Phys. Lett.*, vol. 78, pp. 2667, 2001.
- [120] V. Roy, A. Djurišić, W. Chan, J. Gao, H. Lui and C. Surya, "Luminescent and structural properties of ZnO nanorods prepared under different conditions," *Appl. Phys. Lett.*, vol. 83, pp. 141, 2003.
- [121] C. H. Ahn, Y. Y. Kim, D. C. Kim, S. K. Mohanta and H. K. Cho, "A comparative analysis of deep level emission in ZnO layers deposited by various methods," *J. Appl. Phys.*, vol. 105, pp. 013502-013502-5, 2009.
- [122] L. Wu, Y. Wu, X. Pan and F. Kong, "Synthesis of ZnO nanorod and the annealing effect on its photoluminescence property," *Optical Materials*, vol. 28, pp. 418-422, 2006.
- [123] A. Janotti and Van de Walle, Chris G, "Native point defects in ZnO," *Physical Review B*, vol. 76, pp. 165202, 2007.
- [124] H. Haneda, I. Sakaguchi, A. Watanabe, T. Ishigaki and J. Tanaka, "Oxygen diffusion in single-and poly-crystalline zinc oxides," *Journal of Electroceramics*, vol. 4, pp. 41-48, 1999.
- [125] H. Ong, J. Dai, K. Hung, Y. Chan, R. Chang and S. Ho, "Electronic structures of polycrystalline ZnO thin films probed by electron energy loss spectroscopy," *Appl. Phys. Lett.*, vol. 77, pp. 1484-1486, 2000.

## List of references

- [126] T. Yen, D. Strome, S. J. Kim, A. N. Cartwright and W. A. Anderson, "Annealing studies on zinc oxide thin films deposited by magnetron sputtering," *J Electron Mater*, vol. 37, pp. 764-769, 2008.
- [127] Y. Zhao and Y. Jiang, "Effect of KrF excimer laser irradiation on the properties of ZnO thin films," *J. Appl. Phys.*, vol. 103, pp. 114903-114903-4, 2008.
- [128] H. Lu, Y. Tu, X. Lin, B. Fang, D. Luo and A. Laaksonen, "Effects of laser irradiation on the structure and optical properties of ZnO thin films," *Mater Lett*, vol. 64, pp. 2072-2075, 2010.
- [129] K. Kim, S. Kim and S. Y. Lee, "Effect of excimer laser annealing on the properties of ZnO thin film prepared by sol-gel method," *Current Applied Physics*, vol. 12, pp. 585-588, 2012.
- [130] J. O. Barnes, D. J. Leary and A. Jordan, "Relationship between deposition conditions and physical properties of sputtered ZnO," *J. Electrochem. Soc.*, vol. 127, pp. 1636-1640, 1980.
- [131] P. Carcia, R. McLean and M. Reilly, "Oxide engineering of ZnO thin-film transistors for flexible electronics," *Journal of the Society for Information Display*, vol. 13, pp. 547-554, 2005.
- [132] A. Suresh, P. Gollakota, P. Wellenius, A. Dhawan and J. F. Muth, "Transparent, high mobility InGaZnO thin films deposited by PLD," *Thin Solid Films*, vol. 516, pp. 1326-1329, 2008.
- [133] O. Agyeman, C. Xu, W. Shi, X. Zheng and M. Suzuki, "Strong ultraviolet and green emissions at room temperature from annealed ZnO thin films," *Japanese Journal of Applied Physics*, vol. 41, pp. 666-669, 2002.
- [134] P. Hsieh, Y. Chen, K. Kao and C. Wang, "Structural effect on UV emission properties of high-quality ZnO thin films deposited by RF magnetron sputtering," *Physica B: Condensed Matter*, vol. 392, pp. 332-336, 2007.
- [135] A. Chatterjee, C. Shen, A. Ganguly, L. Chen, C. Hsu, J. Hwang and K. Chen, "Strong room-temperature UV emission of nanocrystalline ZnO films derived from a polymeric solution," *Chemical Physics Letters*, vol. 391, pp. 278-282, 2004.
- [136] Y. R. Jang, K. Yoo and S. M. Park, "Rapid thermal annealing of ZnO thin films grown at room temperature," *Journal of Vacuum Science & Technology A*, vol. 28, pp. 216-219, 2010.
- [137] B. Li, Y. Liu, D. Shen, J. Zhang, Y. Lu and X. Fan, "Effects of RF power on properties of ZnO thin films grown on Si (001) substrate by plasma enhanced chemical vapor deposition," *J. Cryst. Growth*, vol. 249, pp. 179-185, 2003.
- [138] Y. J. Kim, Y. T. Kim, H. K. Yang, J. C. Park, J. I. Han, Y. E. Lee and H. J. Kim, "Epitaxial growth of ZnO thin films on R-plane sapphire substrate by radio frequency magnetron sputtering," *Journal of Vacuum Science & Technology A: Vacuum, Surfaces, and Films*, vol. 15, pp. 1103-1107, 1997.

## List of references

- [139] C. Aita, R. Lad and T. Tisone, "The effect of rf power on reactively sputtered zinc oxide," *J. Appl. Phys.*, vol. 51, pp. 6405-6410, 1980.
- [140] L. Wu, Y. Wu, X. Pan and F. Kong, "Synthesis of ZnO nanorod and the annealing effect on its photoluminescence property," *Optical Materials*, vol. 28, pp. 418-422, 2006.
- [141] J. Lee, D. Lee, D. Lim and K. Yang, "Structural, electrical and optical properties of ZnO: Al films deposited on flexible organic substrates for solar cell applications," *Thin Solid Films*, vol. 515, pp. 6094-6098, 2007.
- [142] J. Hoon, K. Chan and T. Tou, "Zinc oxide films deposited by radio frequency plasma magnetron sputtering technique," *Ceram. Int.*, 2012.
- [143] G. A. Kumar, M. R. Reddy and K. N. Reddy, "Effect of substrate temperature on structural and optical properties of nanostructured ZnO thin films grown by RF magnetron sputtering," in *Nanoscience, Engineering and Technology (ICONSET), 2011 International Conference on*, 2011, pp. 56-60.
- [144] H. Chang, K. Huang, C. Chu, S. Chen, T. H. Huang and M. Wu, "Low-resistivity and high-transmittance indium gallium zinc oxide films prepared by co-sputtering In<sub>2</sub>Ga<sub>2</sub>ZnO<sub>7</sub> and In<sub>2</sub>O<sub>3</sub> targets," *ECS Transactions*, vol. 28, pp. 137-148, 2010.
- [145] Y. Yoshino, K. Inoue, M. Takeuchi and K. Ohwada, "Effects of interface micro structure in crystallization of ZnO thin films prepared by radio frequency sputtering," *Vacuum*, vol. 51, pp. 601-607, 1998.
- [146] P. Prepelita, R. Medianu, B. Sbarcea, F. Garoi and M. Filipescu, "The influence of using different substrates on the structural and optical characteristics of ZnO thin films," *Appl. Surf. Sci.*, vol. 256, pp. 1807-1811, 2010.
- [147] M. Oh, S. Kim, D. Hwang, S. Park and T. Seong, "Formation of Low Resistance Nonalloyed Ti/ Au Ohmic Contacts to n-Type ZnO by KrF Excimer Laser Irradiation," *Electrochemical and Solid-State Letters*, vol. 8, pp. G317-G319, 2005.
- [148] A. Takagi, K. Nomura, H. Ohta, H. Yanagi, T. Kamiya, M. Hirano and H. Hosono, "Carrier transport and electronic structure in amorphous oxide semiconductor, a-InGaZnO<sub>4</sub>," *Thin Solid Films*, vol. 486, pp. 38-41, 2005.
- [149] R. Martins, E. Fortunato, P. Barquinha and L. Pereira, *Transparent Oxide Electronics: From Materials to Devices*. Wiley, 2012.
- [150] V. Assuncao, E. Fortunato, A. Marques, H. Aguas, I. Ferreira, M. Costa and R. Martins, "Influence of the deposition pressure on the properties of transparent and conductive ZnO: Ga thin-film produced by rf sputtering at room temperature," *Thin Solid Films*, vol. 427, pp. 401-405, 2003.
- [151] P. Carcia, R. McLean and M. Reilly, "Oxide engineering of ZnO thin-film transistors for flexible electronics," *Journal of the Society for Information Display*, vol. 13, pp. 547-554, 2005.

## List of references

- [152] J. Chang, H. Wang and M. Hon, "Studying of transparent conductive ZnO: Al thin films by RF reactive magnetron sputtering," *J. Cryst. Growth*, vol. 211, pp. 93-97, 2000.
- [153] M. Nakata, K. Takechi, S. Yamaguchi, E. Tokumitsu, H. Yamaguchi and S. Kaneko, "Effects of excimer laser annealing on InGaZnO<sub>4</sub> thin-film transistors having different active-layer thicknesses compared with those on polycrystalline silicon," *Jpn J Appl Phys*, vol. 48, pp. 115505-115505-6, 2009.
- [154] P. M. C. Barquinha, "Transparent oxide thin-film transistors: production, characterization and integration," University of Lisbon 2010.

## Appendices

### Appendix A: Derivation of TFT Drain current at linear regime

From Figure A-1 by applying the gradual channel approximation (GCA) assumption  $y$  is parallel to the channel, and the carrier density per unit area in the channel depends on  $y$  or in other words on the potential  $V(y)$ , whereas  $x$  is the direction perpendicular to the active layer[7].

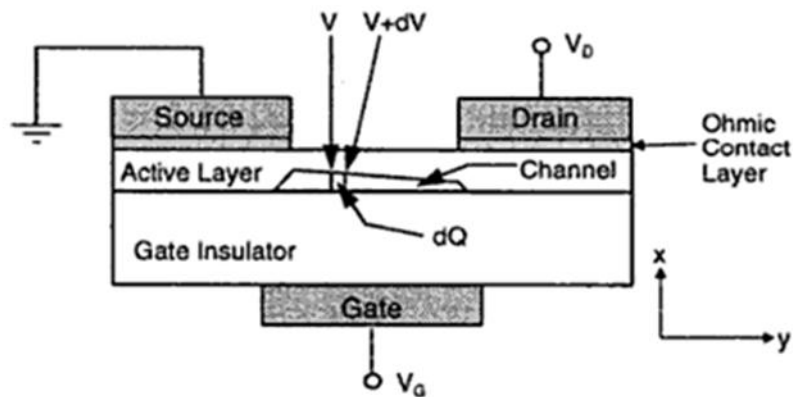


**Figure A-1:** Cross-sectional view of the channel region of a TFT used to drive gradual channel approximation [7].

Let us consider the case of gate voltage being higher than threshold voltage  $V_{th}$ , in  $y$  direction, the mobile charge  $Q_i$  is given by:

$$Q_i = -C_o (V_G - V_{thY}) \quad (A.1)$$

Where:  $C_o$  : is the capacitance per unit area of gate dielectric.

$V_{thY}$  : the threshold voltage in  $y$  direction.

Now let us assume the channel potential  $V$  is zero, then the induced charge  $Q_i$  is a function of  $y$ , then equation (1.A) becomes as:

$$Q_i = -C_o (V_G - V_{thY} - V) \quad (A.2)$$

## Appendices

We can now begin developing the expression for current – voltage characteristics. The current induced by the majority carrier density along the channel can be given as:

$$I_D = W \mu_{ny} Q_i E_y \quad (\text{A.3})$$

Where: W: is the width of the TFT channel

$\mu_{ny}$ : is the carrier mobility

$E_y$ : is the electric field in y direction.

$$J_n = \frac{I_n}{A} = q \left( \frac{\mu_n n E + D_n \frac{dn}{dy}}{dy} \right) \quad (\text{A.4})$$

From five equation approximation to ignore the diffusion term ( $D_n \frac{dn}{dy}$ ). The current caused only by drift current, and taking the integration for both sides.

$$I_D = \frac{W}{L} \mu_{ny} \int_0^L Q_i \, dy \quad (\text{A.5})$$

By substituting  $Q_i$  from equation (A.2) in equation (A.5) above:

$$I_D = - \frac{W}{L} \mu_{ny} \int_0^L C_O (V_G - V_{thy} - V) \, dy \quad (\text{A.6})$$

By integration of the current increment from  $y=0$  to  $L$ , which is from  $V=0$  to  $V_D$ , we obtain the gradual channel expression for the drain current:

$$I_D = C_O \mu_{ny} \frac{W}{L} \left[ (V_G - V_{thy}) V_D - \frac{V_D^2}{2} \right] \quad (\text{A.7})$$

When  $V_D \ll V_G$  then the drain current can be written can be written as:

$$I_D = C_O \mu_{ny} \frac{W}{L} \left[ (V_G - V_{thy}) V_D \right] \quad (\text{A.8})$$

**Appendix B: PL spectra of ZnO deposited at 20% O<sub>2</sub> in Ar ,RT, 2mTorr at various RF powers**

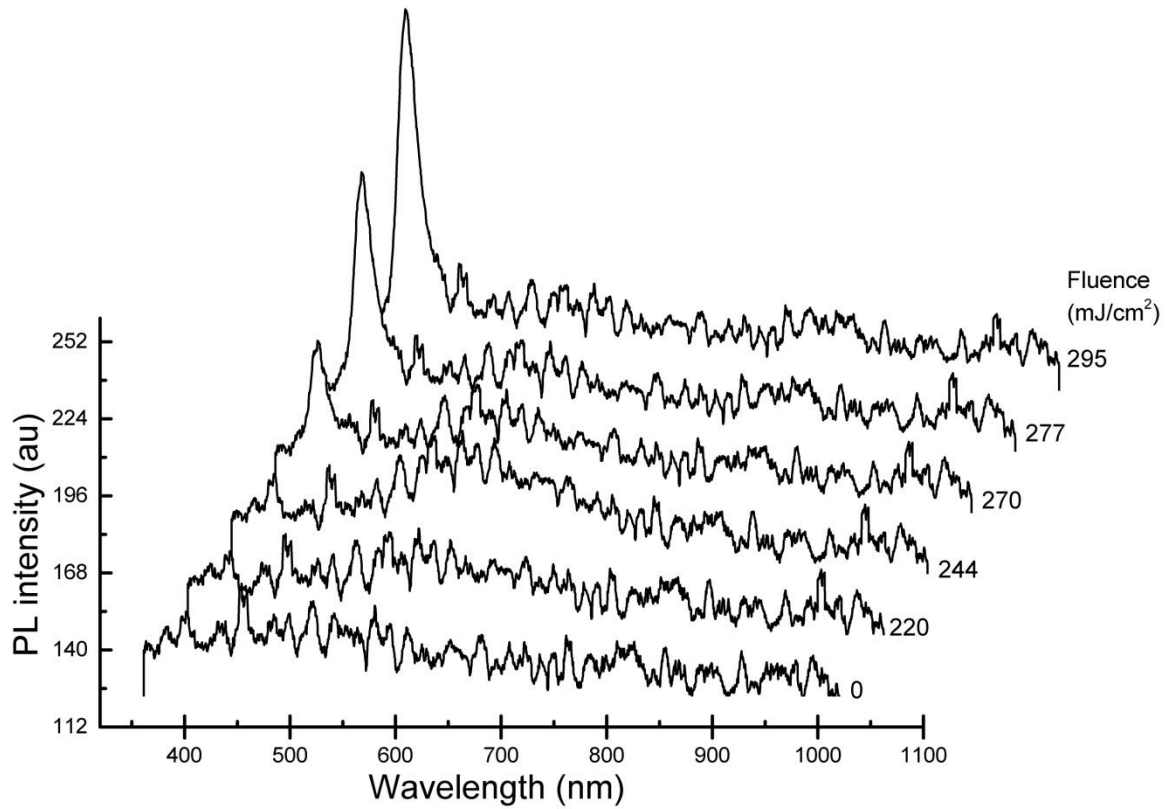


**Figure B-1:** Evolution of PL spectra of laser annealed ZnO deposited at 100W, 20% O<sub>2</sub> in Ar at RT.

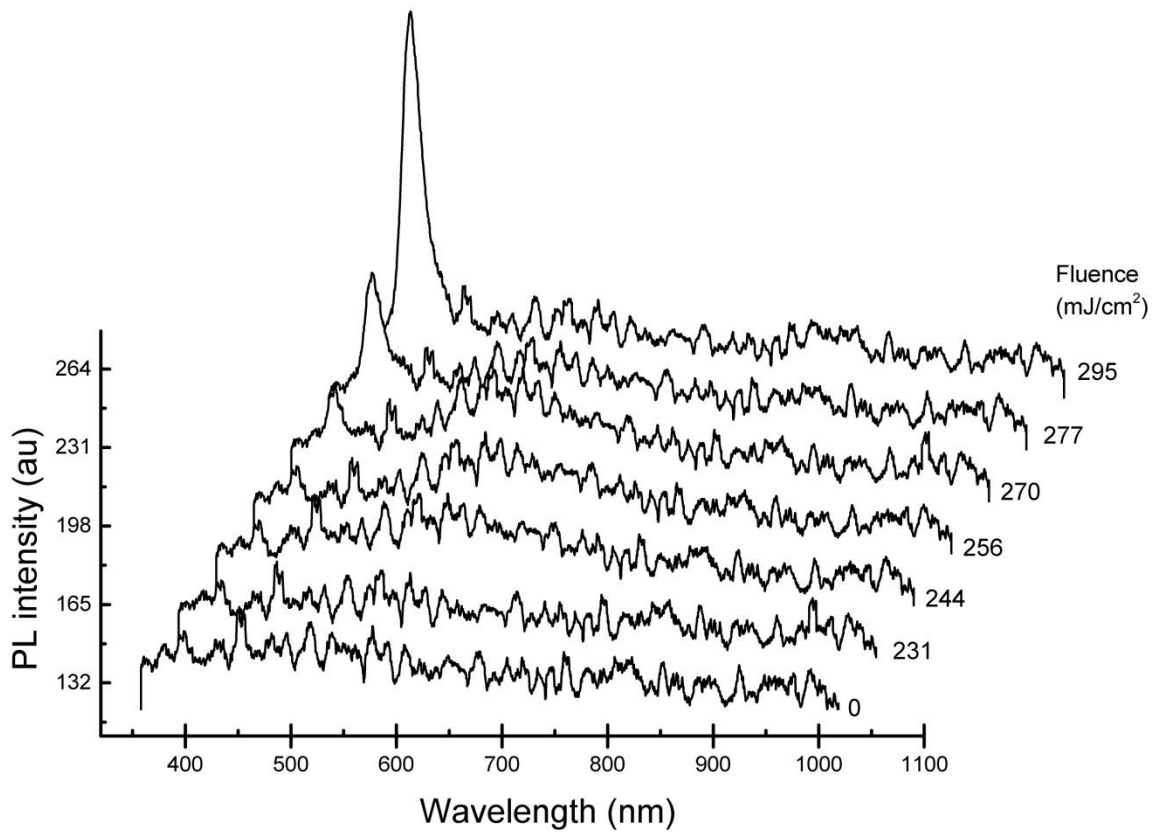


**Figure B-2:** Evolution of PL spectra of laser annealed ZnO deposited at 200W, 20% O<sub>2</sub> in Ar at RT.

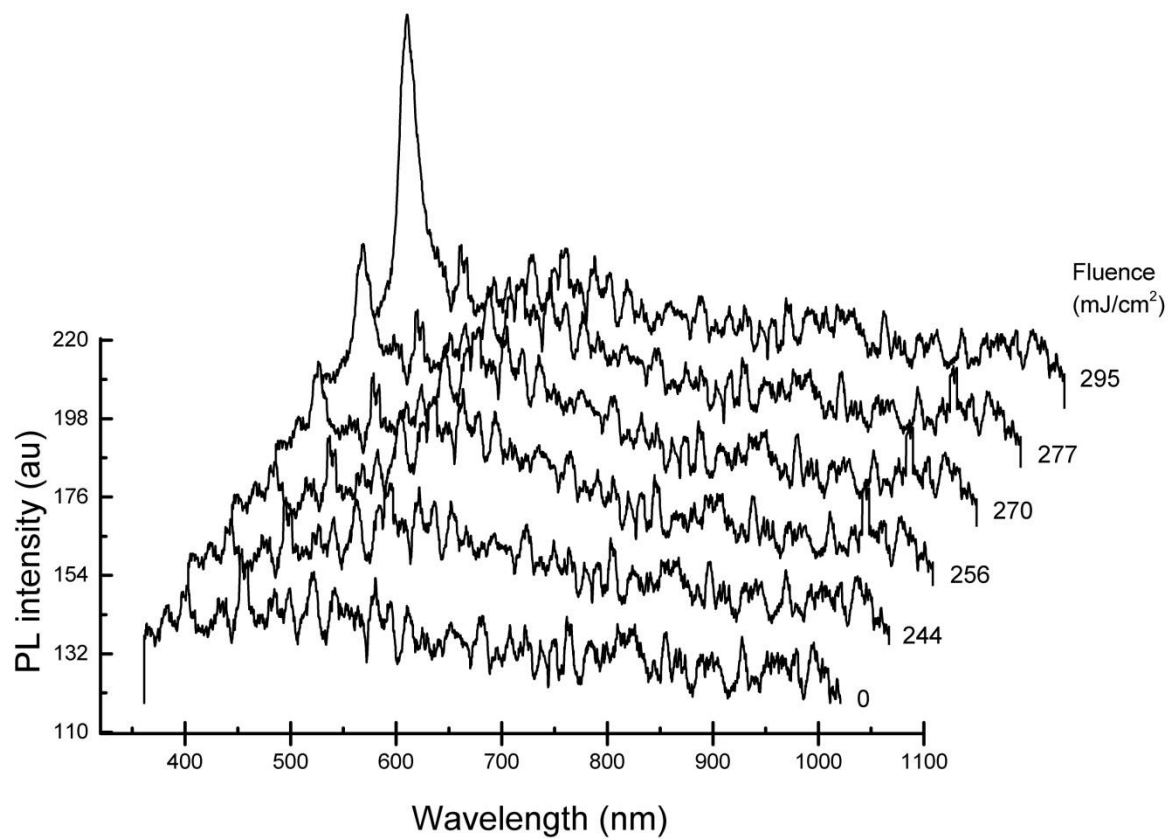


**Figure B-3:** Evolution of PL spectra of laser annealed ZnO deposited at 300W, 20% O<sub>2</sub> in Ar at RT.